Testing and Modeling of Machine Properties in Resistance Welding

Wu, Pei; Bay, Niels Oluf

Publication date:
2004

Document Version
Publisher's PDF, also known as Version of record

Ph.D Dissertation

Testing and Modeling of Machine Properties in Resistance Welding

Pei Wu

Technical University of Denmark

August 2004

Publication No. IPL.161.04
MM.04.41

Ph.D Dissertation

Technical University of Denmark

August 2004

Publication No. IPL.161.04
MM.04.41

PREFACE

This thesis is presented as the requirements of the Danish Ph.D degree at the Technical University of Denmark (DTU).

The work has been carried out from September 2001 to August 2004 at the Department of Manufacturing Engineering and Management (IPL), at the Technical University of Denmark, under supervision of Prof. Dr. Techn. Niels Bay, Associate Prof. Dr. Wenqi Zhang and Prof. Shuoshi Ma.

In this period, a month's stay at De Nayer Institute, Belgium, was included.

I would like to address my sincere thanks to my supervisors, Prof. Niels Bay, Associate professor Wenqi Zhang and Prof. Shuoshi Ma, for their valuable encouragement and discussions on my study, especially their strict academic attitude and conscientious working style have influenced me deeply, which will be of great benefit to me in my future research work.

The project has been financed by the Technical University of Denmark, whose support is most appreciated.

I also wish to thank Patrick V. Rymenant, Rudi V.de Moer and Werner Wandenbussche for receiving me and the cooperative work during my stay at De Nayer Institute, Belgium.

It has been a great pleasure for me to work at IPL, DTU. I appreciate the help of my colleagues. Thanks are due to Dr. Poul Henningsen, Associate professor Jan L. Andreasen, Dr. Lars Kristensen and Lars P. Holmbæck for helping me solving problems in the experiments. Thanks also go to Dr. Quanfeng Song and Dr. David D. Olsson for their valuable discussions. Special thanks are given to secretary Pia Holst Nielsen for her kind assistance in many aspects during my stay in Denmark, as well as to Flemming Jørgensen for his assistance in photographing.

Furthermore, I would like to express my acknowledgements to Associate professor Tonny W. Rasmussen, Associate professor Wulf Oelschlägel, and professor Ole Tønnesen from the Ørsted • DTU, for their valuable advices on the experimental scheme and help with measuring proof resistances.

Also love and gratitude give to my wife Xiuqin Fan and daughter Xiaoyu Wu for their support without complaining me about doing less housework.

Finally, I wish to express my appreciation to all colleagues and friends who have assisted me in my work and life in Denmark.

Pei Wu

Copenhagen

August, 2004

ABSTRACT

The objective of this work has been to test and model the machine properties including the mechanical properties and the electrical properties in resistance welding. The results are used to simulate the welding process more accurately.

The state of the art in testing and modeling machine properties in resistance welding has been described based on a comprehensive literature study.

The present thesis has been subdivided into two parts:

Part I---- mechanical properties of resistance welding machines
Part II---- electrical properties of resistance welding machines

In part I, the electrode force in the squeeze stage has been measured for two machines. It was found that for the same level of electrode force, the pneumatic machine takes longer time to build up and stabilize the force to the static value due to the compressibility of the air. The hydraulic one is very fast to reach and stabilize to the static electrode force, and the time of stabilizing does not depend on the level of the force.

An additional spring mounted in the welding head improves the machine touching behavior due to a soft electrode application, but this results in longer time of oscillation of the electrode force, especially when it is lower than the spring force.

The work in part I is focused on the dynamic mechanical properties of resistance welding machines. A universal method has been developed to characterize the dynamic mechanical behaviour of C-frame machines. The method is based on a mathematical model, in which three equivalent machine parameters were determined, i.e. equivalent moving mass, equivalent damping coefficient and equivalent spring constant. A specially designed breaking test is applied for determining these three parameters. The method, which is confirmed by a series of “supported breaking tests” as well as real projection welding tests, is easy to realize in industry, since tests may be performed in situ.

In part II, an approach of characterizing the electrical properties of AC resistance welding machines is presented, involving testing and mathematical modelling of the weld current, the firing angle and the conduction angle of silicon controlled rectifiers with the aid of a series of proof resistances. The model predicts the weld current and the conduction angle (or heat setting) at each set current, when the workpiece resistance is given.

As a part which was not originally planned, a new approach for determining the dynamic resistance in resistance welding by measuring the voltage on the primary side and the current on the secondary side is suggested. This method increases the accuracy of measurement because of higher signal – noise ratio, and allows in-process application without any wires connected to the electrodes. In order to test the reliability of such an approach, the results are compared with those obtained by the conventional method. Furthermore, the proposed method is used to measure the faying surface contact resistance.

NOMENCLATURE

Mechanical Properties of Resistance Welding Machines

$t_{squeeze}$: Squeeze time;

t_{stable}: Stabilizing time of electrode force;

m: equivalent, lumped moving mass;

b: equivalent damping coefficient;

k: equivalent damping coefficient;

F: total action force delivered by the moving electrode;

F_r: reaction force from the workpiece;

x: relative displacement between electrodes;

n: the number of points in the measuring signal;

L_0: initial length of disk spring;

h: height of the ring;

d: diameter of the pin;

S_0: pre-deflection of the spring;

D_i: inside diameter of disk spring;

D_e: outside diameter of disk spring;

δ: thickness of disc spring;

s: deflection of disc spring;

K: stiffness of disk spring;

Electrical Properties of Resistance Welding Machines

SCR: silicon-controlled rectifiers;

N: transformer turn ratio;

u_1: instantaneous applied voltage;

U_1: magnitude of applied voltage in RMS (peak value = $\sqrt{2}\,U_1$);

ω: natural frequency of the applied voltage;

α: firing angle, angular position of the SCR triggering relative to the applied voltage zero crossing;

φ: power-factor angle;

τ : time constant;

θ: conduction angle of SCR;

R_1: machine primary resistance;

L_1: machine primary inductance;

R_2: machine secondary resistance;

L_2: machine secondary inductance;

R_m: equivalent machine-circuit resistance;

L_m: equivalent machine-circuit inductance;

R_w: workpiece resistance;

R_t: equivalent total resistance, $= R_m + R_w$;

$i(t)$: weld current time function;

L_t: total inductance, $= L_m$;

$\frac{di}{dt}$: current time rate of change;

n: the number of points in the measuring signal;

Z: total impedance;

Z_m: machine circuit impedance;

ΔZ: impedance change;

r_0: radius of conductor;

δ: "skin depth" of conductor;

f: signal frequency (Hz);

μ: permeability of material;

σ: electrical conductivity of material;

ρ: resistivity of material;

R: resistance of conductor;

L: length of the conductor;

A: section area of the conductor;

R_x: unknown resistance;

V: voltage applied to unknown resistance;

I_1: current applied to unknown resistance;

X_L: machine inductive reactance;

ΔX_L: change of inductive reactance;

CONTENTS

Chapter 1

Introduction to Resistance Welding

In this chapter, a brief introduction is given to resistance welding technology explaining the basics of the welding process, followed by an overview of the resistance welding machine and the objectives of the present project.

1.1 Basics of Resistance Welding

Resistance welding is a process used to join metallic parts with the welding heat generated by the resistance offered by these parts to the passage of an electrical current. It dates back to more than one century ago. In 1886 E. Thomson [1]. described a melt joint between two metal pieces established due to resistance heating, which was the initiated resistance welding stereotype. Before the turn of the century, butt welding of bars and chains were introduced to industry as the first applications of resistance welding. After more than one hundred years of development, this technology includes a big family of variants, including spot welding, projection welding, seam welding and butt welding. Despite the invention of a number of more exotic welding processes in recent decades, such as laser welding which has replaced some traditional resistance welding applications, the unique advantages of resistance welding have kept as one of the most productive and competitive joining technologies in automotive, aerospace and other metal processing industries. In this report, mainly spot welding and projection welding will be studied [2-6].

1.1.1 Principle of Resistance Welding

The principle of resistance welding is based on Joule heating. The workpieces are clamped between the electrodes by applying an electrode force, then an electric current passes through the top and bottom electrodes and heats the workpieces by Joule heating. When the temperature at the interface reaches the melting point of the material, a molten nugget begins to form and grow. When the welding current is switched off, this nugget will solidify to form a weld that joins the workpieces together. The generated heat is expressed as the following equation according to Joule's law:

$$Q(t) = \int_0^T R(t) \cdot I^2(t) \cdot dt \qquad (1\text{-}1)$$

Where

Q = heat developed [J]

R = ohmic resistance [Ω]
I = welding current [A]
t = time [s]
T = total weld time [s]

It can be seen that the resistance of the materials plays an important role in resistance welding. For example, there are seven different ohmic resistances in resistance spot welding, as shown in Fig. 1.1, which are:

- R_1, R_7: resistances of electrodes.
- R_2, R_6: electrode-workpiece contact resistance, which depends on the surface conditions of both the workpieces and the electrodes, the shape and size of the electrodes as well as the magnitude of the electrode force.
- R_4: workpiece-workpiece faying surface contact resistance, which depends on the surface condition of the materials, with or without coating layer, and the level of the electrode force.
- R_3, R_5: base material resistance of workpieces, which depends on the electrical properties of the materials.

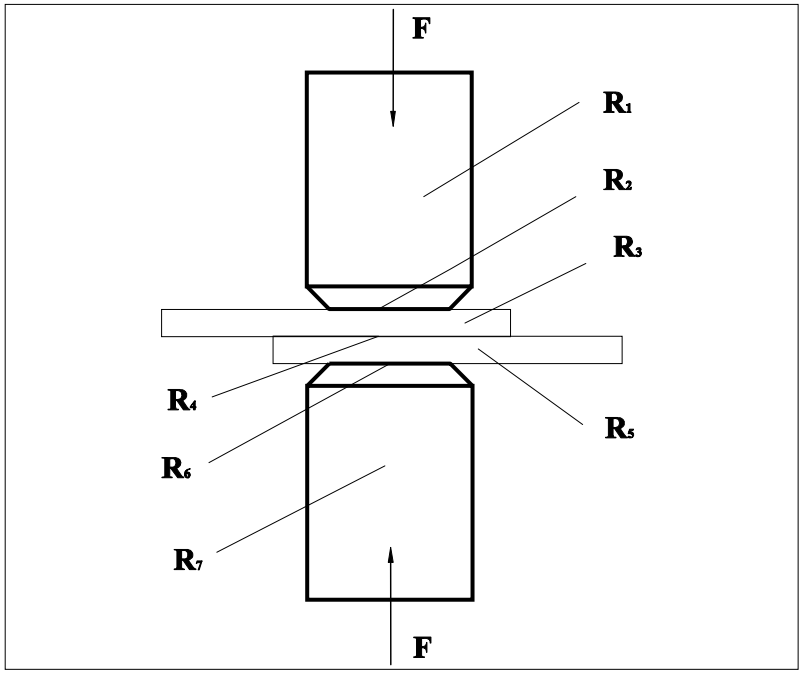

Fig. 1.1 ohmic resistances in resistance spot welding

The resistance distribution and corresponding heat distribution are shown in Fig. 1.2. Among these resistances, R_4 is the highest, but R_3, R_5 have to be high as well (good electrical-conductivity materials are difficult to resistance weld), ensuring that the heat is sufficient for the formation of a weld nugget at the interface between workpieces. Heat will also be generated in other locations mentioned above (R_1, R_7, R_2, and R_6) in proportion to the resistance of each, which is usually useless heat representing the electrical loss. It should be minimized, unless in some special cases where it may be used for improving the heat balance.

One way of minimizing the heat development in and around the electrodes is to use copper alloys for the electrodes, because copper alloy has good electrical and thermal conductivities. Another way is by using water-cooling inside the electrodes.

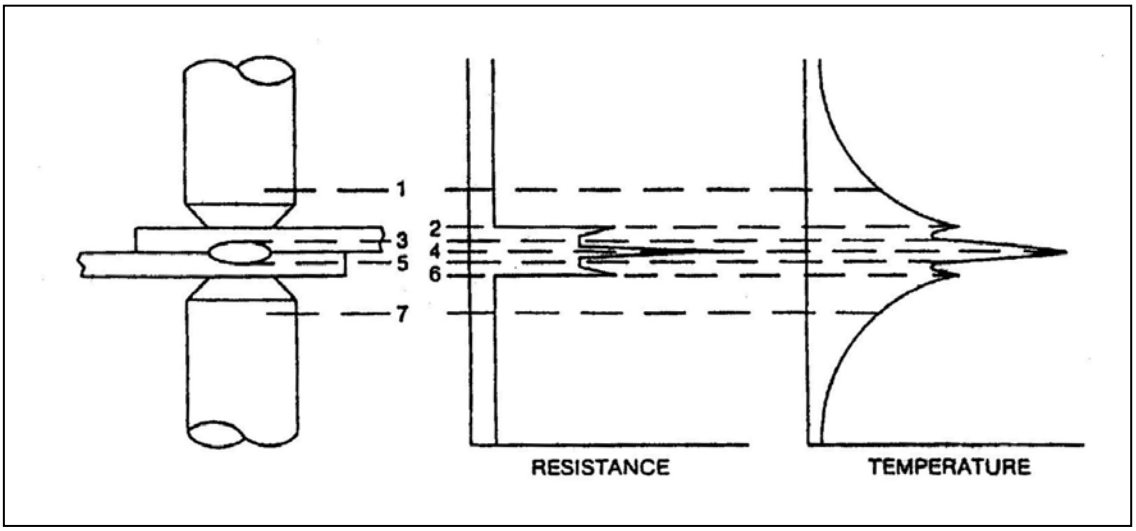

Fig. 1.2 Resistance and heat distributions in resistance spot welding

1.1.2 Process of Resistance Welding

Taking the resistance spot welding as an example, a typical welding process is broken down into three distinct periods [7], as shown in Fig. 1.3.

- **Squeeze time.** The electrodes come together and the parts to be joined are compressed between the electrodes, the compression force is built up to a specified amount before the current is passed through.

- **Weld time.** In this period, the weld current is applied, the metals are being heated enough to melt and fuse together to form what is called a weld nugget. The force is continuously applied and the deformation of workpieces continues.

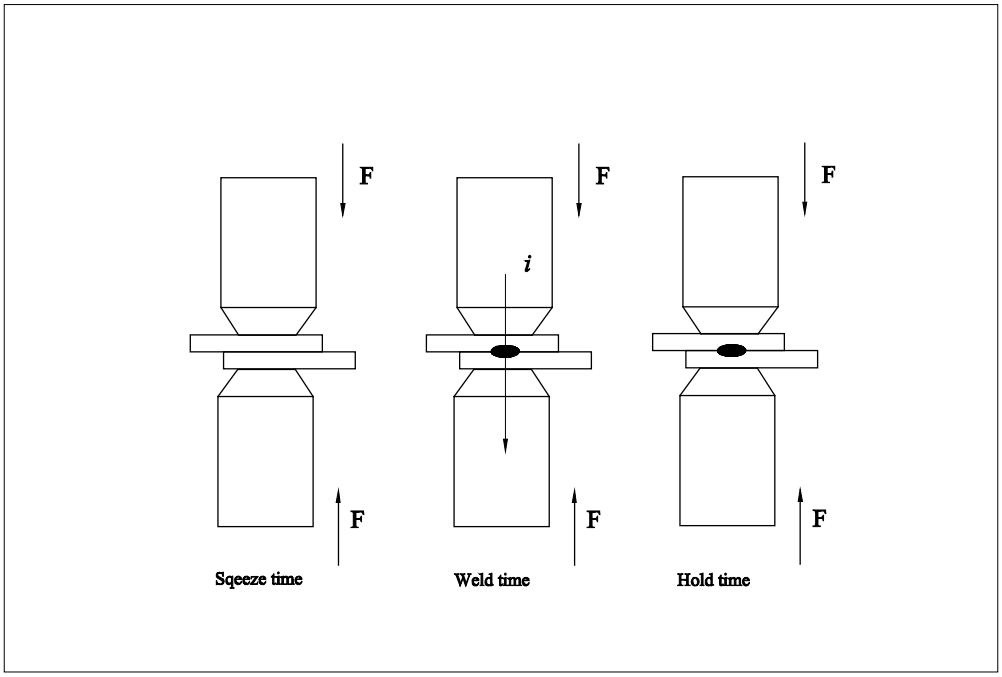

Fig. 1.3 — Process of resistance spot welding

- **Hold time.** The weld current is ceased but the electrode force is still applied. During this period, the weld nugget cools and the metals are forged under the force of the electrodes. The continuing electrode force helps to keep the weld intact until it solidifies, cools, and weld nugget reaches its adequate strength before the electrode force is finally released.

1.2 Spot and Projection Welding Machines

In making a resistance weld, the machine used must deliver the correct amount of current, localize it at the point where welding is desired and apply the proper pressure at the correct time. The transformer and electrode system must also be cooled due to the heat generated using high current in resistance welding. Therefore, a resistance welding machine is basically composed of following systems:

- Electrical system
- Mechanical system
- Control system
- Cooling system

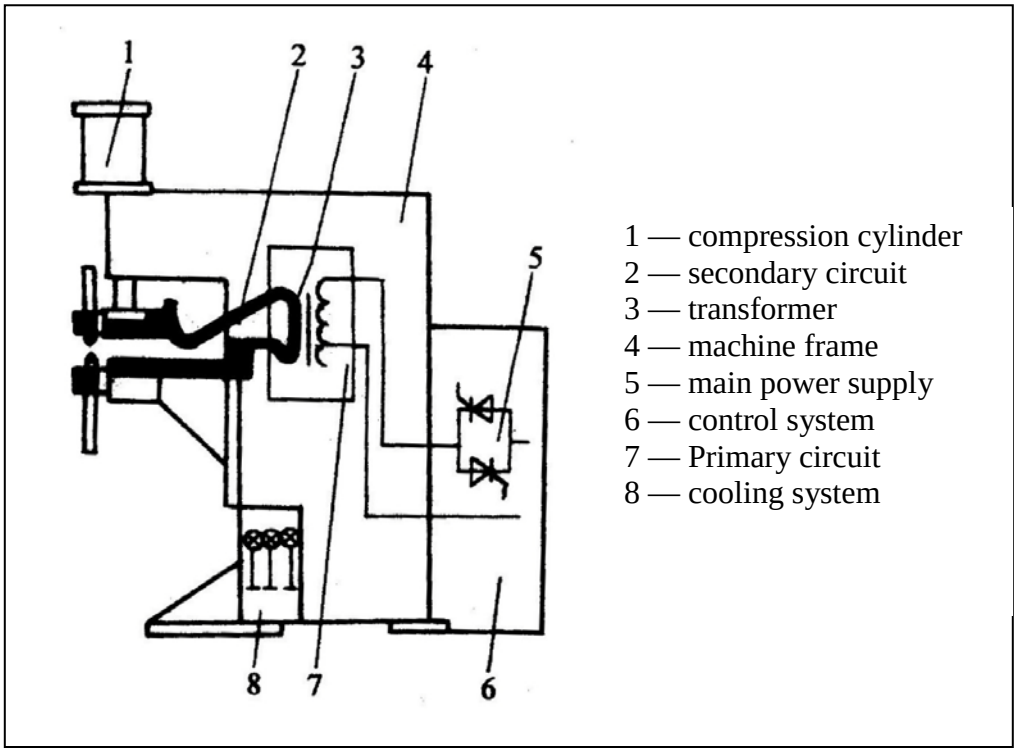

Fig. 1.4 — Sketch of spot welding machine

A sketch of resistance spot welding machine is shown in Fig. 1.4.

1.2.1 Electrical System

The electrical system of resistance welding machine supplies electrical power to the weld in high current and low voltage, the major parts are the welding transformer and the secondary circuit including the electrodes which conduct the welding current to the work. According to the electrical operation, the welding machines are classified as AC, DC and CD machines, which utilize alternating current, direct current and current from capacitor discharge, respectively.

1.2.1.1 AC Resistance Welding Machine

Most resistance welding machines are single-phase AC machines. This is the type of machine most commonly used, because it is the simplest and least expensive in initial costs, installation and maintenance. The electrical circuit is shown in Fig. 1.5 - A. The power from the single phase of main power is applied to the primary side of the welding transformer through a switch (anti-phase dual silicon-controlled rectifiers), converted by

the transformer and output high current (low voltage) on the secondary side. The profile of welding current is as shown in Fig. 1.5-B.

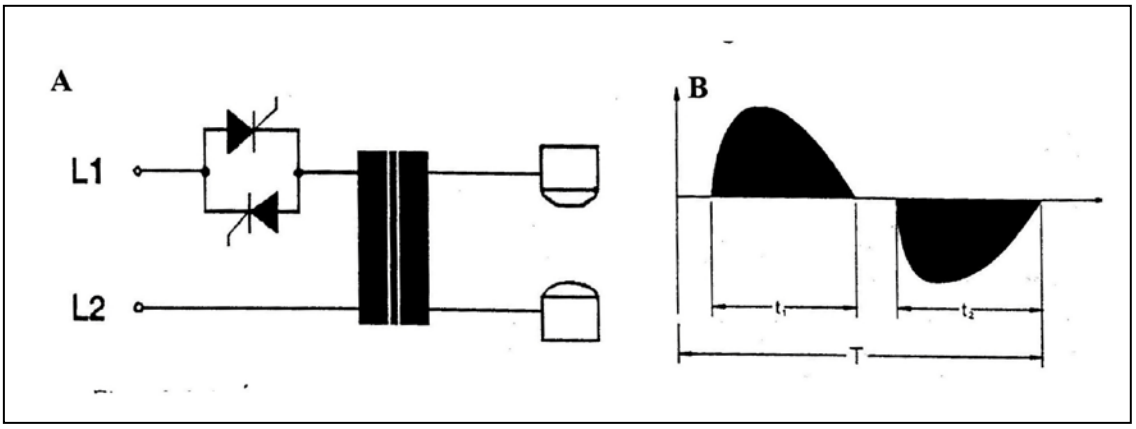

Fig. 1.5 ***A*** *— Sketch diagram of electrical circuit of single-phase AC machine;* ***B****— Welding current profile of single-phase AC machine.*

In AC resistance welding, the welding current flows with positive and negative half cycles, there is zero heat or current between these two half cycles. This is called cycling, which can cause some undesirable effects in welding smaller and thinner parts, where the weld time is typically under 3 cycles, because the weld may cools effectively between the half cycles, this will result in loss of the heat required to make a good weld.

Another negative effect of cycling is that when the heat is not applied constantly throughout the duration of the weld, the nugget growth can be irregular. Variations in the weld nugget are directly related to the quality and strength of a weld.

Other AC disadvantages are unbalanced line loading and lower power factors due to the inherent inductive reactance in the machine.

1.2.1.2 CD Resistance Welding Machine

The capacitor discharge type of resistance welding machine utilizes capacitor, charging the energy from the main power source to a specific level. The total capacitor energy is released in a very short time to the weld through a welding transformer, producing the current required to make the welding. Fig. 1.6 shows the electrical circuit and weld current profile of this type of machine. A three phase AC power supply is rectified to DC by means of a rectifier, and this direct current is fed into a capacitor, the energy is stored in the capacitor until the circuit is interrupted by a thyristor.

One advantage of the CD resistance welding machine compared with the AC machines is that it has a higher power factor and balanced line loading because of the three-phase power supply. Another advantage is that there is no cycling as in AC machines and the

current is applied directly to the work pieces without any heat loss. The CD resistance welding machine is advantageous when welding formulation requires high current in a short weld time such as in some projection welding applications.

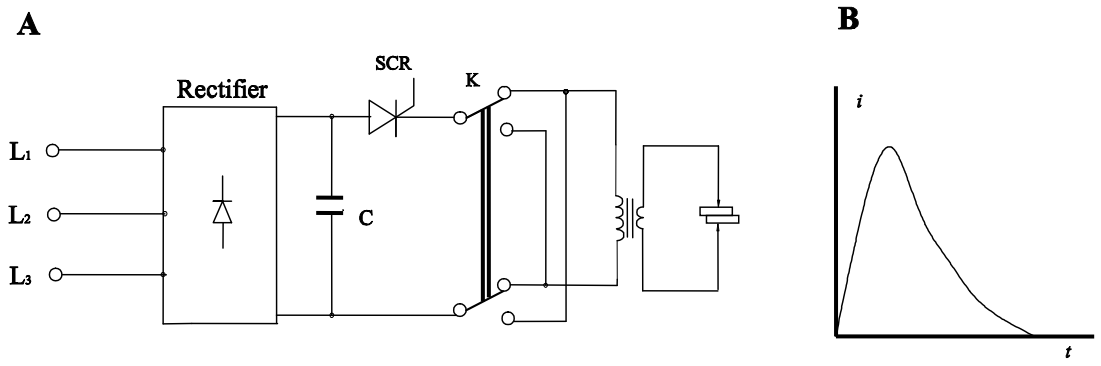

Fig. 1.6 ***A*** *— electrical circuit of CD machine;*
B *— Profile of weld current;*

Capacitor discharge type of resistance welding machines have, however, limitations. One of the limitations is speed. The power supplies need time to raise the charge of the capacitors to the level at which they can supply the required energy to make the weld. In many automated systems, poor and inconsistent welds can occur if welding is attempted before the capacitors are fully charged. Another limitation is that the welding current waveform is limited to that of a capacitor discharging a high current for a short amount of time, typically under 2 cycles. This release of energy over a short period of time can cause excessive weld splash and surface burning. Also the capacitor has a big size, high cost and short service life, so the CD machines are mainly low volt-ampere resistance welding machines.

1.2.1.3 DC Resistance Welding Machine

▪ DC Inverter Machine

Inverter machine is a new type of resistance welding machine developed in the 1980s, its electrical circuit is as shown as Fig. 1.7. The incoming three-phase AC current passes through a rectifier bridge which changes or rectifies the current to a DC current, which is then fed into a capacitor placed across the DC bus, filtering out the noise and minimizing the ripple effect left over from the rectification process, providing a more steady and constant DC reference current. This DC reference current is inverted by the inverter to provide a bi-polar square wave with middle frequency, for example, 1000 Hz or 2000 Hz. The transformer converts the high voltage down and low current up before it comes to a pair of diodes (rectifier) which rectify the bi-polar wave form to keep the current flowing in one direction. Finally, a DC current with little ripple is output to the work.

DC inverter resistance welding machine has many advantages over both AC and capacitor discharge type machines. Compared to AC machines, it has the advantage of no off-time, no unbalanced line loading and no inductive losses, thus having high efficiency of heat put to the parts. It operates at high frequency, thus the size and weight of the transformer can be smaller and lighter. The response time is fast, thus the feedback can be used to realize the constant-current control, which is the most important advantage [8].

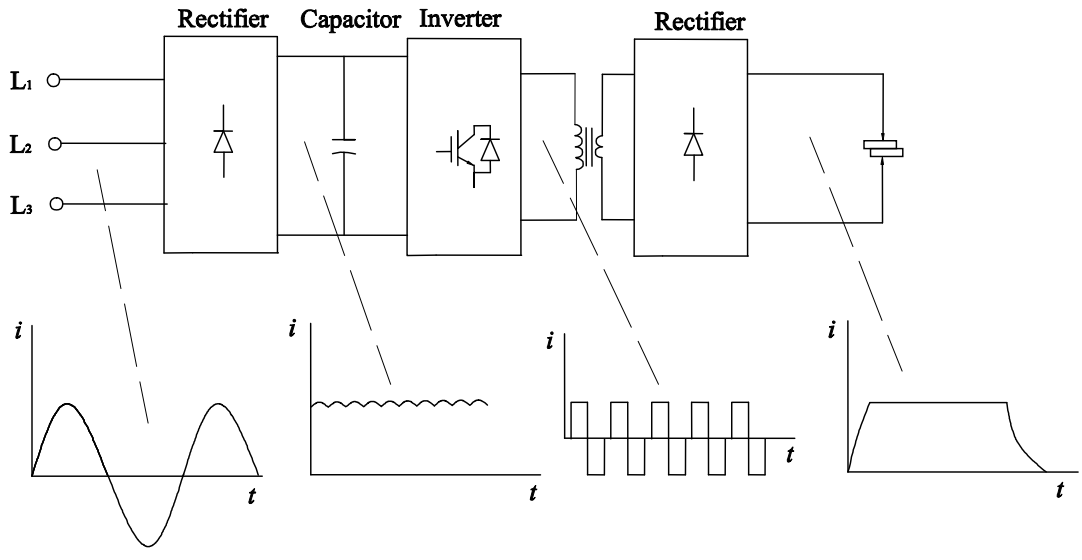

Fig. 1.7 — Electrical circuit of inverter resistance machine

▪ DC Rectifier Machine

Most rectifier type of machines are powered in three-phase. The incoming power is input at the primary of the transformer, and the output at the secondary of the transformer is fed into a rectifier bank, then the rectifiers provide the DC current to the welding circuit. The profile of welding current is as shown in Fig. 1.8. Some machines use half-wave rectification as shown in Fig. 1.9(A), in this case, the transformer secondary is wye connected. Other machines have full-wave rectification with the transformer secondary connected in delta arrangement as shown in Fig. 1.9(B).

For this type of machine, it has the same advantages as DC inverter machine characterized by three-phase input and DC-current output, which includes: balanced line loading, no inductive loss and higher power factor. The heat efficiency is also higher due to no zero current crossing as in the AC machine.

The DC rectifier machine needs higher-power diodes, so the size is large and the costs are high. The machine is consuming more energy during the conduction.

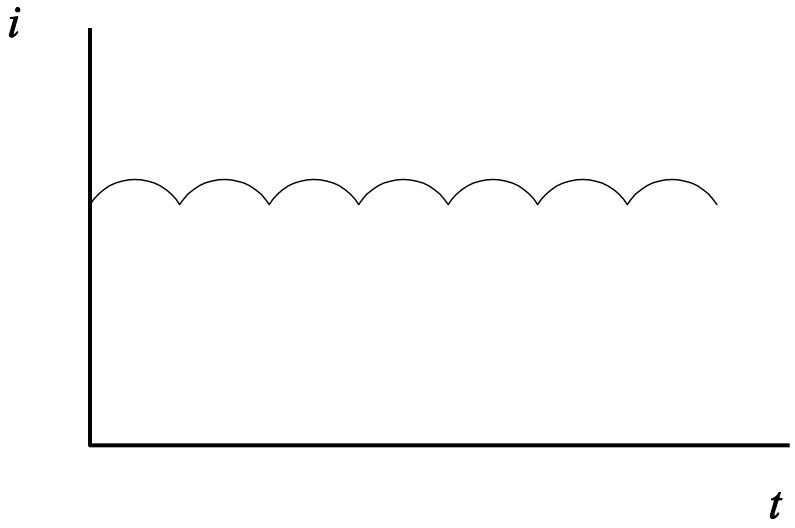

Fig. 1.8— Circuit profile of inverter resistance welding machine

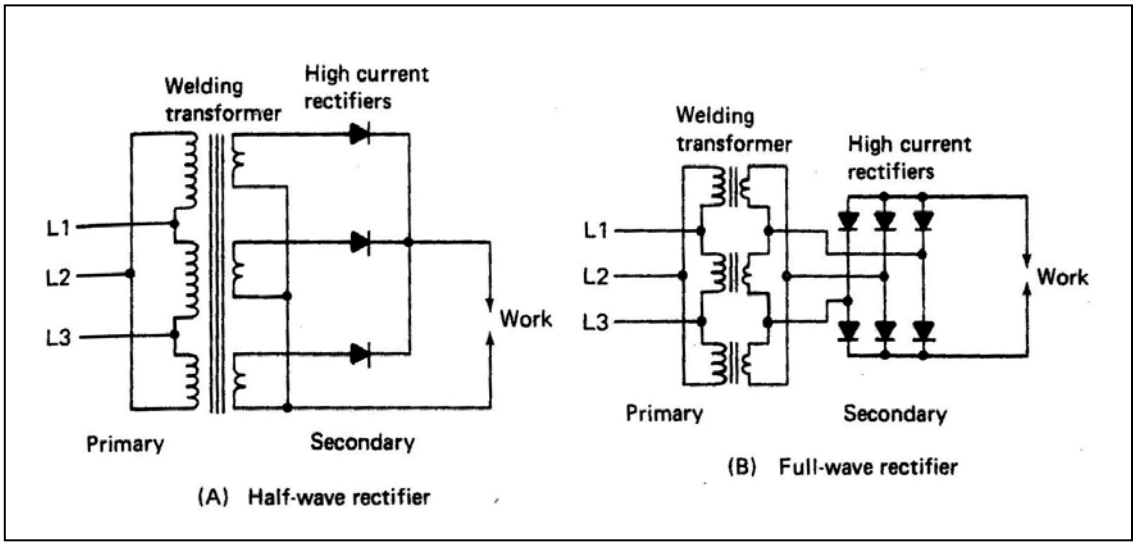

Fig. 1.9 — Electrical circuit of inverter resistance welding machine

1.2.2 Mechanical System

The mechanical system of resistance welding machines is used to hold the workpiece and apply the welding force. For all types of welding machines, the mechanical system and secondary circuit designs are essentially the same, the major parts include pneumatic or hydraulic mechanisms, machine frame and some associated accessories. A general overview of each part is shown in Fig. 1.10. The following sections will mainly focus on the characteristics of resistance welding machines with air-operated mechanism and hydraulic mechanism.

1.2.2.1 Air-Operated Machines

Air-operated machines are the most popular type. It is mainly used for small size of machines, under 300 kVA, because when high forces are required, air cylinders and valves will be quite large, operation will be slow, and air consumption will be high.

Compared to hydraulic operation, the air machines can operate very rapidly and are easily set up for welding, providing much faster electrode follow-up because of the compressibility of air. The fast electrode follow-up is particularly important when spot and projection welding relatively thin sections, this will be discussed in more detail later. In addition, air-operated machines are low in noise during the operation.

Generally, three types of double-acting air cylinders are employed. These are illustrated in Fig. 1.11. In all these cases, air for the pressure stroke enters at port **A** and exhaust at port **B**. For the return stroke, the air enters at port **B** and exhaust at port **A**.

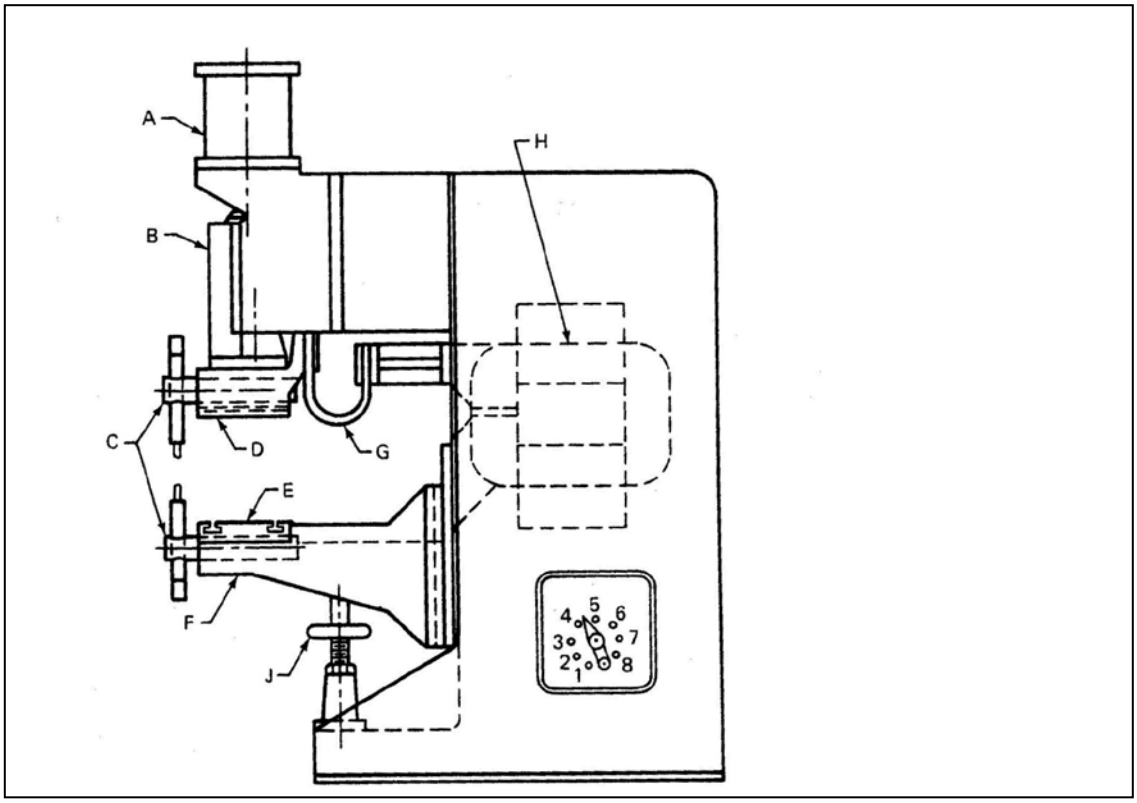

A - air or hydraulic cylinder
B - ram
C - spot welding attachment
D - upper platen
E - lower platen
F - knee
G - flexible conductor
H - transformer secondary
J - knee support

Fig. 1.10 — Overview of mechanical system of spot and projection welding machine

Fig. 1.11 (A) shows a fixed-stroke cylinder with stroke adjustment. The adjuster **K** adjusts the limits of the travel of piston **P** and electrode opening.

Figure 1.11 (B) shows an adjustable-stroke cylinder with a dummy piston. The dummy piston **R** is attached to the adjusting screw **K** which positions this piston. Chamber **L** is connected to port **A** through the hollow adjusting screw. The stroke of the force piston **P** is adjusted by the position of the dummy piston **R** above it. This cylinder design responds faster than a fixed-stroke cylinder because the volume **L** above piston **P** can be made smaller than that of a fixed-stroke cylinder of the same size.

Figure 1.11 (C) shows an adjustable-retractable stroke cylinder. With this type, a third port **X** is connected to chamber **H** above the dummy piston **R.**

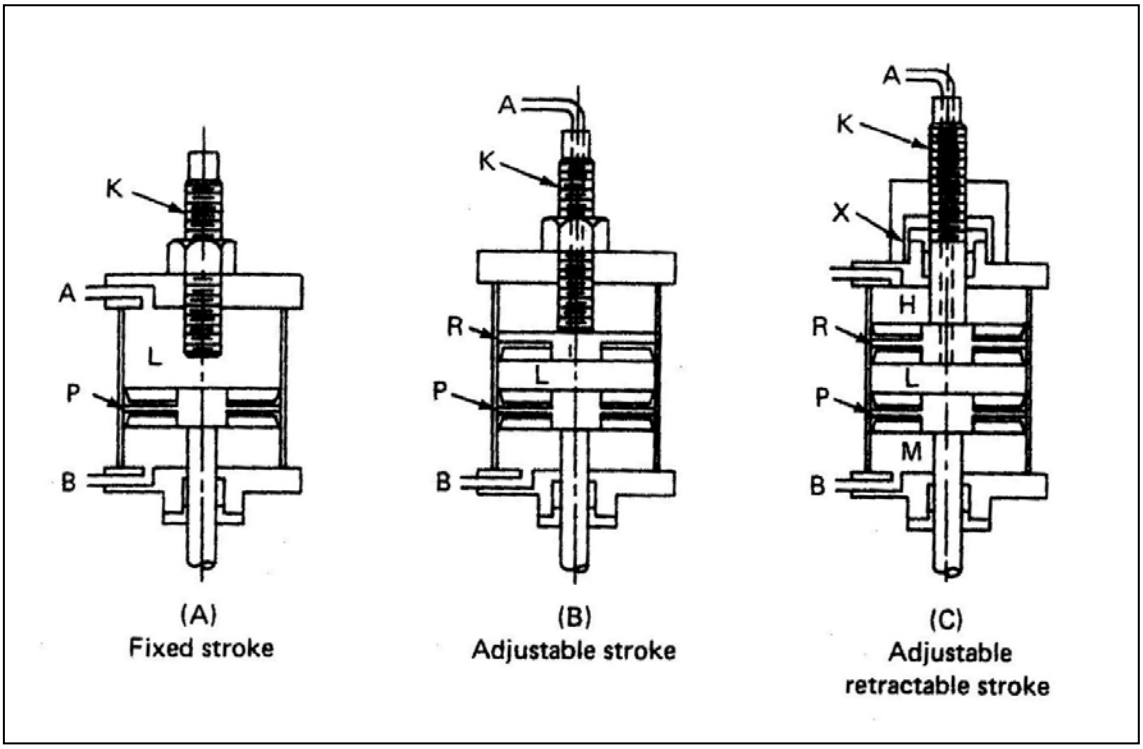

Fig. *1.11 — Air cylinders in resistance welding machines*

1.2.2.2 Hydraulic Machines

The designs for hydraulic cylinders are generally similar to those for air operated cylinders (Fig. 1.10), the difference is that the hydraulic cylinders are generally smaller in diameter because the high pressures can be developed with a fluid system.

As mentioned above, the hydraulic system makes a heavier noise from the pump during the operation, the operation and response speeds are slower due to nearly no compressibility of hydraulic fluids, any movement of the piston needs the fluid filling the whole system.

1.2.3 Control System

The objectives of the control system of welding machines are basically to:

- Provide signals to control machine actions, making the machine working automatically following the sequence of welding steps.
- Start and stop the flow current to the welding transformer.

- Control the magnitude of the current.

Furthermore, in recent years, the new-developed control systems even have the functions of on-line monitoring the welding quality. In servo-driven spot weld gun, the force is also controlled using the feedback control system.

There are three general groups of controls:

- Timing and sequencing controls
- Welding contactors
- Auxiliary controls

The timing and sequencing control is to control the sequence and duration of the steps of a complete resistance welding cycle. The basic steps are: Squeeze time, weld time, hold time and off time.

The contactor is used to close and open the primary power line to the welding transformer, working like a switch. For example, the silicon-controlled rectifiers (SCR) are the common devices for switching the single-phase AC resistance welding machine, as shown in Fig. 1.12.

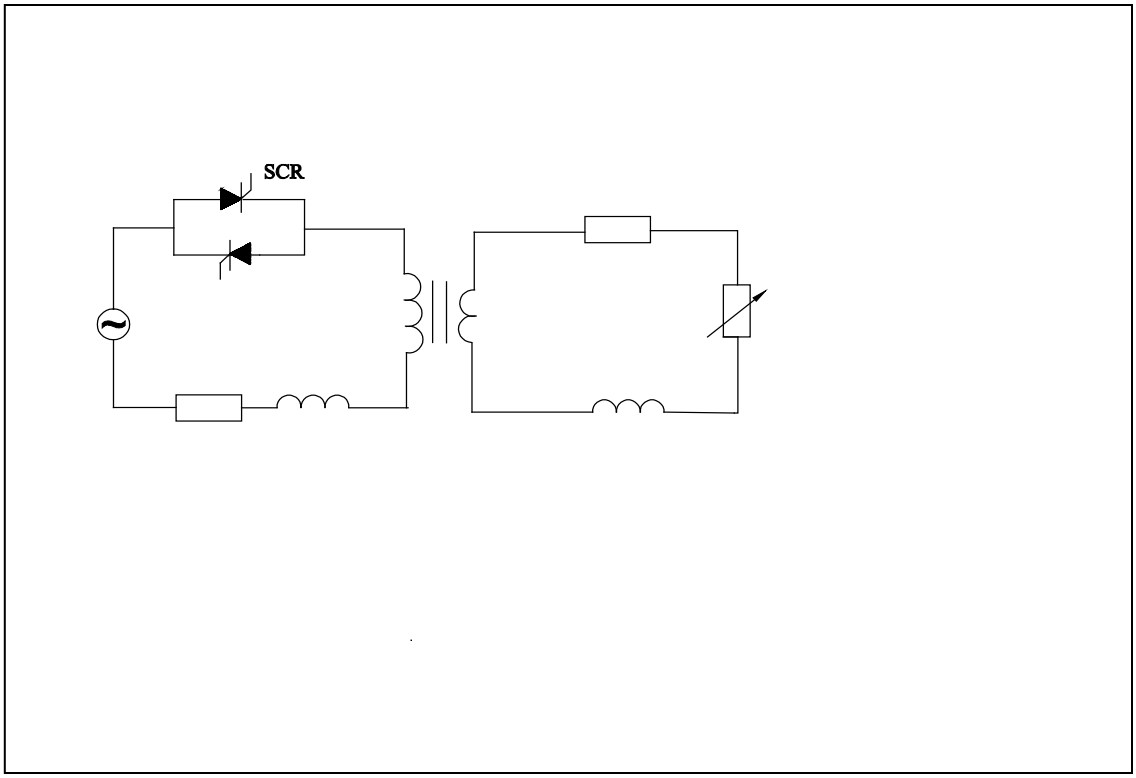

Fig. 1.12 An equivalent circuit of AC single-phase machine

The auxiliary controls are used to control the heat or current output of the welding machine, including adjustable taps on the welding transformer primary and electronic heat control circuit. A tap switch changes the ratio of transformer turns for major adjustment of welding current, while the electronic heat control is used for intermediate setting or fine adjustment of current. In AC single-phase machines, the electronic heat control circuit is used to control the firing angle or conduction angle of SCR for adjusting the welding current. (see Fig. 1.13).

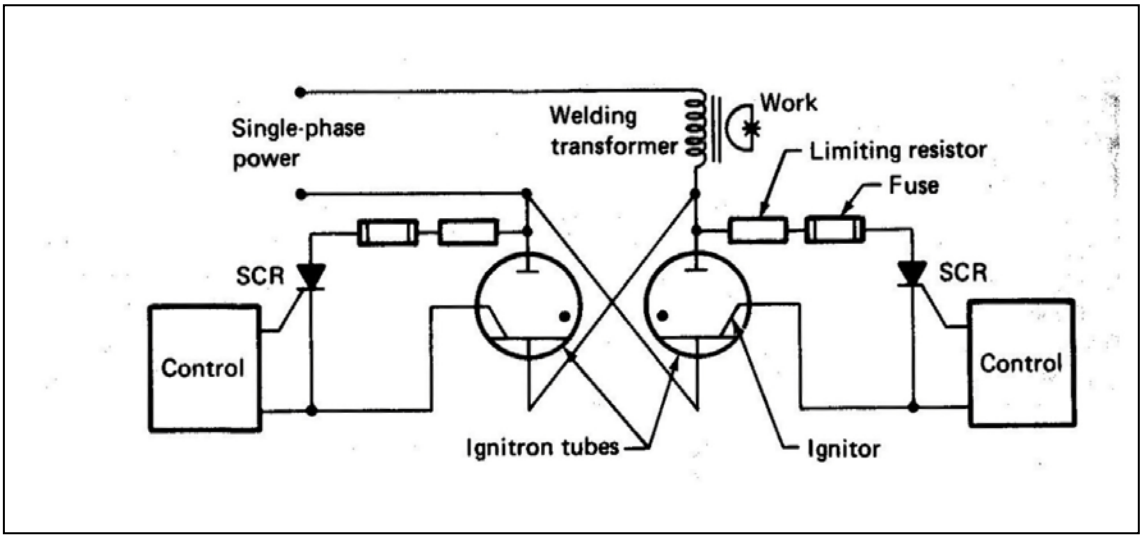

Fig. 1.13 — Electronic heat control circuit of AC single-phase machine

1.2.4 Cooling System

Most resistance welding machines use water cooling, the elements needed cooling include: SCR, secondary coil of welding transformer, welding circuit and electrodes. A closed-loop cycling system with distillation water is commonly used as the cooling system for resistance welding equipments.

Part I

Mechanical Properties of Resistance Welding Machines

Chapter 2

Literature Review and Objectives of New Investigation on Mechanical Properties of Resistance Welding Machines

2.1 Introduction

As mentioned earlier, a resistance spot welding or projection welding machine consists of two major subsystems: mechanical and electrical. The characteristics of the mechanical subsystem, such as moving mass, machine stiffness and friction, play significant roles in functionality and performance of a welding machine, and subsequently influence the choice of optimum welding parameter ranges, the scatter of the quality of the weld joints and electrode service life. Due to its importance and complexity, it has drawn much attention in several decades.

2.2 A Review on Mechanical Machine Properties

According to published literature, research on the effect of mechanical properties of spot welding machines started around 1940 [10], and it has been paid more attention since the 1980s. Most of the early researches were focused on the dynamic mechanical properties.

The static machine properties are specified in ISO 669 standard [11] from 1981 and no marked changes and modifications have been noticed so far.

2.2.1 Static Mechanical Properties

The ISO standard [11] specifies the contact defects, including eccentricity or horizontal shift of the electrode (***g***) and deviation of electrodes (***α***), in resistance spot or seam welding machines**,** see Fig. 2.1. It illustrates the definition and corresponds either to two aspects of the figure or to two successive loads as represented by the following formulae:

$g = b - a$, (***g*** expressed in millimeter)

$\alpha = \alpha_1 - \alpha_2$ (***α*** expressed in radians)

Fig. 2.2 specifies the contact fault in projection welding as a result of machine deformations. For any electrode force, the eccentricity ***h,*** between the clamping plates obtained by application of the nominal electrode force in relation to the unloaded state, and deviations of electrode ***α,*** being given by the formulae:

$h = b_1 - b_2$ (in millimeter)

$$\alpha = \frac{b_1 - b_2}{100} \quad \text{(in radians)}$$

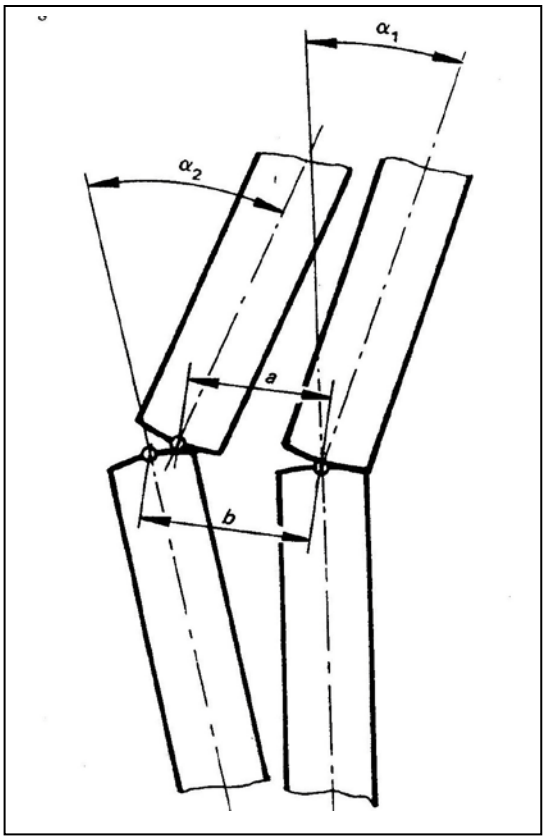

Fig. 2.1 — Contact defects in resistance Spot or seam welding

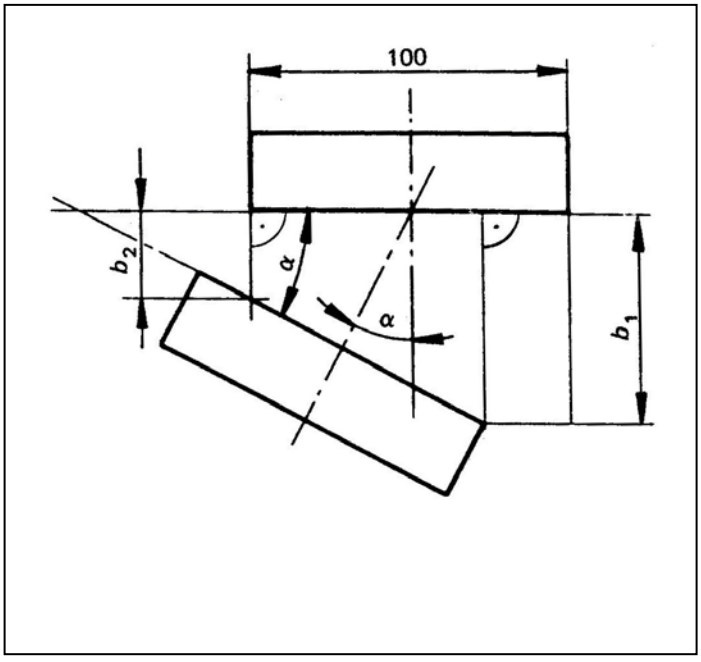

Fig. 2.2 — Contact defect in projection welding

The general test conditions for measuring these terms are recommended, the test machine should be adjusted in such a way that maximum stroke of the electrode, maximum throat depth and maximum throat gap, the load should be at 10%-50%-100% of the maximum electrode force.

The results obtained are given for each value of the force. However, this proposed standard does not yet determine the quantitative values of these effects and their permissible boundaries.

2.2.2 Dynamic Mechanical Properties

In about 1940, research was first published describing the problems associated with the dynamic mechanical properties of resistance spot welding machines. W. F. Hess and R. A. Wyant investigated the influence of the weight of the moving electrode element and friction between the electrode bits and welding jig on electrode control during electric current switch on for press type spot welding machines (which were then the latest type) [10]. From the results it was concluded that these factors influenced the welding pressure and consistency of results for different electrodes.

Satoh and Katayama (in 1965) carried out a research into the effects of the mechanical properties of a spot welding machine on the upper electrode stroke. They concluded that the spot welding of aluminum alloy was greatly influenced by the stroke of the upper electrode [12].

In 1970s, some works dealing with the differences in machine types were published. For example, Granowski and Williams investigated the influence of machine type on electrode life for welding zinc-coated steels [13]. Kolder and Bosman studied the influence of equipment on the weld lobe diagrams of HSLA steel [14]. Satoh and his coworkers concluded that the machine type was an important factor in weld performance based on their experiments on four types of welding machines [15, 16].

Since 1984 [17], focus has been on the individual dynamic mechanical machine properties.

2.2.2.1 The Factors Affecting the Dynamic Mechanical Properties of Resistance Welding Machines

The dynamic mechanical properties of resistance welding machines are normally considered to be governed by the following factors [10, 18-20]:

a) *The mass of the moving electrode elements.* The moving masses determine the inertia of moving electrode elements. Not only should the pistons with their sealing elements, the piston rod and fixing plate be considered as part of those masses, but also the other moving parts, such as the current leads.

b) *The friction between the moving and stationary electrode parts*. The frictional forces have a damping effect on the system during all motive processes. The dominant friction force appears between piston rods and cylinder wall, acting as the sliding friction force in case of sliding guides, and rolling friction force in case of rolling guides. Further friction forces may appear in the spring assemblies and the current leads.

c) *The rigidity of the welding machine*. The rigidity of the machine influences the dynamic mechanical machine properties acting as the elastic forces. It is determined by the stiffness of piston rod, the upper and lower electrode arms, the machine frame and lower arm support. Additionally to these must be added the effect of the compressed air in the cylinder and eventually that of an additional spring assembly.

d) *The air/hydraulic compression system*. This involves the filling and emptying of the cylinder, and thus influences the electrode force. The properties of the compression system are determined by all the devices of the pressure circuit, such as the properties of valves, fluid properties and piping, etc.

2.2.2.2 Effects of Dynamic Mechanical Properties on Weld Process and Weld Quality

Satoh and Katayama (in 1987) [21] manufactured a spot welding machine with four types of configurations for experimental use, as shown in Fig 2.3:

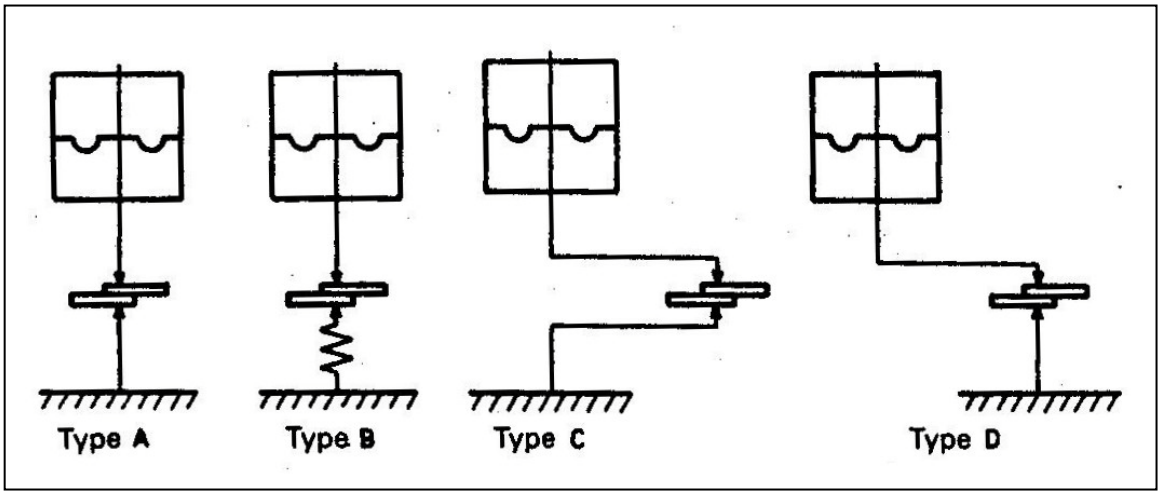

Fig. 2.3— Four types of spot welding machine configuration for experimentation

- **Type A:** Direct electrode force applied from upper electrode and high rigidity of lower electrode;
- **Type B:** Direct electrode force applied from upper electrode and low rigidity of lower electrode which was supported by a coil spring;
- **Type C:** Eccentric electrode force applied from upper electrode and low rigidity in both upper and lower electrode arms;
- **Type D:** Eccentric electrode force applied from upper electrode and different rigidity in upper and lower electrode arms;

For all of these four arrangements (with different force loading way and electrodes stiffness), the effects of moving mass and friction upon weld quality (nugget diameter) and electrode life were examined. The tests were carried out by welding cold rolled steel plates of thickness 0.8 mm under the different combinations of moving mass and friction.

It was concluded that the moving mass exerts little influence on nugget diameter but the influence of friction is considerable. But when upper and lower electrode arms have low rigidity (in type B, C, D), the influence of friction on nugget diameter is small. This was explained by the fact that even if friction on the electrode bit is high there will be an easy flow of metal from the thermally expanded weld along the direction of the electrode axis.

Regarding the electrode life, it was concluded that the impact energy between the electrode and the member is an important factor, which is related to moving mass, friction as well as the stiffness of electrode arms. However, when rigidity of the electrode arms is low (Type B, C, D), no big difference of effects of moving mass and friction on electrode life was observed. This was explained as the effects of these two factors are being absorbed by the low rigidity of the electrodes. The effects of the compression system properties were not discussed in this report.

Hahn et al. (in 1990)[22] designed an experimental device for robot use based on single-phase alternating current spot welding tongs, on which the moving masses were varied by adding extra mass. The stiffness was adjusted by using a specially designed spring unit, and different variation in friction was obtained by replacing the welding cylinders. In addition, the influence of pneumatic and hydraulic compression systems on mechanical properties was compared. 1 mm-thick deep-drawn steel sheets were used for tests, and weld quality was evaluated by examining the nuggets on the basis of metal metallographic sections as well as quantitatively measuring the tensile-shear strength.

The main conclusions drawn in this research include:

- The static mechanical properties and dynamic touching behavior are primarily determined by the moving masses and stiffness of electrode arms. The hydraulic

cylinder exhibits low force peak and low force-decay time during both touching and follow-up stages due to its smaller mass and higher damping.

- The necessary follow-up for spot welding tongs of an industrial robot is largely determined by the bending energy stored in the electrode arms. Therefore, the system stiffness and moving mass in spot welding tongs of steel sheets have no influence on quality of the weld joint just below the splash limit, but affecting the scatter in strength. With less moving mass and stiffness, reduction in scatter of strength values was found.

Dorn and Xu (1992-1995) [23-25] investigated the influence of moving mass, friction and rigidity of lower electrode arm, independently as well as in combination, on touching and follow-up behaviors as well as on weld quality with a simulation device developed for this purpose. The results showed:

- The influence of mass, friction and stiffness of lower electrode arm on the dynamic machine properties is very complex. It is a coupled influence and sometimes contradictory. The touching and follow-up behaviors cannot be improved simultaneously by optimizing these factors, but their favorable and unfavorable combinations were determined.

- Low rigidity of the lower electrode arm is favorable to touching behavior, i.e. short oscillation of electrode force, but for follow-up behaviour, it is not only dependent on lower electrode rigidity, but also on the moving mass and friction.

- Friction and stiffness of the lower arm have the most vigorous effect on weld quality because of the change in the mean electrode force during follow-up.

- No clear influence of moving mass on weld quality was detected.

In recent studies, Tang et al. ([26], in 2000; and [27], in 2003) performed a systematic investigation of the influence of mechanical machine characteristics on the welding process and the weld quality. The tests were carried out on pedestal-type welding machine by varying the mechanical machine parameters. The stiffness of the lower electrode structure was modified by adding springs, as shown in Fig. 2.4; friction in the welding machine was varied by using a specially designed device mounted between the upper and lower electrode structures, as shown in Fig. 2.5; and the moving mass was changed by adding an additional mass to the moving electrode element, as shown in Fig. 2.6; Weld quality refers to tensile-shear strength, and materials used in the experiments were steel and aluminum sheets commonly used in automotive applications.

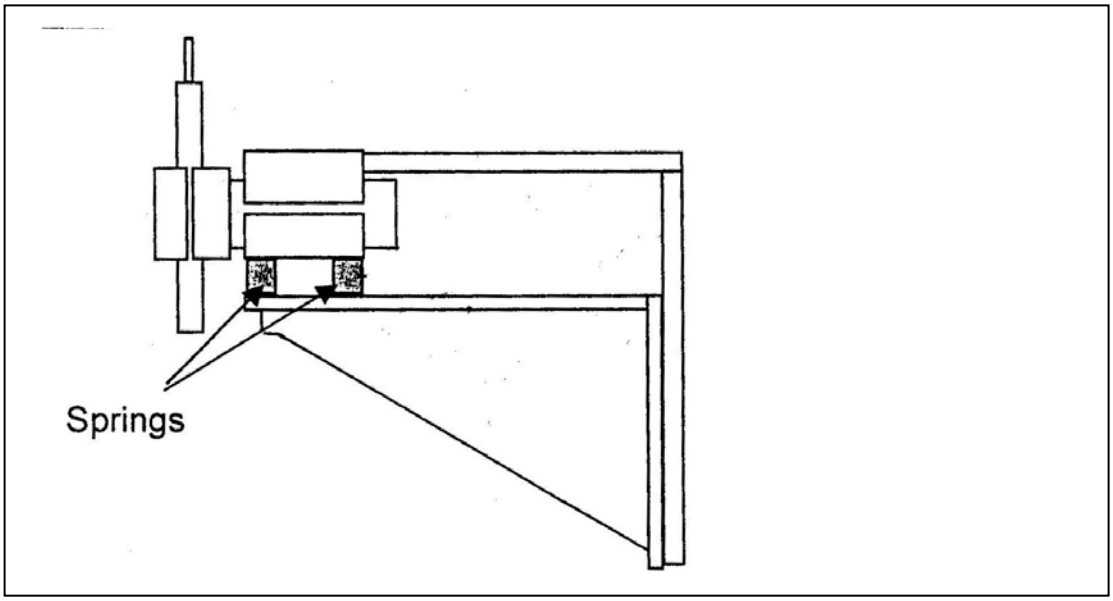

Fig. 2.4 — Modification of machine stiffness

The results showed that the mechanical characteristics of resistance spot welding machines, such as stiffness, friction, and moving mass, have a complex influence on the resistance welding process and weld quality. The welding force is an important parameter in resistance spot welding, which is directly related to mechanical machine characteristics. Electrode displacement during welding is also important because it reflects the expansion, melting, growth, and solidification processes. So the influence of these mechanical characteristics can be explained by analyzing the process signatures, for which the force and displacement were chosen.

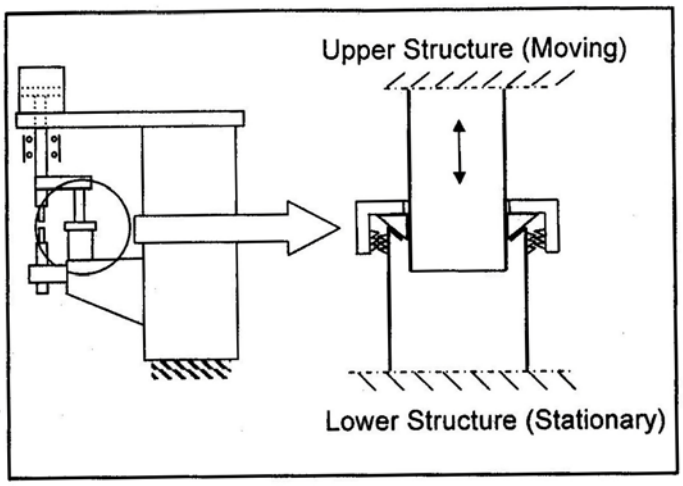

Fig. 2.5— Modification of machine friction

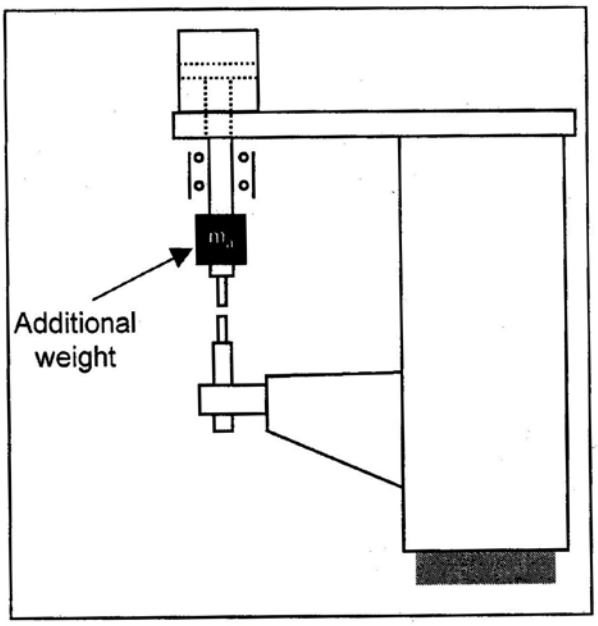

Fig. 2.6— Modification of moving mass

The research finally concluded that machine stiffness has a positive influence on expulsion prevention and weld quality. Specifically, high stiffness can reduce electrode misalignment, increase expulsion limits, and provide forging effect, thus high stiffness was recommended in this research. Machine friction should be reduced whenever possible because of its negative effects on weld quality. It also confirmed that moving mass does not significantly affect the process and quality of resistance spot welding.

In 1997, K. Fujimoto et al. investigated the relationship between dynamic properties of loading system and weldability in resistance welding. They pointed out that high current density spot welding develops a large electromagnetic force between the electrodes. This electromagnetic force causes fluctuations of the load, which in turn adversely affects the weldability. The load fluctuations vary depending on the loading system stiffness, friction, or response. The research resulted in suggestions on designing and optimizing the loading system [23-25].

2.2.2.3 Measuring the Dynamic Mechanical Properties of Resistance Welding Machine

The dynamic mechanical properties of resistance welding machine are commonly characterized by measuring two parameters: electrode force and electrode displacement. For example, Krause and Lehmkuhl [17, 30] investigated the electrode force profile at two stages: i.e. touching and follow-up. In evaluating the dynamic mechanical properties, a factor *K* was used:

$$K = \frac{F_1 + F_2 + F_3}{3 \times F_{st}}$$

Where $F_1 \sim F_3$ are the values of the first three force amplitudes, and F_{st} is the value of the set or actual electrode force, Fig. 2.7.

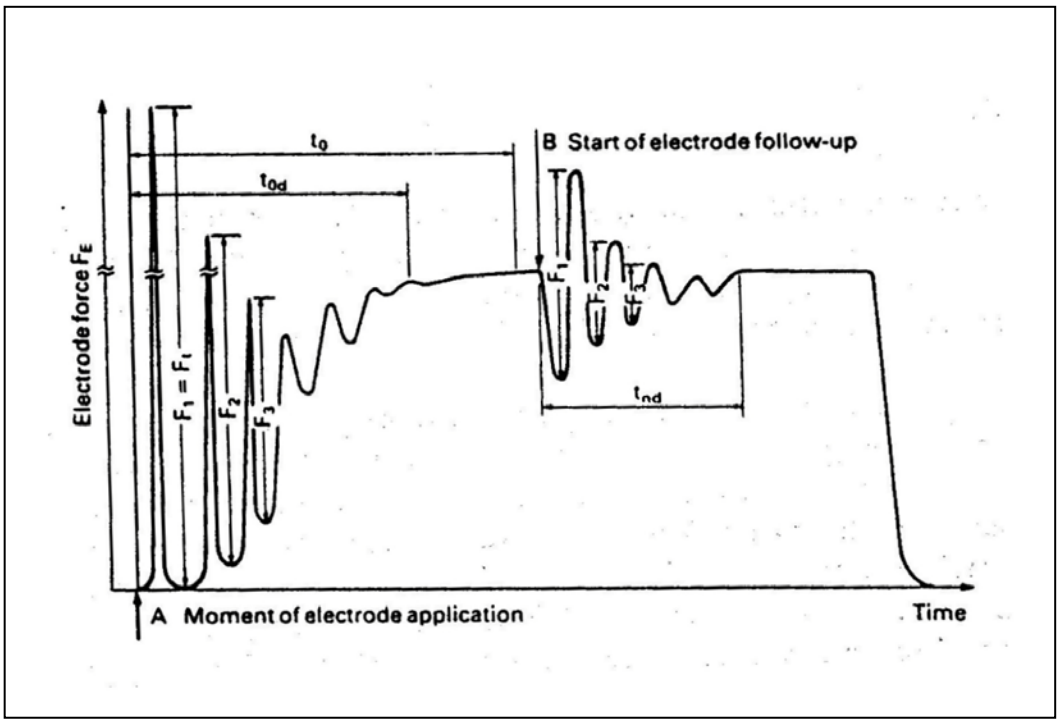

Fig. 2.7 —Diagram of electrode force during welding

M. Malberg [31] measured electrode displacement with a special designed device when investigating maximum follow-up capacity. Based on the electrode displacement measurements, the speed, kinetic energy and acceleration of the moving electrode were calculated. The results were used to identify or evaluate the mechanical differences of machines, and to try to transfer the optimum welding variables from one machine to the other. Three machines were tested.

2.2.2.4 Modeling the Dynamic Mechanical Properties of Resistance Welding Machine

Römer et al. [18] used a single-mass vibratory unit as a substitute of a resistance spot welding machine with C-frame, with the assumption of rigid frame of the machine, as shown in Fig. 2.8.

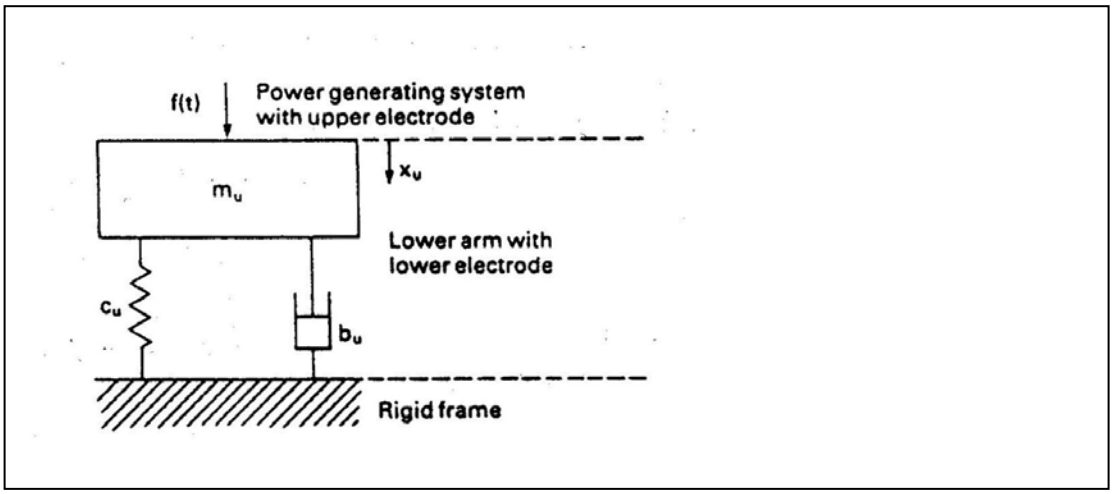

Fig. 2.8 —Single-mass vibration unit as substitute system for a resistance welding machine

They assumed that when the electrode is applied, as the result of sudden contact between two electrodes, an oscillation is induced in the lower electrode by a shock *f(t)*. The shock function is:

$$f(t) = \frac{I}{m} \cdot \delta(t)$$

where m is the moving mass of the upper electrode element, I is the shock intensity and $\delta(t)$ is the Dirac delta function, i.e.

$$\delta(t) = \begin{cases} 0 & for \quad t \neq 0 \\ 1 & for \quad t = 0 \end{cases},$$

Thus the differential equation for describing the response of the lower electrode by the shock excitation is:

$$m_u \ddot{x}_u + b_u \dot{x}_u + c_u x_u = f(t)$$

The solution is:

$$x_u = \frac{I}{m_0 \omega} \cdot e^{-D_u t} \cdot \sin(\omega t) \quad (\text{where: } D_u = \frac{b_u}{2m_u}) \qquad (2\text{-}1)$$

where:

m_u, b_u, c_u, are the mass, damping and stiffness of lower electrode element. ω is the characteristic frequency.

By analyzing the solution of this equation, the requirements for improving the touching behavior (oscillation behaviour used in the paper) was realized, as summarized in table 2.1.

Table 2.1 Summary of demands for good touching behaviour

Lower electrode	**Upper electrode**
Mass / small	Mass / small
Damping / small	Damping / large
Stiffness / small	Application speed /constant

In the welding phase, when the metal is heated by the flow of current, it will soften or collapse. As a result of this, the electrodes move towards one another in the direction of the electrode force. The upper electrode is accelerated downwards by the prestressed force F_0, the movement is described by the equation:

$$m_0\ddot{x}_0 + b_0\dot{x}_0 = F_0 \qquad (2\text{-}2)$$

The solution is thus:

$$x_0(t) = \frac{F_0}{4m_0D_0^2}\cdot\left[2D_0t - (1-e^{-2D_0t})\right] \quad (D_0 = b_0/2m_0) \qquad (2\text{-}3)$$

The movement of the lower electrode is still based on equation (2-1). The follow-up movement of the electrode is thus the sum of movements of the upper and lower electrode, and the speed expressions for both electrodes were deduced. By analyzing their mathematical expressions, the requirements for improving the follow-up behaviour were summarized, as listed in Table 2.2.

Table 2.2 Summary of demands for good follow-up behaviour

Lower electrode	**Upper electrode**
Mass / small	Mass / small
Damping / large	Damping / large
Stiffness / large	

Comparison of the requirements of the optimized mechanical parameters for good touching and follow-up behaviours shows that sometimes they are contradictory (Table 1 and 2), the optimum selection of these parameters, such as damping and stiffness, can

only be done with reference to a specific machine. In both processes the moving mass should be as small as possible. A way of improving the dynamic mechanical machine characteristics by inserting an additional spring damping element between the upper electrode and the piston rod was suggested.

Z. Feng et al. [32] developed two analytical models in describing the electrode displacement during the squeeze cycle of air-operated resistance spot welding machines. Model 1 was called the weld head model, describing the electrode motion during the approaching stage, prior to contact; Model 2 was called the dynamic response model, describing the electrode motion (bouncing characteristics) after contact and before firing the welding current.

- **Model 1. Approaching stage**

The air compression system of the machines was simplified as the model shown in Fig. 2.9.

Based on Newton's second law and the ideal gas law, the following equations were given:

$$PA\frac{dx}{dt}+\frac{dP}{dt}A(x+x_0)=P_iQ$$

$$PA-F_f=m\frac{d^2x}{dt^2}$$

where A is the cross area of cylinder, x_0 is the initial position of piston.

- **Model 2. Bouncing stage**

In bouncing stage, the mechanical system was simplified as a lumped parameter system, as shown in Fig. 2.10.

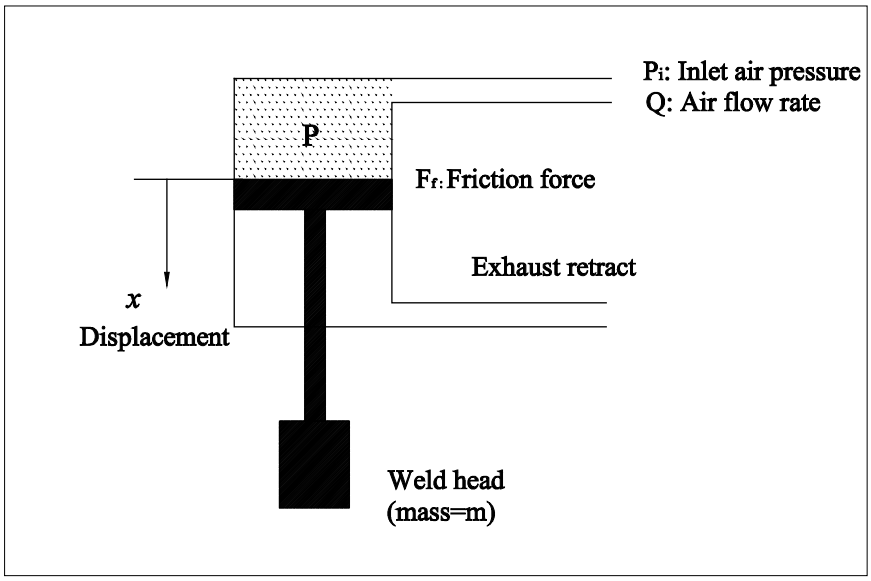

Fig. 2.9 — Mechanical model of weld head motion

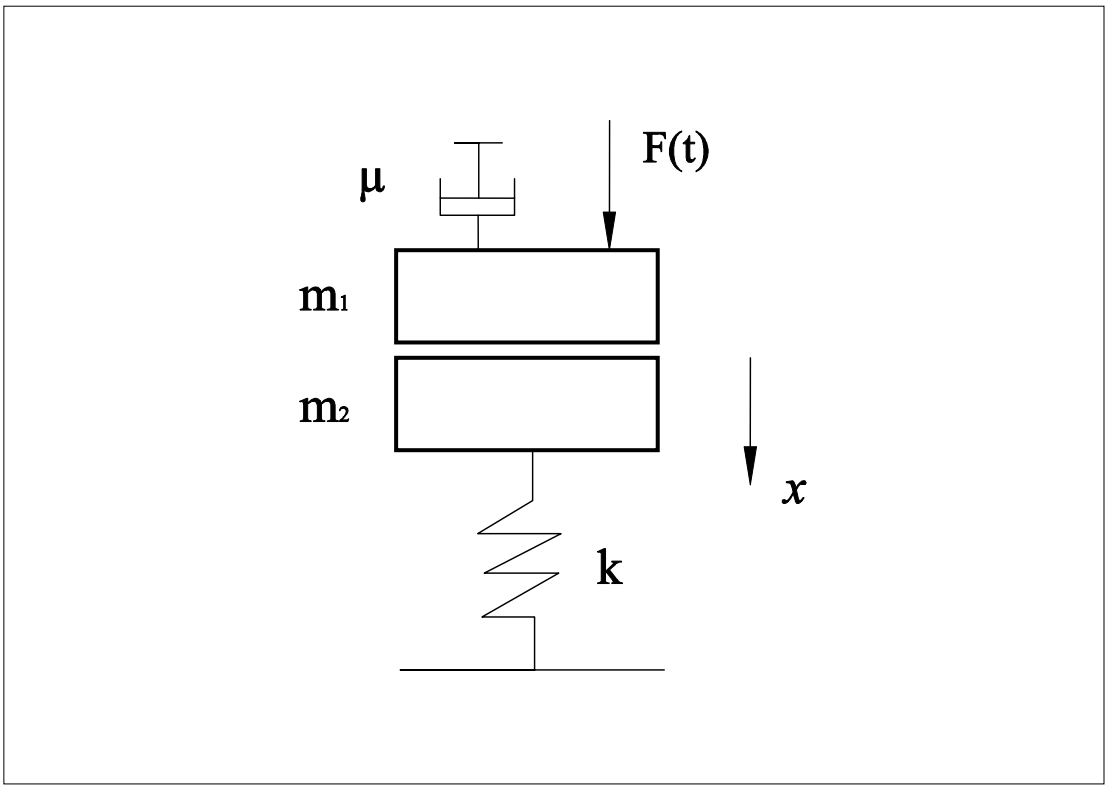

Fig. 2.10 — Mechanical model for bouncing stage

Under the assumptions: no separation of m_1 and m_2 after impact, and m_2 has a velocity of V_0 just before impact, two equations were created:

Force equilibrium equation: $m\frac{d^2x}{dt^2} + \mu\frac{dx}{dt} + kx = F(t)$; $\quad m = m_1 + m_2$

With initial conditions: $x(0) = 0$; $\quad \frac{dx(0)}{dt} = V_{init}$

Momentum equilibrium equation: $V_{init} = \frac{m_2}{m}V_0$

where: μ = damping coefficient; k = stiffness;
m_1 = mass of upper electrode system; m_2 = mass of lower electrode system;
$F(t)$ = force from air cylinder;

By using these models, the approaching velocity, impact force, bouncing frequency, pressure build-up, and force stabilizing time can be estimated. The models were validated by experimental tests.

2.3 Conclusions of Literature Studies and Proposals for New Investigations

The mechanical machine properties are divided into static and dynamic ones. The static properties, such as eccentricity and deviation of electrodes, mainly affect the shape of the weld due to contact errors of the electrodes.

The dynamic mechanical machine properties include so-called touching behaviour and follow-up behaviour, occurring in two phases of a welding cycle respectively: i.e. in the squeeze phase and in the welding phase. In the squeeze phase the moving electrode approaches and touches the weld parts prior to welding, causing an impulse and a sharp increase of the electrode force, and then follows an oscillation of the load until it reaches its set, static value. This load fluctuation results in high electrode wear but unrecognizable influence on weld quality since the electrode force can be stabilized before current flow if the squeeze time is set appropriately.

In the welding phase, a slight movement of the electrodes towards each other takes place due to plastic deformation of the work pieces as they soften or melt. Especially in projection welding, the electrode force drops in a brief, initial phase during welding due to collapse of the projection causing oscillations of the load or even loss of contact between electrode and work piece, resulting in poor weld quality. To ensure good weld quality fast follow-up speed of the electrode is thus essential to compensate for the deformation or collapse of the weld parts. This is the most important feature as regards dynamic mechanical characteristics of resistance welding machines.

Therefore, the dynamic mechanical machine properties mainly influence the weld quality and electrode service life. Some researchers believe, they may be of even greater importance than the machine electrical properties, especially when spot welding thin sheet metals, aluminum alloys and projection welding complex material combinations.

The dynamic mechanical characteristics are normally considered to be governed by four factors: moving mass, stiffness, friction and compression system. In order to investigate the influence of these factors on dynamic machine behaviour as well as on weld process and weld quality, simulation devices or specially designed machines for experimental use has been employed, on which the parameters, such as moving mass, friction, stiffness of the machine can be varied. The results have shown that the influence is complex, it is impossible to say which of the four factors has the greatest effects, sometimes contradictory effects appear or it depends on the specific machines. For example, low stiffness of the lower electrode arm is favorable to the touching behavior but unfavorable to the follow-up. A conclusion in common is that the moving mass has an insignificant influence on weld quality.

The electrode force is the most direct parameter reflecting the mechanical properties of resistance welding machines. The electrode displacement is related to welding nugget formation, splashing etc. Therefore these two parameters are commonly measured when investigating the mechanical machine properties and their effects on weld quality.

No modeling methods for simulation of the dynamic mechanical behaviour in practice have been presented. Ref. [18] gives the mathematical models for qualitative analysis, providing a guideline for modifying the machine design, for example, adding additional springs in the electrode head or increasing the stiffness of lower electrode to improve the follow-up behaviour. Ref. [32] only modeled the touching behaviour of air-operated machines, difficulties are that it is very hard to determine the machine parameters involved in the models due to the difference of machine structures.

In summary, these researches have provided a basic understanding of the effects of machine mechanical properties on weld process and weld quality, and of modifying the machine design in order to improve the machine mechanical properties. But most of the investigations are limited to qualitative analysis presenting no modeling methods for simulation of the dynamic behaviour in practice.

The objective of the investigation of mechanical properties of resistance welding machines in this Ph.D. project is mainly focused on:

Systematically testing the mechanical properties of resistance welding machines, to identify the key parameters characterizing the machine mechanical properties which cause differences from one machine to another;

Based on the results of testing and analysis, to develop a generic mathematical model, which is applicable to most types of machines no matter how the machine structures are, for simulation of the dynamic mechanical behaviour;

Developing a method which is easy to be applied in industry to identify the parameters required in the models.

Chapter 3

Equipments and Measuring System used in the Project

In this chapter, the equipments and measuring system employed in this project are described. In order to test the mechanical and electrical properties of resistance welding machines, four parameters have been measured in the project, they are: electrode force, electrode displacement, weld current, and primary voltage (voltage on the primary side of the welding transformer). Which or how many of these parameters that are needed to be measured depend on the objective of each test. An overall introduction will be given in the following.

The measuring system is modified for the specific purpose of this project based on the one initially developed by Michael Malberg [31, 33]. All signals from the transducers are connected to a computer, which collects the signals as function of time and record them as a data file for subsequent processing. The control and data acquisition of the system is performed by a special program developed using the software LABVIEW. The measuring system is shown in Fig. 3.1.

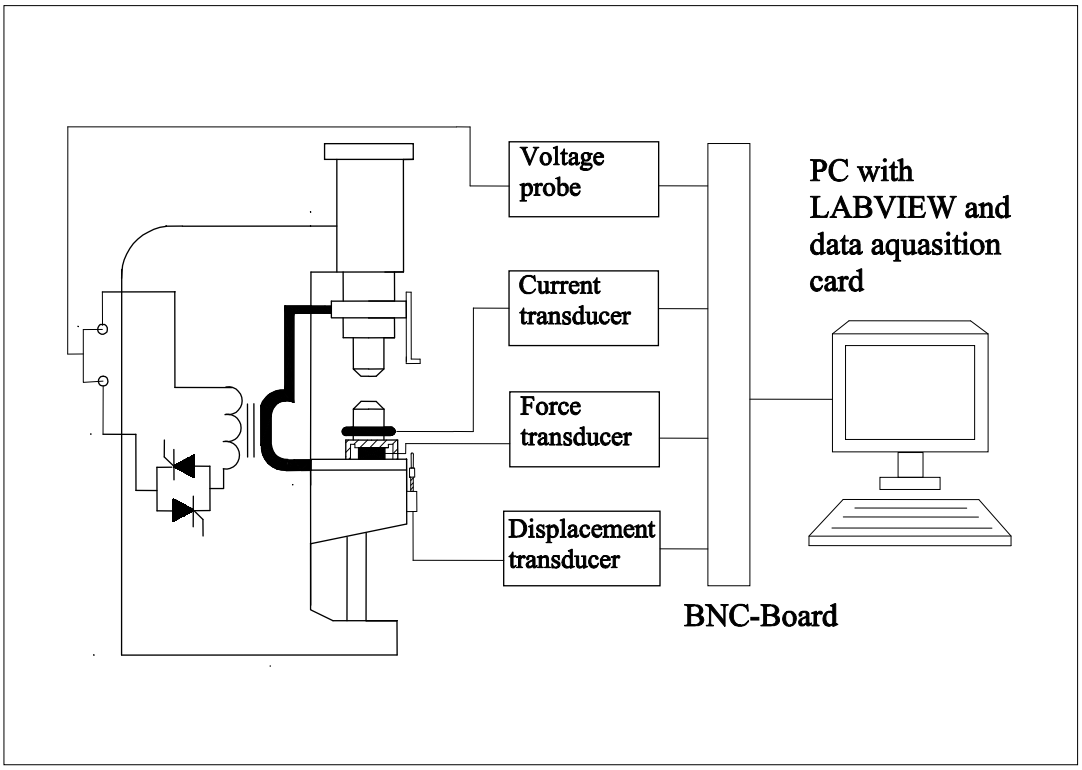

Fig. 3.1— Fundamental illustration of the measuring system used in the project

The measuring equipments used in this project are listed in Table 3.1.

Table 3.1 — Measuring equipments used in the project

Signal	Equipment	Measuring range
Displacement between two electrodes	Displacement sensor: Burster type 8713-25 + DC power supply, 5V	25 mm, ±0.2%
Electrode force	BAM-transducer + Amplifier: Kistler 5007	0-120 KN
Primary voltage	High voltage differential probe	± 3500 V, Attenuation ratio: 1/500
Welding current	TECNA – 1430 weld tester (Rogowski coil + integrator)	0- 200 kA
Data acquisition card	National instruments DAQ-700	100 KHz-A/D 12 bit ± 5V
Data acquisition software	National instruments LABVIEW	Version *6i*

3.1 Description of Measuring Equipments

Primary voltage

The primary voltage is the input line voltage to the resistance welding machine, which is a high voltage (400 V in Denmark). This high voltage is measured directly by a high voltage differential probe (the attenuation ratio is set to 1/500 during measurements), with which the voltage is attenuated to around 0.8 V which is suitable for recording by computer with a data acquisition system, see Fig. 3.1. The calibration was carried out by measuring the input and output signal with a digital multimeter, the

calibration equation is:

$$U_p = 498.78 \times U + 0 \qquad (3\text{-}1)$$

where: U_p = primary voltage, [V];
U = signal amplitude, [V];

Welding current

The welding current is measured using a Rogowski coil encircling the electrode. When current runs through the electrodes, a potential is induced in the coil due to the large magnetic field, as described in the following equation:

$$U_{ind} = -M \frac{dI}{dt} \qquad (3\text{-}1)$$

where U_{ind} = induced potential in the coil
M = mutual induction coefficient
I = welding current
t= time

The induced potential is proportional to the current changes in the electrodes. M is a constant for the specific coil. The signal from the coil is integrated in an integration unit which converts the signal to a voltage proportional to the welding current running through the electrodes. The calibration equation is [31, 33] (corresponding to the setting of maximum current 50 kA on the current measuring meter):

$$I = 15.562 \times U - 0.41 \qquad (3\text{-}2)$$

where: I =Welding current, [kA];
U = signal amplitude, [V];

Electrode force

The electrode force is measured directly using a force transducer of which the central part is a piezoelectric crystal. The force transducer is mounted directly below the lower electrode, as shown in Fig. 3.2. The piezoelectric crystal is placed inside the force transducer housing. When an electrode force is exerted on the piezoelectric crystal, electric charges are formed on the crystal surface in proportion to the rate of change of that force. A charge amplifier, Kistler 5001, is connected to integrate the electric charges to give a signal proportional to the applied force and large enough to measure. In this way the crystal is located in an induction free field. Therefore precise measurements can be achieved even in large magnetic fields.

However cooling is necessary to avoid thermal expansion of the metallic house during welding.

The force transducer together with the amplifier was calibrated on a hydraulic 10-ton press, see Fig. 3.3. The setting of the amplifier is as follows:
Transducer sensitivity: 4.20
Filter type: At "Long" position
Transducer sensitivity range: 1…11
Output amplification: 5×10^3

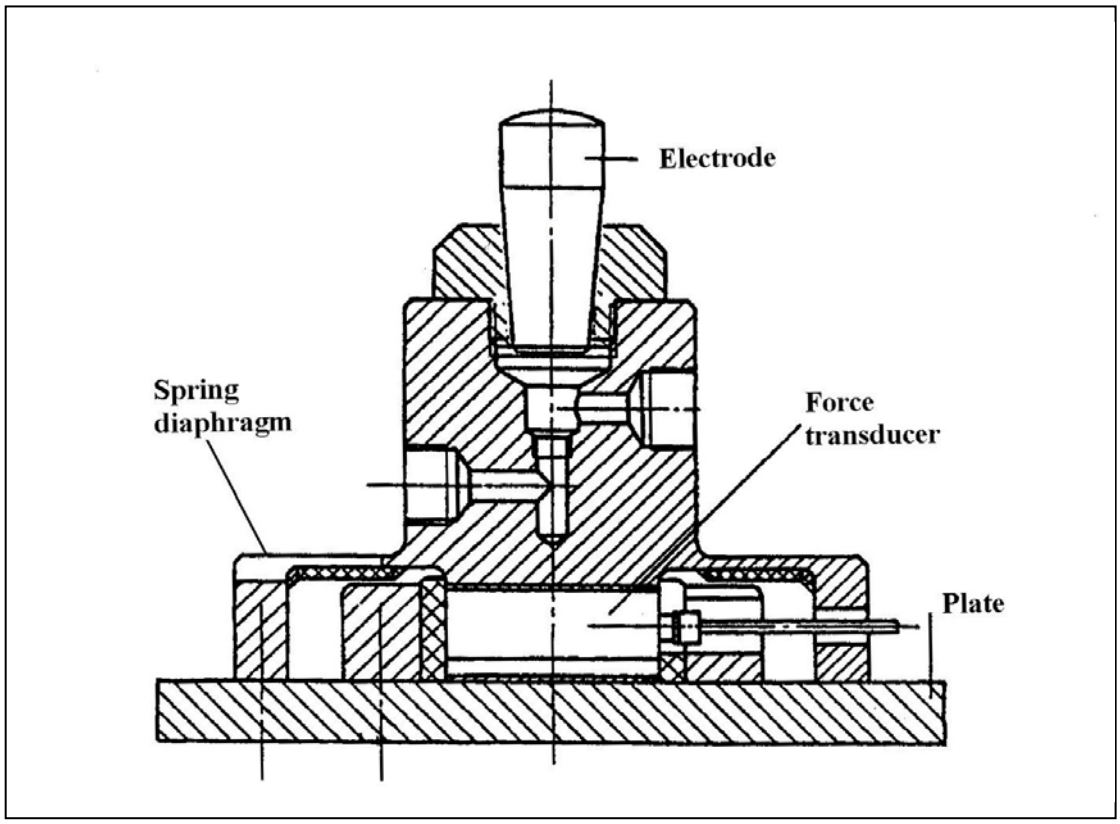

Fig. 3.2— Force transducer using piezoelectric crystal for measuring the electrode force

The force is loaded on the transducer in steps of 0.5 kN from 0 to 12 kN, then unloaded from 12 kN to 0 kN. The output voltage at each load is measured by a multimeter (Metex M-3650 CR). By plotting the load curve with respect to the output voltage and performing a curve fitting, the calibration equation is obtained:

$$F = 1.0241U + 1.7943 \qquad (R^2=0.9995) \qquad (3\text{-}3)$$

where: F = electrode force, [kN];
U = signal amplitude, [V];

Note that in Fig. 3.4 the curve does not go through zero, implying that a pre-load of around 1.8 kN is needed for elastically deforming the transducer housing before the piezoelectric cell inside the housing is loaded.

Electrode displacement

A resistive displacement transducer has been used to measure the mutual displacement of electrodes, the principle of the transducer is shown in Fig. 3.5. It can be seen that the basic part of the transducer is a sliding resistance, which needs 5V DC power. The displacement transducer is mounted on the lower electrode plane and is

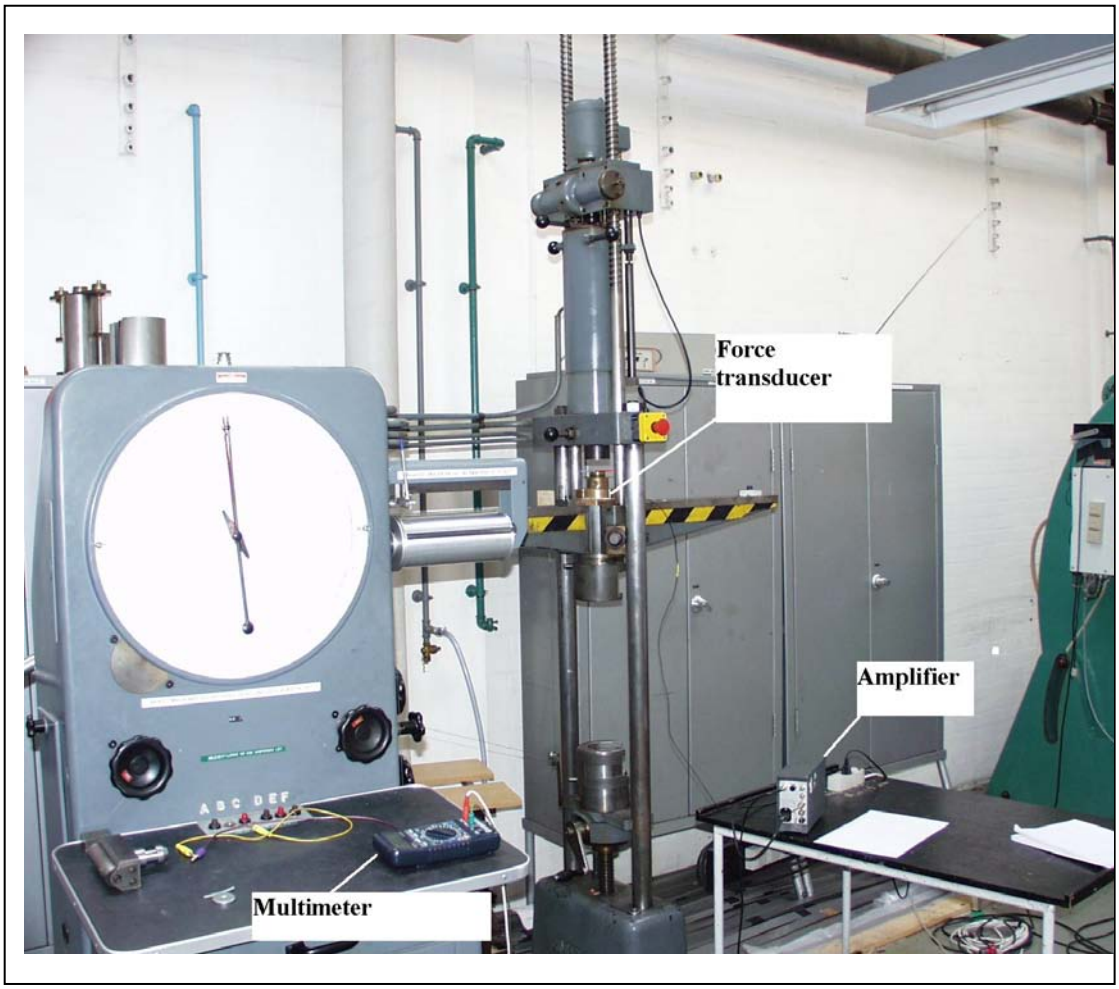

Fig. 3.3 — Set-up for calibration of the force transducer

connected to the upper electrode plane by touching a piece of contact metal mounted on the upper electrode, see Fig. 3.6. This method gives a direct measurement of the displacement between the electrodes. The calibration was carried out by measuring the displacement with a digital caliper and measuring the voltage output with a digital

multimeter, the calibration equation is:

$$x = 5.2 \times U + 0 \qquad (3\text{-}4)$$

where: x = electrode displacement, [mm];
U = signal amplitude, [V];

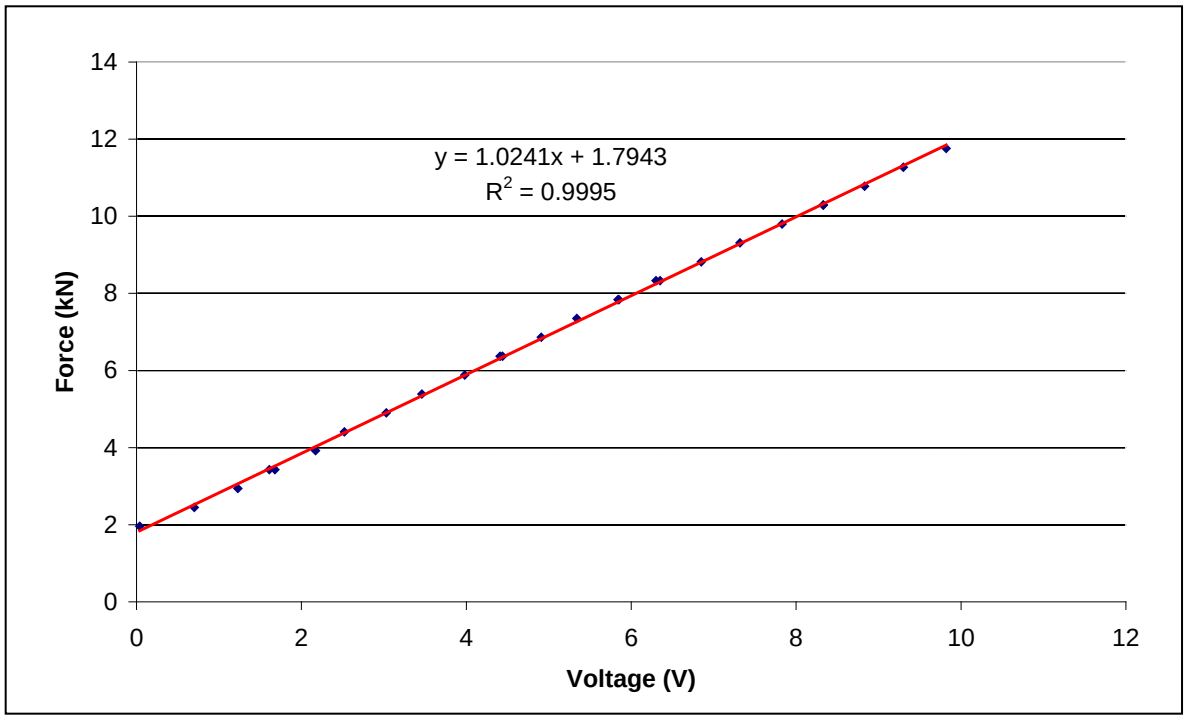

Fig. 3.4 — Force calibration curve

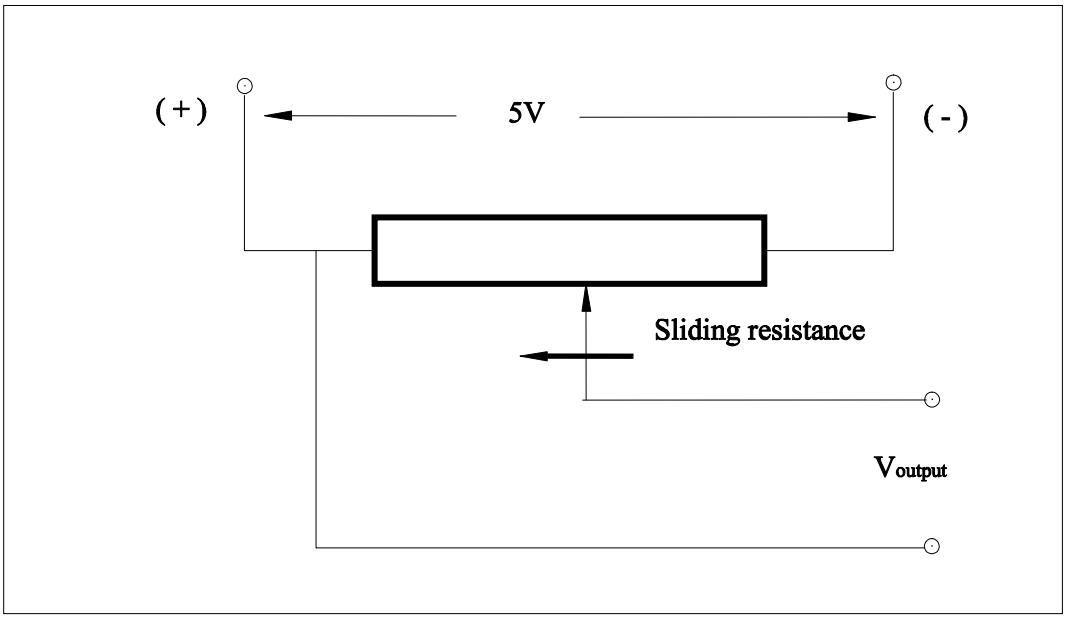

Fig. 3.5 — Principle of displacement transducer

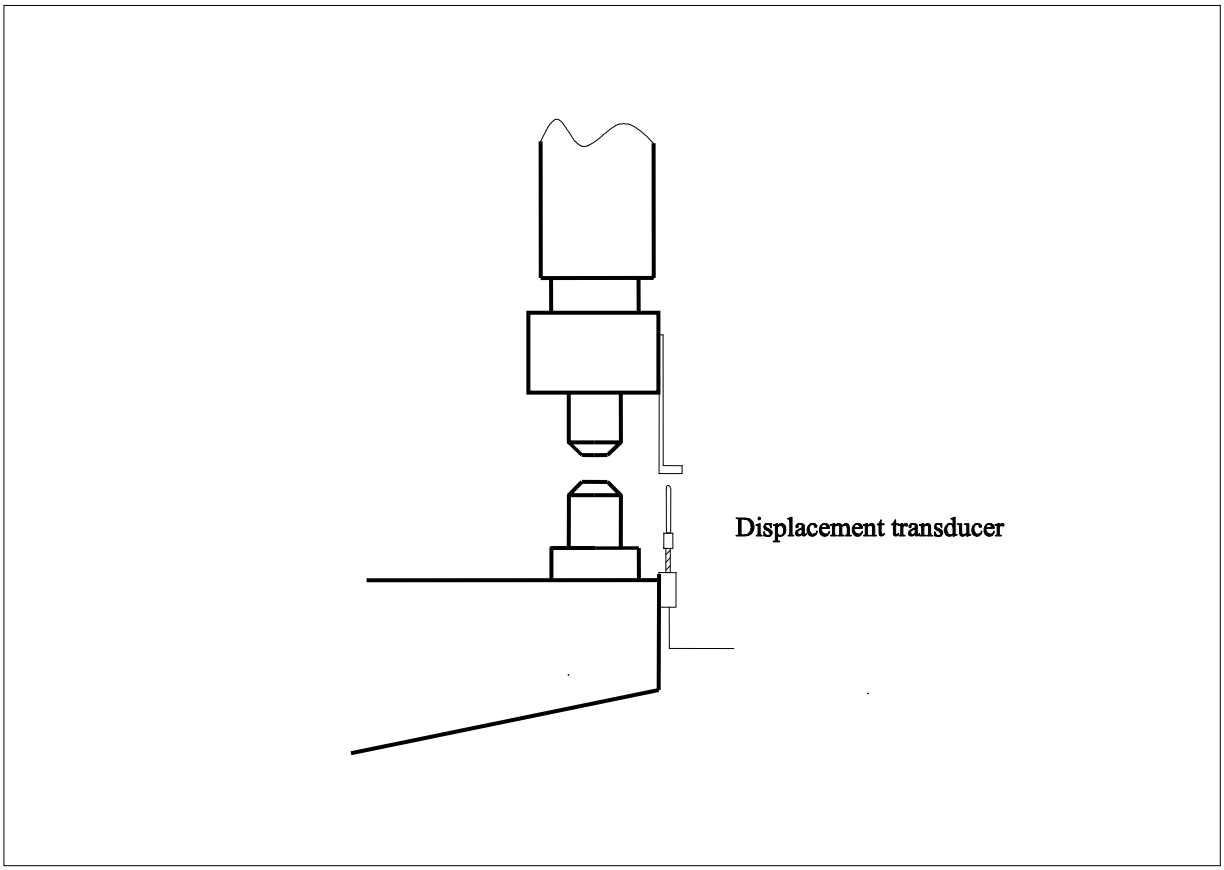

Fig. 3.6 — The displacement transducer mounted on the lower electrode plane

Chapter 4

Measurement of Electrode Force in Squeeze Phase of Welding Cycle

As mentioned earlier, in the squeeze phase of the welding cycle, the upper electrode descends and suddenly touches the lower electrode, thus inducing an oscillation in the electrode system. This causes fluctuations of the electrode force before it builds up and reaches its set static value, resulting in high electrode wear but no recognizable influence on the weld quality, because the electrode force can stabilize before the current firing if the squeeze time is set appropriately. Therefore, how fast the machine is able to build up the force to the set static value and how long it takes to stabilize to this value, which characterizes the touching behaviour of the machines, has importance in evaluating the machine mechanical characteristics and correctly setting the welding variables in operation. The criteria is that the squeeze time ($t_{squeeze}$) should be set greater than the stabilizing time of electrode force (t_{stable}) of the machine at each load level. i.e.

$$t_{squeeze} > t_{stable}$$

4.1 Measurement of Electrode Force

4.1.1 Measuring Strategy

Without starting the electrical system, the electrode force is measured at each level by means of a piezoelectric force transducer mounted under the lower electrode (see Fig. 3.1). The different levels of electrode force are set by adjusting an air/hydraulic pressure valve mounted on the machine, the value of the pressure is displayed on a pressure gauge. The electrode set force can be calculated by multiplying the displayed pressure with the cylinder cross section area. By exporting the measured data to Microsoft Excel the curve of the force as a function of time is plotted. Thus the stabilizing time of the electrode force can be read from the force curve. The relationship between the real value (measured value) and set value of the electrode force (by setting the pressure for a given machine) can also be obtained, which will be

helpful and convenient for accurately setting the requested electrode force in production.

A dummy piece of steel is placed between the two electrodes in order to protect the

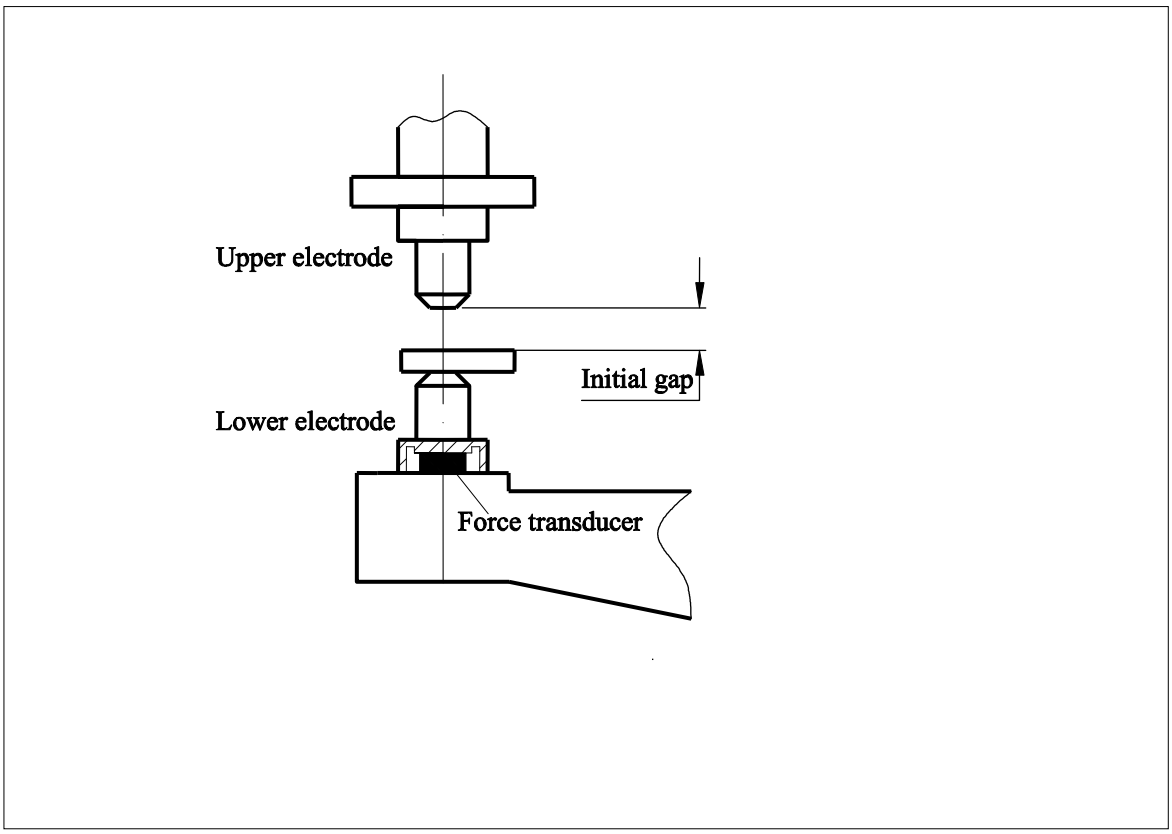

Fig. 4.1— Arrangement of measuring the electrode force

electrode tips from damage, 2 mm is adjusted as the initial gap, covering the proposed gap range of 1-2 mm in real production [34] (as shown in Fig. 4.1).

The tests are performed on two machines located in the lab of IPL, DTU. The specifications of these machines are described in appendix A.

4.1.2 Measurement on TECNA-250kVA-AC Machine

As an example, Fig. 4.2 shows a measured load curve for a TECNA-250kVA-AC machine (with a pneumatic cylinder, but no additional springs in the welding head). It can be seen that a hard contact of electrode application causes a force impulse which is much higher than the set static force, followed by a damped oscillation. After damping the oscillation, the force continues to increase for a certain period of time until it reaches the set static value. Table 4.1 shows the time necessary for stabilizing

the electrode force on its static value, and the air pressure corresponding to each resulted static force. These data are useful when setting the electrode force in operation. Fig. 4.3 shows the stabilizing time as a function of the set static electrode force. It can be seen that the higher the static force is set, the longer stabilizing time is required.

Table 4.1 — Stabilized time of electrode force for TECNA machine

Set value of pressure gauge (bar)	Static electrode force (kN)	Stabilizing time (ms)
0.8	2.9	522
1.4	4.1	566
1.6	5.3	669
2.0	6.6	723
2.4	7.6	772
2.3	7.5	764
2.5	7.9	781
2.8	9.2	864
3.0	10.0	874
3.4	11.0	908

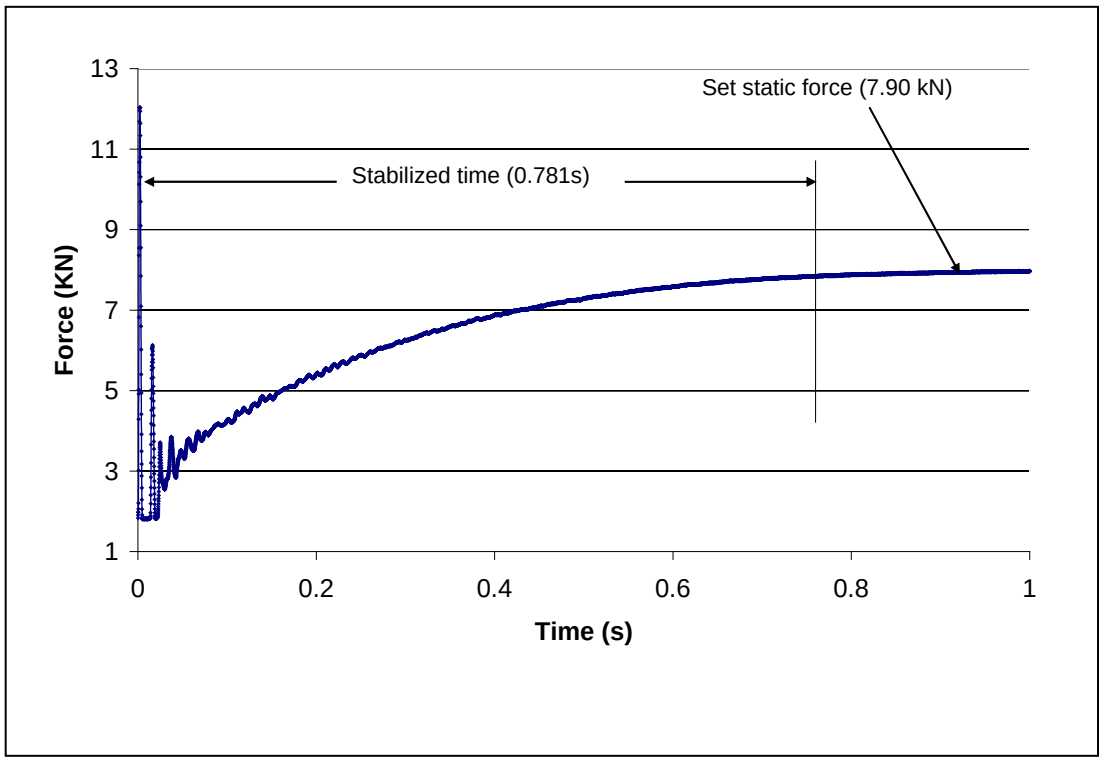

Fig. 4.2 —Curve of electrode force for TECNA machine

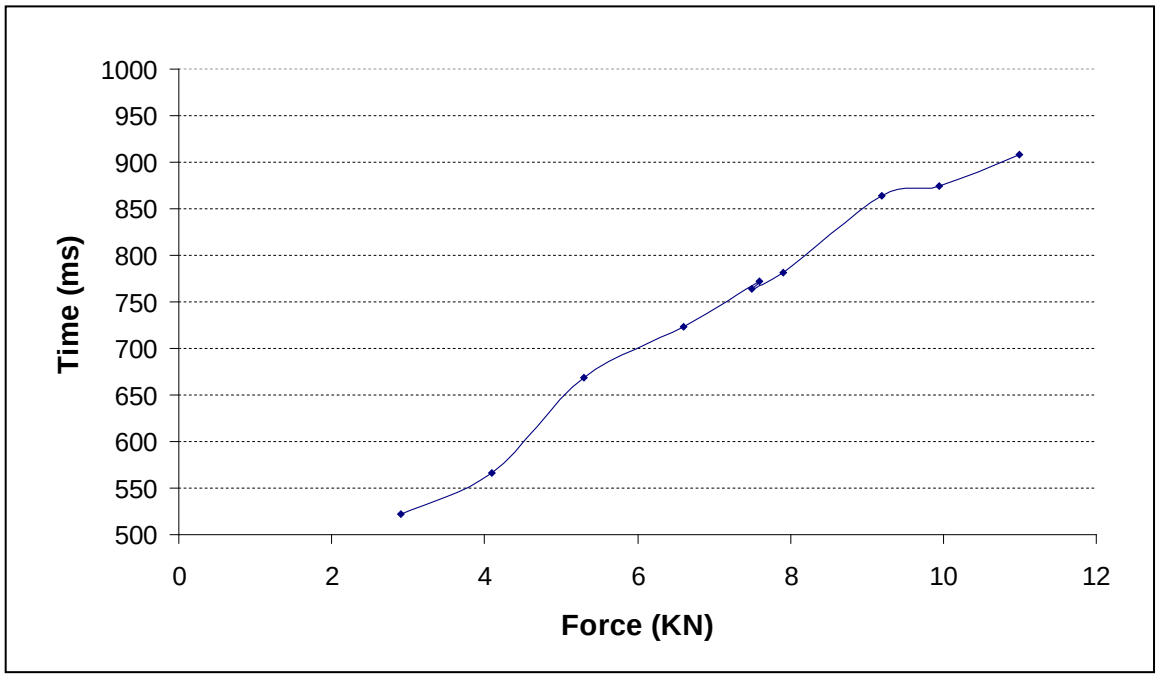

Fig. 4.3 — Stabilizing time of electrode force as a function of the set static electrode force for TECNA machine

4.1.3 Measurement on EXPERT-DC-Inverter Machine

Fig. 4.4 and 4.5 show the measured curves for an EXPERT-DC-Inverter hydraulically operated machine. For this machine, there are three additional springs mounted in the compression system for improving the dynamic mechanical behaviour of the machine, as shown in Fig. 4.6. The stiffness of the springs are: $k_1 < k_2 < k_3$ (k_1= 0.214 kN/mm, k_2 = 2.38 kN/mm, k_3 = 4.487 kN/mm), as shown in Fig. 4.7. During the electrode application, the force is increased at three different slopes by compressing the springs one by one, reducing the impact between the electrodes. So it is a soft electrode application which is of great benefit to the electrode wear.

Table 4.2 shows the time taken for stabilizing the electrode force on its static value, and the hydraulic pressure corresponding to each resulted static force, which can be a reference for setting the electrode force in operation.

Fig. 4.8 shows the stabilized time as a function of the set static electrode force. It is interesting to note that the stabilizing time is decreasing with increasing set static electrode force until around 5.7 kN, and above that, the stabilizing time tends to be a constant. This might be attributed to the fact that when the moving electrode falls and contacts the other electrode, an impact is caused. When the electrode force is low, implying that the compression from the cylinder is low, the springs will be able to spring back, thus a vibration with damping decay will be excited by the impulse,

resulting in longer stabilizing time of the electrode force. This can clearly be seen when comparing Fig. 4.4 and Fig. 4.5.

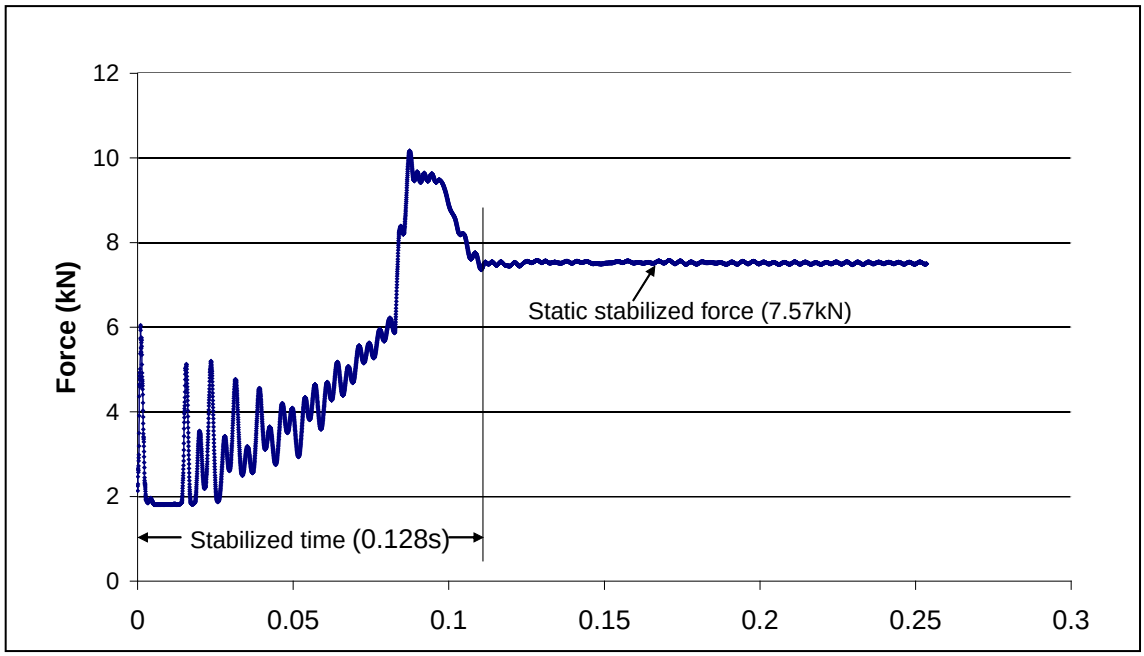

Fig. 4.4 — Curve of electrode force for EXPERT machine at static stabilized force 7.57 kN

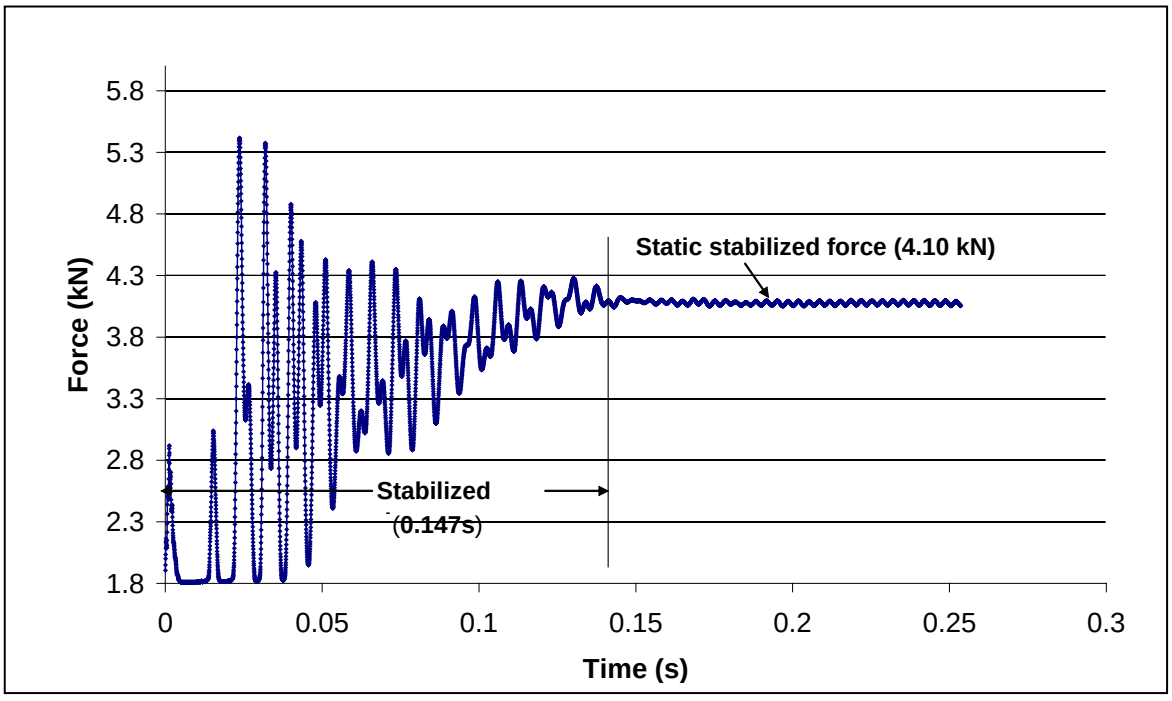

Fig. 4.5 — Curve of electrode force for EXPERT machine at static stabilized force 4.1kN

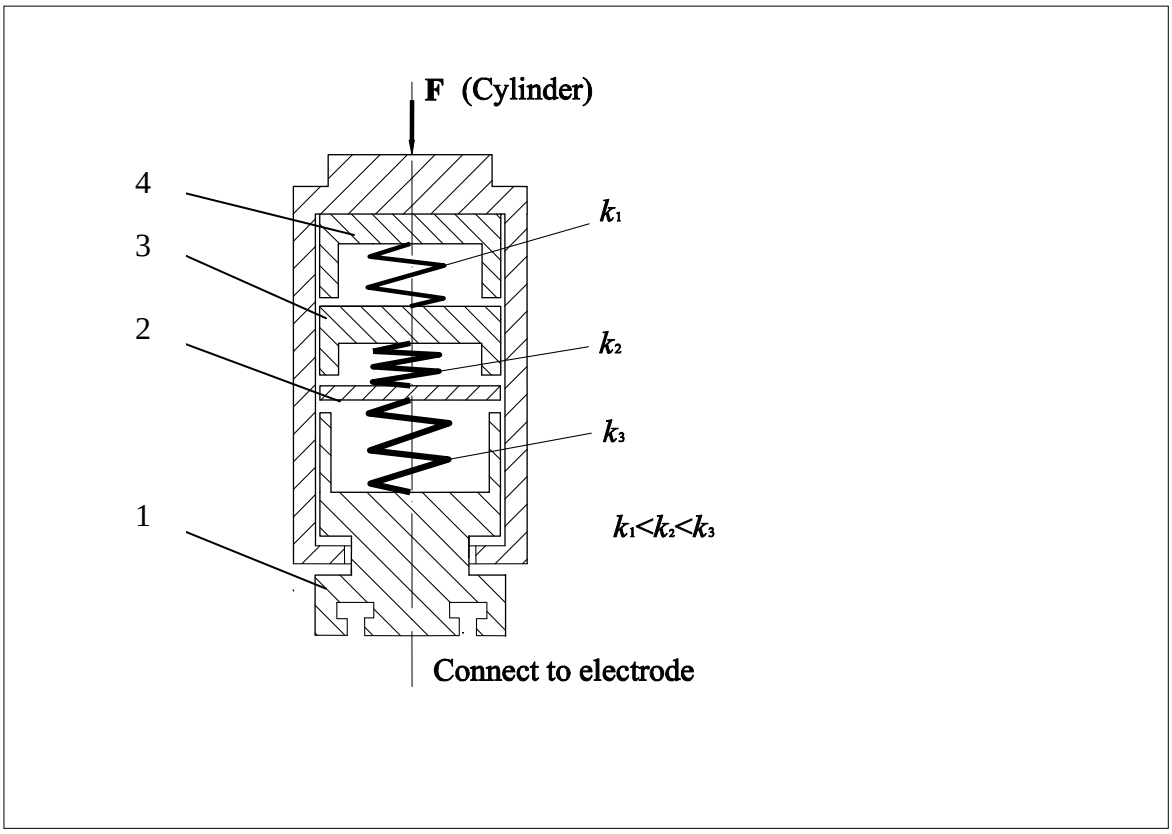

Fig. 4.6 — Sketch of welding head with additional springs for EXPERT-DC-inverter

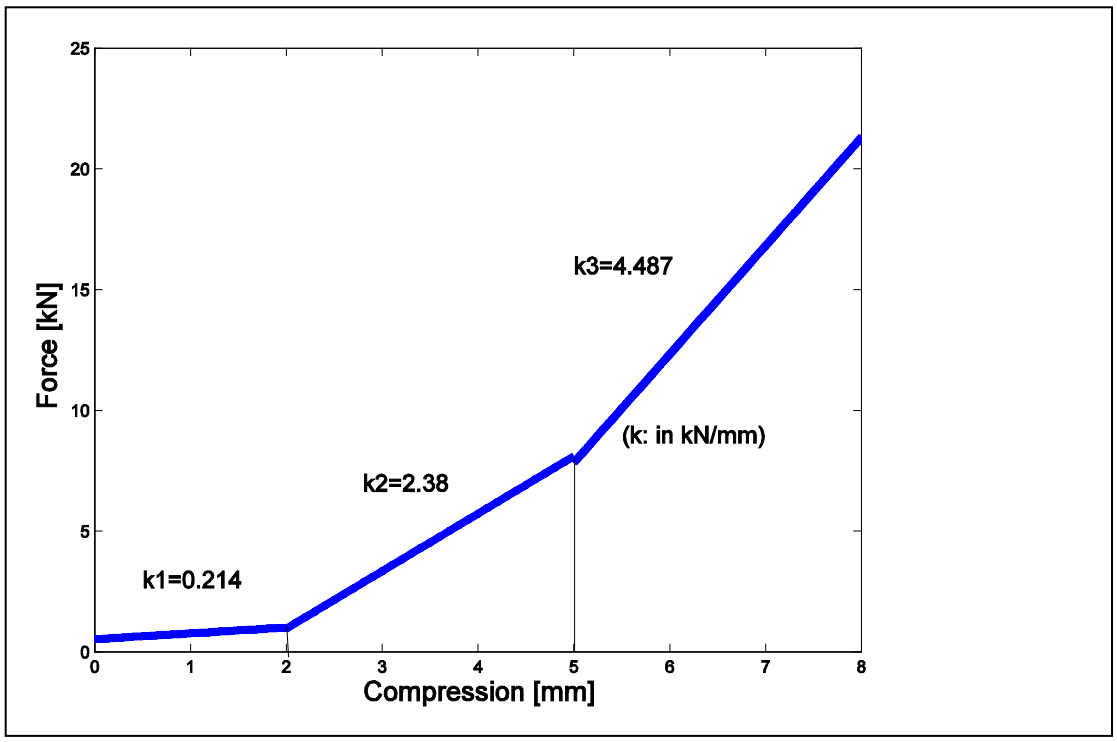

Fig. 4.7 — Stiffness of the springs

On the contrary, when the electrode force is set high, implying that compression from cylinder is high, the springs will not be able to spring back, thus less oscillation will be produced, and the electrode force will stabilize faster (see Fig. 4.4).

The reason why the stabilizing time is not changed when the static electrode force is higher than 6.32 kN (see table 4.2), is that the build-up time of the hydraulic force is fast and independent of fluid pressure because of nearly no compressibility of the cylinder liquid.

Table 4.2 Stabilizing time of electrode force for EXPERT machine

Stabilized static force (kN)	Adjustment of pressure (scale)	Stabilizing time (ms)
3.00	0.03	176
3.00	0.05	176
3.10	0.10	176
3.10	0.20	176
3.47	0.40	165
4.10	0.60	147
4.62	0.80	132
5.15	1.00	133
5.70	1.20	127
6.32	1.40	128
7.13	1.60	128
7.34	1.80	128
7.57	2.00	128
8.06	2.20	128
8.62	2.40	128
9.06	2.60	128

Comparing Fig. 4.2 and Fig. 4.4, which represent almost the same static electrode force, it can be seen that the air-operated machine (TECNA) takes much longer time to stabilize the electrode force after the decay of oscillation because of the larger compressibility of the air in a pneumatic system compared to the hydraulic one. Furthermore, the compression of air is proportional to the pressure. This explains the phenomenon that the higher electrode force implies a longer stabilizing time for the air-operated TECNA machine.

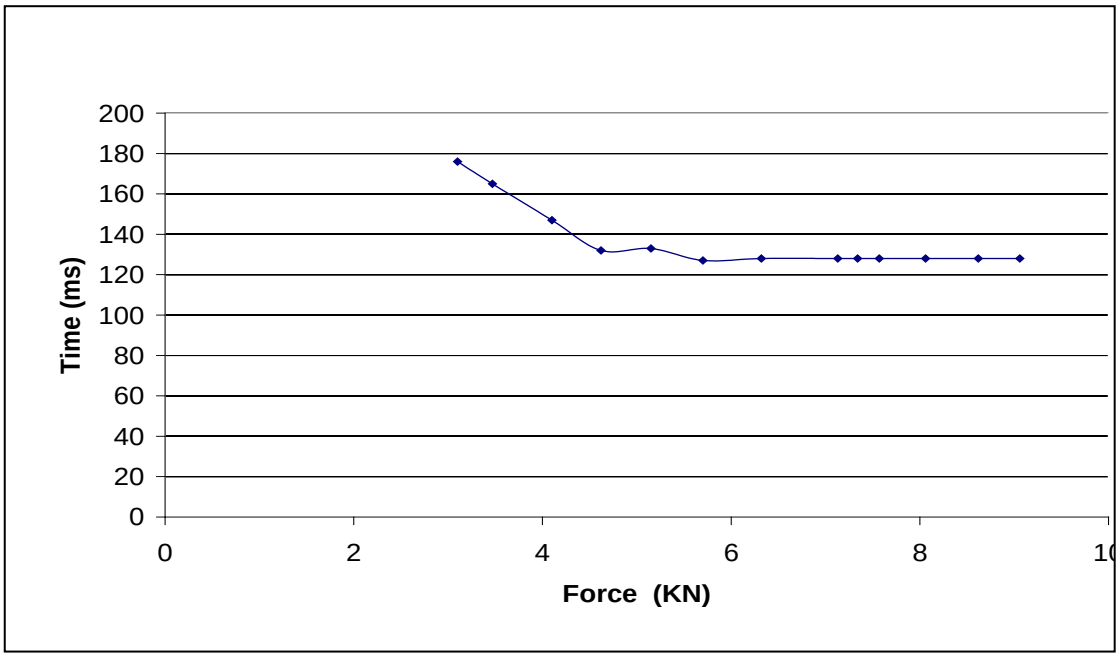

Fig. 4.8 — Stabilizing time of electrode force as a function of set static electrode force for EXPERT machine

4.2 Conclusions

Without firing the electrical system, the electrode force was measured for two machines. Based on the measurements, the time required for building-up and stabilizing the static electrode force, the so called stabilizing time of the electrode force, has been determined. This will provide a basis for choosing the squeeze time in production, which should be greater than the stabilizing time of the electrode force.

For the same level of electrode force, the pneumatic machine takes a longer time to build up and stabilize the force to the static value due to the compressibility of the air. The larger the force, the longer the stabilizing time. The hydraulic machine is very fast to reach and stabilize to the static electrode force, and it seems that the stabilizing time does not depend on the level of the force.

The additional springs mounted in the welding head gives a soft electrode application, because the impact between electrodes is reduced, but a longer-time oscillation especially when the electrode force is low.

Chapter 5

Testing and Modeling of Dynamic Mechanical Properties of Resistance Welding Machines

As mentioned in Chapter 2, the dynamic mechanical machine properties have a great influence on weld quality and electrode service life in spot and projection welding. They may be of even greater importance than the electrical ones, especially when projection welding complex material combinations. Also, in numerical simulation of the welding process, these characteristics, such as the maximum follow-up speed of the machine, have to be considered [35].

The dynamic mechanical machine properties include touching behaviour as well as follow-up behaviour. The follow-up behaviour appearing in the welding phase is the most important feature as it influences the weld quality.

In the present project, a mathematical model characterizing the follow-up behaviour of resistance welding machines has been developed, which is applicable to most types of machines no matter how the machine structures are.

A specially designed test set-up (a mechanical breaking test) developed at IPL, DTU was applied and further developed to identify the machine parameters required in the model. The model was verified by performing a series of mechanical tests as well as real projection welds.

5.1 Mathematical Model of Mechanical System

A sketch of the mechanical system of a resistance welding machine with a C-frame is shown in Fig. 5.1. From the point of view of dynamics, the electrode follow-up behaviour is mainly governed by the mass of the moving electrode system, damping, and machine stiffness. However, these parameters are very difficult to determine directly in practice due to the complexity of machine constructions. Even if it can be determined for some machines, the method might not be applicable to other machines because of the difference of the machine structures. Therefore, in this project, the mechanical machine parameters have been equivalent to the electrode central line (line *O-O* in Fig. 5.1), and a mechanical model of lumped parameters representing the dynamic response of resistance welding machine is adopted, as illustrated in Fig. 5.2,

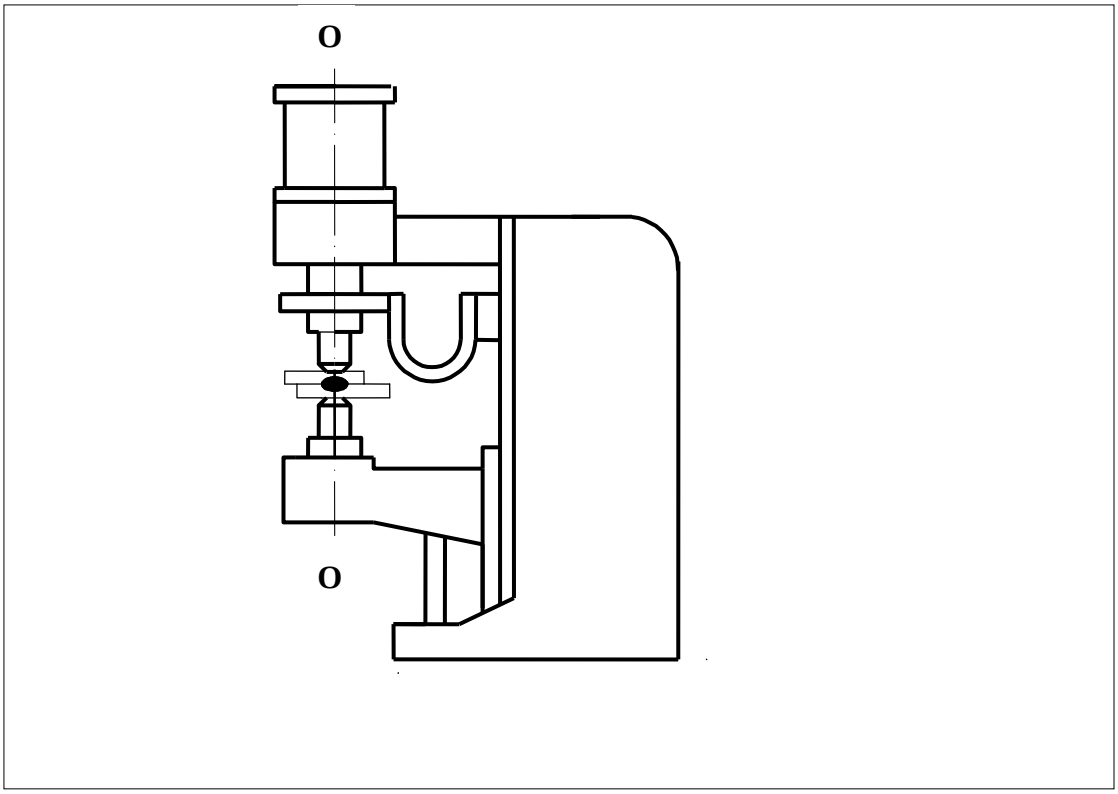

Fig. 5.1 — A sketch of resistance welding machine with C-frame

where m is the equivalent, lumped moving mass, including all moving masses (piston, sealing elements, electrode holders, etc.) and equivalent masses such as those from the flexible band conductors in the secondary circuit.

b is the equivalent damping coefficient, which is mainly caused by friction on the moving components in the compression system.

k is the equivalent spring constant, governed by the stiffness of piston rod, upper and lower electrode arms, machine frame including lower electrode arm support, and by the influence of compressed air or liquid in the cylinder and possible additional springs in the moving head.

F is the total action force delivered by the moving electrode, including force delivered by the compression system in the cylinder and the force of gravity, i.e.

$$F = F_{\text{cylinder}} + mg$$

F_r is the reaction force from the work piece on the moving electrode. After the squeeze stage, the electrode force is stabilized and reaches its set static value. At this moment, one may assume: $F = F_r$.

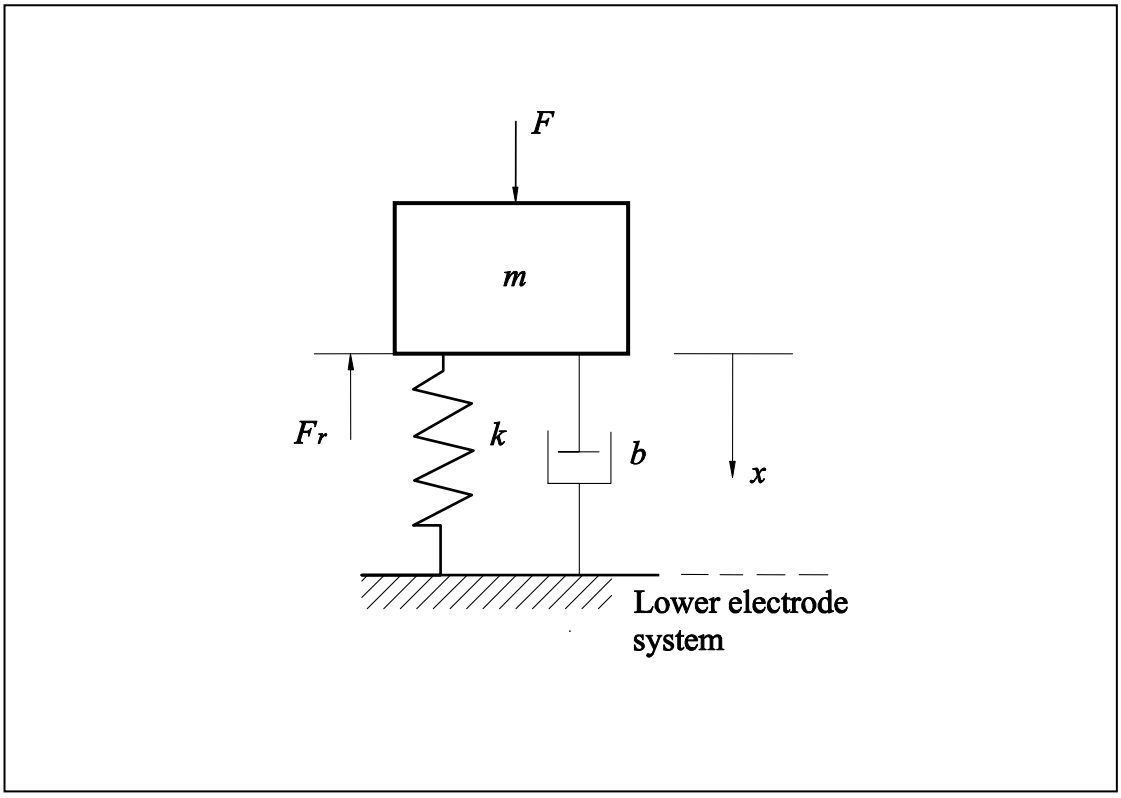

Fig. 5.2 — Mechanical model representing the dynamic response of resistance welding machine

When the current is applied, the reaction force decreases due to softening or melting of the weld parts resulting in plastic deformation of the parts and, in case of projection welding, rapid collapse of the projection. The electrodes will move towards each other under the action of the compression force and elastic spring back of the electrode arms. The relative movement between the two electrodes can be described by the following equation according to Newton's second law:

$$m\frac{d^2x}{dt^2} + b\frac{dx}{dt} + kx = F - F_r \qquad (5\text{-}1)$$

5.2 Principle of Identifying the Mechanical Machine Parameters

To solve the mathematical model above, the characteristic mechanical machine parameters (m, b, k) must be determined first. In the special case of no reaction force from the work piece, i.e. $F_r = 0$ corresponding to sudden collapse of the projection in

projection welding or splash formation in spot welding, Eqn. (5-1) is reduced to:

$$m\frac{d^2x}{dt^2}+b\frac{dx}{dt}+kx=F \qquad (5\text{-}2)$$

Experiments with sudden collapse of the load support are carried out in a special test set-up earlier designed at IPL, DTU [31, 36]. The test system is schematically illustrated in Fig. 5.3 and 5.4. A hardened steel pin (DIN 6325, high grade alloy steel 100Cr, 58~62 HRC), provided with a small notch in the middle, as shown in Fig. 5.5, is loaded to fracture by a punch mounted on the upper electrode. This simulates the momentary removal of load support occurring in resistance welding due to projection collapse or splash. After pin fracture the two electrodes are temporarily not in mechanical contact, resulting in the upper electrode moving down rapidly under the action of the force F delivered by the load cylinder, and the lower electrode bouncing up due to spring back of the prior loaded lower arm. The force F supplied to the upper electrode by the cylinder is assumed to be constant neglecting variation of cylinder pressure during pin fracture considering that the change of cylinder volume is very small. This implies that the relative movement between the two electrodes is represented by Eqn. (5-2). Different levels of fracture load are applied by employing pins of different diameters d. Since the upper electrode is moving freely, i.e. without support from the lower one after breaking of the pin, the test is named the *"free breaking test"*.

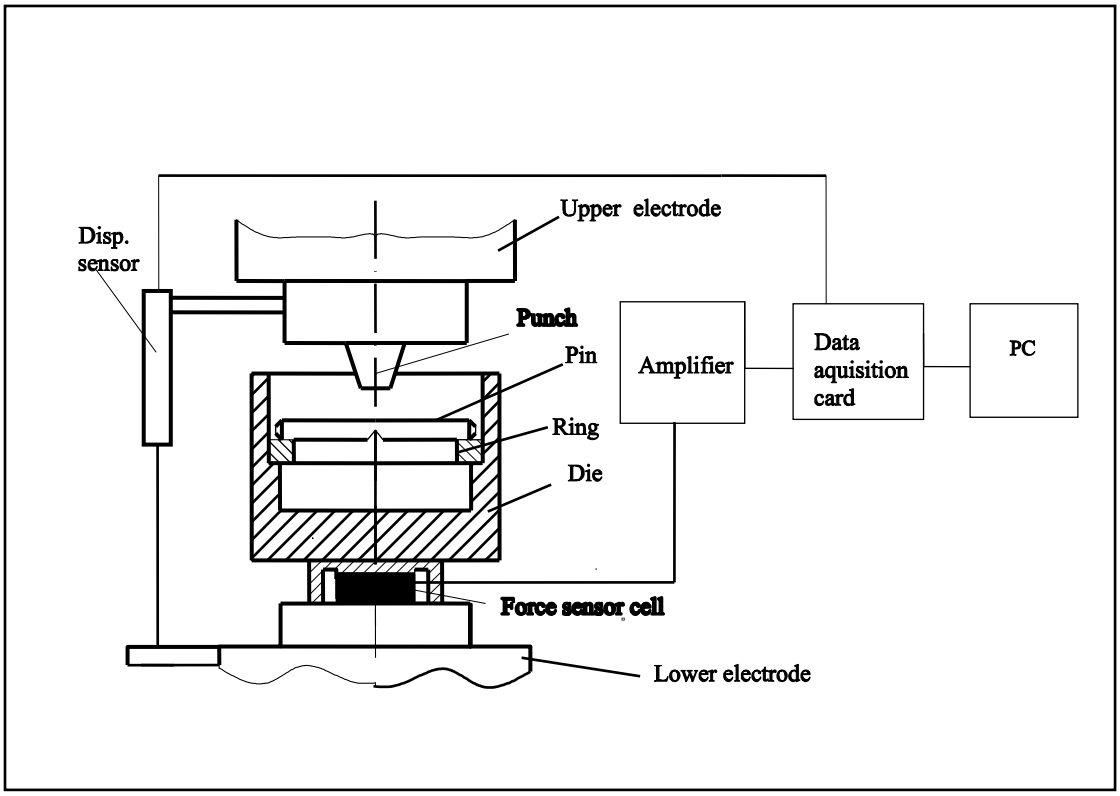

Fig. 5.3 — Experimental set-up and measuring system

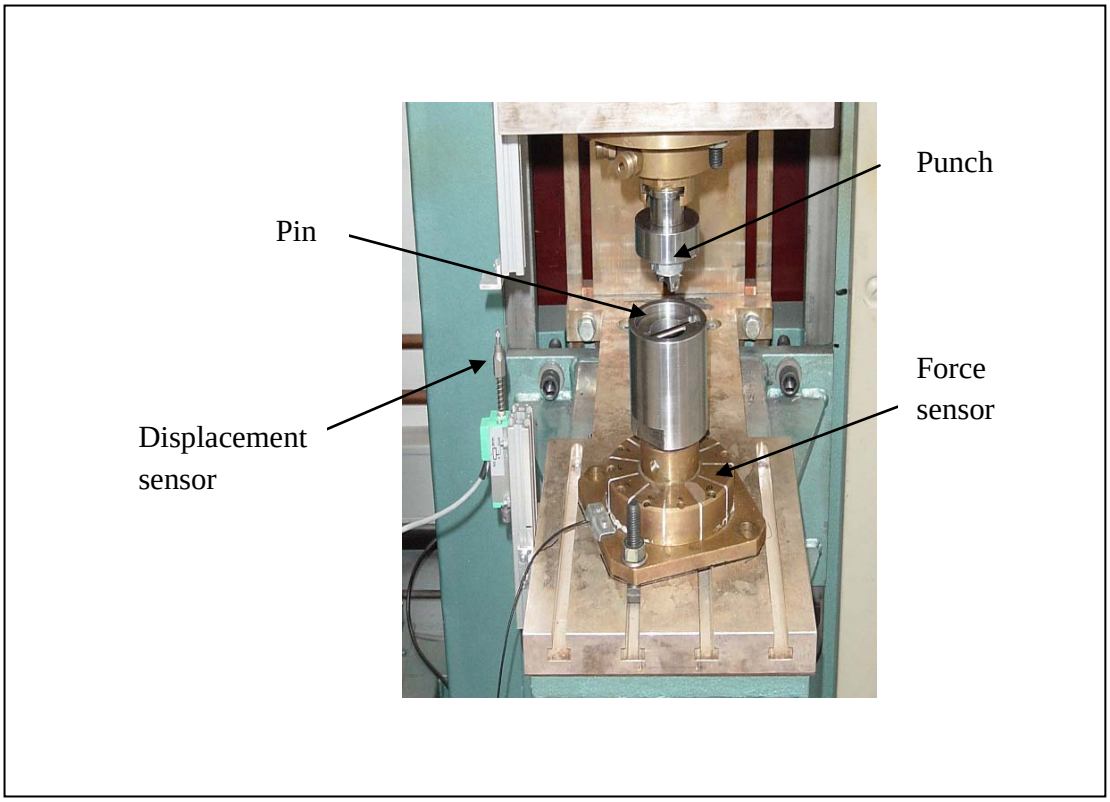

Fig. 5.4 — Photograph of the set-up of free breaking test

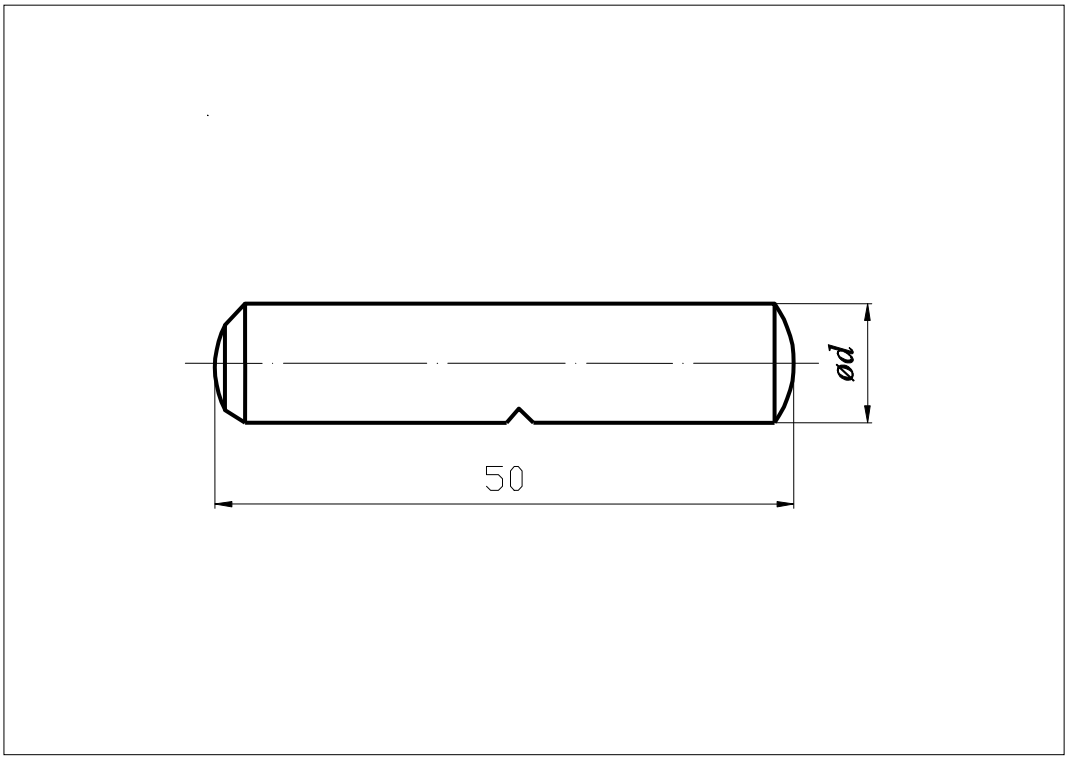

Fig. 5.5 — Geometry of the pin

During testing, the relative displacement x between the upper and lower electrode is measured by a resistive type displacement transducer, see Fig. 5.3. The total action force F (equal to the breaking force of the pin) is measured by a piezoelectric load transducer mounted on the supporting plate of the lower electrode. Measurements are recorded on a PC adopting a LABVIEW data acquisition program. A sampling frequency of 30 kHz ensures enough data points for subsequent numerical differentiation to determine the velocity $\dot{x}$ and acceleration $\ddot{x}$. For a more detailed description of the measuring equipment and measuring system, see Chapter 3.

Eqn. (5-2) can be numerically presented on matrix form:

$$\begin{bmatrix} \ddot{x}_1 & \dot{x}_1 & x_1 \\ \ddot{x}_2 & \dot{x}_2 & x_2 \\ \cdots & \cdots & \cdots \\ \ddot{x}_n & \dot{x}_n & x_n \end{bmatrix} \begin{Bmatrix} m \\ b \\ k \end{Bmatrix} = \begin{Bmatrix} \mathrm{F} \\ \mathrm{F} \\ \cdots \\ \mathrm{F} \end{Bmatrix}, \qquad [A] \cdot \begin{Bmatrix} m \\ b \\ k \end{Bmatrix} = [F] \tag{5-3}$$

In Eqn. (5-3), n corresponding values of x, $\dot{x}$ and $\ddot{x}$ for a given breaking test with an action force F are inserted, which actually corresponds to the measured data points of each parameter. The mechanical machine parameters m, b, k are thus determined by solving the n equations using least-squares method in MATLAB [37].

5.3 TECNA-250kVA-AC Machine

5.3.1 Free Breaking Test

Free breaking tests were performed on a single-phase TECNA-250kVA-AC welding machine provided with an air-actuated loading system (see Appendix A). The range of fracture forces investigated was 2-10 kN, which is the commonly used load range for the machine. Approximately 64 tests, with fracture loads rather evenly distributed within this range were carried out using four different pin diameters (ø 4, ø 5, ø 6 and ø 8 mm) and varying depth of the notch. Fig. 5.6 shows the typical load and displacement curves measured in the free breaking test when using a ø 5 mm pin. The pin fractures at a load F = 4.72 kN, after which the force drops to zero indicating that the two electrodes are separated and no reaction force exerted on the electrode head. The reason, why the force curve shown in Fig. 5.6 does not drop to null, is that a pre-load of 1.79 kN is needed for elastically deforming the transducer housing before the piezoelectric cell inside the housing is loaded as mentioned in Chapter 3. The time range **AB** shown in the figure corresponds to the duration of electrodes separation after pin fracture. This is the time range of interest in the test. After the time **AB**, the

two electrodes hit each other implying an abrupt increase in the load.

Cutting the data corresponding to the range **AB** of the curves and inserting it into Eqn. (5-3), the parameters *m, b, k* at each load are identified, see Table 5.1. In order to assess the quality of the regression by using Eqn. (5-3), the coefficient of determination R^2 (illustrated in Appendix B) is calculated for each test. A good fitting for each test is indicated by the high value of the R^2.

Fig. 5.7 shows the determined values of equivalent mass *m* and damping coefficient *b* as a function of the breaking load. The equivalent mass is seen to be almost constant, i.e. independent of the load, and an average value of 75 kg is adopted, while the equivalent damping coefficient is noticed to increase with increasing load.

Fig. 5.8 shows the equivalent spring constant versus the breaking load. Large scatter is observed, which might be due to the fact that the spring constant has much smaller influence on the electrode displacement than the other two parameters, since the term *kx* in Eqn. (5-1) is much smaller than the two first terms. For this reason it is chosen to adopt the average value 150 kN/m, independent of the load. The assumption of constant mass and stiffness of the mechanical system is intuitively correct, since they are related to the structure of the mechanical machine components. On the other hand the equivalent damping coefficient *b* is a function of the load, since it is mainly dominated by friction on the moving components. The relation between damping coefficient and load is obtained by regression analysis of the *F-b* curve (the regression quality is assessed using a correlation coefficient: *R-squared value* defined in Microsoft Excel, see Appendix B) in Fig 5.7. For the investigated machine, one gets:

$$b = 1528.9 \times F^{0.2678} \quad [\text{kg/s}] \qquad (5\text{-}4)$$

where *F* is the breaking load in kN. In summary, the final machine parameters *m* and *k* are identified as averaged values at different loads, whereas parameter *b* is based on Eqn. (5-4), see Table 5.1.

Fig. 5.9 shows a good agreement between experimentally measured and theoretically predicted displacement computed with the determined machine parameters at a load *F* = 8.1 kN (*m* = 75 kg, *b* = 2677 kg/s, *k* = 150 kN/m), while Fig. 5.10 showing the results at a load *F* = 9.93 kN (*m* = 75 kg, *b* = 2905 kg/s, *k* = 150 kN/m) represents the poorest agreement among the tests, and yet still shows acceptable correlation (*R*=0.981). The correlation coefficients *R* (the definition of the correlation coefficient *R* see Appendix B) for assessing the fitting quality at all test loads are listed in the last column in Table 5.1. In general, the agreement between measured and predicted displacement curves is good, indicating that the proposed way of identifying the mechanical machine parameters is applicable.

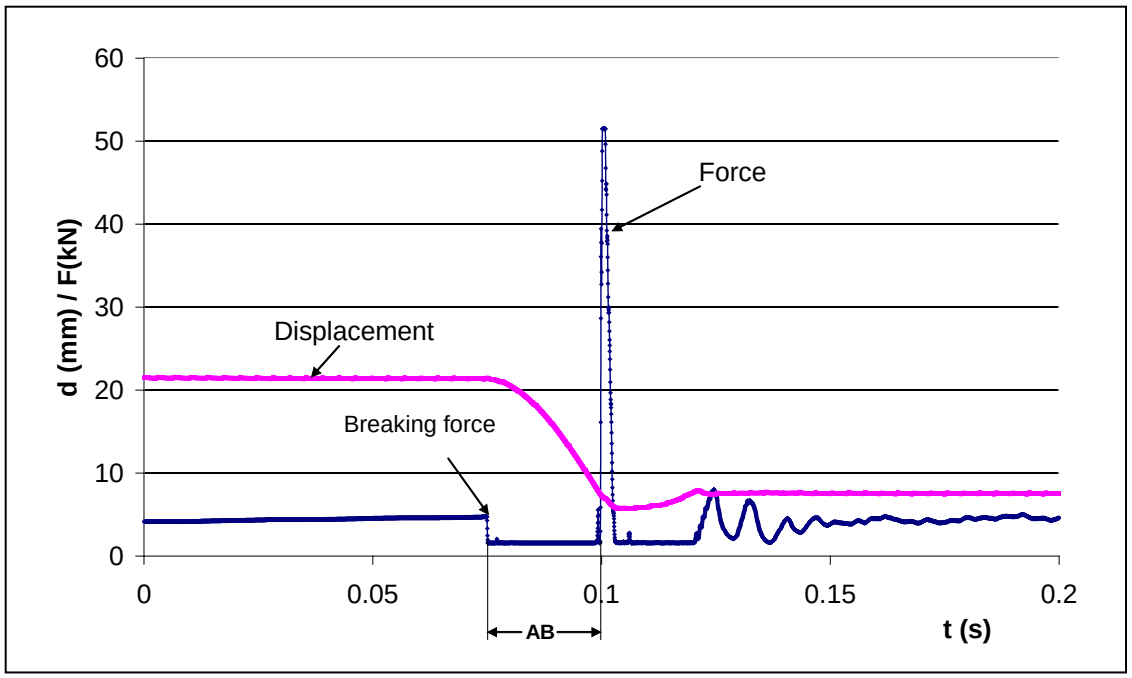

Fig. 5.6 — Measured load and displacement as functions of time for free breaking test on TECNA machine, fracture load 4.72 kN.

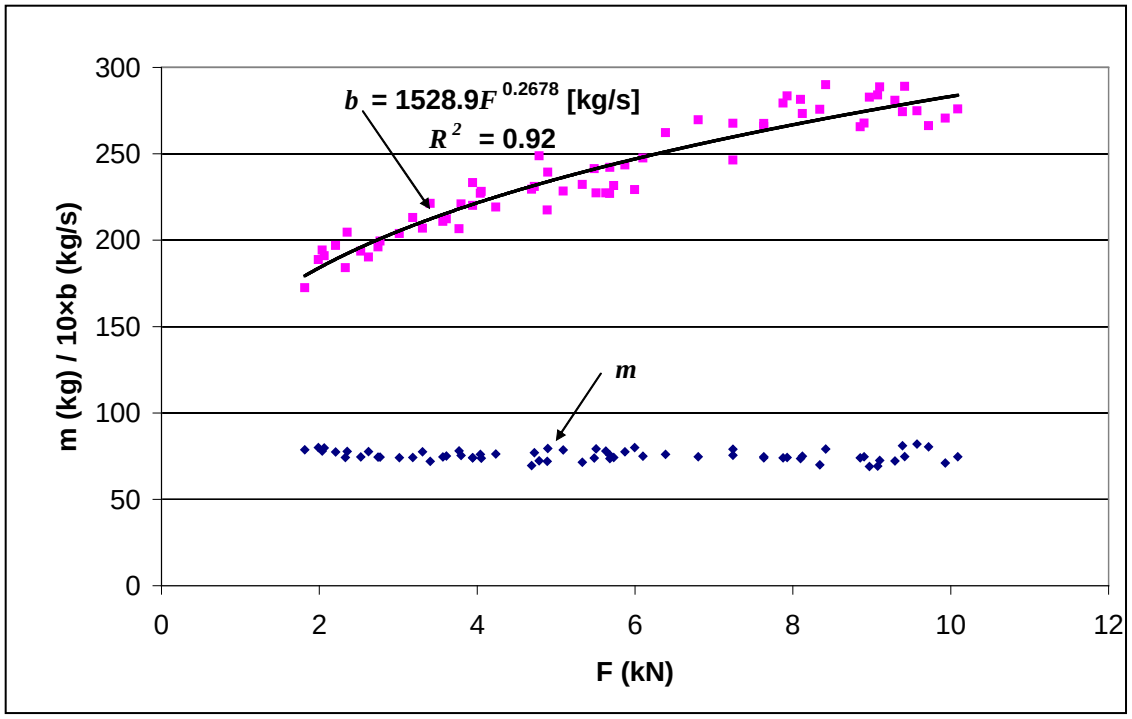

Fig. 5.7 — Equivalent mass and damping coefficient as a function of load.

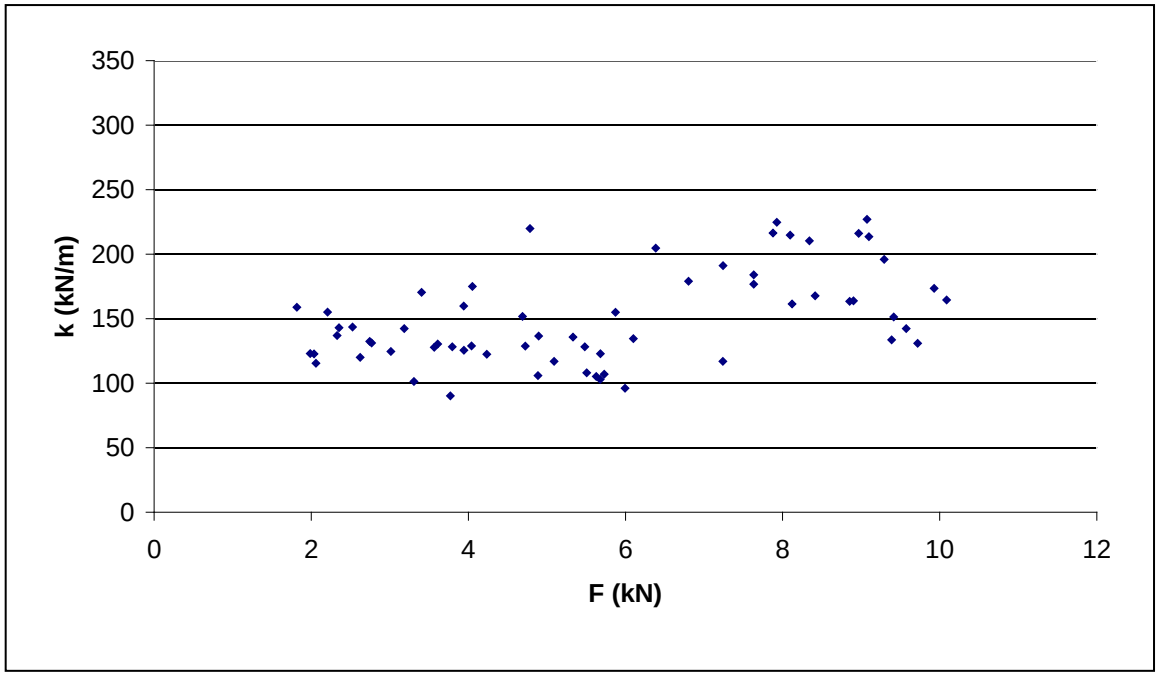

Fig. 5.8—Equivalent spring constant as a function of load.

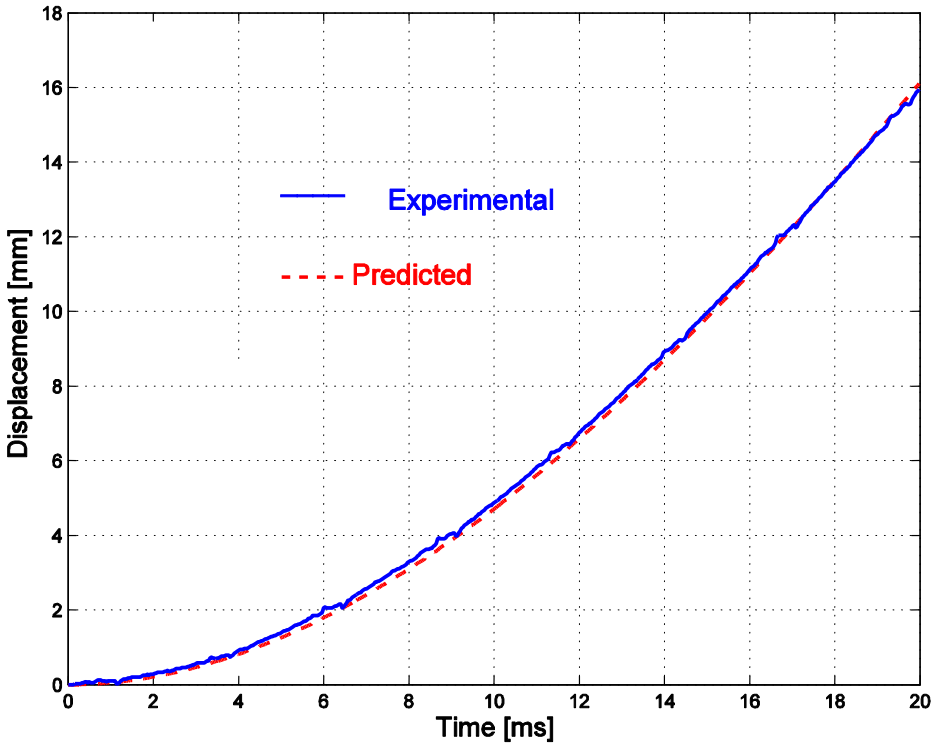

Fig. 5.9 — Experimental vs. predicted displacement at 8.1 kN.

Table 5.1 —Identified values of *m, b, k* for TECNA-250kVA-AC machine

Test No.	Breaking force F (kN)	Tested			calculated	
		Mass *m* (kg)	Damping coefficient *b* (kg/s)	Spring constant *k* (N/m)	*b* (kg/s)	*R*
1	5.3332	71.5	2323	135701	2394	1
2	4.8866	72	2175	105924	2338	1
3	10.089	74.7	2760	164486	2839	1
4	8.9688	69	2828	216149	2751	1
5	2.061	79.8	1910	115431	1856	0.9998
6	1.987	80	1888	122939	1838	0.9998
7	4.04	76	2272	128839	2222	1
8	3.4046	72	2213	170405	2123	1
9	4.8954	79.4	2394	136619	2339	1
10	5.506	79.2	2274	108096	2414	1
11	7.6325	74	2658	176775	2635	1
12	7.926	74.2	2835	224684	2662	0.9998
13	4.6905	69.5	2295	151745	2313	1
14	4.2356	76.3	2192	122429	2250	1
15	2.6226	77.6	1903	120035	1979	1
16	1.8161	78.7	1725	158813	1794	0.9999
17	5.8729	77.5	2435	155040	2456	1
18	2.3538	77.7	2046	143008	1923	0.9999
19	2.2072	77.4	1969	155117	1890	0.9999
20	2.036	78	1943	122724	1850	0.9998
21	8.3412	70	2758	210336	2698	0.9999
22	9.93	71	2707	173489	2827	1
23	9.074	69.2	2841	226958	2760	0.9998
24	6.3861	76	2623	204653	2512	0.9998
25	7.6325	74.7	2676	184059	2635	0.9999
26	8.8544	74	2656	163461	2742	0.9999
27	4.7243	77	2311	128721	2317	1
28	5.091	78.6	2284	116890	2364	1
2	9.294	72.2	2810	196028	2778	0.9999
30	7.8769	74	2794	216450	2657	0.9998
31	8.1213	75	2733	161380	2679	0.9999
32	5.995	80	2293	96109	2470	0.9999
33	7.2402	79	2464	116915	2598	1
34	4.7849	72.3	2488	219838	2325	0.9998

35	6.1006	75	2476	134517	2481	1
36	8.4153	79.1	2900	167692	2705	1
37	9.388	81	2744	133593	2785	1
38	5.4831	73.9	2414	128212	2412	1
39	5.6803	73.6	2421	122856	2434	1
40	9.7198	80.4	2663	130922	2811	0.9999
41	4.0515	73.8	2282	174996	2224	0.9999
42	9.5735	82	2749	142294	2800	1
43	3.5652	74.5	2109	127839	2149	1
44	3.609	75.1	2124	130393	2156	1
45	5.6796	75.7	2271	102901	2434	1
46	5.7292	74.2	2316	107013	2440	1
47	3.1847	74.2	2131	142293	2085	1
48	3.9423	74.1	2201	125529	2208	1
49	3.7957	75.4	2210	128281	2185	1
50	2.3294	74.2	1841	137011	1917	0.9999
51	3.0136	74.1	2039	124533	2054	0.9999
52	2.7692	74.4	1995	131171	2008	0.9999
53	3.7712	78.1	2066	90229	2182	0.9999
54	2.5249	74.5	1937	143563	1959	0.9999
55	3.942	74	2333	159817	2208	0.9999
56	7.2415	75.5	2677	191160	2598	0.9999
57	8.9033	74.7	2678	163806	2746	0.9999
58	5.629	78	2274	105261	2429	0.9999
59	6.8016	74.7	2697	179092	2555	0.9999
60	2.7448	74.4	1961	132424	2004	1
61	3.3069	77.5	2069	101321	2106	0.9999
62	9.4156	74.8	2890	151318	2787	0.9999
63	8.0968	73.6	2815	214730	2677	0.9999
64	9.099	72.5	2887	213573	2762	0.9999
Averaged		***m* = 75.38281**		***K* = 149821.66**		

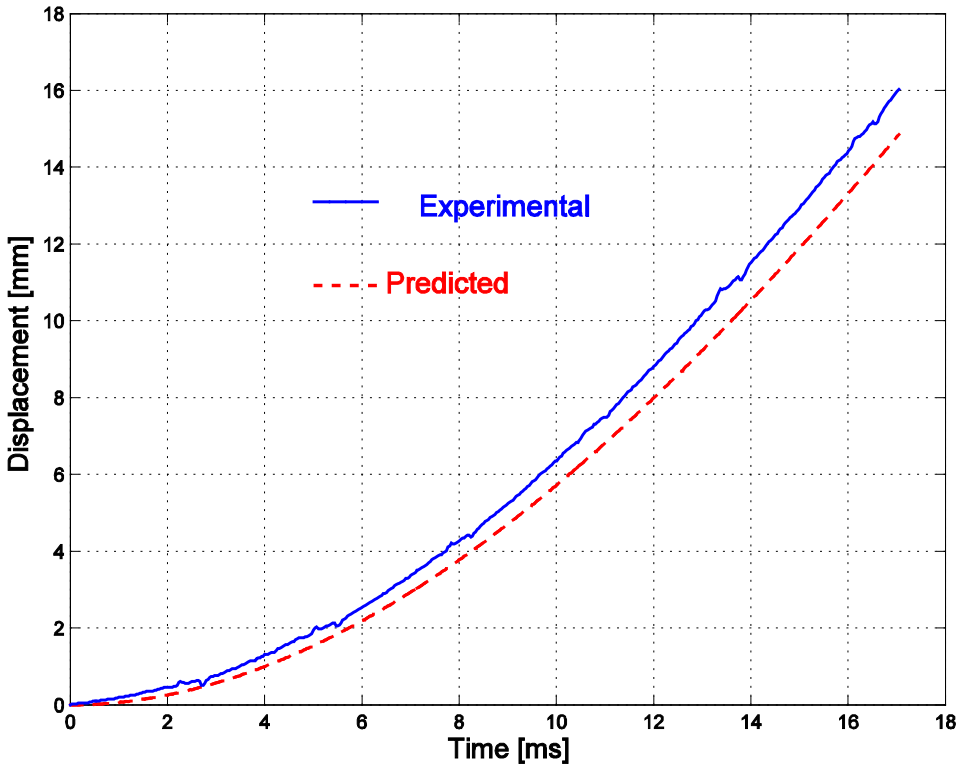

Fig. 5.10 — Experimental vs. predicted displacement at 9.93kN.

5.3.2 Validation of the Model

5.3.2.1 Supported Breaking Tests

In order to evaluate the validity of the mathematical model and the test method described above for the case, with a reaction force present after pin fracture ($F_r \neq 0$), disk springs (Belleville washer) are added in the breaking test (see Fig. 5.11). Fig. 5.12 shows a photograph of the device. In this way a reaction force F_r is introduced, which is varied by varying the stiffness level changing the number of springs as well as the way of stacking them.

Three basic disk springs (DIN 2093)[38] are used, of which the definition and specification are described in Table 5.2 and Fig. 5.13. Six different spring setups are applied by stacking different combinations of three basic springs in series or parallel. This is illustrated in Fig. 5.14 and Table 5.3.

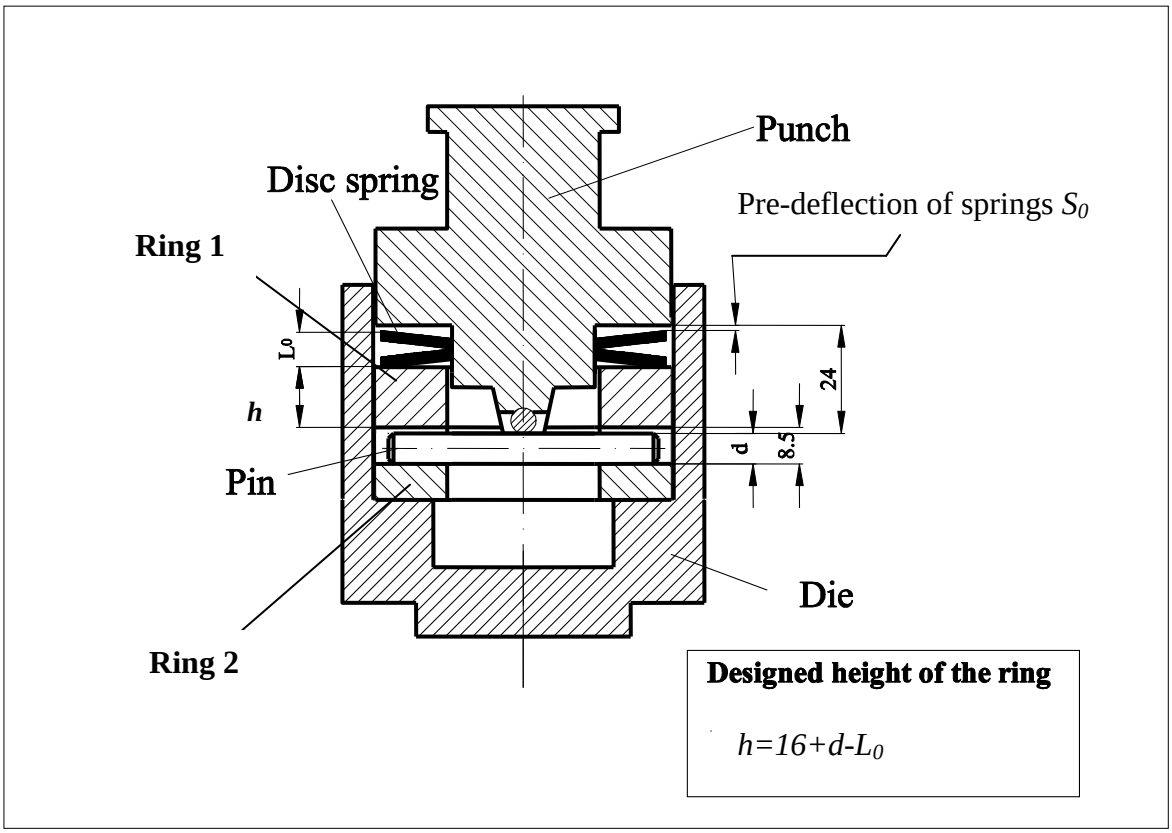

Fig. 5.11 — Supported breaking test set-up with disk springs providing reaction force

Table 5.2 — Selection of disc springs

Disc spring	*De* [mm]	D_i [mm]	*t* [mm]	L_0 [mm]	Force *F* [N]	Deflection s [mm]
No. 1	56	28.5	1.5	3.45	2621	1.46
No. 2	56	28.5	2.0	3.60	4438	1.20
No. 3	56	28.5	3.0	4.30	11441	0.97

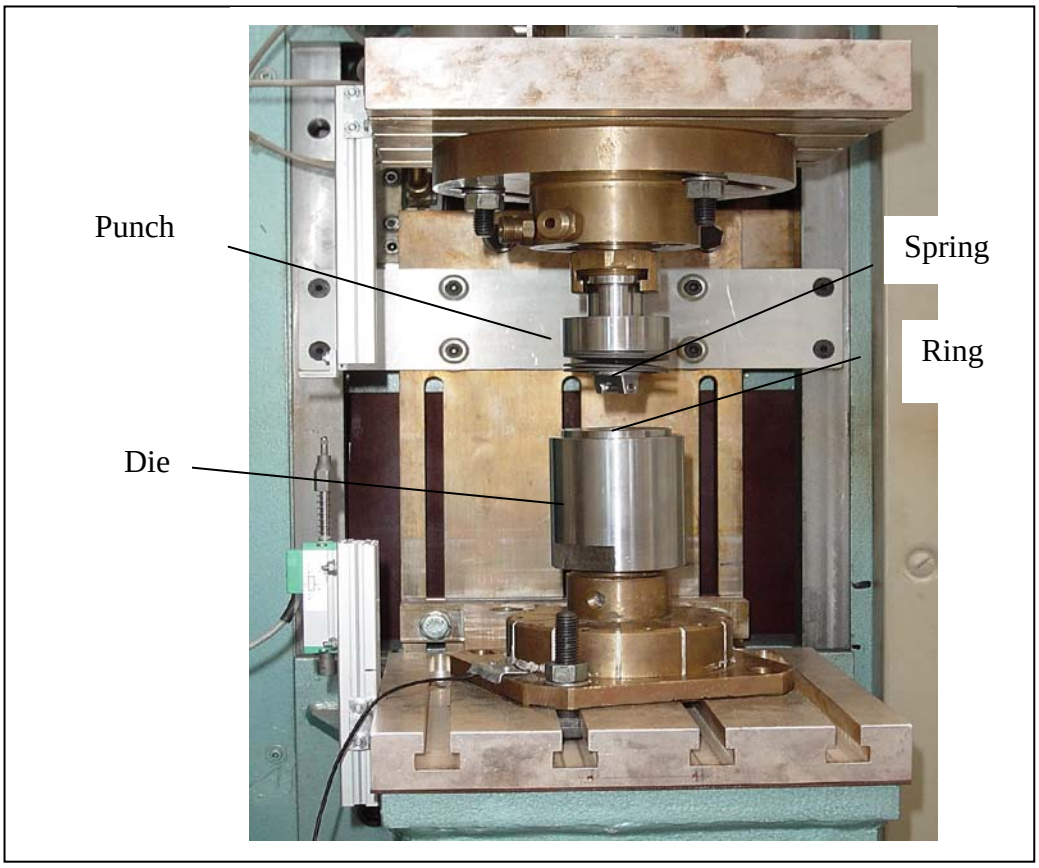

Fig. 5.12 — Photograph of breaking test set-up with disk springs providing reaction force

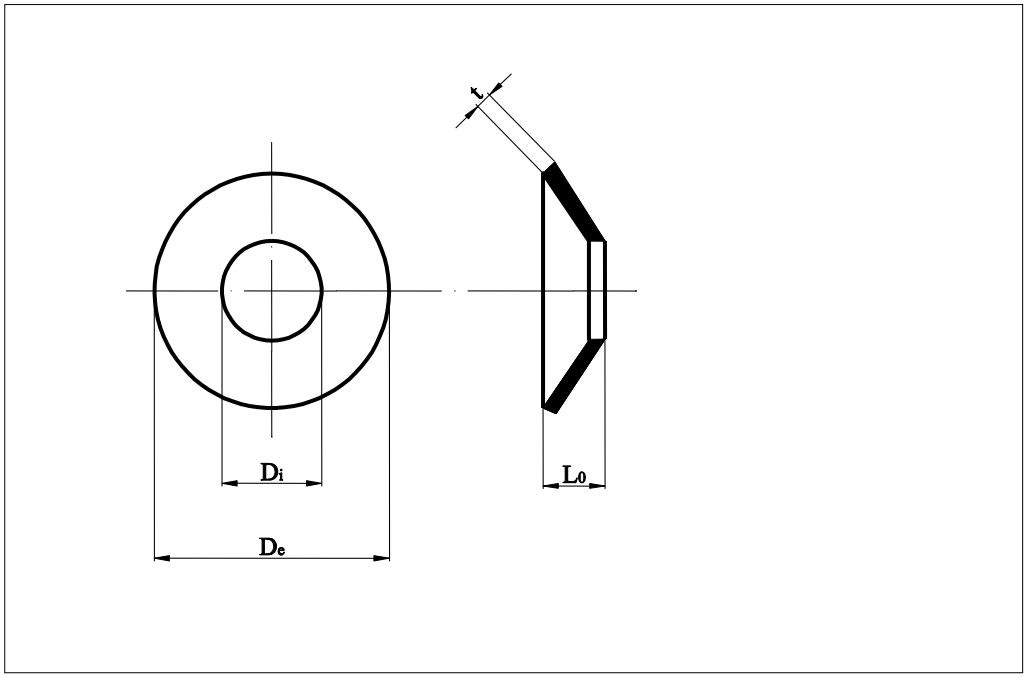

Fig. 5.13 — Description of disc spring

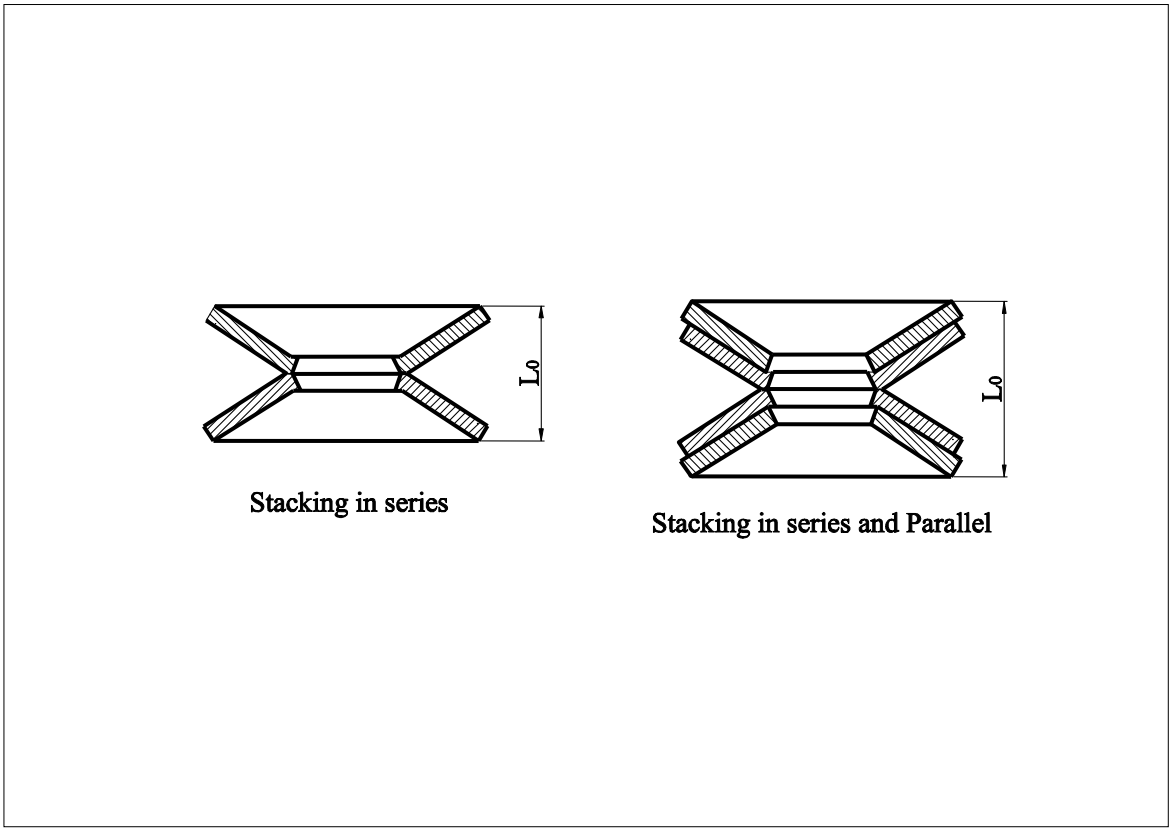

Fig. 5.14 — Stacking of the disc springs

Table 5.3 — Stacking and combination of disk springs

Stacking case	Spring combination	Overall height L_0 [mm]	Force F [kN]	Deflection s [mm]	Stiffness K [kN/mm]
In series	2×No.1	6.9	2.621	2.92	0.984
In series	2×No.2	7.2	4.438	2.40	1.849
In series and parallel	4×No.1	10.3	5.242	2.92	1.795
In series and parallel	(2× No. 1) + (2 ×No.2)	11.0	7.059	2.66	2.654
In series and parallel	4 × No. 2	11.6	8.876	2.4	3.698
In series	2×No. 3	8.6	11.441	1.94	5.897

The tests, named as *"supported breaking test"*, correspond to normal welding operations, where a remaining reaction force exists during collapse of the projection. The springs are slightly pre-loaded ensuring a reaction force on the moving electrode just after pin fracture (The pre-deflection of the springs is achieved by adjusting the

height *h* of the ring in each case of using different spring combination and the pin, see Fig. 5.11, and Table 5.4).

It should be noted, that the load *F* in Eqn. (5-1) in these experiments is the total action force just before pin fracture. Due to the slight pre-load of the springs this load is a little greater than the net pin breaking force.

Fig. 5.15 shows an example of the measured load and displacement curves, where fracture occurs at a total load of 10.5 kN. After fracture the force drops abruptly and then increases linearly with superimposed fluctuations due to the springs (curve part **AB**). The relative displacement of the electrodes is determined theoretically by inserting the values of *m, b and k* identified by the free breaking tests and the measured action force *F* (at point **A**) and oscillating reaction force F_r (between **AB**) into Eqn. (5-1). Solving for *x* is a vibration problem of one degree of freedom system under the excitation of an arbitrary force (because F-F_r in Eqn. (5-1) is an arbitrary force). The solution is the well-known Duhamel's integral [39]. The solution was obtained by numerical integration based on trapezoidal approximation.

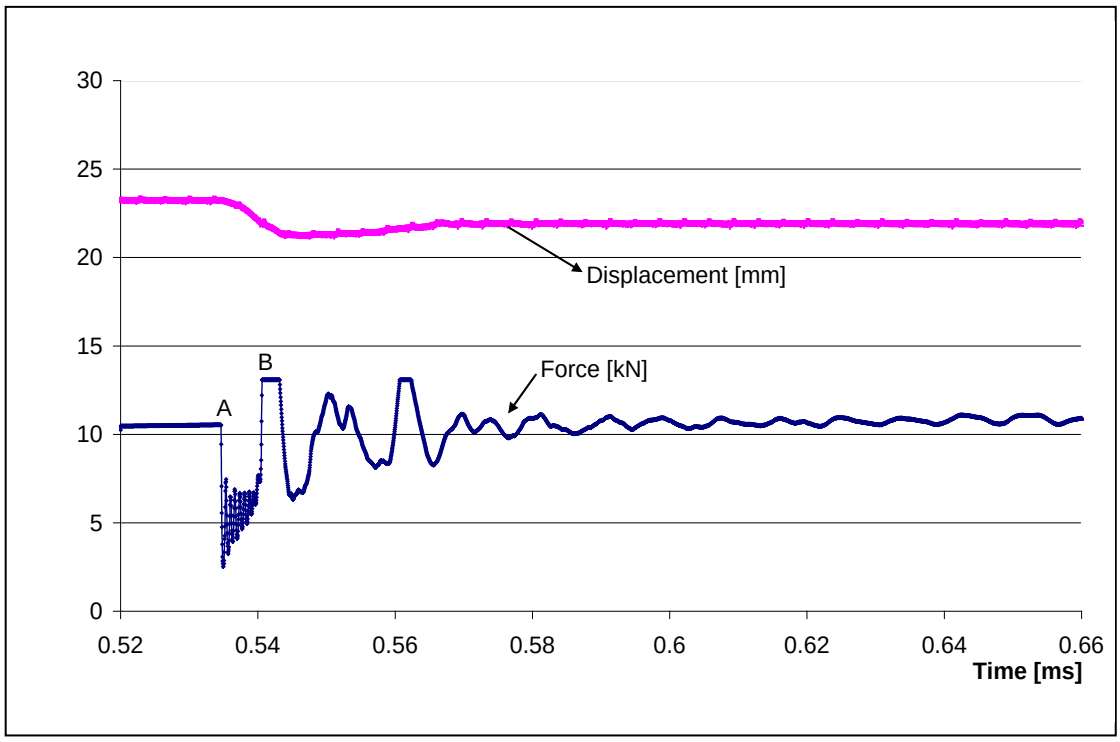

Fig. 5.15 — Measured curves in supported breaking test

Table 5.4 — Design of height of the ring

Pin diameter ***d*** **(mm)**	**Stacking of the springs**	**Height of the springs** L_0 **(mm)**	**Pre-deflection of the springs** S_0 **(mm)**	**Height of the ring** ***h*** **(mm)**
4	2×No.1 in series	6.9	-0.4	13
	2×No.2 in series	7.2	-0.7	13
	4×No.1 in series and parallel	10.3	-0.8	10
5	2×No.1 in series	6.9	-0.4	14
	2×No.2 in series	7.2	-0.7	14
	4×No.1 in series and parallel	10.3	-0.8	11
	(2×No.1)+ (2×No.2) in series and parallel	11	-0.5	10
6	2×No.1 in series	6.9	-0.9	15
	2×No.1 in series	7.2	-0.7	15
	(2×No.1)+ (2×No.1) in series and parallel	10.3	-0.8	12
	(2×No.1)+ (2×No.2) in series and parallel	11	-0.5	11
	(2×No.2)+ (2×No.2) in series and parallel	11.6	-0.6	10.5
8	2×No.1 in series	6.9	-0.4	17
	2×No.2 in series	7.2	-0.7	17
	(2×No.1)+ (2×No.1) in series and parallel	10.3	-0.8	14
	(2×No.1)+ (2×No.2) in series and parallel	11	-0.5	13
	(2×No.2)+ (2×No.2) in series and parallel	11.6	-0.6	12.5
	2×No.3 in series	8.6	-0.6	15.5
Ten rings with the heights as shown in right column were made		*h*= 10, 10.5, 11, 12, 12.5, 13, 14, 15, 15.5, 17		

All in all 12 supported breaking tests were carried out in the load range 4.5-10.9 kN with different reaction forces (different set-up of springs). The corresponding machine mechanical parameters *m, b, k* determined by the free breaking tests are shown in Table 5.5. The agreement between experimental and predicted displacement curves for the supported breaking tests are assessed by calculating the correlation coefficient *R*, as presented in Table 5.5 showing reasonably good results. Fig. 5.16 gives an example of comparison of measured and predicted displacement curve at a load F = 6.52 kN.

Table 5.5—Test results of supported breaking test on TECNA-250kVA-AC machine

Test No.	Action force F (kN)	Determined by free breaking test			R
		m (kg)	b (kg/s)	k (N/m)	
1	6.03	75.4	2474	149822	0.997
2	5.03		2350		0.998
3	5.43		2405		0.996
4	5.66		2432		0.995
5	4.49		2286		0.999
6	6.516		2526		0.998
7	6.28		2501		0.999
8	6.95		2570		0.998
9	5.38		2399		0.999
10	7.095		2584		0.998
11	10.87		2897		0.995
12	10.51		2871		0.996

5.3.2.2 Projection Welding Tests

To further verify the model, a series of projection welding tests were carried out using TECNA-250kVA-AC machine, joining rings in stainless steel sheet (W.Nr. 1.4301) to disks in mild steel (W.Nr. 1.0037) provided with an annular projection, see Fig. 5.17.

Totally 17 tests were performed, the welding conditions and results are illustrated in Table 5.6. Among these tests, the weld time was chosen to be 2, 3, 4 cycles, the current was selected just below or just above the expulsion limit causing splash formation. During the experiments, the electrode force, the relative displacement between two electrodes and the weld current were recorded. An example of the data recorded is shown in Fig. 5.18. For this test, an electrode force of 4.4 kN was chosen,

the weld time was 4 cycles, and the weld current was 16.3 kA. The weld stage part ranging from time A to B in Fig. 5.18 was selected for subsequent analysis.

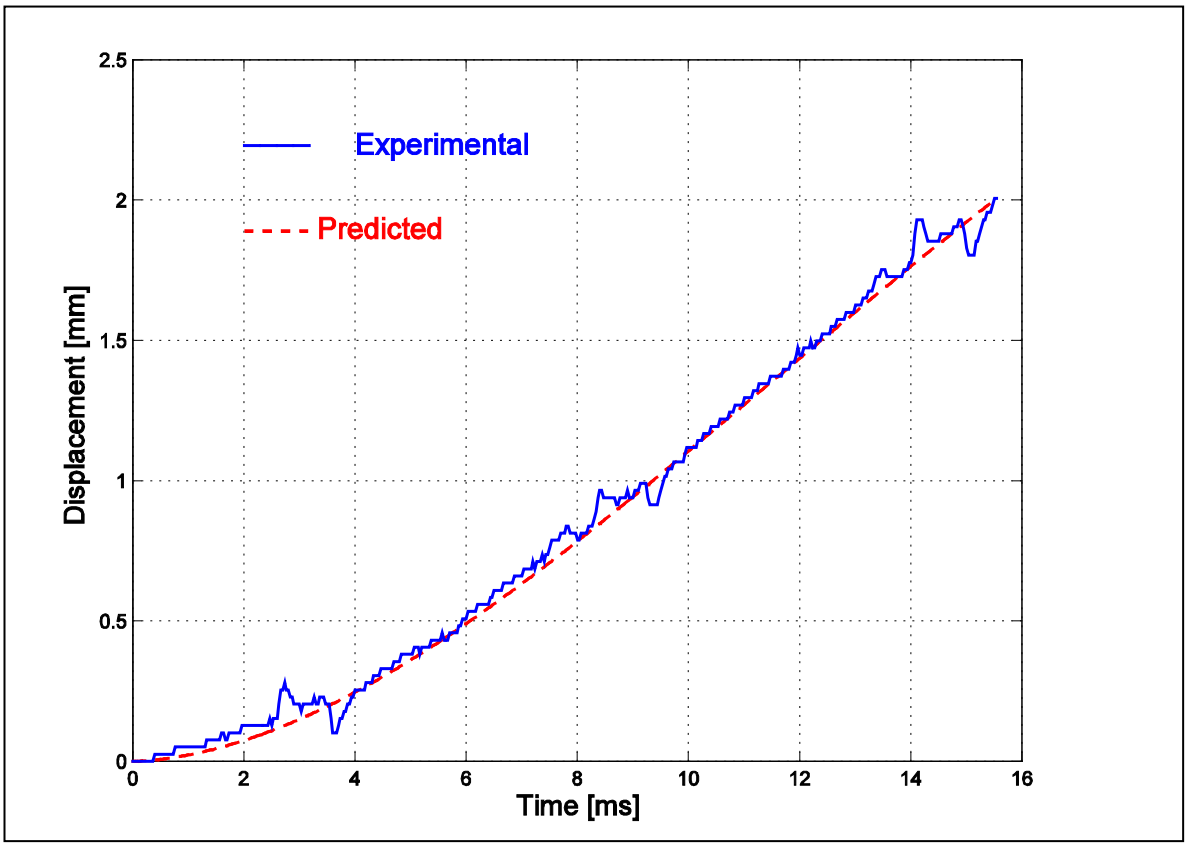

Fig. 5.16 — Example on experimental and predicted displacement in supported breaking test at a load of 6.52 kN.

Reading off from Fig. 5.18 the electrode force prior to current flow, F = 4.5 kN, and the measured reaction force F_r (the force in range of **AB**) as function of time during the welding stage and inserting into the mathematical model Eqn. (5-1), the relative displacement was computed.

In this way, the predicted time-displacement curves for all the tests were computed based on the model. Note that the machine parameters m, k still are inserted as the averaged values identified by the free-breaking test, and that parameter b is inserted as the value calculated according to the action force F (see Table 5.6). It was noticed that the correlation coefficient R is low for some tests in assessing the agreement between predicted and measured relative electrode displacement during the weld stage. This might be due to the measured displacement curve with relatively high fluctuations. But by observing the curves, actually an acceptable agreement in pattern or trend was found. The column "*agreement*" in Table 5.6 refers to this qualitative evaluation.

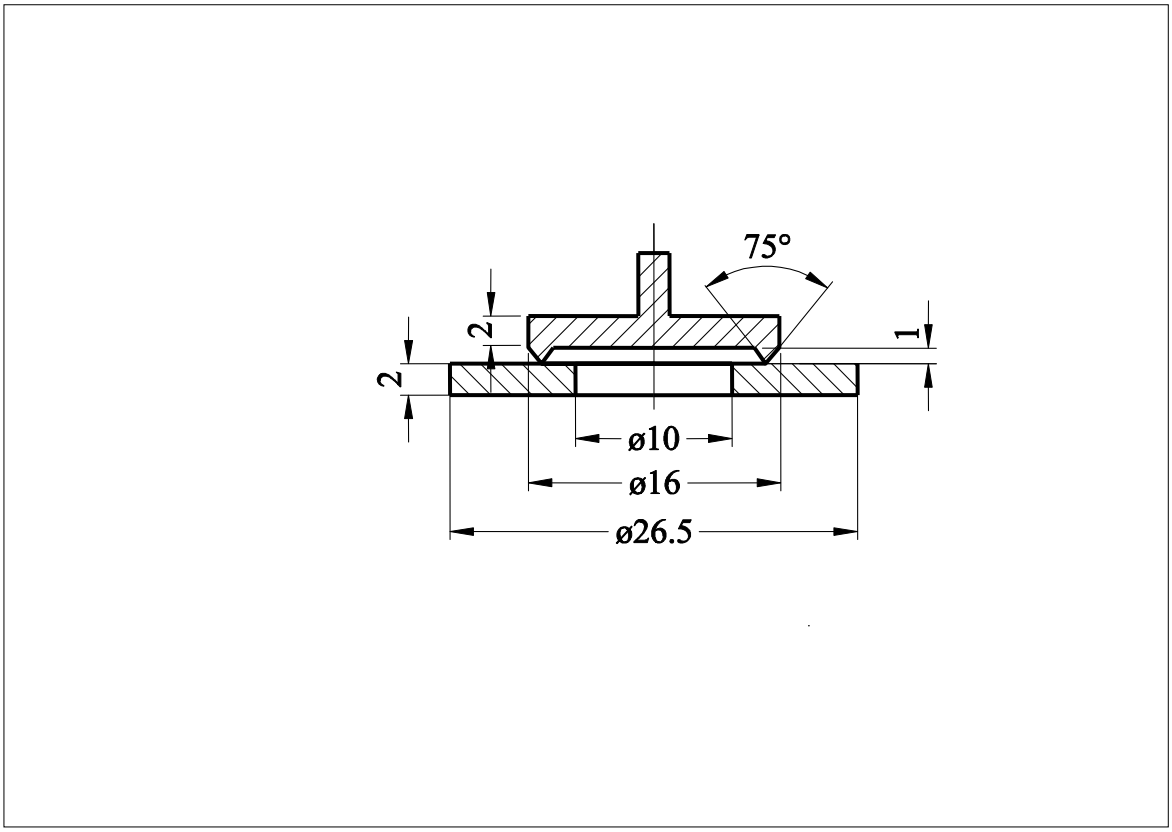

Fig. 5.17 — Geometry of projection welding work pieces.

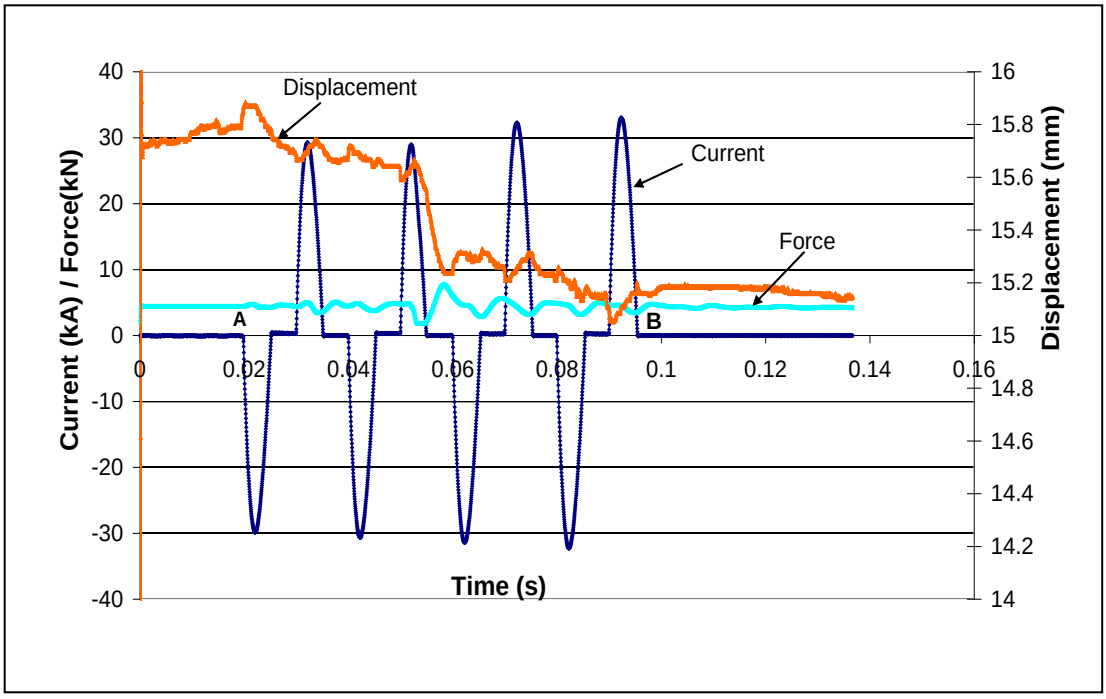

Fig. 5.18 — Measured curves for projection welding

Table 5.6— Welding condition and results of projection welding on TECNA machine

Test No.	Weld time [Cycle]	Force *F* [kN]	Weld current [kA]	Calculated *b* [kg/s]	*R*	Weld Quality	Agreement
1*	4	4.53	16	2291	0.951	good	good
2	3	4.45	17	2281	0.899	big splash	good
3	2	4.48	18.6	2284	0.680	good	acceptable
4	2	4.44	18.9	2279	0.842	splashed	acceptable
5	4	4.40	16.3	2274	0.763	splashed	acceptable
6	4	4.30	16.6	2260	0.899	splashed	Good
7	4	4.31	18.9	2262	0.846	splashed	acceptable
8*	4	4.29	20	2258	0.910	splashed	good
9	3	4.38	14.9	2271	0.715	Good weld	good
10	3	4.37	16	2269	0.573	Small splash	acceptable
11	3	4.37	17	2269	0.814	good	good
12	2	4.32	18	2263	0.586	splashed	good
13	2	4.35	18.6	2267	0.556	Small splash	acceptable
14	2	4.36	17.1	2268	0.691	splashed	acceptable
15	3	6.80	17	2555	0.796	Small splash	good
16	3	6.73	17	2548	0.740	good	good
17	3	6.74	17	2549	0.894	good	good

Fig. 5.19 gives two examples (the tests with * in Table 5.6) on the comparison between predicted and measured relative electrode displacement during the welding stage showing rather good agreement.

The curves for the remaining 15 tests are shown in Appendix C. In these curves, the electrode force during welding is shown additionally.

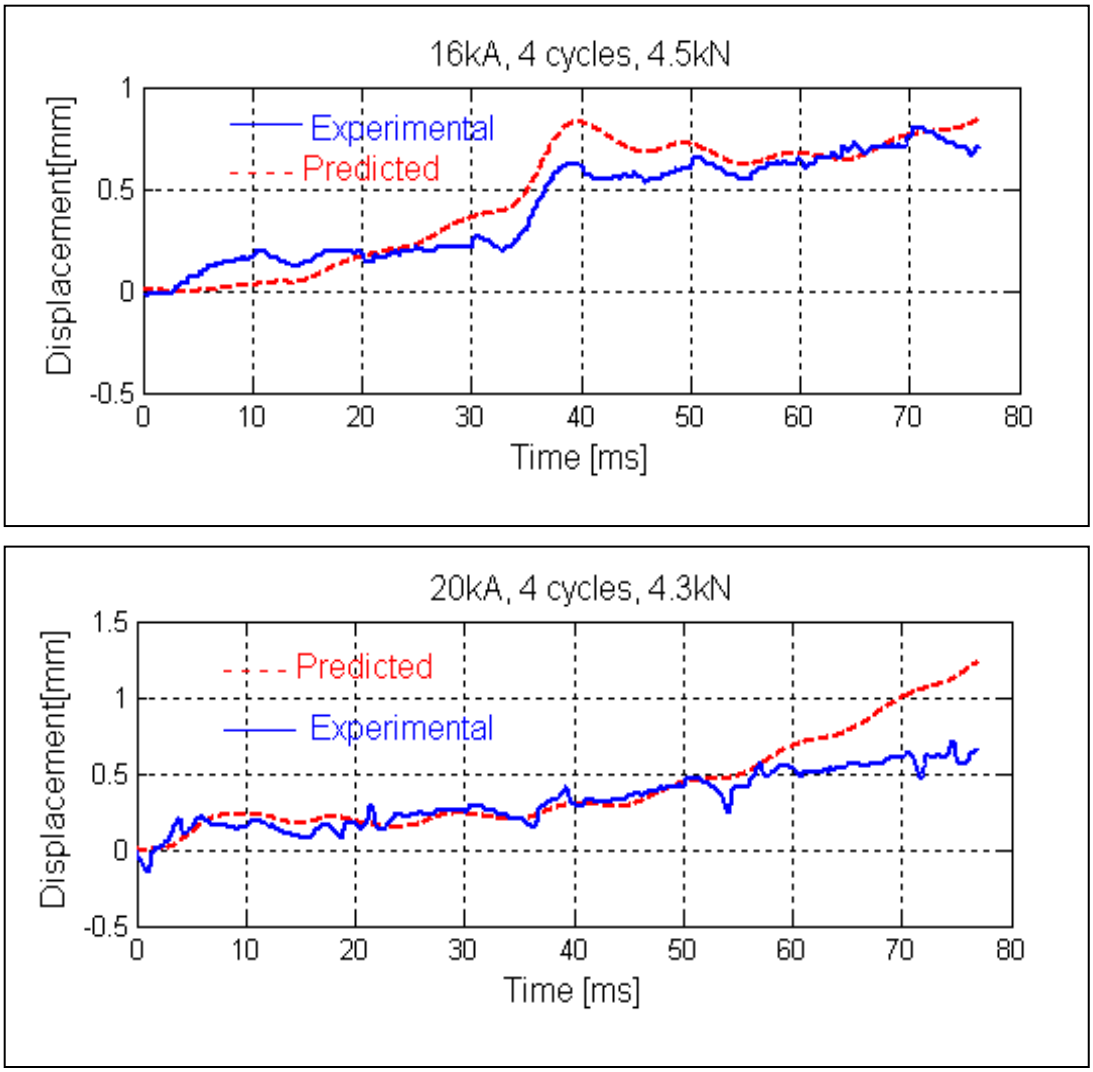

Fig. 5.19 — Comparison of tested and predicted displacements.

5.4 EXPERT-DC-Inverter Machine

The same method and procedure were used on a hydraulically operated EXPERT-DC-Inverter machine (see Appendix A).

5.4.1 Free Breaking Test

Free breaking tests were carried out on the EXPERT machine for identification the mechanical parameters *m*, *b*, and *k*. The commonly used load range of this machine is 2-10 kN in welding the mild steel, stainless steel and aluminum sheets. All in all 63

tests were performed, with fracture loads rather evenly distributed within the range of 4.3-11.8 kN using four different- diameter pins (ø 4, ø 5, ø 6 and ø 8 mm) and varying depth of the notch on the pin. Fracture loads below 4.3 kN were not able to be applied due to the fact that the pin (ø 4 pins were employed for low fracture load) was fractured immediately when the punch was moving down and touching the pin. The operation procedure of the test includes two steps: first moving down the punch on the pin until the process is stabilized and then starting the press system again to break the pin for the measurement. However, since the back pressure of this machine which is adjusted by the flow control valve 2 in Fig. 5.20 is very low in order to get a high force in the welding stage, a high pressure is required to initiate movement of the piston. This implies that the punch speed or falling impact is high, which is different from the pneumatic TECNA machine (see Fig. 5.21). In this machine, the low-force electrode head descent is obtained by supplying pressure in the cylinder in both lower and upper chamber. When the descent is finished (after the squeeze stage) the back pressure is removed in order to obtain the welding force [41].

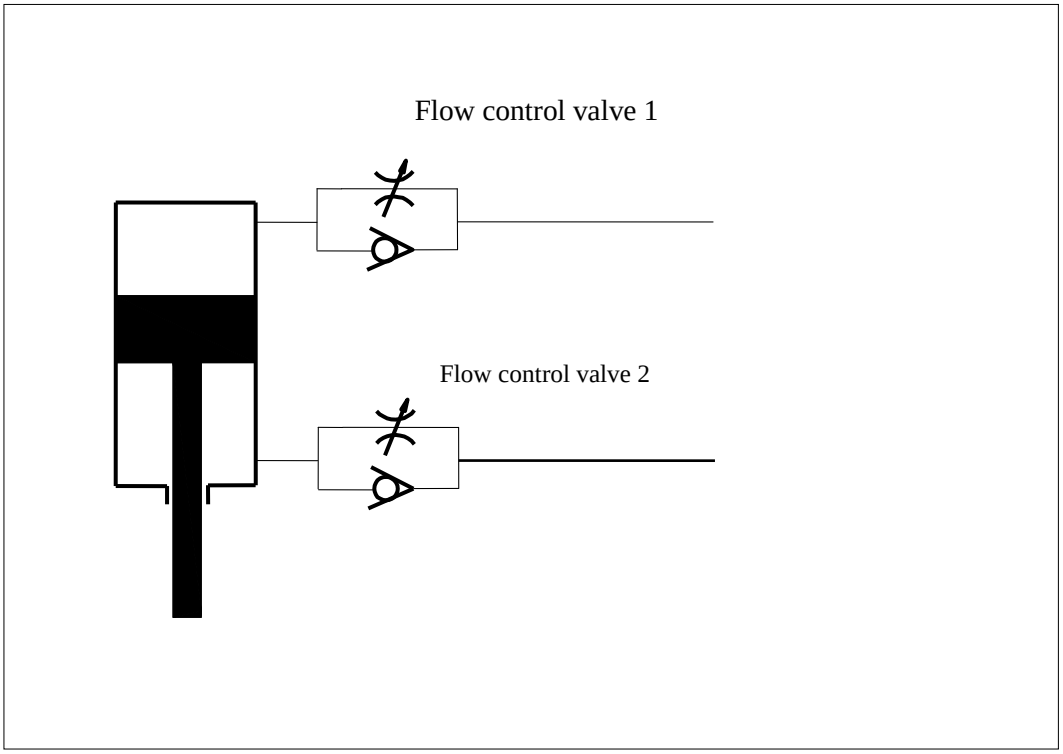

Fig. 5.20 — High force head descent in hydraulic EXPERT machine

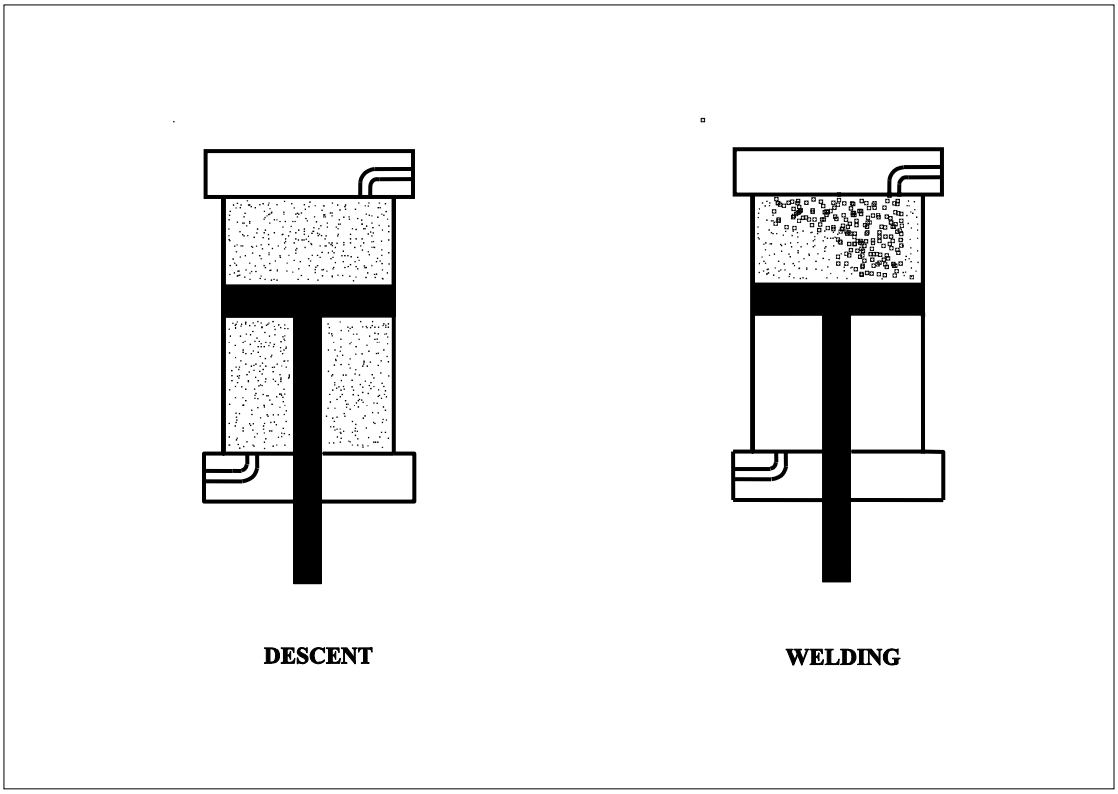

Fig. 5.21 — Low force head descent in pneumatic TECNA machine

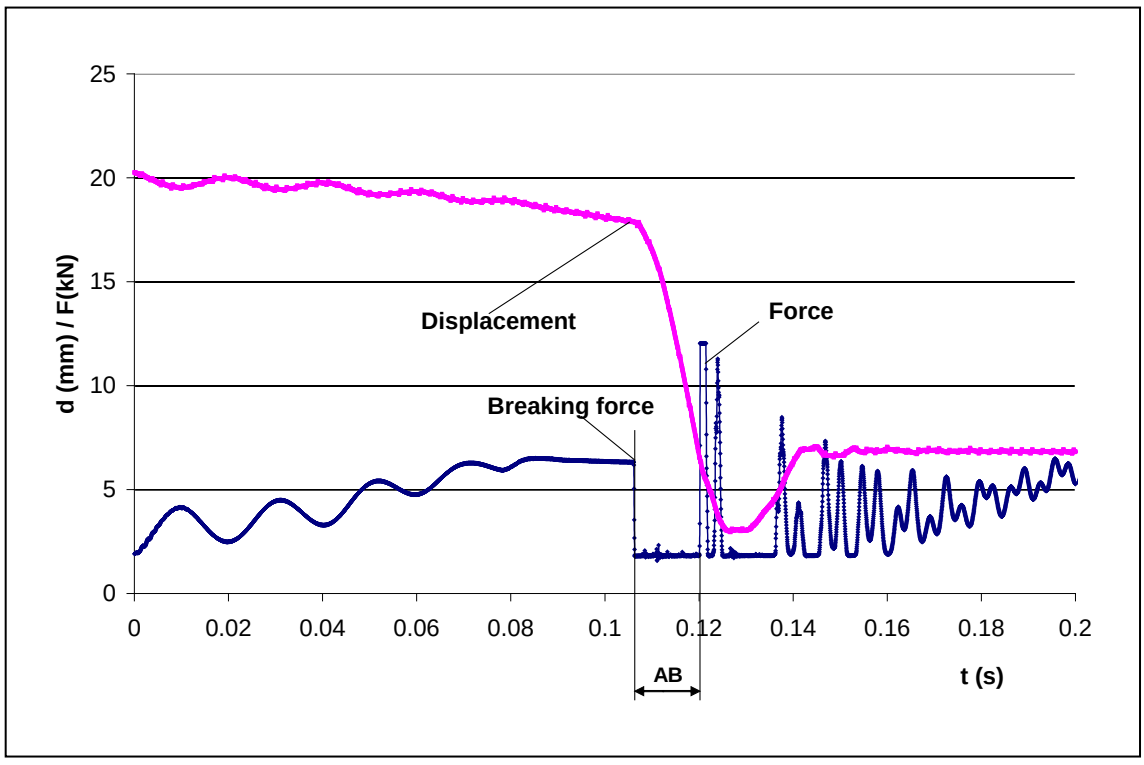

Fig. 5.22— Measured load and displacement as functions of time for free breaking test on EXPERT machine, fracture load 6.18 kN.

Fig. 5.22 shows the typical load and displacement curves measured in the free breaking test when using a ø5 mm pin. The pin fractures at a load F = 6.18 kN, after which the force drops to zero indicating that the two electrodes are separated and no reaction force exerted on the electrode head. Note that the force curve shown in Fig. 5.21 does not drop to zero due to the force transducer characteristics, which was explained earlier. The time range **AB** shown in the figure corresponds to the duration of electrodes separation after pin fracture. This is the time range of interest in the test. After the time **AB**, the two electrodes hit each other and a new vibration is excited. In addition, it is noticed that fluctuations in the force appear during build-up to the static value due to the springs in the welding head.

Inserting the data corresponding to the range **AB** of the curves into Eqn. (5-3), the parameters m, b, k at each load are identified, see Table 5.7. Fig. 5.23 — 5.25 show the curves based on the determined values (in Table 5.7) of equivalent mass m, damping coefficient b and spring constant k. They are all functions of the breaking force. The relationship between each of these parameters and the breaking force is determined by regression analysis of the curves, and corresponding regression equations are obtained. For the investigated machine, one gets:

$$m = 4.7229F + 8.8676 \quad [\text{kg}] \qquad (5\text{-}5)$$

$$b = 299.36F + 329.71 \quad [\text{kg/s}] \qquad (5\text{-}6)$$

$$k = 34.811F + 150.94 \quad [\text{kN/mm}] \qquad (5\text{-}7)$$

where F is the breaking load in kN.

Comparisons of the experimental displacement curves based on free breaking tests with the theoretical displacement are done with the parameters determined by the equations above. The agreement is assessed by calculating the correlation coefficient R. For all test loads, see the last column in Table 5.7. In general, the agreement between measured and predicted displacement curves was good, indicating that the proposed way of identifying the mechanical machine parameters is applicable. As an example, Fig. 5.26 shows the results at a load F = 5.897 kN (m = 36.7 kg, b = 2095 kg/s, k = 356.22 kN/mm), indicating a good correlation (R = 0.9999).

It should be remembered that, three additional springs are mounted in the weld head of this machine (see Fig. 4.6). The electrode force is applied through the springs in order to get a soft electrode application and fast follow-up speed. Large scatter is observed in the spring constant k in Fig. 5.25, as earlier observed on the TECNA machine. This might be due to the fact that the spring constant has much smaller influence on the electrode displacement than the other two parameters, since the term

kx in Eqn. (5-1) is much smaller than the two first terms.

In the free breaking test, the support is removed when the pin is fractured. The electrode head will move down rapidly. The motion of the head system is actually a problem of three degree of freedom system, but only the movement of part 1 (object 1 in Fig. 4.6) which represents the movement of upper electrode is of interest. The motion of part 1 is a dynamic process, which may be faster than movement of the other parts due to its smaller mass and due to the action of the spring, or it may be at same speed as the remaining part of the electrode head, depending on the load and how much the spring k_3 is compressed. This means that the amount with which mass, damping and stiffness are contributing to the movement is dynamic and variable.

The exact model and solution should be based on the theory of a three degree of freedom system. The problem is that it's very difficult to determine all the vibration parameters required in the model, but actually it is not necessary to do so. Therefore, to develop a simple and equivalent model which is easy to implement is desired. Considering the movement of part 1 is still governed by four factors, i.e. force F (delivered by piston), moving mass m, damping b and stiffness k, the same model as that without additional springs is used. These equivalent parameters m, b, k are determined by matching the experimental and theoretical results. That is the reason why all of these three parameters are functions of the load instead of constants.

Table 5.7 — Identified values of *m, b, k* for EXPERT-DC-Inverter machine

Test No.	Breaking Force F (kN)	Measured			Calculated			
		m (kg)	b (kg/s)	k (N/m)	m (Kg)	b (kg/s)	k (N/m)	R
1	4.90	31.5	1764	410537	32.0	1798	321674	0.9998
2	5.62	36.0	2050	352666	35.4	2014	346741	0.9998
3	6.34	38.4	2224	335696	38.8	2227	371548	0.9999
4	4.48	31.5	1703	301590	30.0	1671	306893	0.9999
5	4.31	30.0	1610	364932	29.2	1620	300937	0.9997
6	4.78	32.4	1784	350705	31.5	1762	317497	0.9998
7	5.53	36.0	2003	283332	35.0	1985	343473	0.9999
8	5.34	34.8	1956	376604	34.1	1928	336820	0.9999
9	4.94	33.2	1849	326115	32.2	1810	323056	0.9999
10	7.05	37.2	2358	405578	42.2	2440	396323	0.9998
11	6.04	39.0	2125	281854	37.4	2139	361338	0.9999
12	5.97	38.3	2119	306063	37.1	2117	358786	0.9999
13	6.34	38.4	2224	335696	38.8	2227	371548	0.9999
14	5.90	36.0	2094	351036	36.7	2095	356220	0.9999
15	5.21	34.7	1899	254927	33.5	1890	332413	0.9999

16	5.38	34.0	1963	330660	34.3	1942	338369	0.9999
17	6.13	37.1	2108	389548	37.8	2165	364373	0.9995
18	6.10	39.6	2232	338270	37.7	2155	363155	0.9998
19	7.36	42.6	2479	383954	43.6	2534	407250	0.9997
20	5.59	38.3	2064	293165	35.3	2003	345533	0.9999
21	5.11	34.0	1899	306976	33.0	1858	328650	0.9999
22	5.34	35.0	1958	302803	34.1	1928	336831	0.9999
23	6.31	38.4	2185	311819	38.7	2219	370597	0.9999
24	5.77	36.2	2057	312288	36.1	2057	351799	0.9999
25	7.51	39.9	2567	478384	44.3	2576	412197	0.9999
26	4.64	31.4	1734	290738	30.8	1719	312463	0.9999
27	6.55	40.0	2310	356768	39.8	2291	378952	0.9999
28	4.57	31.5	1727	281988	30.5	1698	310026	0.9999
29	6.28	37.4	2187	347771	38.5	2210	369553	0.9999
30	5.31	35.7	1959	279629	33.9	1919	335786	0.9999
31	6.15	36.2	2143	339341	37.9	2169	364854	0.9999
32	7.20	38.4	2396	391881	42.9	2485	401579	0.9999
33	6.32	38.6	2249	314988	38.7	2222	370946	0.9999
34	6.78	36.2	2294	414538	40.9	2358	386785	0.9999
35	7.73	43.0	2599	418073	45.4	2644	420029	0.9998
36	7.89	45.2	2709	427366	46.1	2692	425599	0.9999
37	9.75	58.0	3238	416228	54.9	3248	490351	0.9998
38	9.83	56.6	3237	431452	55.3	3271	492962	0.9998
39	8.85	51.7	2974	436977	50.7	2980	459171	0.9997
40	10.59	59.0	3493	550031	58.9	3500	519588	0.9996
41	11.53	65.3	3788	564291	63.3	3781	552311	0.9996
42	11.78	65.0	3864	613557	64.5	3856	561014	0.9996
43	8.25	46.0	2792	458430	47.8	2799	438131	0.9999
44	9.67	55.8	3259	483387	54.5	3225	487562	0.9998
45	9.86	55.4	3295	509521	55.4	3280	494002	0.9998
46	9.07	50.5	3012	467891	51.7	3045	466676	0.9998
47	10.88	57.4	3571	630181	60.2	3585	529510	0.9998
48	9.51	50.2	3161	550867	53.8	3177	481993	0.9999
49	9.97	53.9	3337	556730	56.0	3314	498006	0.9999
50	10.16	56.5	3405	552036	56.9	3371	504620	0.9998
51	8.67	50.0	2926	453702	49.8	2925	452751	0.9998
52	9.86	54.0	3280	528165	55.4	3281	494176	0.9997
53	10.68	63.5	3546	473414	59.3	3527	522721	0.9997
54	10.05	60.3	3336	433862	56.3	3337	500616	0.9997
55	10.63	62.3	3569	492226	59.0	3510	520807	0.9998
56	4.48	30.8	1515	467084	30.0	1669	306719	0.9997
57	5.34	34.8	1968	393520	34.1	1928	336831	0.9999

58	4.59	31.4	1661	424829	30.5	1704	310722	0.9998
59	4.99	32.3	1812	389752	32.4	1824	324647	0.9999
60	5.62	34.7	2048	356591	35.4	2012	346578	0.9999
61	5.70	34.3	2065	380204	35.8	2036	349363	0.9999
62	8.19	49.7	2790	354022	47.5	2781	436042	0.9999
63	6.52	37.9	2289	378625	39.6	2280	377734	0.9999

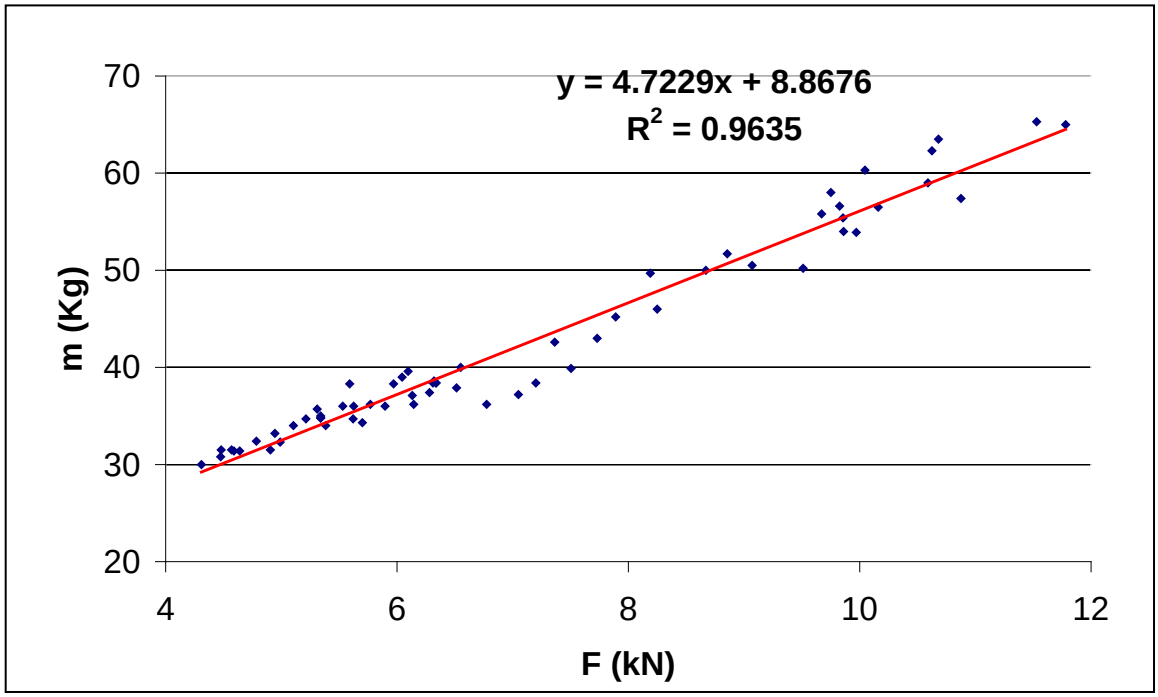

Fig. 5.23 — Equivalent mass as a function of load for EXPERT machine

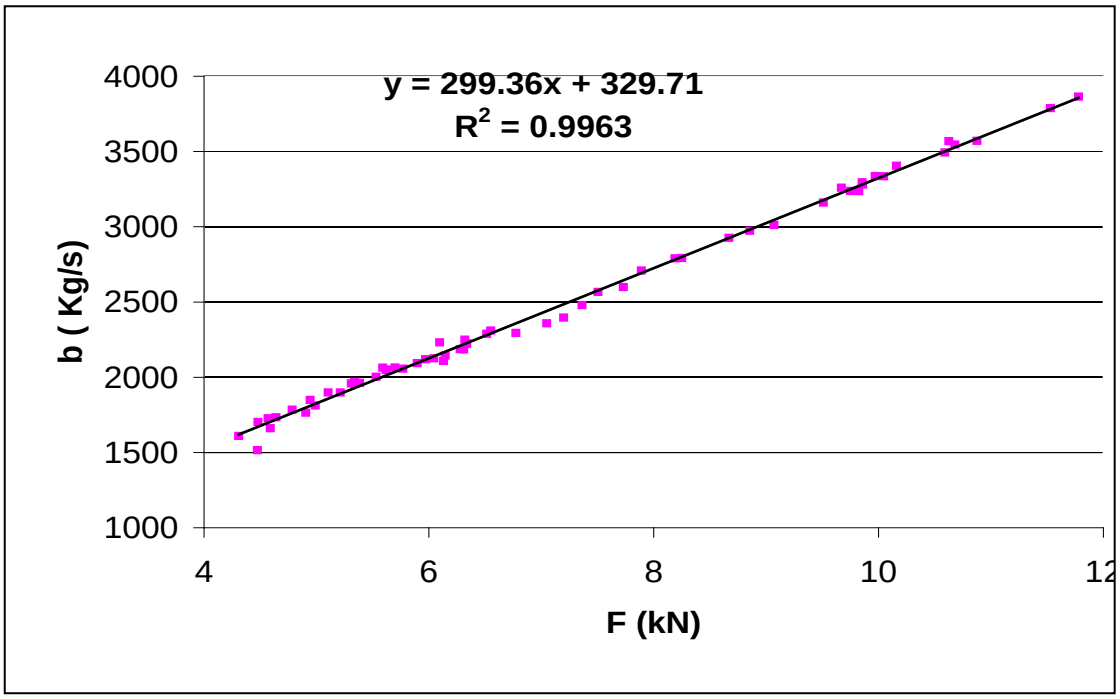

Fig. 5.24 — Equivalent damping coefficient as a function of load for EXPERT machine

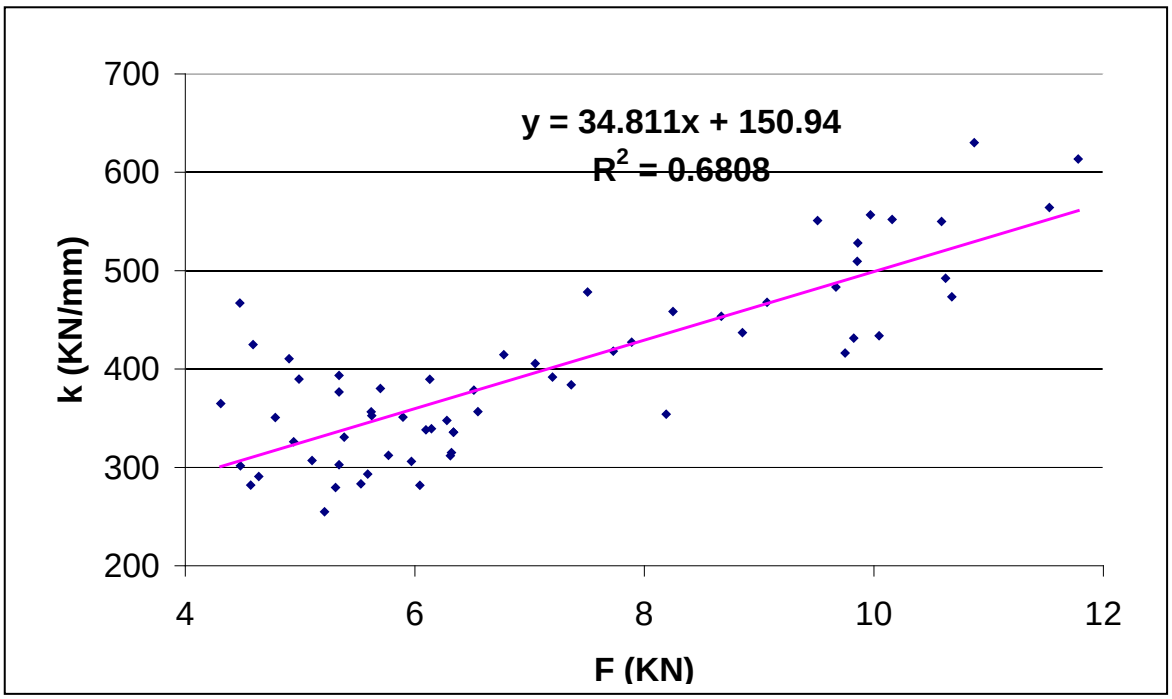

Fig. 5.25 — Equivalent spring constant as a function of load for EXPERT machine

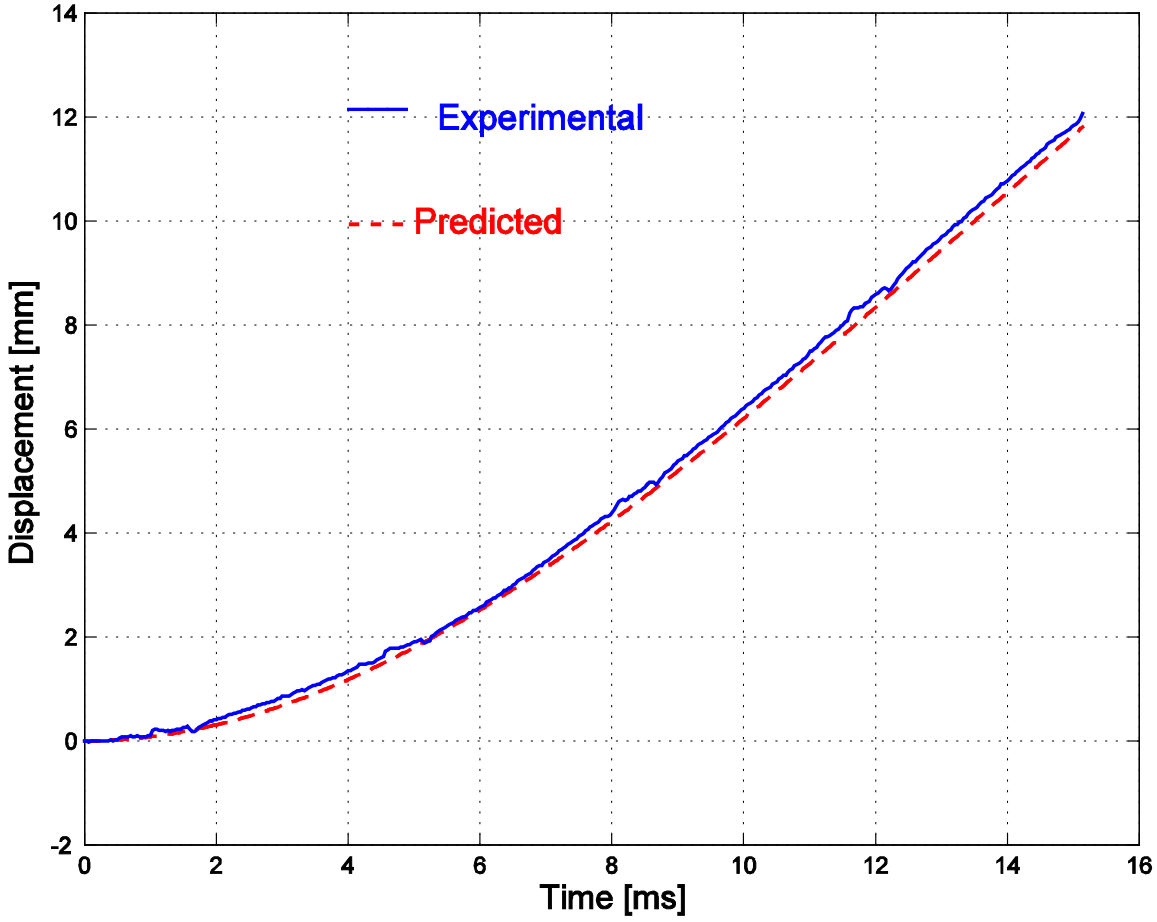

Fig. 5.26 — Experimental vs. predicted displacement in free breaking test at 5.897kN

5.4.2 Validation of the Model

5.4.2.1 Supported Breaking Test

In order to evaluate the validity of the model applied for the EXPERT machine, the supported breaking tests were carried out, in which a reaction force is introduced by disk springs after pin breaking. The device is shown in Fig. 5.11.

Fig. 5.27 shows an example of the measured load and displacement curves, where fracture occurs at a total load of 9.75 kN. After fracture the force drops abruptly and then increases linearly with superimposed fluctuations due to the springs (curve part **AB**). The relative displacement of the electrodes is determined theoretically by inserting the values of *m*, *b* , *k* identified by the free breaking tests, the measured

action force F and oscillating reaction force F_r into Eqn. (5-1).

All in all 12 supported breaking tests were carried out in the load range 4.92-11.1 kN with different reaction forces (different set-up of springs). The test results are shown in Table 5.8. A good agreement between experimental and predicted displacement for most tests is seen by assessing the correlation coefficient R. Fig. 5.28 gives a comparison at a load F = 6.07 kN, which is an example of good agreement (R =0.9957).

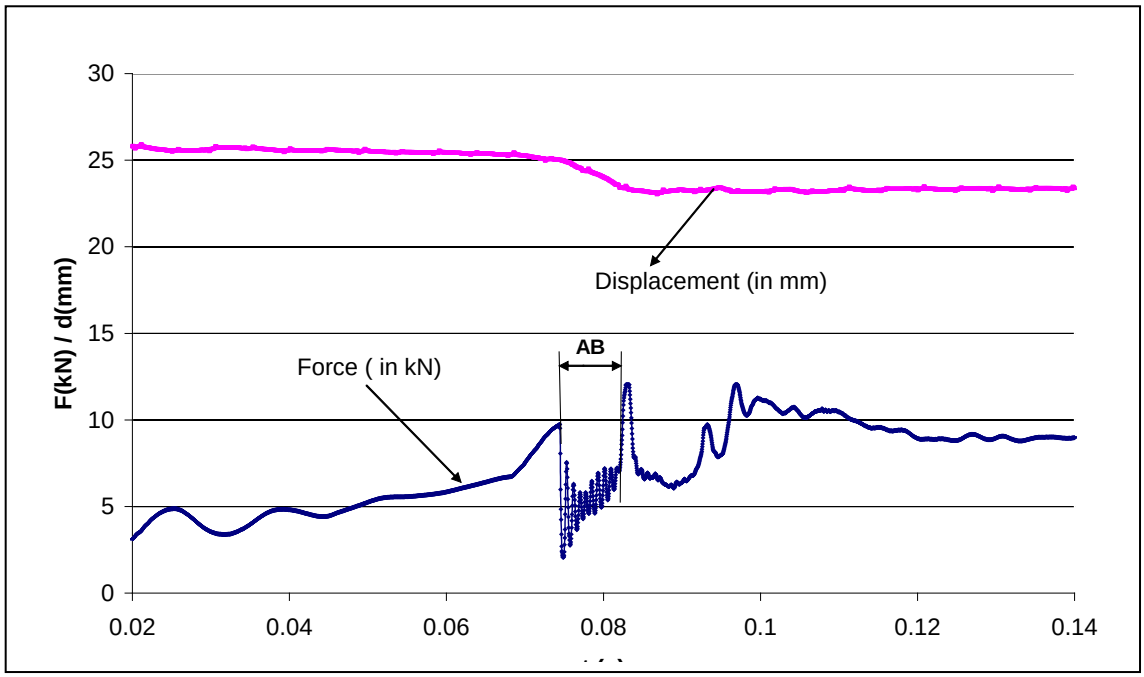

Fig. 5.27 — Measured curves in supported breaking test for EXPERT machine

Table 5.8 — Test results of supported breaking test for EXPERT machine

Test No.	Action force F (kN)	Calculated			R
		m (kg)	b (kg/s)	k (N/m)	
1	5.53	35	1984	343271	0.9980
2	5.91	36.8	2099	356673	0.9981
3	4.92	32.1	1803	322210	0.9975
4	5.92	36.8	2102	357021	0.9949
5	6.09	37.6	2153	362939	0.9975
6	6.27	38.5	2207	369205	0.9926
7	6.72	40.6	2340	384696	0.9902
8	6.07	37.5	2147	362243	0.9957
9	6.28	38.5	2208	369379	0.9973
10	8.6	49.5	2903	450141	0.9956
11	9.75	54.9	3247	490173	0.9774
12	11.1	61.2	3650	536994	0.9642

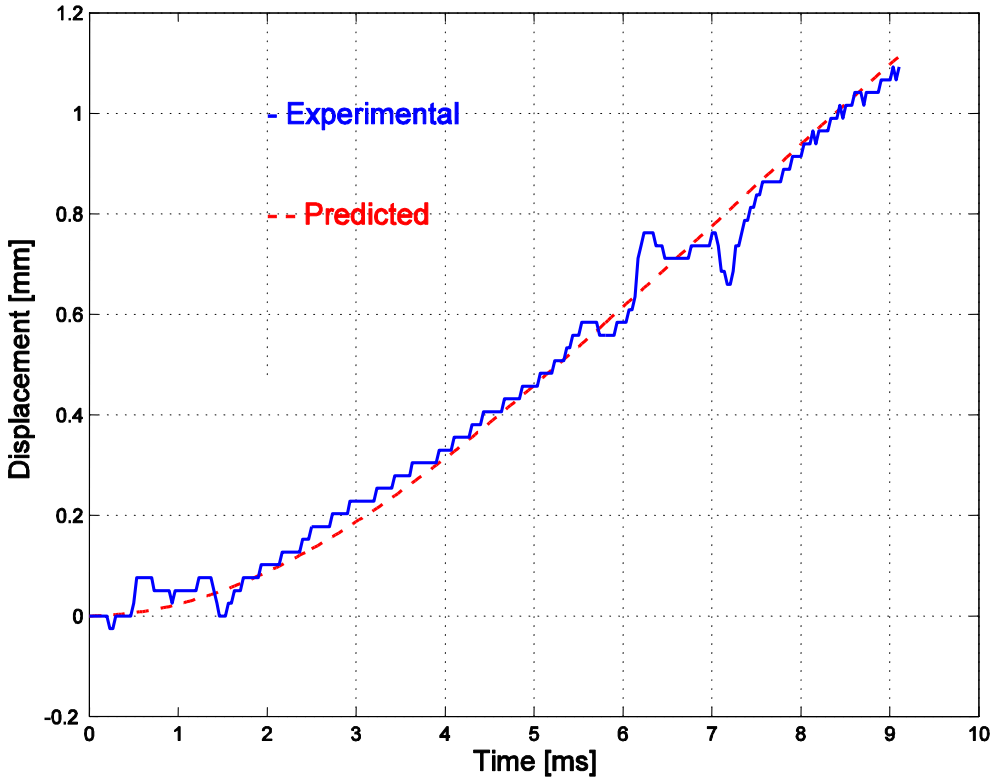

Fig. 5.28 — Experimental vs. predicted displacement in supported breaking test at 6.07 kN

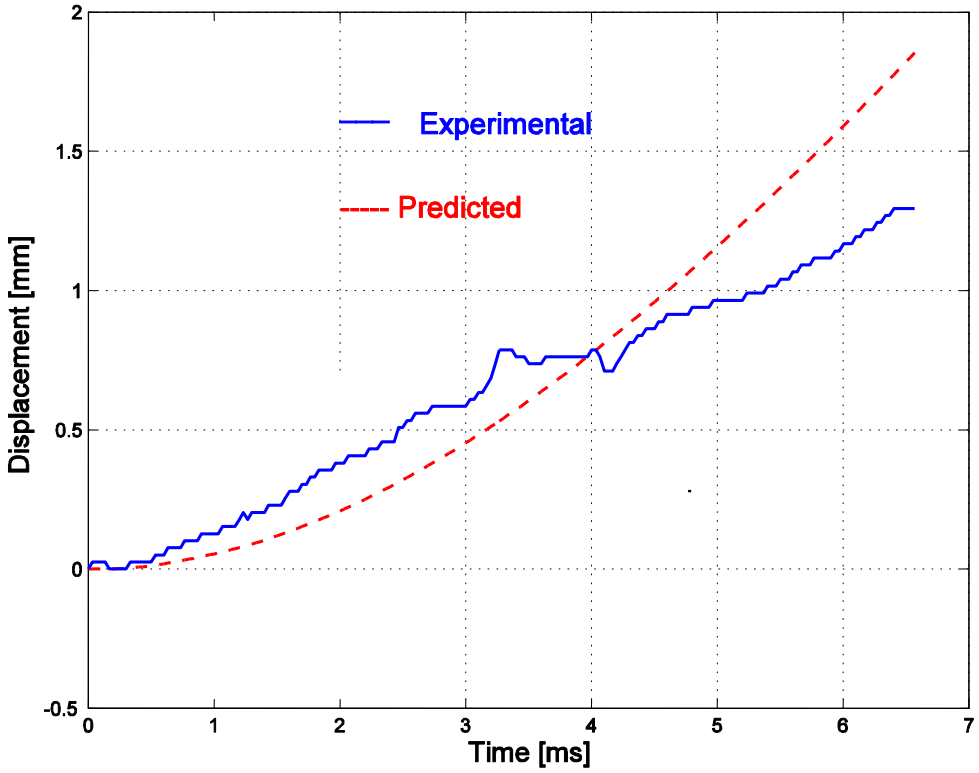

Fig. 5.29 — Experimental vs. predicted displacement in supported breaking test at 11.1 kN

Fig. 5.29 shows the test at load F = 11.1 kN, which has the lowest value of R=0.9642, but the agreement is still acceptable.

5.4.2.2 Projection Welding Tests

A series of projection welding tests were carried out on this machine by using the same specimens as mentioned before, joining rings in stainless steel sheet (W.Nr. 1.4301) to disks in mild steel (W.Nr. 1.0037) provided with an annular projection, see Fig. 5.17.

Table 5.9 — Welding conditions and results of projection welding on EXPERT machine

Test No.	Weld time (ms)	Force (kN)	Weld current (kA)	Calculated			Weld quality	Fit
				m **(kg)**	***b*** **(Kg/s)**	***k*** **(N/m)**		
1	80	5.93	16	36.9	2105	357369	Good weld	bad
2	60	5.89	18	36.7	2093	355977	Good weld	bad
3	60	5.90	18	36.7	2096	356325	Good weld	bad
4	60	5.84	20	36.4	2078	354236	Good weld	bad
5	60	5.97	25	37.1	2117	358762	splash	bad
6	60	5.93	27	36.9	2105	357369	splash	bad
7	20	5.84	28	36.4	2078	354236	welded	bad
8	60	5.95	18	37.0	2111	358065	Good weld	bad
9	60	5.92	18	36.9	2102	357021	Good weld	bad
10	60	5.95	20	37.0	2111	358065	Small splash	bad
11	60	5.84	20	36.4	2078	354236	Small splash	bad

All in all 11 tests were carried out, the welding conditions and results are illustrated in Table 5.9. Among these tests, the weld time was chosen as 20, 60, 80 ms. The current was selected just below or just above the expulsion limit causing splash formation. During the experiments, the electrode force, the relative displacement between the two electrodes and the weld current were recorded. An example of the data recorded is shown in Fig. 5.30. For this test, an electrode force of 5.95 kN was chosen, the weld time was 60 ms, and weld current was 18 kA. The welding stage part ranging from time of **AB** in Fig. 5.30 was selected for subsequent analysis.

Reading off from Fig. 5.30 the electrode force prior to current flow, F = 5.95 kN, and the measured reaction force F_r (the force in range of **AB**) as function of time during the welding stage and inserting into the mathematical model Eqn. (5-1), the relative displacement was computed.

In this way, the predicted displacements for all the tests were calculated based on the model using machine parameters m ,b, k identified by free-breaking tests. Unfortunately, bad agreement appeared between experimental and predicted electrode displacements for all the tests were yielded. The predicted displacement is bigger than the experimental one. Fig. 5.31 gives an example, in which the upper figure shows the predicted displacement comparing to the measured one and the lower figure is the measured electrode force corresponding to the welding stage.

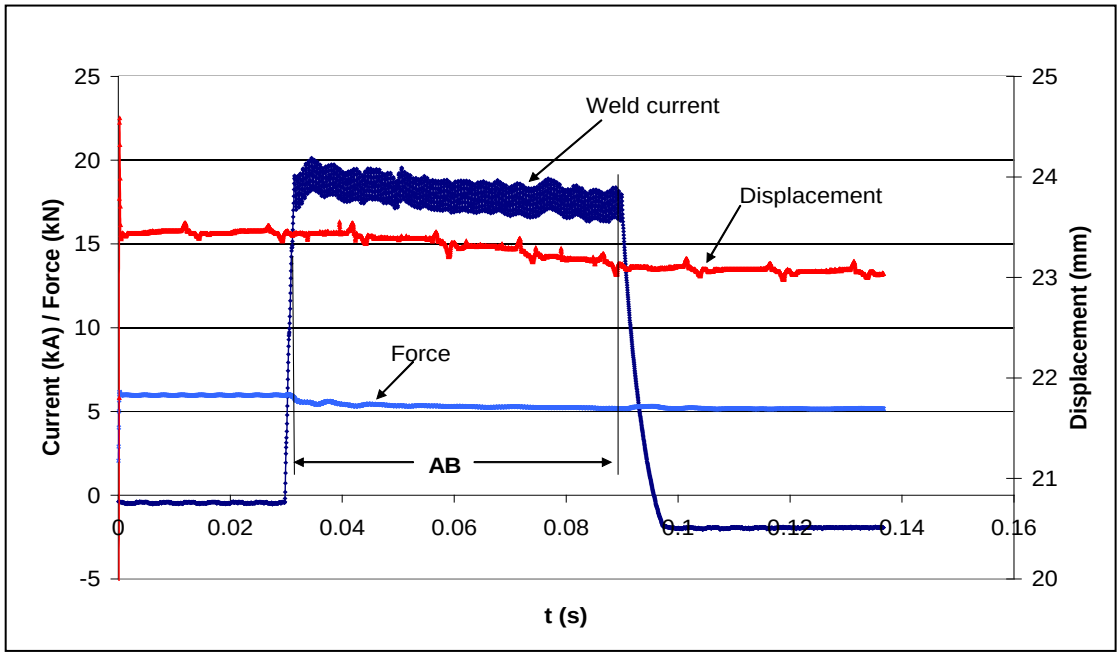

Fig. 5.30 — Measured curves for projection welding

A possible explanation to, why the model does not work in case of projection welding, may be the effect of the electromagnetic force, which is the only difference appearing between the welding condition and pure mechanical breaking test.

It is known that when an electric conductor is placed in a strong magnetic field it is exerted to an electromagnetic force, the so called *Lorentz force*. In resistance welding, where high currents are applied, a strong magnetic field is established implying that the Lorentz force is of importance. The magnetic field formed in the secondary circuit of resistance welding machine as well as the Lorentz forces exerted on electrodes and

electrode arms are illustrated in Fig. 5.32. It can be seen that F_1 forces the electrodes apart from each other, thus decreasing the electrode force; F_2 has the tendency of pushing the electrode head to the side, thus increasing the friction or damping. Michael Malberg modeled and tested the Lorentz force for this machine [31].

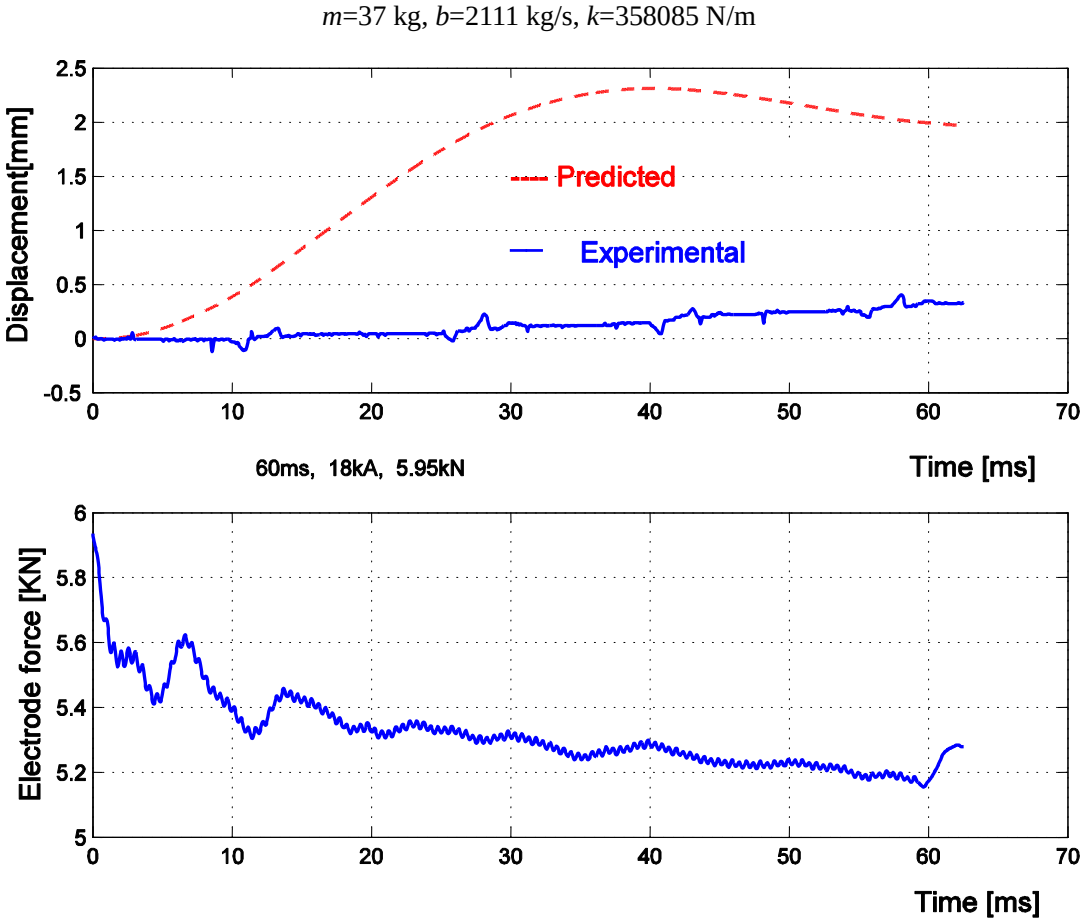

Fig. 5.31 — Displacement comparison and measured electrode force

His investigation concluded that the Lorentz force in resistance welding is mainly dependent on the size of the welding window and the welding current, small window and high current results in high Lorentz force. Fig. 5.33 shows the Lorentz force as a function of welding current for a fixed size of the welding window [31] of 1550 cm^2. In the present projection welding, the welding window size is 1395 cm^2, so the Lorentz force is larger than that shown in Fig. 5.33 in case of the same welding current.

As mentioned earlier, the Lorentz force decreases the reaction force and increases the friction (damping) in resistance welding. But only the damping increase results in a decrease of the predicted displacement in Eqn. (5-1) compared to the experimental

one, because the variation of the reaction force caused by the Lorentz force has been accounted for in the computation model by using the actual, measured force as the input of F_r.

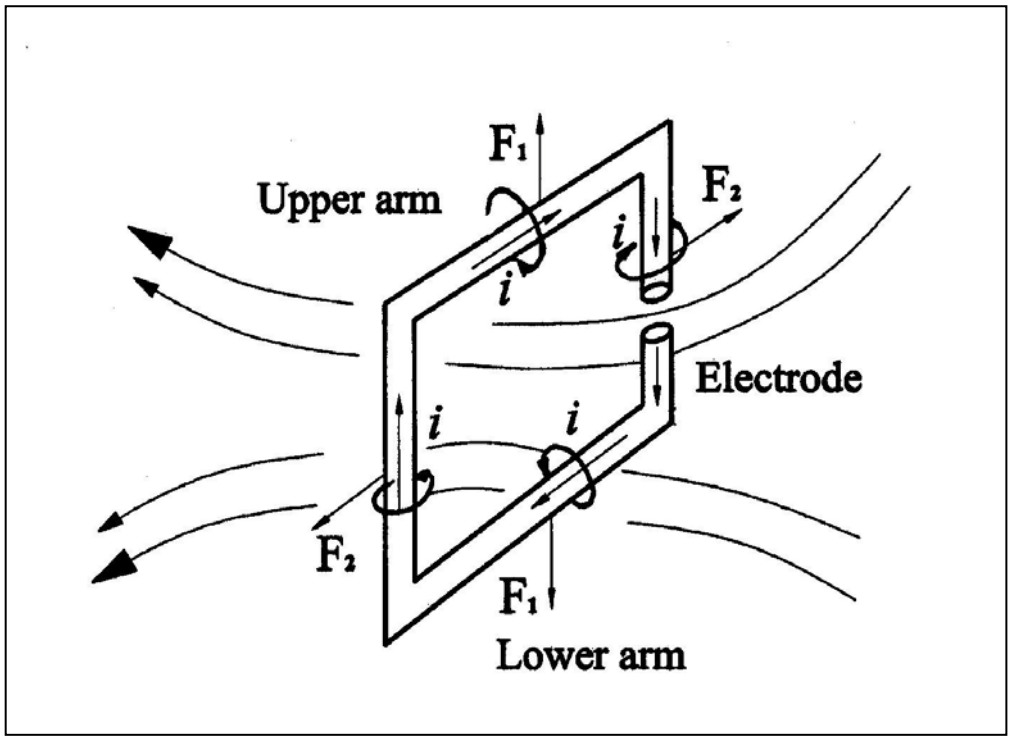

Fig. 5.32 — Magnetic field of secondary circuit and Lorentz forces

For the machine in question, the effect of Lorentz force is more significant than in the TECNA machine earlier investigated. This is due to the higher friction in the high pressure hydraulic cylinder and lower stiffness of the piston rod. Furthermore, since it is a DC machine, the magnetic field acts constantly throughout the welding. As regards the TECNA AC machine, a welding cycle consists of current starting at zero and gradually increasing to a positive peak value, decreasing to zero, gradually increasing to a negative peak value and then decreasing again to zero, implying that the magnetic field strength is variable, and sometimes becomes to zero. When comparing the Fig. 5.18 and Fig. 5.30, one can clearly see that for the EXPERT machine the force decreases when input of current is started (Fig. 5.30), but at this movement, the weld has not yet been soften and melted. Fig. 5.34 shows the amplified force curve of Fig. 5.30 by changing the axes scale, It can be seen that the force further decreases during the welding and does not reestablish to the set force even by the end of welding due to the slow response capacity of the

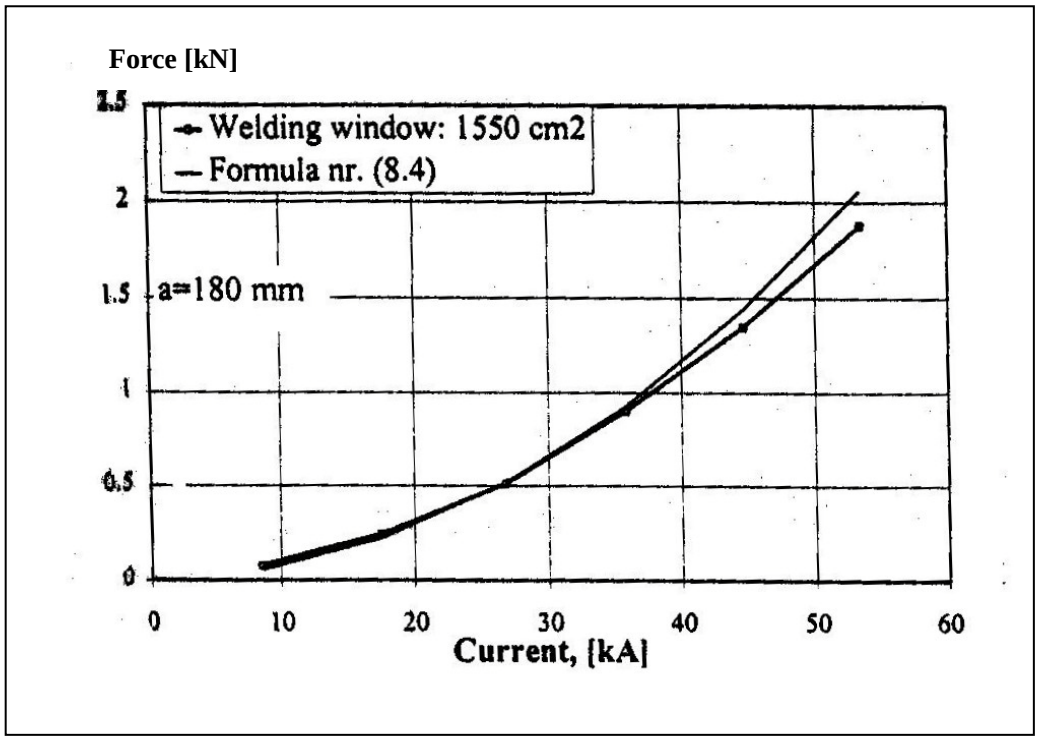

Fig. 5.33 — Lorentz force as a function of welding current for EXPERT machine

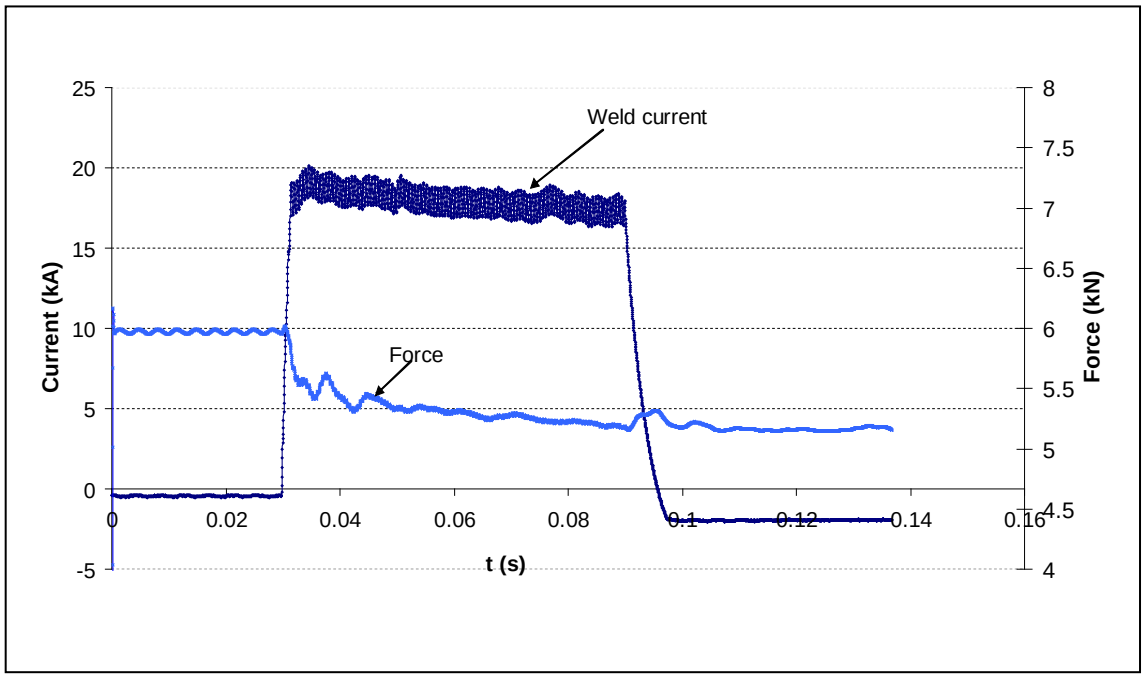

Fig. 5.33 — Amplified force curve based on Fig. 5.30

hydraulic system, i.e. the fluid is not able to completely refill the cylinder after displacement of the piston. However, this is not the case for the TECNA machine illustrating that the Lorentz force has more influence on the EXPERT machine.

In summary, the effect of Lozentz force in projection welding on the EXPERT DC machine with a hydraulic system is significant. The Lorentz force increases the damping, resulting overestimated predictions of the displacement.

To further proof the preceding explanation, a computation trial of the projection welding listed in Table 5.9 increasing the damping coefficient *b* one hundred times and keeping the other parameters unchanged is carried out. The results indicate that the agreement between predicted and experimental displacements is much improved (see Table 5.10). Fig. 5.34 shows the curves for the test of number 8 in Table 5.10.

Since the EXPERT machine provided with three additional springs is quite special, no further work, such as revising the model, was proceeded.

Table 5.10 — results of projection welding on EXPERT machine

Test No.	Weld time (ms)	Force (kN)	Weld current (kA)	Calculated			Weld quality	R
				m (kg)	*b* (Kg/s)	*k* (N/m)		
1	80	5.93	16	36.9	2105	357369	Good weld	0.94
2	60	5.89	18	36.7	2093	355977	Good weld	0.96
3	60	5.90	18	36.7	2096	356325	Good weld	0.95
4	60	5.84	20	36.4	2078	354236	Good weld	0.95
5	60	5.97	25	37.1	2117	358762	splash	0.95
6	60	5.93	27	36.9	2105	357369	splash	0.94
7	20	5.84	28	36.4	2078	354236	welded	0.94
8	60	5.95	18	37.0	2111	358065	Good weld	0.96
9	60	5.92	18	36.9	2102	357021	Good weld	0.96
10	60	5.95	20	37.0	2111	358065	Small splash	0.99
11	60	5.84	20	36.4	2078	354236	Small splash	0.96

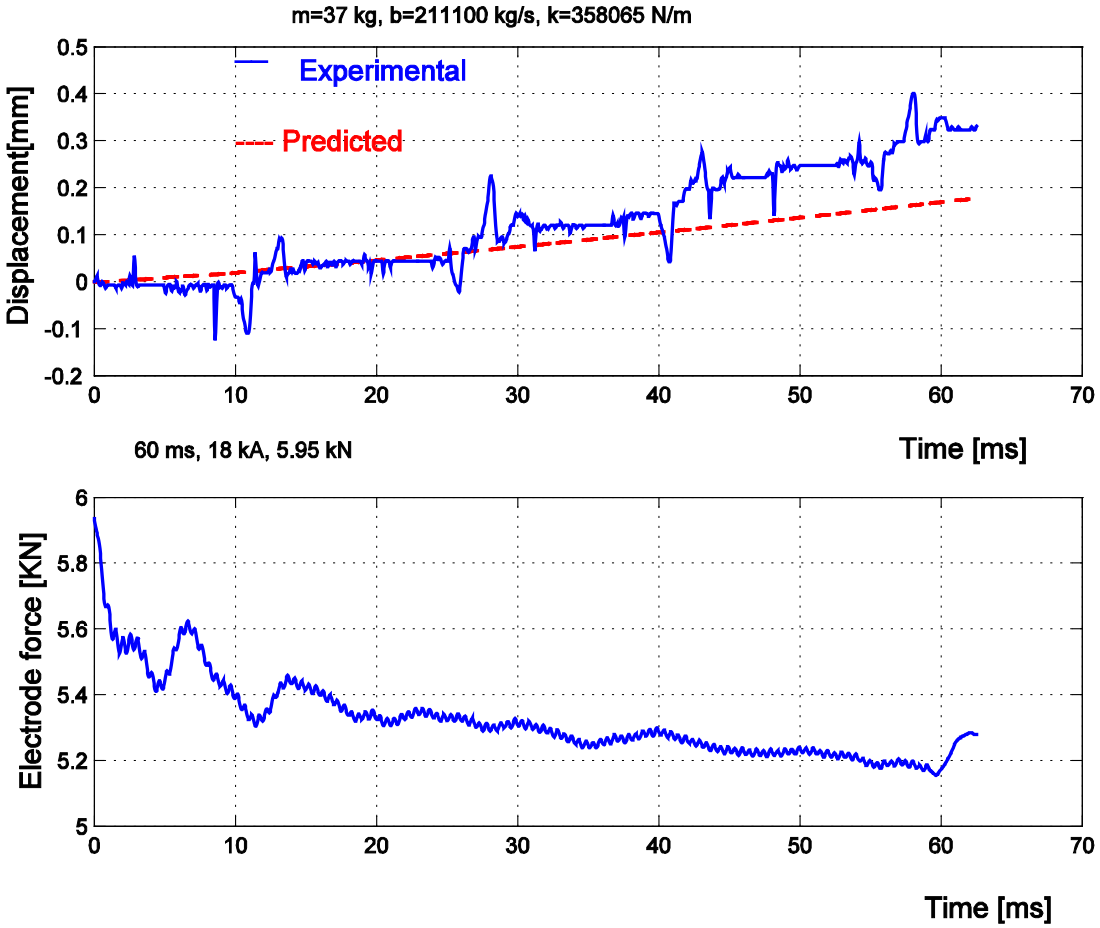

Fig. 5.34 — Displacement comparison and corresponding measured electrode force in the case of increased damping coefficient

5.5. Conclusions

The structure of the mechanical system of resistance welding machines varies with the type of machine, and this has substantial influence on the dynamic mechanical response of the machine. The present project proposes a method to characterize the dynamic mechanical behaviour of the machines based on a mathematical model involving three equivalent machine parameters, i.e. equivalent moving mass, equivalent damping coefficient and equivalent spring constant. A specially designed breaking test is applied for determining these parameters. The method, which is confirmed by a series of projection welding tests on an air-operated machine without additional springs in the welding head, is easy to realize in industry, since tests may be performed in situ.

The reason why the model works with supported breaking test but not projection welding on the EXPERT machine is attributed to the influence of the electromagnetic

force. Due to the low stiffness of piston rod and high friction in the hydraulic cylinder, the electromagnetic force increases the damping of the electrode movement during welding. The model needs to be revised if applying it to this machine.

The model may furthermore be applied in numerical simulation of resistance welding implying more accurate computations by accounting for the interaction between process and machine characteristics. Besides improving process analysis and optimisation of the welding parameters it may also be helpful to improving machine design.

Part II

Electrical Properties of Resistance Welding Machines

Chapter 6

Literature Review and Objectives of New Investigation on Electrical Properties of Resistance Welding Machines

6.1 Introduction

In resistance welding the required heat development is ensured by electrical resistance heating. The resistance welding machine generates a high electrical current with a relatively low voltage over the workpieces whereby the required heat is developed. This is done in a very short time, typically between 10 and 500 milliseconds. In order to optimize the welding process and thus ensure the weld quality, it is therefore of interest to characterize the electrical capacities of resistance welding machines.

6.2 A literature Review

Much effort has been devoted to the study of describing the welding current and electrode voltage characteristics in order to measure the dynamic resistance of workpieces and welding power. Especially, the dynamic workpiece resistance, which is closely related to the welding progression, can be used to monitor welding process or estimate weld quality together with other signals such as the dynamic electrode displacement [47-54]. The values which should be used to describe the electrical relationships in alternating current resistance welding was the issue of discussion. G. Weber [55-56] found that the alternating current-voltage characteristic does not represent a linear relation, the workpiece resistance therefore cannot be described by Ohm's law. The physical causes for this are temperature variations in the workpiece during welding, which contravene one of the essential conditions of Ohm's law, constant temperature. Accordingly, the methods of the complex calculation cannot be used for analyzing the electrical process during AC resistance welding. He suggested that instant-related welding current-electrode voltage characteristics should be used, resulting in instant-related workpiece resistance and power values. From this point of view, using the peak value of welding current is of special interest, while the associated electrode voltage value then numerically is taken at the instant of the peak current, in order to avoid inductive influences.

In most researches, the welding current and electrode voltage were measured in the secondary circuit of resistance welding machine, thus the dynamic resistance was determined for the welding process monitoring. But this causes some problems. Firstly, the amplitude of the

secondary voltage signal is quite small and thus it may easily be distorted by induction noise, especially when a low welding current is applied. The problem is deteriorated when welding at high current, and using a loop for detecting the voltage across the electrodes since the voltage leads connected to the electrodes must span the thickness of the workpiece. Secondly, the voltage leads may interfere with the welding robot risking disconnection to the electrodes during movement of the welding gun.

Yongjoon[57-58] proposed a measuring system in which the measurement of current and voltage was carried out on the primary circuit without any extra monitoring system in the secondary circuit. Based on this, a technology of monitoring the welding process and estimating the weld quality by using the primary dynamic resistance was suggested. The dynamic resistance was calculated also by using the instantaneous values obtained at the moment when the current reaches its peak in order to obtain the pure dynamic resistance without the inductive reactance.

Some valuable works were done in modeling the electrical properties of single phase AC machines with thyristors. Ref. [59] dealt with the nonlinear modeling of the electrical subsystem associated with the resistance spot welding process, in which switched-state, thyristor driven, linear and nonlinear transformer models have been developed, which characterize the electrical dynamics. The research addressed phenomena like transient inrush currents and nonlinear control strategies. The machine dependent parameters used in the models were estimated by a least squares estimation technique on the experimental data; the transformer parameters were determined with direct measurement tests, including impedance tests, signal generation tests and closed secondary tips tests. In Ref. [60], a mathematical model was employed to describe the part voltage and weld current based on an equivalent circuit, but no method was available to determine the machine dependent parameters required in the model.

In Ref. [61], a procedure for electrical characterization of resistance welding machines was proposed involving testing with inserted proof resistances in the secondary circuit determining the current-voltage characteristics and power on the primary as well as on the secondary side of the transformer. The method is very useful to evaluate the machine output capacity, how much power input to the machine is transferred to the weld. Also a method for transferring electrical parameter settings from one machine to another was suggested in this research, based on comparison of welding current- electrode voltage characteristics between machines.

6.3 Conclusions of Literature Studies and Proposals for New Investigations

The heat input required in resistance welding is generated by Joule heating $E = I^2Rt$. The resistance R necessary for heat generation in the welding process is realized by contact resistance between the faying surfaces of the parts to be joined as well as resistance in the base materials. The level and duration of current during welding are controlled by the electrical system of the machine. Therefore, the electrical properties of resistance welding

machines directly determine the heat provided to the weld. For an AC machine, their values are preset in the controller by selecting the heat percentage (or the rms current) and the desired number of weld cycles. The heat percentage is associated with the conduction angle of anti-phase dual silicon-controlled rectifiers (SCR); the number of cycles are normally used as a measure of weld time. One cycle equals to 0.02 s if the resistance welding machine is fed by a power system with 50 Hz frequency.

Due to the individual electrical characteristics of machines, such as the difference in impedance of machine circuit, the same applied primary voltage creates different level of weld current in different machines, and the same workpiece resistance inserted in the secondary circuit of the different machines will cause different variation of the weld current. It is often difficult to optimize the process parameter settings for achieving a stable production and high quality of complex joints, and no general method exists to transfer the optimum welding parameters from one machine to another. Running-in and optimization of new industrial production is therefore based on trial-and-error experiments implying a large number of tests. Although numerical simulation of the welding process may facilitate this issue, necessary machine data are needed to support the simulations in order to obtain reliable results [62-63]. It is thus of great importance to develop a method of characterizing the electrical system of resistance welding machines identifying the main electrical machine parameters and quantifying the difference from machine to machine.

According to literature, early studies were mainly focused on estimating the weld quality or controlling the welding process by investigating the welding current-electrode voltage characteristics of the resistance welding machine. Some valuable works were done for modeling the weld current and part voltage, as well as the machine's electrical output characteristics, but a reliable link between the settings and the output of the machine were lacking, and no method for determining the electrical machine parameters required for numerical modeling is available.

The objective of the investigation of electrical properties of resistance welding machines in this Ph.D. project is mainly focused on:

Systematical testing the electrical properties of resistance welding machines, in order to identify the key parameters characterizing the electrical machine properties varying from one machine to another; to develop a method for determining these key parameters, which is easy to apply in industry.

Based on the results of testing and analysis, to develop a mathematical model, which is able to predict the weld current at each setting when the workpiece resistance is given, establishing a relationship between input settings and machine output, which will facilitate parameter setting in operations and data support for numerical simulation of the welding process.

Chapter 7

Testing and Modeling of Electrical Properties of Resistance Welding Machines

In this chapter, a mathematical model of the circuit for single-phase AC machines is proposed in form of an equivalent *R-L* series circuit. By means of short-circuit testing or closed secondary tips test, the electrical machine circuit parameters are identified. Inserting different proof resistances the conduction angle (or heat setting) and the variation of weld current are calculated for different current settings. The proof resistances are constant ohmic resistances with values covering the whole range of common welding operations on the machine investigated. The mathematical model is compared with experimental measurements.

7.1 Equivalent Circuit and Model

In single-phase AC machines with anti-phase dual silicon-controlled rectifiers (SCR) the basic construction of the main power circuit has the same principle outline from machine to machine. The resistance welding machine circuit can be treated as a sum of resistances and inductive reactances in series, capacitance playing an insignificant role in the circuit[60]. Resistances involve both bulk and contact resistances, bulk resistances existing in all buses and conductors (such as ram, band conductor and base plate) of the circuit as well as the transformer coil resistance, while the contact resistances mainly appear at the interfaces of bus and conductor connections. Inductances include the self-inductance of each bus or conductor section as well as loop inductance of the secondary circuit. Based on these assumptions, the complete equivalent circuit can be simplified as shown in Fig. 7.1, where the primary and secondary circuits are coupled by an ideal transformer, i.e. neglecting the magnetizing reactance and core losses.

Further simplification necessary to obtain the entire equivalent circuit is realized by reflecting the primary voltage source and impedances into the secondary circuit. The primary circuit impedance is converted to the secondary circuit equivalent impedance by dividing the former with the squared turn ratio of the transformer. The applied voltage (nominal voltage of the power system) is also referred to the secondary circuit by dividing with the transformer turn ratio, as shown in Fig. 7.2.

All secondary machine impedances including those reflected from the primary circuit are combined together with the reflected power system, resulting in one series of R_m-L_m pair.

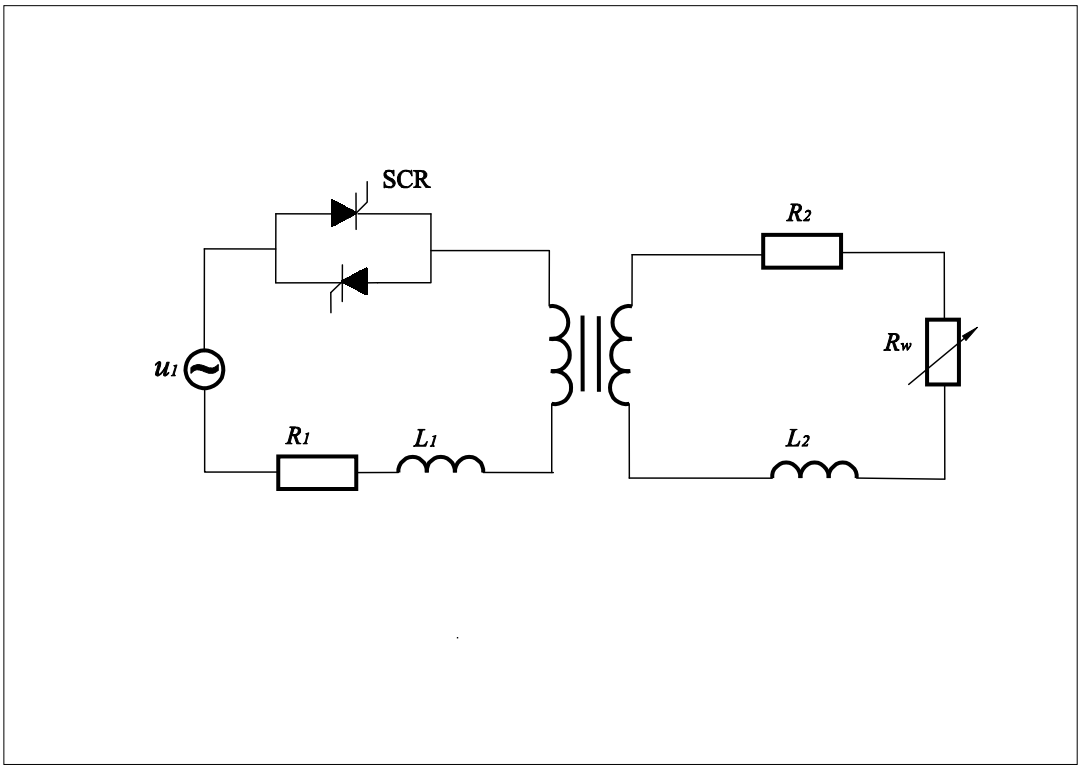

Fig. 7.1 — Complete equivalent circuit.

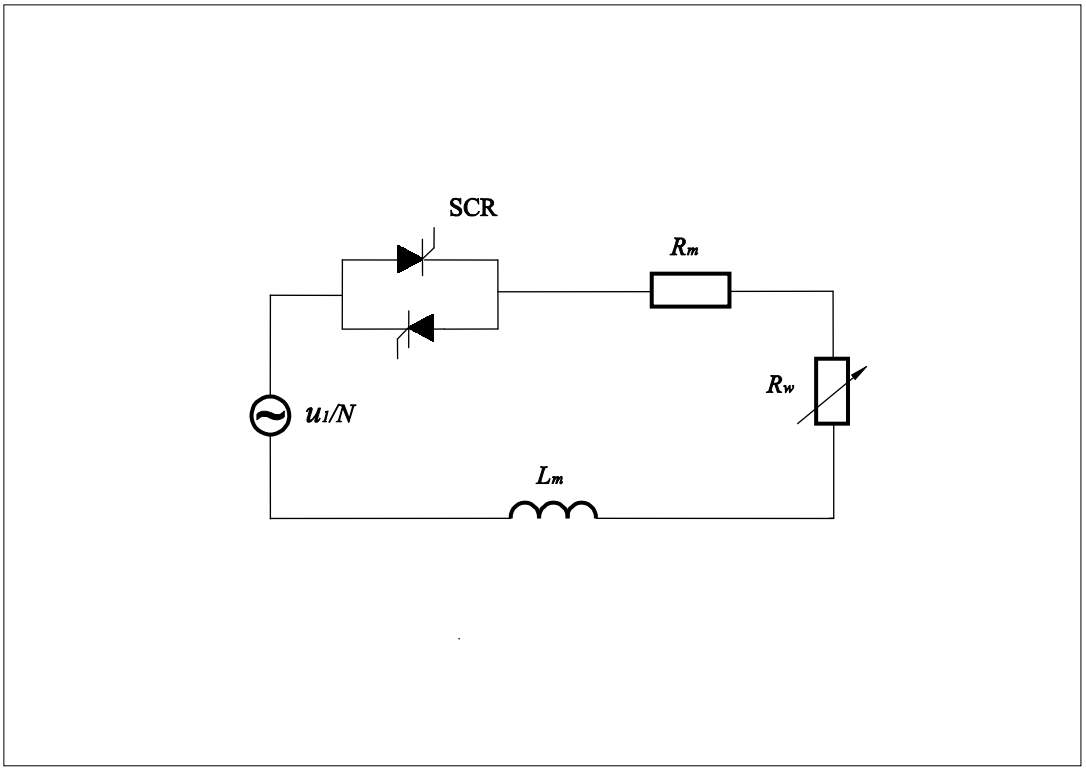

Fig. 7.2 — Simplified equivalent circuit

R_m and L_m represent the total equivalent resistance and total equivalent inductance of the machine. Once a given machine is installed, many components are fixed for that installation (*e.g.* the cable and conduit), and the machine impedance or R_m and L_m do not change significantly implying that they may be considered to be constant.

The only circuit variable, the weld parts, may be assumed to induce a pure resistance R_w, consisting of bulk as well as contact resistances. Contact resistances appear as workpiece–to-electrode and workpiece–to–workpiece contact resistances. The workpiece resistance (or part resistance) cannot be considered constant, it varies with material combination, electrode load, temperature, surface condition etc.

A SCR functions like a power switch, where turn-on is controlled by a gate pulse from the control circuit, and turn-off occurs at the instant when the current reverses in polarity. Its resistance, which is very small when conducting current, is converted and included in machine resistance R_m.

In summary, the circuit of Figure 7.2 is simply a series *R-L* circuit connected to a sinusoidal voltage source, where the total resistance consists of a constant machine-circuit resistance and a variable weld part resistance. The mathematical model can now be derived as Eqn. (7-1) inserting the voltage drop of the *R-L* circuit:

$$\frac{u_1}{N} = R_t \cdot i(t) + L_t \frac{di}{dt}$$

$$\frac{\sqrt{2}}{N} U_1 \sin(\omega t + \alpha) = R_t \cdot i(t) + L_t \cdot \frac{di}{dt} \qquad (7\text{-}1)$$

Solving Eqn. (7-1) yields the resulting weld current as a function of time:

$$i(t) = K \sin(\omega t + \alpha - \varphi) - K \sin(\alpha - \varphi) e^{-\frac{t}{\tau}} = i_1 + i_2 \qquad (7\text{-}2)$$

where: $K = \dfrac{\sqrt{2} \cdot U_1}{N \cdot Z}$, $\quad Z = \sqrt{R_t^2 + (\omega L_t)^2}$ (7-3)

φ = power-factor angle [$\varphi = tg^{-1}(\dfrac{\omega L_t}{R_t})$] (7-4)

τ = time constant ($\tau = \dfrac{L_t}{R_t}$) (7-5)

Fig. 7.3 shows the waveform of the current given in Eqn. (7-2) and the applied voltage u_1. θ represents the conduction angle, i.e. the conduction period of the SCR. From Eqn. (7-2) and Fig. 7.3 it is noticed, that the weld current consists of two parts, the first term (i_1) representing the steady component and second one (i_2) the transient component, which decays exponentially. Due to the necessity of switch-on and switch-off of the SCR in

each half cycle, the transient current (i_2) exists in each half cycle, implying that the weld current is not a sinusoidal wave.

Considering the symmetry of positive and negative half cycles of the weld current, the model is only shown for the positive half cycle.

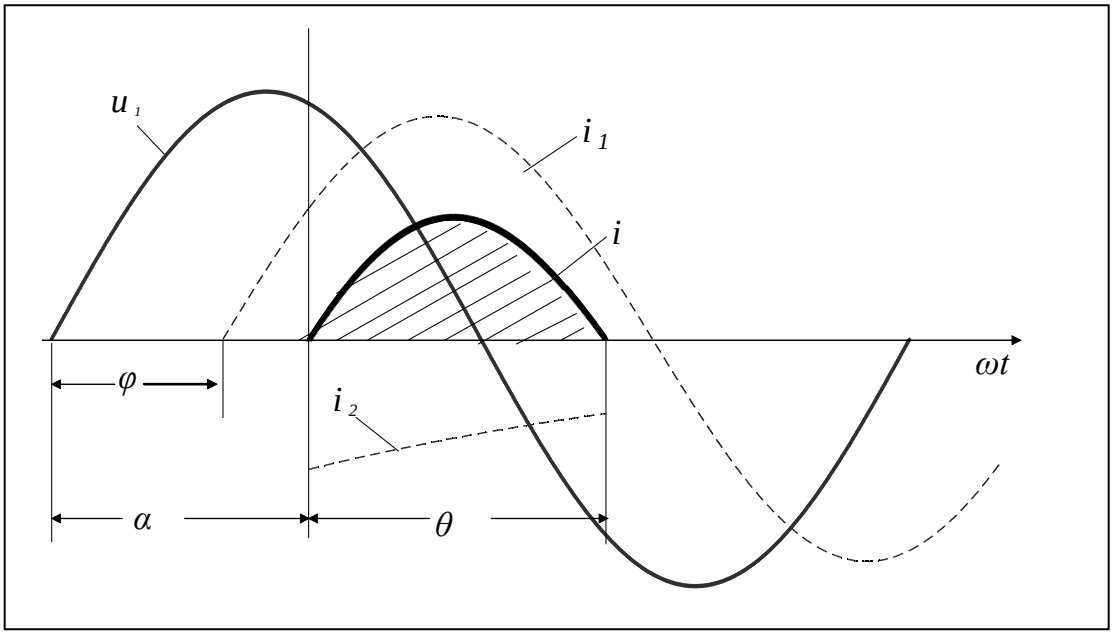

Fig. 7.3 — Waveforms of voltage and currents.

7.2 Relation between Firing Angle α and Conduction Angle θ

Turning off the SCR corresponds to the weld current *i(t)* crossing zero and reversing in polarity, i.e.:

$i = 0,\ \omega t = \theta$

inserted into Eqn. (7-2) yields:

$$\sin(\theta + \alpha - \varphi) = \sin(\alpha - \varphi)e^{-\frac{\theta}{tg\varphi}} \qquad (7\text{-}6)$$

Solving for α one gets:

$$\alpha = tg^{-1}\left(-\frac{\sin(\theta-\varphi) + e^{-\frac{\theta}{tg\varphi}}\sin\varphi}{\cos(\theta-\varphi) - e^{-\frac{\theta}{tg\varphi}}\cos\varphi}\right) \qquad (7\text{-}7)$$

which is the relationship between firing angle α and conduction angle θ. Inserting Eqn.(7-7) into Eqn.(7-2) gives the weld current as a function of ωt and the following parameters: conduction angle θ, power-factor angle φ and total impedance Z, i.e.:

$$i = f(\omega t, \theta, \varphi, Z) \qquad (7\text{-}8)$$

This illustrates that the weld current (amplitude as well as phase) is related to the conduction angle θ, and may be adjusted by changing θ. In practice, the controller microprocessor calculates the conducting-elapse time of the SCR according to the set current or heat percentage, which will be used to control the firing of the SCR.

7.3 Determination of Machine Impedance

As previously mentioned, the machine-circuit resistance and inductance are constants for the specific machine in question, once it is installed. They are key parameters characterizing the machine's electrical properties. When welding the same parts on different machines, the welding resistance adds to the machine impedance forming the total impedance, which is dependent on the machine, i.e. different current variation may appear on different machines applying the same nominal settings. As an example Fig. 7.4 shows that, if the machine-circuit resistance is equal to or greater than the inductive reactance (70% power factor or greater), *Fig. 7.4a*, a given value of work resistance will increase the machine impedance more than the same work resistance added to a machine with a machine-circuit resistance lower than the inductive reactance, *Fig. 7.4b*.

In order to apply the mathematical model Eqn. (7-1) for calculating the current, it is essential to determine the machine-circuit impedance including resistance R_m and inductance L_m. It might be possible to get this data from the machine manufacturer, but this is not always the case. Additionally, as previously stated, the weld current is no longer a sinusoidal signal, so the machine impedance cannot be determined as the ratio between voltage and current in a short-circuit test. It is thus important to develop a simple, generic method applicable to individual machines for identification of the machine impedance.

In a short-circuit test (closed secondary tips test), R_w=0, Eqn. (7-1) is given by:

$$\frac{u_1}{N} = R_m \cdot i(t) + L_m \cdot \frac{di}{dt} \qquad (7\text{-}9)$$

`

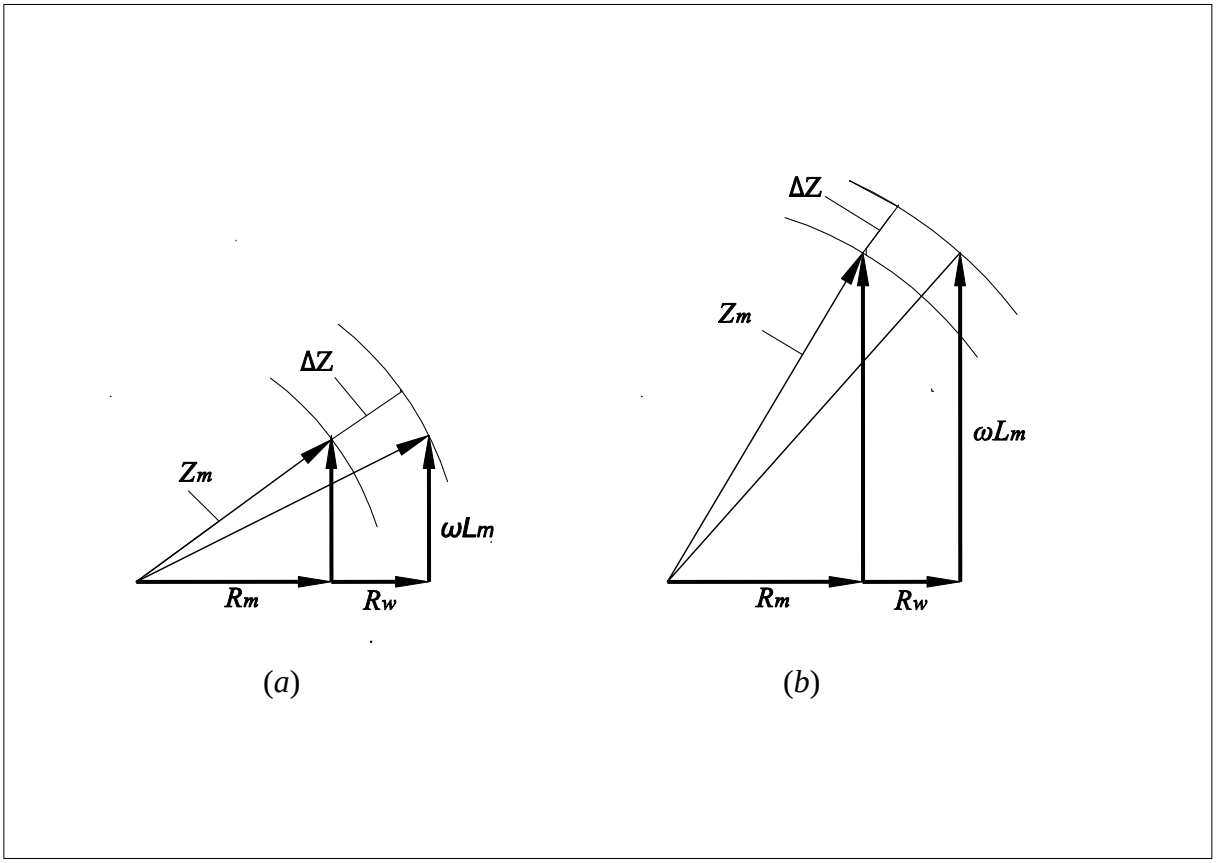

Fig. 7.4 — Impedance change.

The applied voltage $u_1(t)$ is measured directly on the primary side by a high voltage differential probe. Measurement of the applied voltage on the primary side is preferred from measurement of the electrode voltage, since the risk of errors is less likely due to its much higher strength and since wires can be kept away from the weld circuit. The weld current $i(t)$ in the secondary circuit is measured using a Rogowski coil (TECNA-1430, 0-200kA), encircling the electrode (see Figure 7.5). The signals are recorded with a data acquisition board (National instruments DAQ-700) connected to a PC, programmed in software LABVIEW. A detailed description of the measuring system were given in chapter 3. The environment around the welding machine is hostile as regards electrical measurements due to the strong magnetic field generated by the high AC weld current, and special measures were taken to minimize this influence by placing the measuring instruments in a separate room isolated from the welding machine.

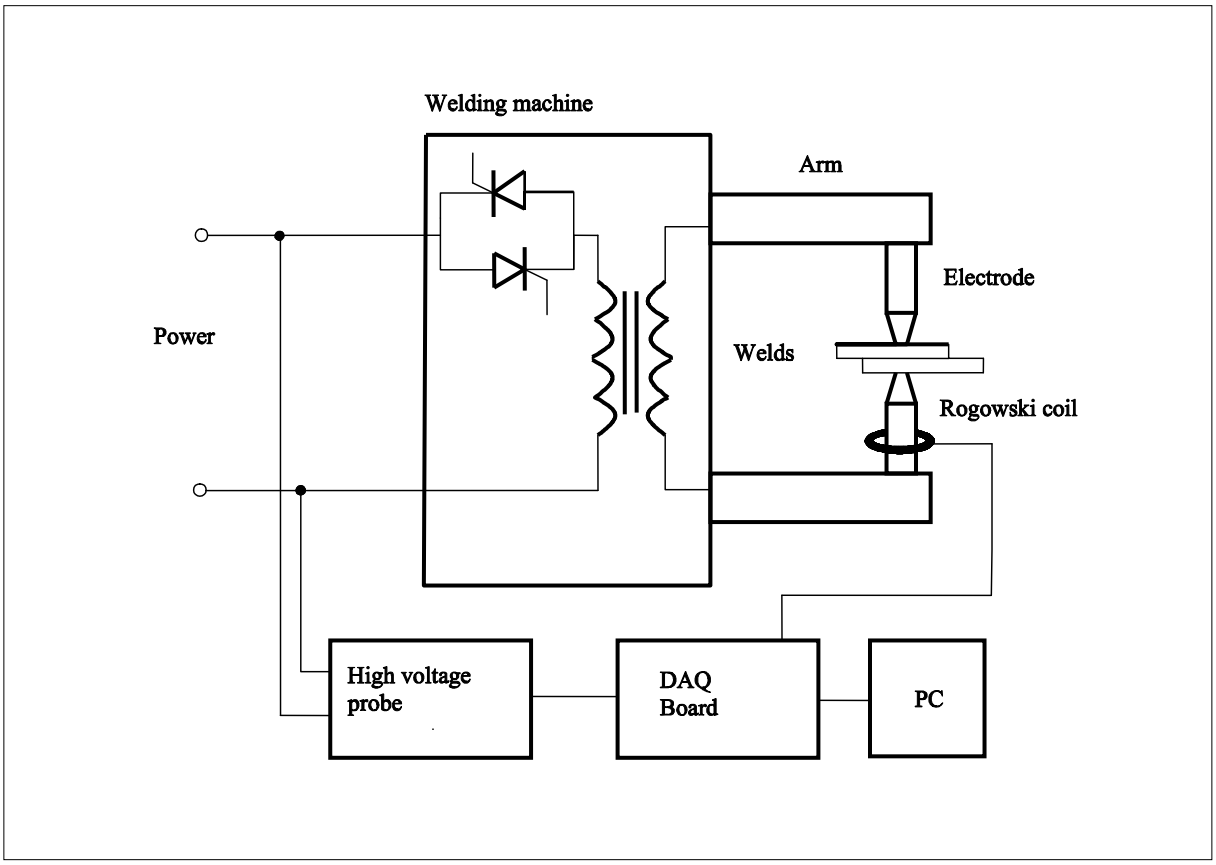

Fig. 7.5 — Experimental set-up.

Applying a sampling frequency of 30 kHz ensures enough data points for subsequent numerical differentiation determining the current rate of change *di/dt.* Eqn. (7-9) can be written in numerical form as:

$$\begin{bmatrix} i(1) & \frac{di}{dt}(1) \\ \dots & \dots \\ i(n) & \frac{di}{dt}(n) \end{bmatrix} \cdot \begin{bmatrix} R_m \\ L_m \end{bmatrix} = \begin{bmatrix} u_1(1)/N \\ \dots \\ u_1(n)/N \end{bmatrix} \qquad (7\text{-}10)$$

In Eqn. (7-10) n corresponding values of u_1, i and di/dt are inserted, and thus the machine parameters R_m, L_m are calculated by least-squares method in MATLAB[37].

The tests were carried out on the single phase AC-machine, TECNA-250kVA, with ISO 5821-type-B-ø6 mm electrodes. Short-circuit testing were carried out by closing the secondary tips without workpieces and with a throat gap of similar size as in sheet metal welding by applying new electrodes of the same material but larger height adjusting for

the sheet thickness. The range of the weld current investigated was covering the range of the machine capacity, weld time was two cycles in order to minimize heat generation, and the measurements in the second positive half cycle were used for computation. Inserting corresponding values of current, current rate of change and voltage in Eqn. (7-10) the machine parameters R_m and L_m were estimated.

Table 7.1 shows calculated values of R_m and L_m, where L_m is given on the form ωL_m. In testing it was noticed, that the two electrodes started to stick together when the set current reached 70 kA. Above this current the values of R_m tend to be constant. This is attributed to the fact that the contact resistance at the interface between the electrode tips is minimized, implying that the identified resistance is close to the real machine-circuit resistance. The machine impedance is thus determined as the averaged value for set currents above 70 kA, which according to Table 7.1 is determined as: **R_m=85 μΩ, ωL_m=164 μΩ.**

Table 7.1— Determination of R_m and L_m for TECNA-250kVA machine

Set current I_{RMS} (kA)	Machine resistance R_m (μΩ)	Machine inductive reactance ωL_m (μΩ)
5	113.00	157.00
10	106.20	161.00
15	101.20	163.00
20	94.40	159.00
25	92.20	157.00
30	92.20	159.00
40	88.20	152.00
50	89.20	167.00
60	87.00	164.00
70	86.00	161.00
80	85.00	161.00
75	85.52	164.10
85	84.90	165.80
90	84.40	166.20
99	84.40	165.90

7.4 Design of Proof Resistances

As earlier mentioned an actual weld joint can be represented by a pure resistance, but the weld resistance changes during welding. In testing the electrical machine properties it is not appropriate to work with changing resistance. Special proof resistances with constant

resistance value and no significant inductance were therefore constructed in form of non-magnetic, circular cylindrical bars in stainless steel (AISI 304).

7.4.1 Selection of Bar Diameters

The diameter of the bars should be chosen to avoid significant change in impedance caused by skin effect, i.e. the effect of increasing resistance with increasing frequency [64]. According to Ref. [64], the following condition must be satisfied:

$$\frac{r_0}{\delta} < 1 \qquad \text{i.e. } r_0 < \delta \qquad (7\text{-}11)$$

Where: r_0 is the radius of conductor (the radius of the bar in our case); δ is the "skin depth".

$$\delta = \frac{1}{\sqrt{\pi f \mu \sigma}} \qquad (7\text{-}12)$$

Where: f --- signal frequency (*Hz*),
μ --- is the permeability of material (*Henries/m*)
σ --- electrical conductivity of material (*Siemens/m*), $\sigma = \frac{1}{\rho}$;
ρ --- resistivity of material ($\Omega \cdot m$);

Table 7.2 shows calculated results, indicated that the maximum diameter of the bar should be under 120.8 *mm* for avoiding the skin effect.

Table 7.2 — Maximum diameter of conductor

Material	σ	ρ	$d_{\max}$
AISI 304 stainless steel	1.39×10^6 *Siemens* /m	$0.72 \times 10^{-6} \Omega \cdot m$	120.8 mm

7.4.2 Selection of Bar Length

The length of the bars was chosen to keep approximately the same throat gap as that in welding of sheet metal. Two special electrodes of the same material and diameter as the standard electrodes were designed as support and current conductors for the proof resistances in order to ensure similar tool holder resistance as in welding, see Fig. 7.6.

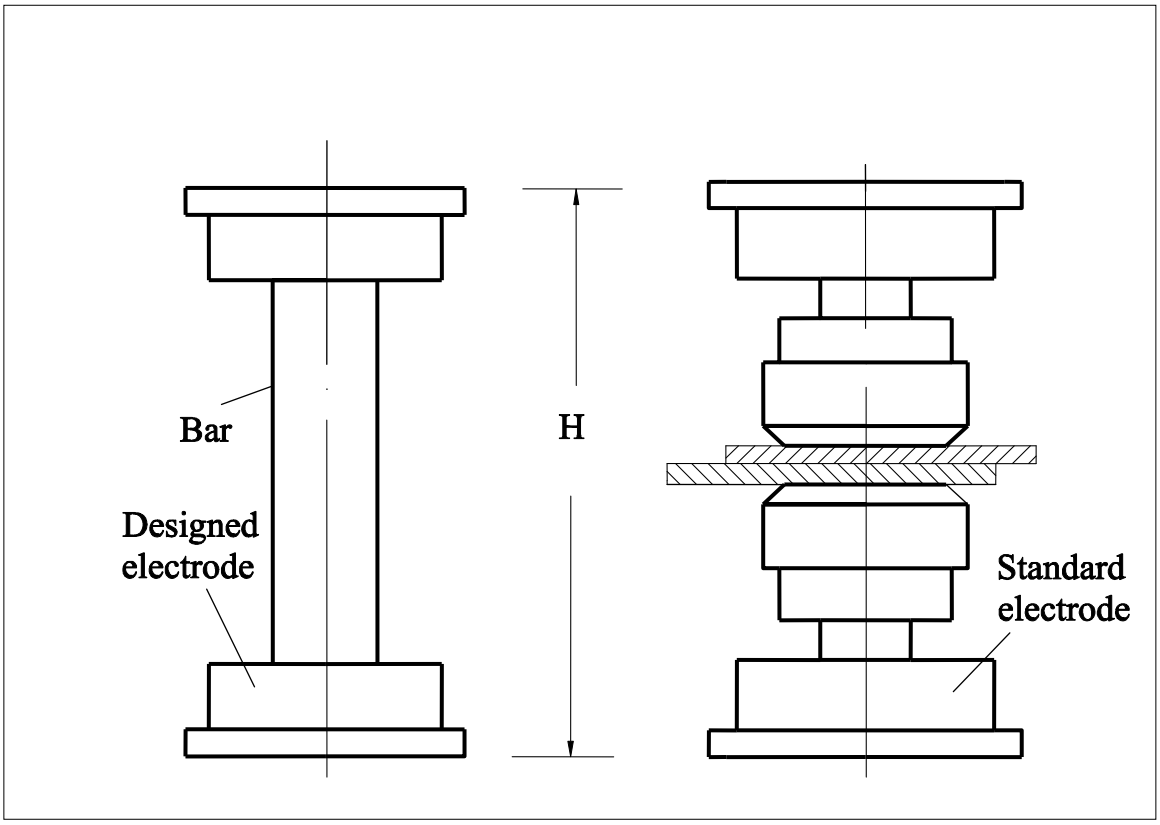

Fig. 7.6— Set-up of proof resistance compared to welding set-up.

7.4.3 Calculation and Measurement of the Resistance of the Bars

The electrical resistance of the bars were calculated and measured. The calculation of bulk resistance was carried out using the following formula[65]:

$$R = \rho \frac{L}{A} \quad (\Omega) \qquad (7\text{-}13)$$

where: L ------- length of the conductor (m);
A ---- Section area of the conductor (m^2) ;

The low resistance measuring technique, i.e. the four-wire method, was applied to measure the resistance of the bar. The four-wire method, which uses two leads to supply current to the unknown resistance and two additional leads to sense the voltage drop across the resistance, eliminates the measurement error caused by test lead resistance and provides the most accurate way to measure small resistances. Fig. 7.7 depicts the equivalent circuit for the four-wire ohms measurement. Test leads are connected from terminals of the voltmeter to the terminals of the unknown resistance. Current I_1 generated by the current source flows through the lead resistance R_1 and unknown resistance R_x , but negligible current I_2 will flow through the lead resistance R_2 and voltmeter, due to the very large internal resistance of the voltmeter (up to 10 $G\Omega$). Thereby, the voltage V detected by the sense terminals will be identical to the voltage developed across the unknown resistance. In this way, the unknown resistance is determined by:

$$R_x = V / I_1 \qquad (7\text{-}14)$$

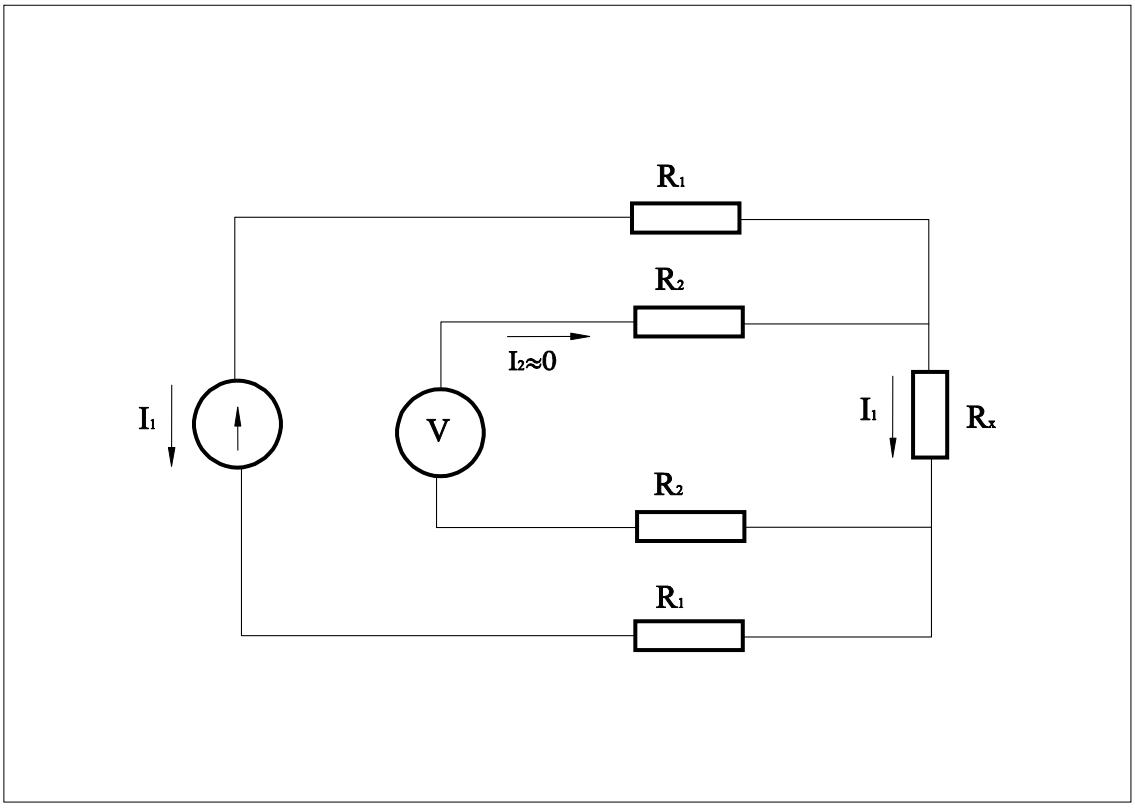

Fig. 7.7 — Equivalent circuit for four-wire ohms measurement

Fig. 7.8 shows a photo of the measurement set-up.

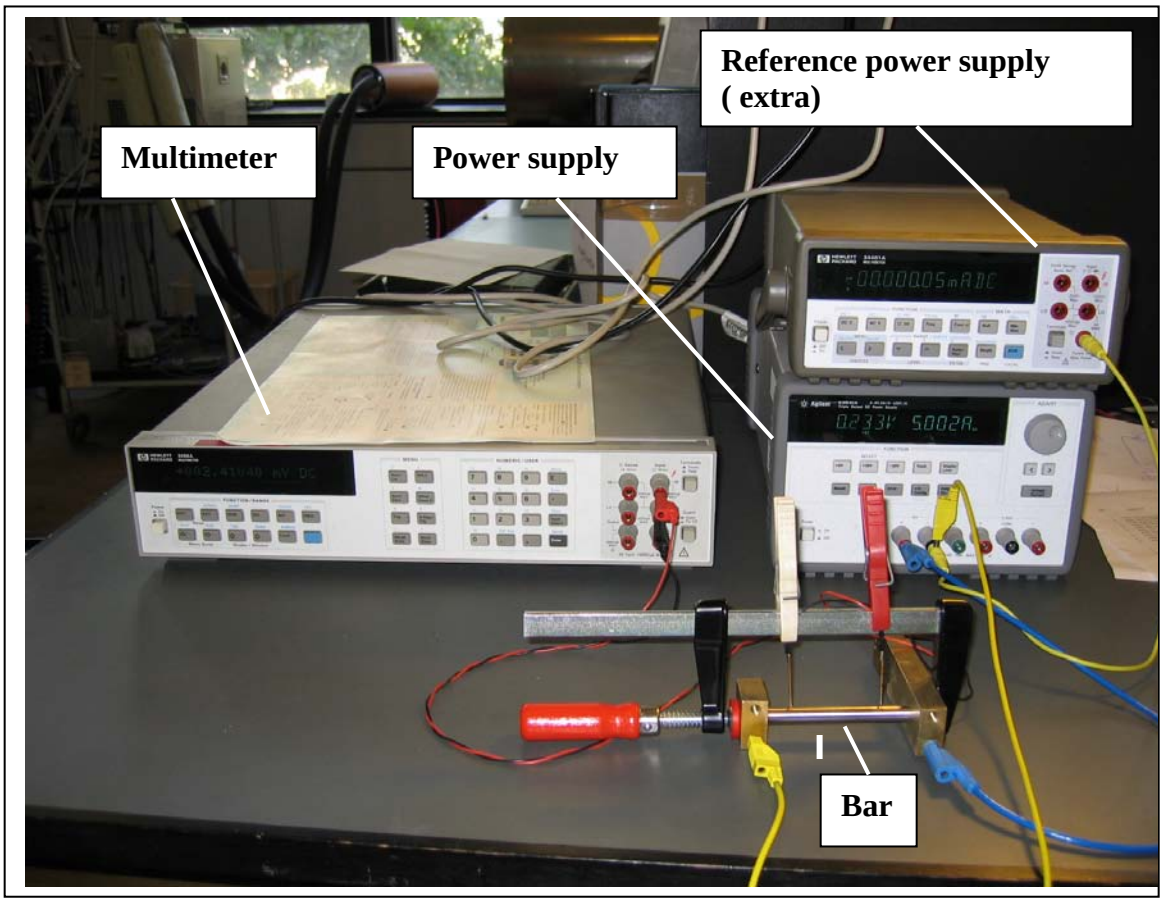

Fig. 7.8— Photograph of measuring the resistance of bar

Table 7.3 — Calculated and measured resistances of bars

Designed Dia. (mm)	Measured Dia. (mm)	Length (mm)	Calculated R ($\mu\Omega$)	Measured R ($\mu\Omega$)
8	8.00	81.11	1162	1174.0
9	9.02	80.93	912	917.0
10	9.98	81.21	748	761.5
12	12.02	80.82	513	516.5
14	14.01	81.32	380	386.5
16	16.01	81.00	290	291.0
18	17.95	81.12	231	249.0
20	19.98	80.91	186	191.0
24	24.00	80.78	129	129.5
30	30.01	81.01	83	80.5

All in all 10 proof resistances were designed and constructed, to cover the range 100-300μΩ, which is the range of work piece resistances normally used in welding on the type of machine in question. Table 7.3 shows the measured and calculated bulk resistances of the test bars. It is seen that the measured values are quite closed to calculated ones, and calculated values will be used for the subsequent study.

7.5 Tests with Proof Resistances

A series of tests were carried out with the proof resistances. The tests were done similarly to the short-circuit tests mentioned earlier, using the same measuring system and the same machine, TECNA-250kVA. Testing was done with 19 different RMS weld current values ranging from 1-34 kA. All proof resistances were tested with each current setting. Current duration was chosen as two cycles, the electrode force was 6.6 kN. Measurements of the weld current and the applied primary voltage were collected by data acquisition on a PC. The second positive half cycle was selected for subsequent analysis ensuring that the dynamic effect of power switch-on is eliminated after this time of running-in. Furthermore, the temperature of the test bar was measured in the entire test period by a thermal couple percussion welded to the bars. A maximum temperature increase of 12 C° was noted, implying that the influence of heating of the resistance during testing can be neglected.

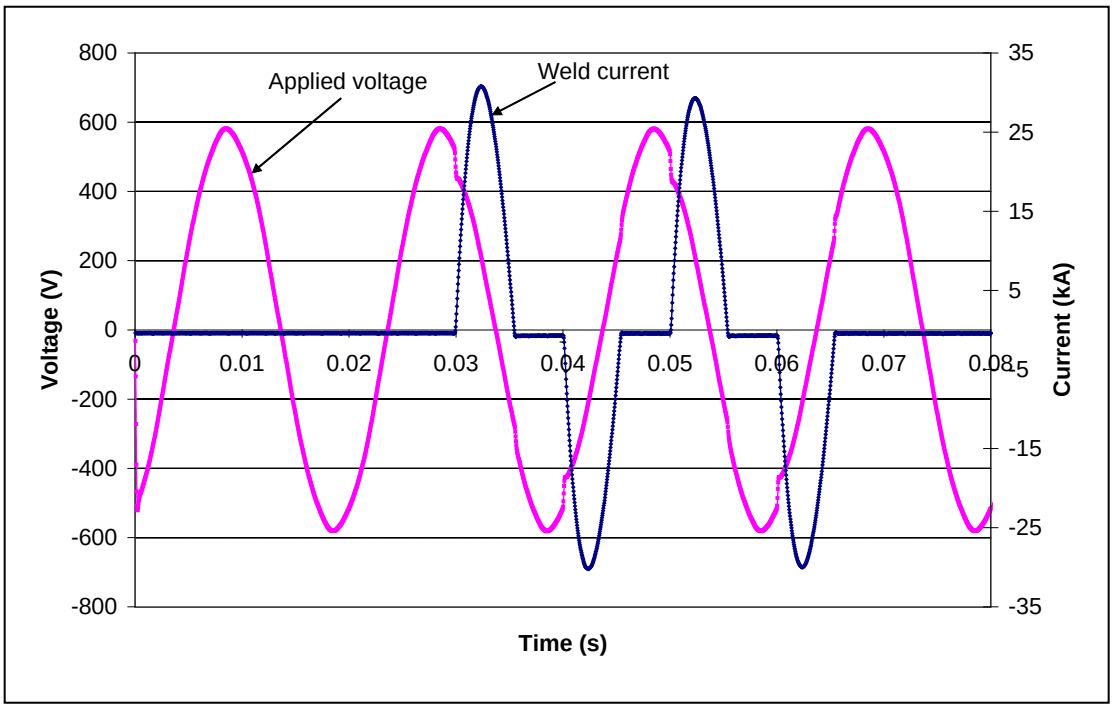

Fig. 7.9 — Test with proof resistance - example on recorded supply voltage and weld current.

Fig. 7.9 shows an example on the recorded supply voltage and weld current. It can be seen that the primary voltage curve has a bend every time the SCR is switched on indicating, that the sudden coupling of load given by the welding machine causes a fluctuation of the power supply voltage.

7.6 Results and Discussions

Applying MATLAB a computer program was developed to solve Eqns. (7-2), (7-4). The firing angle α was found by iteration ensuring good matching between calculated and measured current waveform**.** In the same way the contact resistance at the interfaces between proof bar and electrode tip was determined by iterative calculations trying different values of contact resistance until the curves from the model and the measurement fit well. The average value of contact resistances obtained at a few selected test currents is taken as the final contact resistance for each bar. Table 7.4 shows the determined values of the contact resistance, which is seen to vary in an irregular way with the proof bar diameter. This may be attributed to contact variations caused by the geometrical misalignment and varying surface conditions.

Inserting the estimated value of α in Eqn. (7-2) the current is calculated. Comparison with the measured current curve in Fig. 7.10 shows very good agreement for two quite different proof resistances. Note that the waveforms are non-sinusoidal, especially at low currents. Such good agreement were obtained for all tests, i.e. with all proof resistances and current settings investigated, implying that the model and the method works well.

Table 7.4 —Contact resistances between proof bar and electrode tip

Designed bar Diameter mm	**Contact resistance at different test currents**							**Rc_average μΩ**
	5kA	**10kA**	**15kA**	**20kA**	**25kA**	**30kA**	**34kA**	
8	102	112	104	110	112	109	99	107
9	106	105	96	82	93	88	81	93
10	98	95	100	80	90	79	82	89
12	102	87	100	74	85	67	66	83
14	114	92	102	78	80	72	76	88
16	106	86	92	72	66	65	63	79
18	104	91	102	72	77	68	66	83
20	101	89	88	70	67	64	63	77
24	100	90	83	70	72	65	62	77
30	100	82	78	75	68	67	65	76

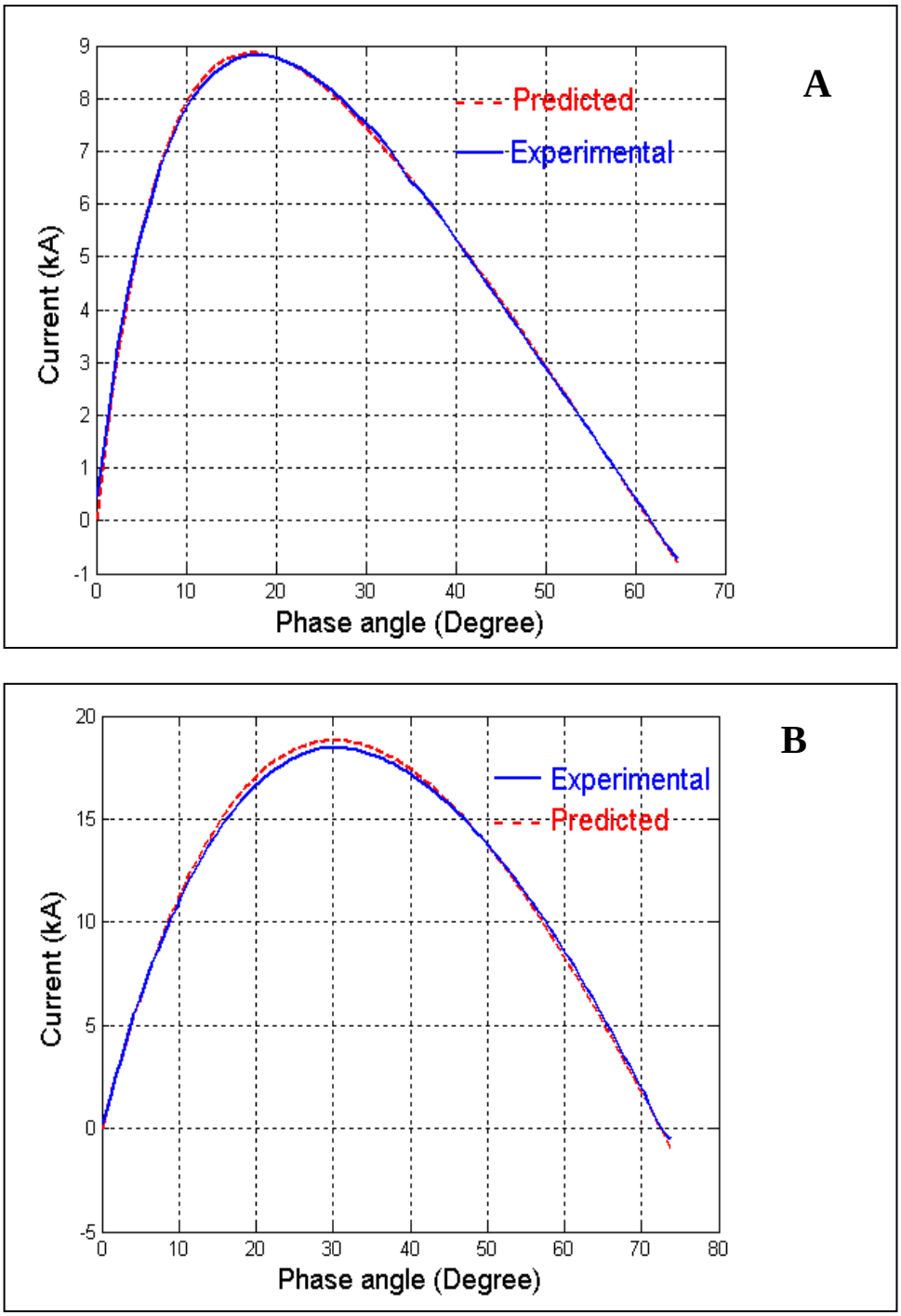

Fig. 7.10 — Comparison between predicted and measured current for two different cases. A—set current 17kA, proof resistance 912 micro Ohm; B—set current 10kA, proof resistance 83 micro Ohm.

The root mean square values (RMS) of the weld current in one half cycle determined by the mathematical model and the experiments were also computed. In summary, the weld current, the firing angle and the conduction angle of the SCR are now all determined as functions of the part resistance. Table 7.5 gives the results at set currents of 12 kA and 13 kA, in which the R^2 assesses the agreement between the measured current curve and the predicted one. The results of the remaining tests are presented in Appendix D.

Figure 7.11 shows the conduction angle versus part resistance and set current. Fig. 7.12 shows a comparison between the calculated weld current and the measured one as a function of part resistance. Good agreement is obtained.

Table 7.5 — Examples of test results at set current 12, 13 kA

Test	Bar diameter (mm)	Set current (kA)	Measured current (kA)	Predicted current (kA)	Firing Angle (degree)	Conduction angle (degree)	R^2
I	8	12	2.56	2.59	131.4	55.0	0.998
	9		3.15	3.24	130.2	57.7	0.9903
	10		3.59	3.60	131.1	58	0.9987
	12		4.66	4.68	130.0	61.8	0.9993
	14		5.25	5.35	130.1	63.6	0.9951
	16		6.36	6.35	129.1	66.9	0.9984
	18		6.77	6.78	129.2	67.9	0.9982
	20		7.54	7.72	127.9	71	0.9931
	24		8.47	8.61	127.4	73.5	0.9963
	30		9.43	9.57	126.9	76.0	0.9972
II	8	13	2.58	2.61	131.2	55.3	0.9979
	9		3.14	3.16	130.9	56.9	0.9978
	10		3.63	3.70	130.2	58.95	0.9926
	12		4.74	4.72	129.7	62.1	0.9961
	14		5.35	5.36	130.1	63.6	0.9956
	16		6.43	6.51	128.2	67.7	0.9967
	18		6.8	6.87	128.8	68.4	0.9961
	20		7.7	7.8	127.5	71.4	0.9973
	24		8.49	8.64	127.3	73.6	0.9955
	30		9.72	9.83	126.05	76.96	0.9980

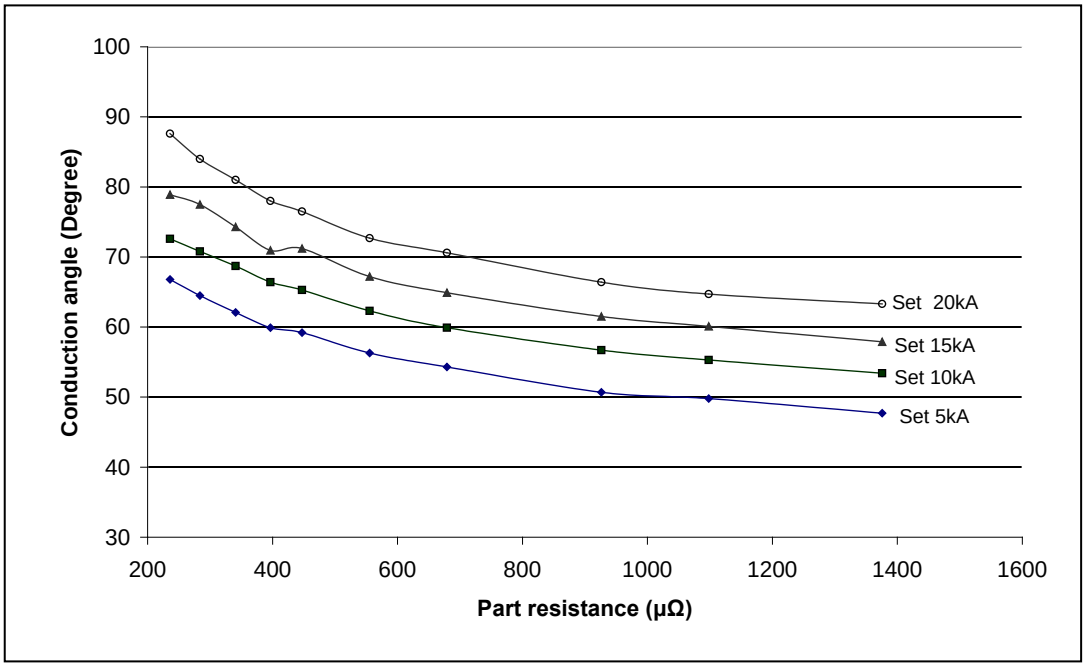

Fig. 7.11 Conduction angle v.s. part resistance at different set currents

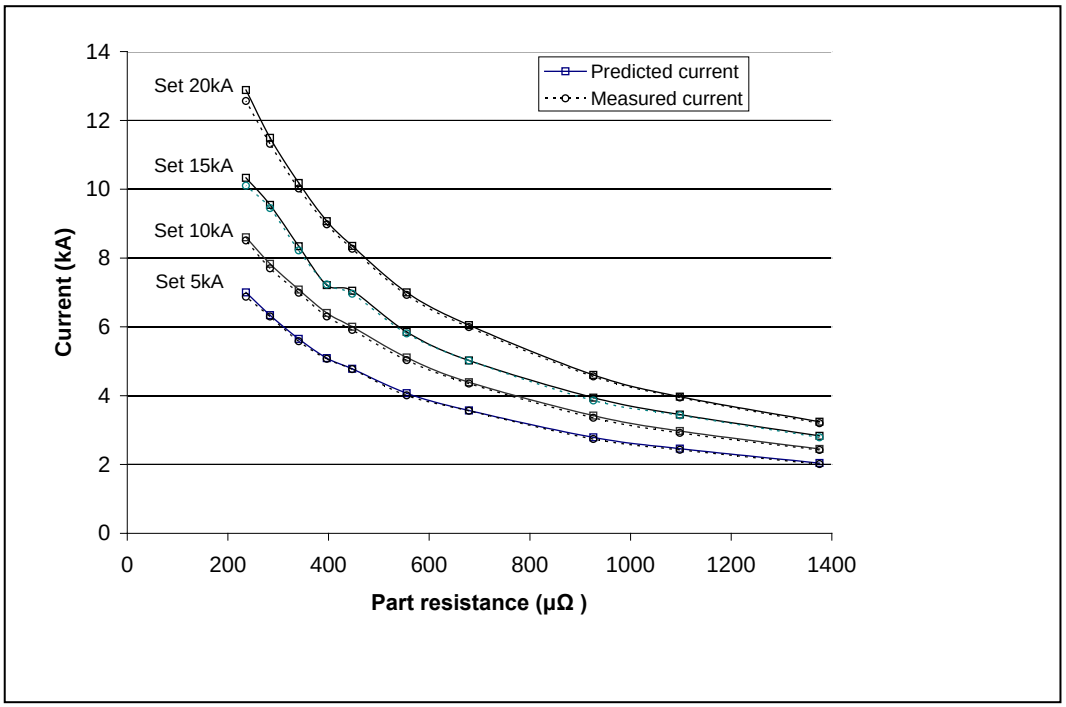

Fig. 7.12 — Modelled and measured weld currents v.s. part resistance at different set currents.

Uncertainty in the predictions by the model may be caused by a few factors such as the transformer losses, which are neglected, the nominal applied voltage (400V of amplitude in RMS in Denmark), which is used for calculation instead of the real voltage. It may deviate from the nominal one, but the results from a traditional AC resistance welding machine show that the errors are acceptably small.

7.7 Conclusions

An installed AC resistance welding machine with a given controller has a constant machine-circuit resistance and inductance, which are the key parameters determining the machine's electrical characteristics and quantifying the difference from machine to machine. Modelling the electric system of the machine as an equivalent circuit simplified to the secondary side of the transformer assuming that the circuit is composed of resistances and inductance in series, a procedure has been proposed for identifying the equivalent machine-circuit resistance and inductance.

Once the part resistances are known, the real weld current can be predicted according to the set value by adopting the model. It is thus possible to take the specific machine characteristics into account when simulating the welding process. The method also provides the possibility of transferring an optimized production from one machine to another, predicting optimized parameter settings on other machines.

Chapter 8

Measurement of Dynamic Resistance in Resistance Spot Welding

This task was not originally planned but during the electrical experiments and literature study, it was noticed how important the measurement of dynamic resistance is during welding. The dynamic resistance represents the welding current-electrode voltage characteristics, relating to the nugget formation, which can be used to monitor the welding process and to establish on-line weld quality control. It can also be used to determine the contact resistance. However, the challenge is that the conventional measuring set-up normally interferes with the welding robot, and the measuring precision is influenced by inductive noise caused by the high welding current. The idea came up to try to apply the method developed in this present project to measure the dynamic resistance and determine the contact resistance.

8.1. Introduction

The dynamic resistance of workpiece in resistance welding is closely related to the welding progression and can be used for monitoring the welding process or estimating the weld quality, together with other signals, such as the dynamic electrode displacement [47-54]. Also the contact resistance between the sheets being welded, i.e. the faying surface contact resistance of workpieces can be estimated by measuring the total dynamic resistance between electrodes [53,67, 68]. The contact resistance is a variable of considerable importance in the practical application of electrical resistance welding, and it is an essential data support in numerical simulation of the welding process[62]. Therefore, accurate measurement of the dynamic resistance in resistance welding is necessary.

According to published literature, the dynamic resistance was determined mostly by measuring the current and voltage across the electrodes at secondary side of transformer [47-54, 67-68, 55-56]. This causes some problems. Firstly, the amplitude of the secondary voltage signal is quite small and thus it can very easily be disturbed by induction noise especially when a low welding current is applied. The problem is deteriorated when a high current is used, and the lead loop resulted in detecting the voltage across electrodes since the voltage leads connected to electrodes must span the thickness of the workpiece. Secondly, the voltage leads leads to interference problems

with the welding robot and the risk of disconnection to the electrodes during movement of the welding gun.

In order to reduce the influence of induction noise on measurement of the voltage, the simplest way is to twist the measuring leads, however this may be only effective enough in laboratory studies. In production environments, the voltage lead loop may not be minimized even when twisting the leads.

In these early studies, the calculation of the dynamic resistance was performed by using the peak current of a half cycle and the voltage at that moment, since *di/dt* equals zero at the peak implying that the induced voltage is zero. In practice, the peaks can be difficult to locate precisely with a computer, as it only samples discrete points of data, especially when a low sampling rate is employed.

Yongjoon [57-58] proposed a technique of monitoring the welding process and estimating the weld quality by using the primary dynamic resistance, and a measuring system was suggested in which the measurement was carried out on the primary circuit without any extra monitoring system in the secondary circuit. The dynamic resistance was calculated by using the instantaneous values obtained at the moment when the current reaches its peak in order to obtain pure dynamic resistance without any inductive reactance. The machine primary resistance R_p was neglected because it was relatively small compared to the other terms included in the calculation when the circuit was referred to the primary side. This method is useful to in-process monitoring, but it can not be used to accurately determine the absolute value of dynamic resistance.

In the present study, a new method of determining the dynamic resistance across the electrodes by measuring the primary voltage and secondary current is suggested. The measurement has little influence from induction noise and no limitations caused by lead connections to the electrodes. The reliability of the method is proven by comparing the dynamic resistance measured by the conventional method with the proposed one. A few examples of applying this method to obtain the contact resistance of faying workpiece surfaces are presented.

8.2. Principle of the Measurement

As mentioned earlier, the circuit of single-phase AC resistance welding machines with silicon controlled rectifiers (SCR) is simplified as an equivalent circuit, as shown in Figure 7.1. The primary circuit is simplified as a sum of primary resistance R_1 and primary inductance L_1 in series. The secondary circuit is simplified as a sum of secondary machine-circuit resistance R_2, work-piece resistance between electrodes R_w and equivalent inductance L_2 in series. The two circuits are coupled by an ideal transformer, neglecting its magnetizing reactance and core losses. The workpiece is considered as a pure resistance (R_w) which is a variable measured between electrodes. In

the primary circuit, the R_1 includes the SCR contactor, the primary winding resistance of the transformer as well as the bulk and contact resistances of leads. L_1 is mainly caused by transformer leakage reactance. In the secondary circuit, R_2 is the added value of

the secondary winding resistance of the transformer and resistance of the secondary circuit, including the bulk and contact resistances of electrode, electrode arm and band conductors. L_2 generally represents the secondary leakage reactance of the transformer.

To analyze the welding machine circuit, an equivalent circuit is formulated by converting the circuit to the secondary side, as shown in Figure 7.2, where the total equivalent resistance of entire circuit R_t is the sum of equivalent machine-circuit resistance R_{m} and workpiece resistance R_w, as expressed as in equation (8-1). The total equivalent inductive reactance X_t which equals the machine-circuit inductive reactance can be expressed as equation (8-2):

$$R_t = R_m + R_w \quad (R_m = R_2 + \frac{R_1}{N^2}) \qquad (8\text{-}1)$$

$$X_t = X_2 + \frac{X_1}{N^2} \quad (X = \omega \cdot L) \qquad (8\text{-}2)$$

where N is the transformer ratio, ω is the natural frequency of the applied voltage.

The applied voltage (power system nominal voltage) is also referred to the secondary by dividing with the transformer turn ratio. From equation (8-1), thus the dynamic secondary resistance R_w across the electrode can be obtained by the total equivalent resistance R_t subtracting the equivalent machine-circuit resistance R_{m}, as shown in equation (8-3), which is the principle of determining the dynamic resistance.

$$R_w = R_t - R_m \qquad (8\text{-}3)$$

8.3. Principle of Determining R_t and R

According to the equivalent circuit in Figure 7.2, the following expression can be derived using the voltage drop of *RL* circuit:

$$\frac{u_1}{N} = R_t \cdot i(t) + L_t \frac{di}{dt}, \qquad (8\text{-}4)$$

where: $L_t = X_t / \omega$.

If the applied voltage u_1 and weld current *i(t)* are measured instantaneously and *di/dt* is obtained by differentiating the signal of the weld current *i(t)*, the parameters R_t, L_t can be

identified using equation (8-4) by curve fitting for a half cycle. The method is the same as that described in Chapter 7 for determining the machine resistance and inductance.

As mentioned earlier, the equivalent machine-circuit resistance R_m (as well as inductance L_m) can be found by performing the test without workpiece (short-circuit test). Once a given machine is installed, many components are fixed for that installation, and the machine impedance (R_m and X_m) is a constant.

8.4. Measuring System

As shown in Figure 7.5, a system is set up to measure the primary applied voltage and weld current.

In order to examine the reliability of the method proposed, the conventional secondary dynamic resistance test is performed as well, see Fig. 8.1, in which the voltage between the electrodes is measured directly by connecting the wires to the electrodes, and the secondary current is still measured by using the Rogowski coil similarly as in Fig. 7.5. The wires for the voltage measurement are twisted in order to reduce the inductive noise. The dynamic secondary resistance is calculated by using the peak current of the half cycle and the voltage at that moment.

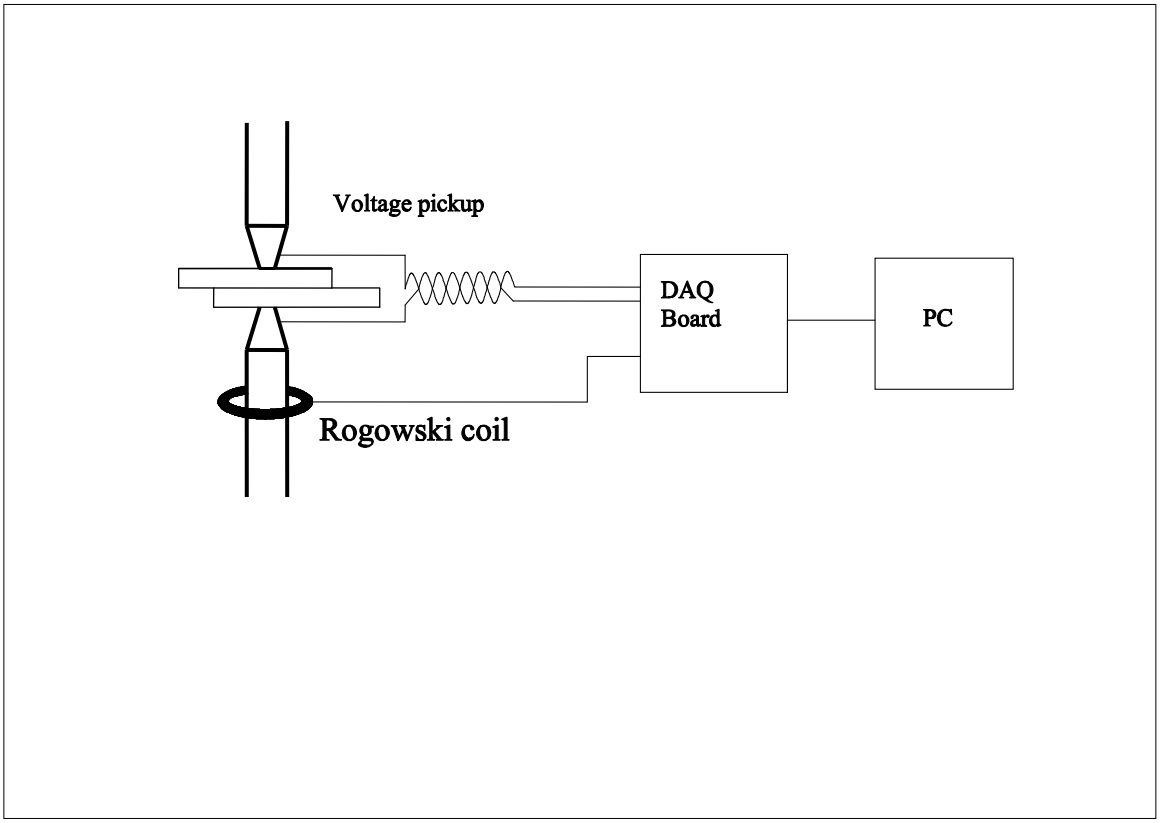

Fig.8.1 — A schematic diagram of conventional measuring system

8.5. Application and Discussion

Tests with both methods, the proposed and the conventional, were conducted on the single-phase TECNA 250-kVA-AC welding machine. The results were compared by plotting the curves together. Fig. 8.2 shows the results for welding mild steel (material: W.Nr.1.0037) sheets in 1.5- to 1.5-mm, welded with welding current 16 kA, electrode force 6.1 kN and welding time 7 cycles, with good weld quality.

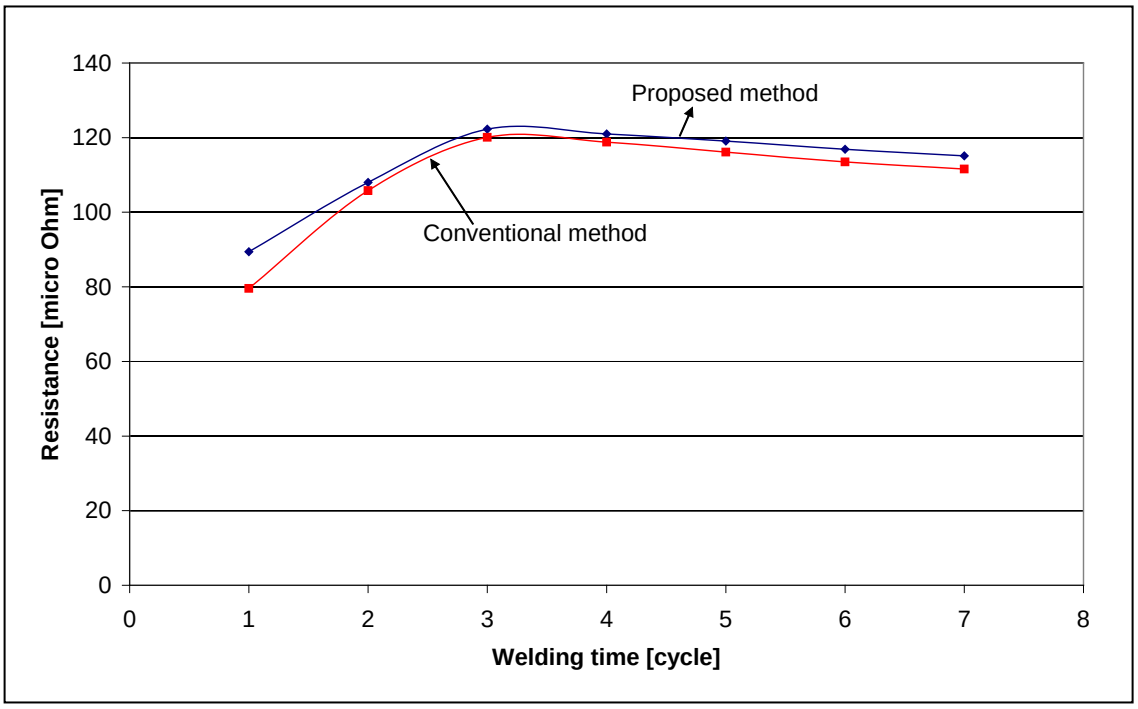

Fig. 8.2 — Comparison of dynamic resistance between proposed and conventional methods for mild steel

Fig. 8.3 shows the results of stainless steel (W.Nr. 1.4301) sheets in 1.5- 1.5mm, welded with welding current 6 kA, electrode force 6.1 kN and welding time 7 cycles. For this weld splashing occurred causing the abrupt decrease in dynamic resistance.

Both examples illustrate that the dynamic resistances obtained by the two methods are very close, and the trend of the curves is similar to that obtained by other researchers [47, 52, 53], indicating that the proposed method is feasible, and possible to apply for monitoring of the welding process and estimation of weld quality.

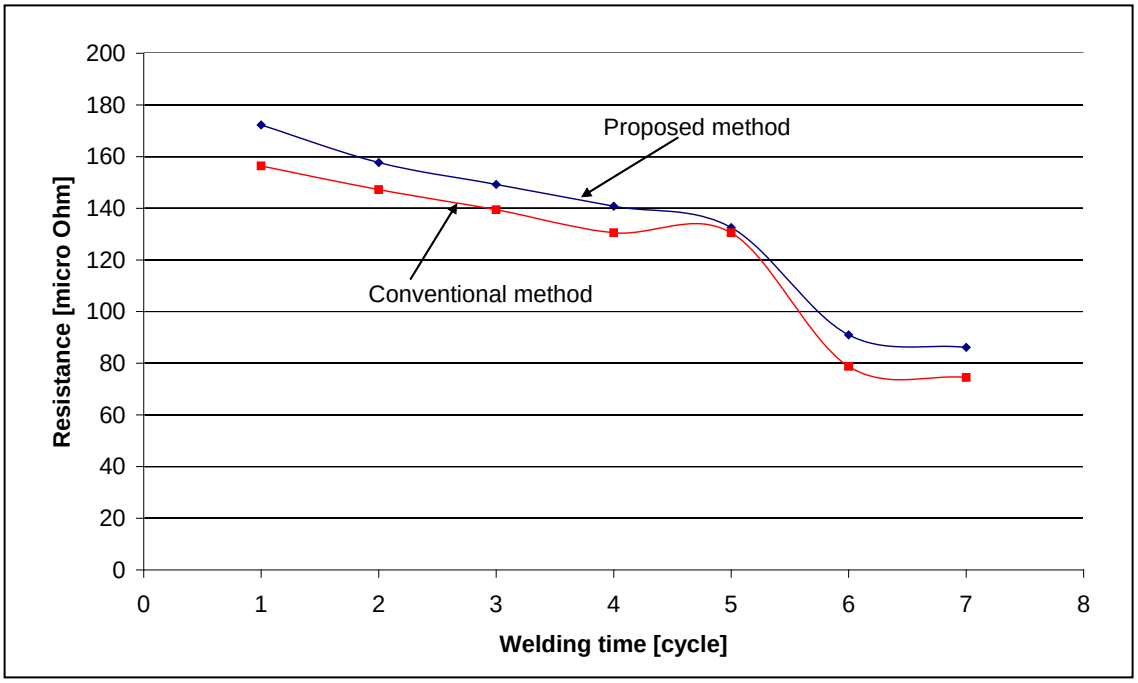

Fig. 8.3 — Comparison of dynamic resistance between proposed and conventional methods for stainless steel

As another example of application of the proposed method, the dynamic faying surface contact resistance of sheet metal in resistance spot welding is determined. For a batch of workpieces with given material and surface conditions, the contact resistance of faying surfaces is important for examining the resistance welding properties of the material. As shown in Fig. 8.4, the contact resistance of faying surface can be obtained from the total dynamic resistance of two-sheet metals subtracting the total contact resistance of one sheet metal with same material, and same thickness as that of two sheets. The base material resistance and electrode-to-workpiece contact resistance are eliminated by subtraction assuming they are the same in two cases. The welds are carried out under the same welding conditions, i.e. same welding current, same electrode force and same welding time.

Fig. 8.5 shows the faying surface resistance of mild steel (W.Nr.1.0037) sheets in 2-2 mm, tested with welding current 9.1 kA, electrode force 4.1 kN and welding time 7 cycles.

Fig. 8.6 shows the faying surface resistance of aluminum alloy (AA 2014) sheets in 2-2 mm, tested with welding current 19.6 kA, electrode force 4.1 kN and welding time 10 cycles.

The results obtained are similar to those noted by other researchers [Ref. 67], i.e. the faying surface contact resistance is approximately 10 μΩ on completion of the weld cycle for aluminum and 30-40 μΩ for steel.

As mentioned earlier, the proposed method is based on the premise that the machine impedance (R_m and X_m) throughout the whole process of welding is constant under different welding conditions, and the total inductance (L_t) equals the machine inductance (L_m) assuming that the workpiece is a pure resistance. It is appropriate to assume that the machine resistance R_m is a constant because the temperature increase of the machine-circuit components is negligible. In order to examine the variation of the machine inductance L_m under different welding conditions, it is calculated at each positive half-cycle using Eqn. (8-4). The machine reactance X_m is calculated by multiplying with the natural frequency ω. The impedance of the tested machine is: R_m=85 μΩ, X_m =164 μΩ. Table 8.1 gives the results of total inductive reactance (X_t) variation through 7 cycles when welding different materials, including mild steel, stainless steel and aluminum. It can be seen that very small variation appears compared to the machine inductive reactance (X_m), illustrating that the total inductive reactance is a constant during welding, which equals the machine inductive reactance.

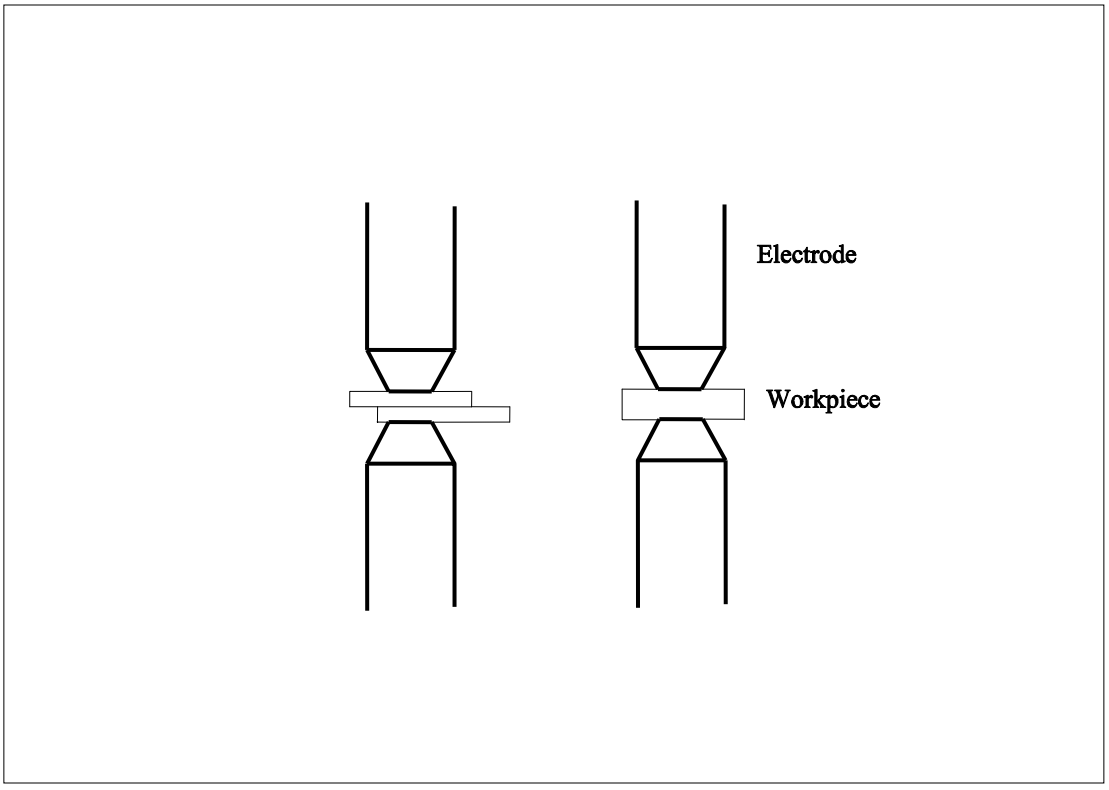

Fig. 8.4 — Experimental arrangement for measuring the faying surface contact resistance

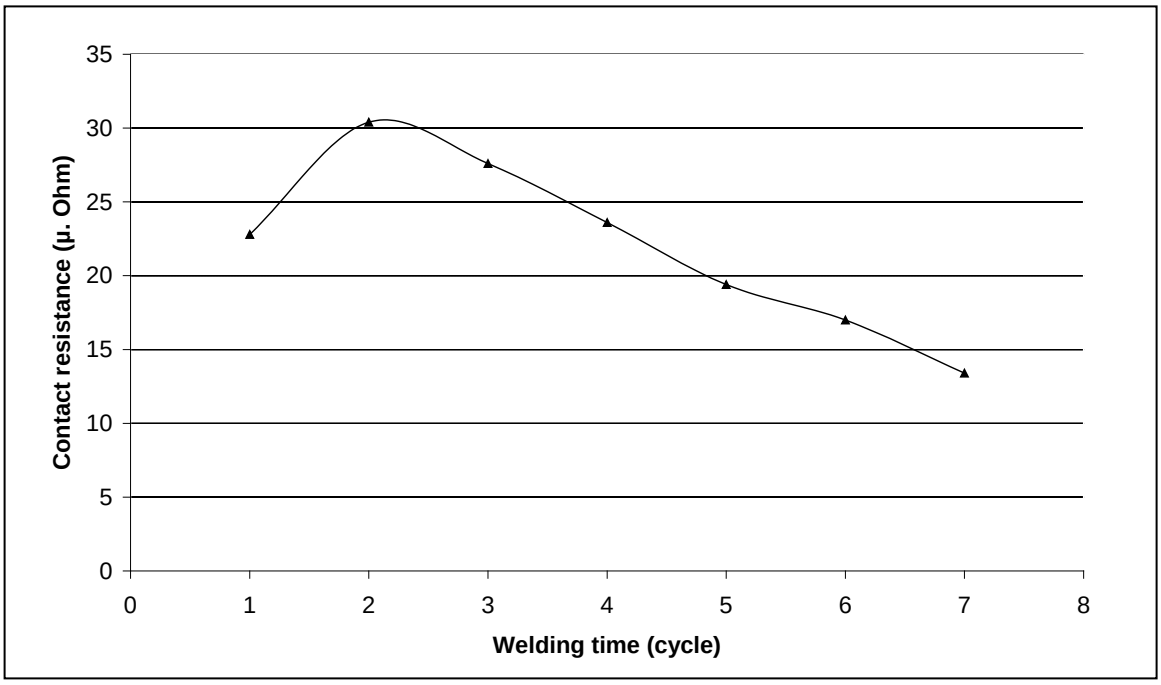

Fig. 8.5 — Faying surface contact resistance of mild steel

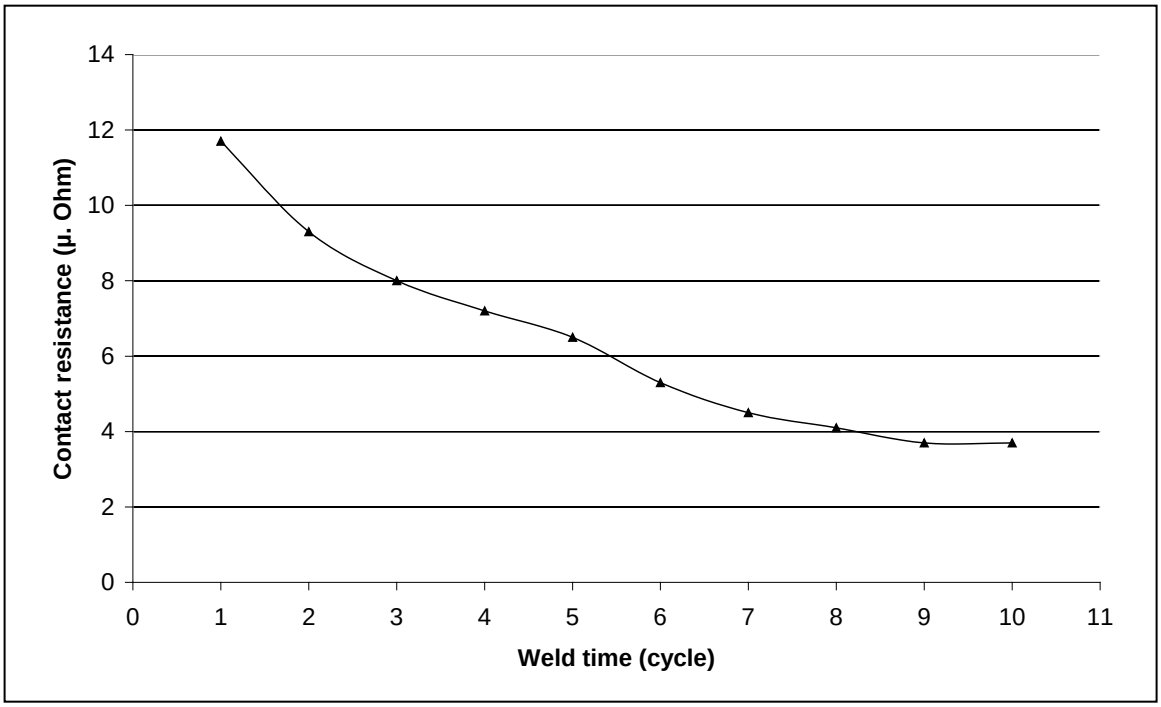

Fig. 8.6 — Faying surface contact resistance of aluminum alloy

Table 8.1. Variation of machine inductive reactance

Specimen	Welding Parameters	Cycle	X_t (μΩ)	Δ X_t (μΩ) (X_t -164)
Steel (W.Nr. 1.0037) 120×60×1.5mm- to - 120×60×1.5mm	11.9 kA, 6 kN, 7 cycles	1	162.6	1.4
		2	158.6	5.4
		3	158.9	5.1
		4	161.8	2.2
		5	162.0	2
		6	161.8	2.2
		7	161.9	2.1
Stainless steel (W.Nr. 1.4301) 120×60×1mm- to - 120×60×1mm	7.4kA, 6kN, 7cycles	1	162.4	1.6
		2	158.2	5.8
		3	160.1	3.9
		4	160.1	3.9
		5	158.9	5.1
		6	159.1	4.9
		7	159.4	4.6
Aluminum 120×60×2mm- to - 120×60×2mm	18.6kA, 3.4 kN, 10 cycles	1	166.7	-2.7
		2	159.8	4.2
		3	159.6	4.4
		4	159.2	4.8
		5	160.1	3.9
		6	159.0	5
		7	160.5	3.5
		8	160.3	3.7
		9	159.5	4.5
		10	159.3	4.7

8.6. Conclusions

A new approach of determining the dynamic resistance has been developed, in which the dynamic resistance is obtained by measuring the voltage in the primary circuit and the current in secondary circuit, with the advantages of higher signal-noise ratio during measurement and no voltage detecting leads connected to the electrodes.

The reliability of the method is proven by comparing the dynamic resistance measured by proposed method and that using the conventional method, testing on two kinds of material: mild steel and stainless steel. The new method is furthermore applied to

measure the faying surface contact resistance for steel and aluminum. Results obtained are in good agreement with those of other authors.

The machine-circuit impedance needs to be identified before the suggested method can be applied for measuring the dynamic resistance. This can easily be realized by conducting a short-circuit test. Once a given machine is installed, the machine impedance will be a constant during welding.

Chapter 9

Conclusions and Proposals for Further Work

The objectives of this Ph.D. project have been accomplished as planned. Based on the comprehensive literature study, the present work has been dedicated to testing and modeling of the electrical and dynamic mechanical properties of resistance welding machines. Some significant results have been achieved, which are important for optimizing process settings and applying computer simulations of resistance welding in order to achieve stable production and high quality of products.

9.1 Testing and Modeling the Dynamic Mechanical Machine Properties

The dynamic mechanical machine properties include touching behaviour as well as follow-up behaviour. The touching behaviour represents the dynamic mechanical machine characteristics in the squeeze phase while the follow-up behaviour represents the dynamic mechanical machine characteristics in the welding phase. The touching behaviour only influences the electrode service life and has no influence on weld quality.

9.1.1 Touching Behavior

How fast the machine is able to build up the force and stabilize it to the set static value, characterizes the touching behaviour of the machines. In production, the squeeze time should be set greater than the stabilizing time of electrode force of the machine at each load level.

In this study, pure mechanical tests for measuring the electrode force and thus determining the stabilizing time at each load were carried out for two machines. One machine was air-operated and the other one hydraulic provided with additional springs in the welding head. It was found that, for the same level of electrode force, the pneumatic machine took longer time to build up and stabilize the force to the static value due to the compressibility of the air. The hydraulic one was very fast to reach and stabilize to the static electrode force, and the stabilizing time did not depend on the level of the load.

The additional springs mounted in welding head provides a soft electrode application, but cause a longer-time oscillation of electrode force compared to the pneumatic one.

9.1.2 Follow-up Behavior

To model the follow-up behaviour, the resistance welding machines with C-frame are simplified as a one-degree-freedom vibration unit. The corresponding mathematical model, involving three equivalent machine parameters: equivalent moving mass, equivalent damping coefficient and equivalent spring constant, has been established. The model is applicable to most type of machines and independent of the machine constructions, i.e. no matter how the machine structure is, it is possible to describe the dynamic response characteristics of the machine by these three parameters. A specially designed test called "*free breaking test*" was employed to identify these three basic parameters required in the model. The model has been verified by so-called "*supported breaking test*" as well as real projection welding on a commonly used pneumatic machine.

The model was also applied to a hydraulic machine with additional springs in the welding head. Good accordance was obtained with the results from supported breaking tests, but not with those from real projection welding tests. The reason is thought to be the influence of the electromagnetic force, implying that the model needs to be modified for this machine, or the mechanical machine parameters should be identified by the "*free breaking test with welding current going through*". The work didn't go further considering the fact that this machine is not a standard, commonly used one.

9.2 Testing and Modeling the Electrical Machine Properties

The electric system of single-phase AC resistance welding machines is represented by an equivalent circuit simplified to the secondary side of the transformer assuming that the circuit is composed of resistances and inductance in series. For an installed machine with a given controller, it has a constant machine-circuit resistance and inductance, which are the key parameters determining the machine's electrical characteristics and quantifying the difference from machine to machine. The workpieces are considered to be a variable resistance, which is replaced with a constant reference resistance made by a stainless steel bar. A procedure has been proposed for identifying the equivalent machine-circuit resistance and inductance.

Once the part resistances are known, the real welding current can be predicted according to the set value adopting the model. It is thus possible to take the specific machine characteristics into account when simulating the welding process. The method

also provides the possibility of transferring an optimized production from one machine to another, predicting optimized parameter settings on the other machine.

Good results have been obtained by using the procedure on the TECNA-250 kVA-AC machine.

9.3 Measurement of Dynamic Resistance

Dynamic resistance across electrodes represents the welding current-electrode voltage characteristics, which is a key parameter used for welding process monitoring and in-process weld quality prediction.

In this study, a new approach of determining the dynamic resistance has been developed, measuring the voltage on the primary circuit and the current in secondary circuit, with advantages of less inductive influence and no measuring lead interference compared to the conventional way of detecting the voltage across electrodes.

9.4 Proposals for Further Work

For mechanical properties of resistance welding machines, based on the test set-up used in this project, future work should be carried out to design a test device in which the "*free breaking test*", force transducer, as well as displacement transducer are integrated, so that it can be easily applied for measurements in situ without or with very little connections to the machine.

The models characterizing both mechanical and electrical characteristics of resistance welding machines developed in this project should further be applied to the simulation software SORPAS, developed for resistance welding analysis at this department.

References

1. **RWMA**, *Resistance Welding Manual*, Fourth Edition, Resistance Welder Manufacturer's Association, 505 Arch St., Philadelphia, Pa. 1989.

2. http://www.weldtechnology.com/rwintroduction .html.

3. **Tomson, E.,** Electric Welding, *The Electrical World*, Dec. 1886.

4. **S A Westgate**, Resistance welding — state of the art. *Welding and Cutting*, 55 (5), 2003, 256-260.

5. **S. A. Westgate**, A general overview of recent deveopments in resistance welding, *Proceedings of 2nd international seminar on advances in resistance welding*, Aachen, Germany, Nov. 2002.

6. **W. H. Kearns,** AWS, *Welding Handbook*, Seventh edition, Miami, Florida, 1980.

7. *Overview of resistance welding*, http://www.livco.com/UMchapter1.pdf.

8. *Basic inverter theory*, http://www.kvawelding.com/basicinvertertheory.html.

9. **Zhengxing Zhu etc.** *Technology of Resistance Welding* , China machine press, Beijing, 2000. (in Chinese)**.**

10. **W. F. Hess and R. A. Wyant,** A method of studying the effects of friction and inertia in resistance welding machines. *Welding Journal,* 1940. 10.

11. ISO 669-1981 **(**E). *Rating of Resistance Welding Equipment*. 10-15, First edition.

12. **T. Satoh and J. Katayama,** A study on the influence of the stroke of the upper electrode on spot welding alloy. *IIW III-272-65*, 1965.

13. **F. J. Gannowski and N. T. Williams**, Advances in resistance spot and seam welding of zinc-coated steel strip. *Sheet Metal Industries*, 49 (11), 1972, 692- 704.

14. **M. W. Kolder and A. W. Bosman,** Influence of the welding equipment on the weldability lobe of an HSLA-steel. IIW Doc. No. III-796-84. Research and Development, Ijmuiden, The Netherlands.

15. **T. Satoh , J. Katayama, and T. Nakano**, Effect of mechanical properties of spot welding machine on spot weld quality. *IIW Doc. No. III-912-88,* 118-122.
16. **T. Satoh, T. Nakamura, and K. I. Matsuyama,** Current status of research and development on resistance spot welding machines in Japan. *DVS-124*, 1989, 70-79.

17. **H. J. Krause and B. Lehmkuhl,** Measuring the dynamic mechanical characteristics of spot and projection welding machines, and measured parameters, measuring procedures and initial results. *Doc. IIW/IIS 111-790-84.*

18. **M. Romer, H. Press and H. Krause**, Mechanical properties of resistance spot welding machines and their mathematical determination. *Welding in the World* 28(9) 1990: 190-196.

19. **M. Lipa**, Mechanical Properties of resistance spot and projection welding machines. *Welding International* 6(8) 1992: 661-667.

20. **M. Lipa**, Mechanical Properties of resistance (especially spot and projection welding) machines. *Welding International* 6(10) 1992: 831-835.

21. **T. Satoh and J. Katayama**, Mechanical properties of spot welding machines and the effects on weld quality. *Welding Technique,* 35(3) 1987: 52-58.

22. **O. Hahn, L. Budde and D. Hanitzsch,** Investigations on the influence of the mechanical properties of spot welding tongs on the welding process. *Welding and Cutting,* no.1 1990: 6-8.

23. **L. Dorn and P. Xu**, Relationship between static and dynamic machine properties in resistance spot welding. *Welding and Cutting,* no.1 1992: 19-22.

24. **L. Dorn and P. Xu**, Influence of the mechanical properties of resistance welding machines on the quality of spot welding. *Welding and Cutting,* no.1 1993: 12-26.

25. **L. Dorn and P. Xu**, Influence of the mechanical characteristics of the machine on the dynamic behaviour in aluminum projection welding. *Welding and Cutting,* no.1 1995: E2-E5.

26. **H. Tang, W. Hou etc.** Force characteristics of resistance spot welding of steels. *Welding Journal* 79(7) 2000: 175-s to 183-s.

27. **H. Tang, W. Hou etc.** Influence of welding machine mechanical characteristics on the resistance spot welding process and weld quality. *Welding Journal* 82(5) 2003: 116-s to 224-s.

28. **K. Fujimoto et al.,** Design and construction of a loading system for resistance welding and its dynamic properties: Optimization of the loading system in high current

density spot welding with a short energizing time (1st Report). *Welding International*, 11(5) 1997:371-377.

29. **K. Fujimoto et al.,** Relationship between loading properties and resistance weldability, and an optimum loading system for weldability: Optimization of the loading system in high current density spot welding with a short energizing time (2nd Report). *Welding International*, 11(5) 1997:378-383.

30. **H. J. Krause and B. Lehmkuhl,** A comparision of the dynamic mechanical characteristics of spot welding machines. *Welding and Cutting*, 1985, 1.

31. **M. Malberg**, Characterization of mechanical and electrical properties of resistance projection welding machine. *Ph.D. dissertation.* Lyngby, DK., Technical University of Denmark, 1997. (In Danish).

32. **Z. Feng et al.,** Analytical models for mechancal dynamics of resistance spot welding machin*e. Resistance Weding: Theory and Applications Conference*, American Welding Society, October 13-16, 1997.

33. **L. Kristensen**, Projection welding of complex geometries. *Ph.D. dissertation.* Lyngby, DK., Technical University of Denmark, 2000.

34. **H. Murakawa and Y Ueda**, Mechanical study of the effect of initial gap upon weldability in spot welding. *Welding International*, 5 (1) 1991: 11-17.

35. **Wenqi Zhang,** Industrial applications of computer simulation in resistance welding. *International Journal for the Joining of Materials*, 15(3), 2003: 9-16.

36. **L. Kristensen and C. B. Hansen,** 1996. Pressvejsning – Mekaniske egenskaber ved pressvejsning (Resistance projection welding – Mechanical properties in resistance projection welding). *M.Sc. thesis*, Lyngby, DK, Technical University of Denmark (In Danish).

37. **A. Biran,** *MATLAB 5 for engineers*, New York, Prentice Hall. 1999: 377-396.

38. www.fjedre.dk.

39. **W. Weaver, JR., S. P. Timoshenko and D. H. Young.** *Vibration problems in engineering*. New York, N. W. Y., Wiley. 1990: 84-93.

40. Instruction manual of EXPERT-DC-Inverter resistance welding machine.

41. Instruction manual of TECNA, Item 810X, resistance welding machine, 1995,7.
`

42. **Pei Wu, Wenqi Zhang and Niels Bay,** A method for identifying the mechanical parameters in resistance spot welding machines. *International Journal for the Joining of Materials*, 15(4), 2003: 26-29.

43. **Pei Wu, Wenqi Zhang and N. Bay,** Determination on maximum follow-up speed of electrode system of resistance projection welders. *International Journal for the Joining of Materials*. 16(2), 2004: 33-36.

44. **Pei Wu, Wenqi Zhang and N. Bay,** Characterization of dynamic mechanical properties of resistance spot welding machines. [submitted to : *Welding Journal*].

45**. Pei Wu**, **Wenqi Zhang and Niels Bay**, Testing and modelling of mechanical characteristics of resistance welding machines. *Proc. 11th Int. Conf. on Joining of Materials – JOM-11, May 25-28, 2003,Hesingør, Denmark.*

46. **Pei Wu, Wenqi Zhang and Niels Bay**, Identification of mechanical parameters for resistance welding machines**.** *Nordic MATLAB Conference*, Oct. 23-24th, 2003, Denmark.

47. **Andrews D R and Bhattacharya S** Dynamic resistance and its application to in-process control of spot welding. *Exploiting Welding in Production Technology*, Vol. I, 1975: 221-227 (Conference paper).

48.**Gould J E**, An examination of nugget development during spot welding using both experimental and analytic techniques, Welding J. 66**,** 1987:1-10s.

49. **Livsits A G**, Universal quality assurance method for resistance spot welding based on dynamic resistance. *Welding J.* 76**,** 1997: 383-390.

50. **Dickinson D W**, Characterization of spot welding behaviour by dynamic electrical parameter monitoring, *Welding J.* 59**,** 1980: 170-176.

51. **Na S J and Park S W**, A theoretical study on electrical and thermal response in resistance spot welding. *Welding J.* 75, 1996: 233-41s.

52. **Roberts W L**, Resistance variations during spot welding. *Welding J.* 30, 1951: 1004- 1019s.

53. **Gedeon S A *et al***, Measurement of dynamic electrical and mechanical properties of resistance spot welds. *Welding J.,* 66**,** 1987: 378-85s.

54. **Min Jou**, Real time monitoring weld quality of resistance spot welding for the fabrication of sheet metal assemblies. *Journal of Materials Processing Technology* 132 2003: 102-113.

55. **Weber G**, Instant-related description of the electrical relationships in the secondary circuit of resistance welding equipment. *Welding and Cutting* 48, 1996: E8-E10.

56. **Weber G *et al,*** Description of the electrical processes in the secondary circuit of resistance welding equipment. *Welding in the World* 33, 1994: 8-13.

57. **Y. Cho and S. Rhee**, New technology for measuring dynamic resistance and estimating strength in resistance spot welding. *Measurement Science and Technology* 11 2000: 1173-1178.

58. **Y. Cho and S. Rhee,** Primary circuit dynamic resistance monitoring and its application to quality estimation during resistance spot welding. *Welding J*. 81, 2002: 104-111s.

59. **Siva Dhandapani, Michael Bridges and Elijah Kannatey-Asibu San Diego**, Nonlinear electrical modeling for the resistance spot welding process. *Proc. of the American control conf*., California, 1999: 182-186.

60. **D. E. Destefan**, Mathematical modeling of part voltage and weld current in resistance welders. *RFP-4218*: 1990: 1-9.

61. **M. Malberg and N. Bay**. Methods for characterizing electrical systems of resistance welding machines, *Welding Journal*, 77(4), 1998: 59-62.

62. **W. Zhang and T. Funder-Kristensen**, Finite element modelling of resistance welding process. *Proceedings of the 8thInternational Conference on Joining of Materials,* Hesingør, Denmark, 1997:266-233.

63. **Quangfeng Song**, Testing and modelling of contact problems in resistance welding. *Ph.D. thesis.* Lyngby, DK., Technical University of Denmark, 2003.

64. **C.T.A. Johnk**. *Electromagnetic Fields and Waves*. New York, NY, John Wiley & Sons. 1975: 521-529.

65. **T. K. Chu and C. Y. Ho**, Thermal conductivity and electrical resistivity of AISI stainless steel. *Thermal Conductivity*, New York, NY Plenum Press, 1978: 88.

66. **Pei Wu, Wenqi Zhang and N. Bay,** Characterization of dynamic electrical properties of resistance spot welding machines. [submitted to :*Welding Journal*].

67. **Thornton P H *et al,*** Contact resistance in spot welding. *Welding Journal,* December,1996:402-412s.

68. **Savage W F *et al***, Dynamic contact resistance of series spot welds, *Welding Journal,* 1978: 43s-50s.

69. Welding control unit TE180 – TECNA
Release softwaren N 5.40
User manual

70. TECNA® , Resistance Welders
Item 810X
Installation and Use Instruction Manual

71. **S. N. Alksandrov, A. B. Mamyrin and M. M Farka,** Installation of the sensor of electrode in resistance welding machines. *Svarochnoe Proizvodstvo,* 1, 1985:30-31.

72. **H. Murakawa and Y. Ueda,** Mechanical study of the effect of initial gap upon weldability in spot welding. *Welding International,* 5 (1), 1991:11-17.

73. **Y. Cho and S. J. Hu and W. Li**, Resistance spot welding of aluminium and steel: a comparative experimental study. *Engineering Manufacturing,* 217(B10), 2003:1355 – 1363.

74. **Brian Rooks,** Feature advances in resistance welding for body-in-white. *Assembly Automation,* 23(2), 2003: 159-162.

75. **Y. Cho and S. Rhee,** Experimental study of nugget formation in resistance spot welding. *Welding Journal*, 82(8), 2003: 195s-201s.

76. **Primoz Podrzaj etc.** Expulsion detection system for resistance spot welding based on a neural network. *Measurement Science and Technology*, 15 (2004) 592-598.

77. **Y. Cho and S. Rhee,** Quality estimation of resistance spot welding by using pattern recognition with neural networks. *IEEE Transactions on Instrumentation and measurement,* 53(2), 2004: 330-334.

78. **K. Matsuyama, etc.,** A real-time monitoring and control system for resistance welding spot welding. *Proceedings of Eleven International Conference on Computer Technology in Welding,* 2002: 183-200.

79. **A. G. livshits**, Universal quality assurance method for resistance spot welding based on dynamic resistance. *Welding Journal,* 76(9), 1997: 383 – 390s.

80. **Justin Shriver, etc.,** Control of resistance spot welding. *Proceedings of the American Control Conference*, San Diego, California, June, 1999: 187 – 191.

81. **Xingqiao Chen and Kenji Araki,** Fuzzy adaptive process control of resistance spot welding with a current reference model. *Proceedings of International Conference on Intelligent Processing Systems*, Beijing, China, 1997: 190 – 194.

82. **A. Kirchheim,** Electrode force as an important process. *Welding and cutting*, 54 (3), 2002: 130 – 131.

83. **Y. V. Kamat,** In-process monitoring of resistance spot welding. *Proceedings of SPIE*, 1993: 650 – 659.

84. **J. P. Boillot, etc.,** Adaptive welding by fiber optic thermograghic sensing: An analysis of thermal and instrumental considerations. *Welding Journal,* 64 (7), 1985: 209s – 217s.

85. **Dawn R. White and Jerald E. Jones,** A hybrid hierarchical controller for intelligent control of welding processes. *Proceedings of the 2nd International Conference on Trends in Welding Research,* Gatlinburg, Tennessee, USA, 14-18 May, 1989: 909 – 915.

86. **G. E. Cook, K. Andersen and R. J. Barrett,** Feedback and Adaptive control in welding. *Proceedings of the 2nd International Conference on Trends in Welding Research,* Gatlinburg, Tennessee, USA, 14-18 May, 1989: 891 – 903.

87. **T. W. Eagar,** resistance welding: A fast, inexpensive and deceptively simple process. *Proceedings of the 3rd International Conference on Trends in Welding Research,* Gatlinburg, Tennessee, USA, 1-5 June, 1992: 347 – 357.

88. **P. Pan and D. F. Watt,** Modeling weld microstructural development in resistance welded high carbon steel. *Proceedings of the 3rd International Conference on Trends in Welding Research,* Gatlinburg, Tennessee, USA, 1-5 June, 1992: 293 – 299.

89. **E. W. Kim,** Analysis of resistance welding spot welding lobe curve. *ScD. Thesis*, MIT, Cambridge, MA (1989).

90. **C. M. Calva**, Correlations between resistance spot weldability and thermal contact conductance. *S. M. Thesis*, MIT, Cambridge, MA (1990).

91. **S. M. Zuniga and S. D. Sheppard**, Determining the strain hardening characteristics in the heat affected zone of a resistance spot weld. *Proceedings of the 3rd International Conference on Trends in Welding Research,* Gatlinburg, Tennessee, USA, 1-5 June, 1992: 643 – 647.

92. **C. P. Chou and C. H. Lu**, Weldability studies of high strength aluminum alloys using GlEEBLE SICO test. *Proceedings of the 3rd International Conference on Trends in Welding Research,* Gatlinburg, Tennessee, USA, 1-5 June, 1992: 763 – 767.

93. **D. R. White and J. A. Carmein**, Integration of process and control models for intelligent control of welding. *Proceedings of the 3rd International Conference on Trends in Welding Research,* Gatlinburg, Tennessee, USA, 1-5 June, 1992: 883 – 887.

94. **Jerry E. Gould and Timothy V. Stotler,** Effects of transformer tap settings on the resistance spot weldability of hot- dipped galvanized steel: nugget development studies. *International congress and exposition,* Detroit, Michigan, February 26 – March 2, 1990.

95. **Dennis E. Destefan,** Calibration and testing facility for resistance welding current monitors. *IEEE Transactions on Instrumentation and Measurement*, 45(2), April 1996: 453 -456.

96. **John R. Birchfield**, How to compare resistance welders. *Welding Design & Fabrication,* Sept. 1986: 56 – 59.

97. **A. M. Luciano and M. Savastano,** Wide band transformer based on a split-conductor current sensor and a Rogowski coil for high current measurement. *Proceedings of the 1995 IEEE Instrumentation and Measurement Technology Conference*, 04/23-26/1995: 454 – 458.

98. **M. prat and T. Desanlis**, Metrological analysis of a high current measurement system. *Proceedings of the 1998 Conference Precision Electromagnetic Measurements*, 07/06-10/1998: 361-362.

99. **Soo Woong Park and Suck Joo Na,** A new current measurement method in resistance spot welding. *IEEE Transactions on Instrumentation and Measurement*, 39 (5), 1990: 767 – 772.

100. **G. R. Archer**, A new system for automatic feed back control of resistance spot welding. *Welding Journal*, Oct. 1959: 987 – 993.

101. **D. N. Waller,** Head movement as a means of resistance welding quality control. *British Welding Journal*, Mar. 1964: 118 – 122.

102. **K. I. Johnson and J. C. Needham,** New design of resistance spot welding machine for quality control. *Welding Journal,* Mar. 1972: 122s – 131s.

103. **O. E. Martin**, Resistance weld for maintaining weld quality. *Welding Journal,* Aug. 1976: 655s – 660s.

104. **R. T. wood, etc.,** A closed-loop control system for three-phase resistance spot welding. *Welding Journal*, Dec. 1985: 26s – 30s.

105. **IEEE Committee Report:** Instrumentation for resistance welding. *IEEE Trans. Ind. Gen. Appl*.,1970: 492 – 495.

Appendix A: Specifications for the Tested Machines

1. TECNA-AC-250 kVA

Location: Technical University of Denmark. Department of Manufacturing Engineering and Management. Building 427

Type description: 8105 TECNA 250 kVA/50% 380 Volt/50Hz

Control unit: TE 180

Electrical Properties

Type of welding current	AC			
Mains voltage	380 V			
Mains frequency	50 Hz			
Nominal power at 50% duty cycle, S_n	250 kVA			
Maximum welding power, S_{max}	810 kVA			
Transformer tap settings	1	2	3	4
Secondary no load alternate voltage U_{20}	8.4 V	9.5 V	10.5 V	11.8 V
Short circuit secondary current I_{20}				85 kA

Mechanical Properties

Force system	pneumatic	
Electrode force	min. -	max. 18.85 kN at 6.5 bar
Cylinder diameter	200 mm	
Throat gap, ***e***, and depth, ***l***,	***e*= -**	***l***=250mm
Mass of movable parts without electrode	35 kg (estimated)	Ref. [31]

2. EXPERT-DC-Inverter-170 kVA

Location: Technical University of Denmark. Department of Manufacturing Engineering and Management. Building 427

Type description : EXPERT 170 kVA/50% , middle frequency 1000 Hz

Control unit: Harms & Wende – HWI 2000 profile

Electrical Properties

Type of welding current	DC Inverter			
Nominal power at 50% duty cycle, S_n	170 kVA			
Maximum welding power, S_{max}	2×130 kVA			
Transformer tap settings	-			
Secondary no load alternate voltage U_{20}	10 V			
Short circuit secondary current I_{20}	60 kA			

Mechanical Properties

Force system	Hydraulic	
Electrode force	min. 800 N	max. 20 kN at 200 bar
Cylinder diameter	100 mm	
Throat gap, ***e***, and depth, ***l***,	$\boldsymbol{e}_{max}$=350mm	***l***=450mm
Mass of movable parts without electrode	20 kg (estimated)	Ref. [31]

Appendix B: Assessing the quality of a regression

In the present thesis, two ways have been used for curve fitting. One is to add the trend line for experimental curve in Microsoft Excel, which is assessed by R-squared value provided by software itself; the other is to fit the given mathematical model, and the fitting quality is assessed by calculating the correlation coefficient.

1. R-squared Value (R^2)

$$R^2 = 1 - \frac{SSE}{SST}$$

Where:

$$SSE = \sum (y_j - \bar{y})^2$$

$\bar{y}$ is the mean of the given y_j values, that is:

$$\bar{y} = \frac{\sum_{j=1}^{n} y_j}{n}$$

and

$$SST = \sum Y_j^2 - \frac{(\sum Y_j)^2}{n}$$

n is the number of points in the given y_j values.

2. Definition of Correlation Coefficient (R)

(a). A data set of N pairs of numbers:

n: 1, 2, 3 ……..N
x: x_1, x_2, $x3$…..…..…..…..…..…..x_N
y: y_1, y_2, y_3…….. y_N

(b). Averages of x and y values

$$\bar{x} = \frac{\sum x_i}{n}, \qquad \bar{y} = \frac{\sum y_i}{n}$$

(c). Standard deviations (σ_x and σ_y) of the *x* and *y* data sets:

$$\sigma_x = \sqrt{\frac{1}{N}\left[\sum (x_i - \bar{x})^2\right]}, \qquad \sigma_y = \sqrt{\frac{1}{N}\left[\sum (y_i - \bar{y})^2\right]}$$

(d). Calculate the covariance between the two data sets

$$\sigma_{xy} = \frac{1}{N}\left[\sum (x_i - \bar{x})(y_i - \bar{y})\right]$$

(e). The correlation coefficient is then defined as:

$$R = \frac{\sigma_{xy}}{\sigma_x \sigma_y}$$

$$= \frac{\frac{1}{N}\left[\sum (x_i - \bar{x})(y_i - \bar{y})\right]}{\sqrt{\frac{1}{N}\left[\sum (x_i - \bar{x})^2\right] \cdot \frac{1}{N}\left[\sum (y_i - \bar{y})^2\right]}}$$

$$= \frac{\left[\sum (x_i - \bar{x})(y_i - \bar{y})\right]}{\sqrt{\left[\sum (x_i - \bar{x})^2\right] \cdot \left[\sum (y_i - \bar{y})^2\right]}}$$

Appendix C:

Results of Projection Welding on TECNA-25kVA-AC Machine

Projection Welding 1.

Weld current: 17kA
Weld time: 4 cycles (60ms)
Electrode force: 4.45 kN
Weld quality: splashed

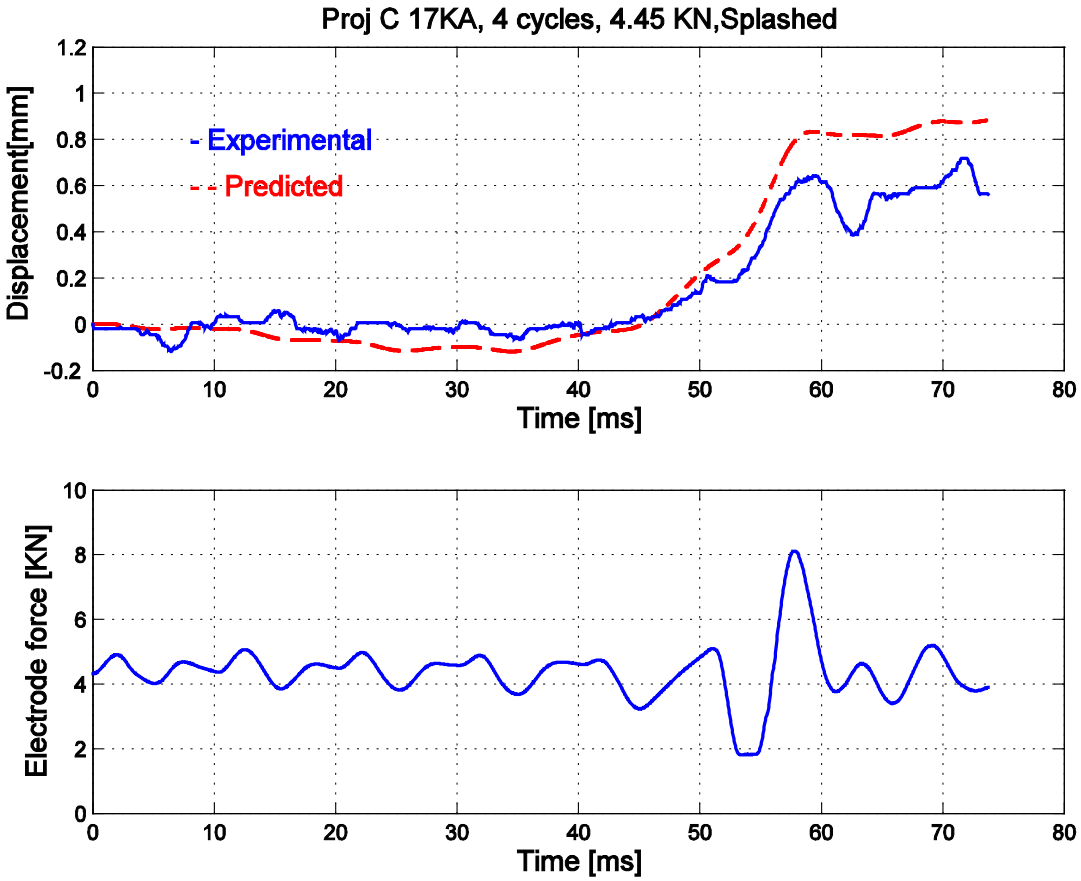

Upper trace — Comparison of tested and predicted displacements
Lower trace — Electrode force

Projection Welding 2.

Weld current: 18.6 kA
Weld time: 2 cycles (40ms)
Electrode force: 4.48 kN
Weld quality: good

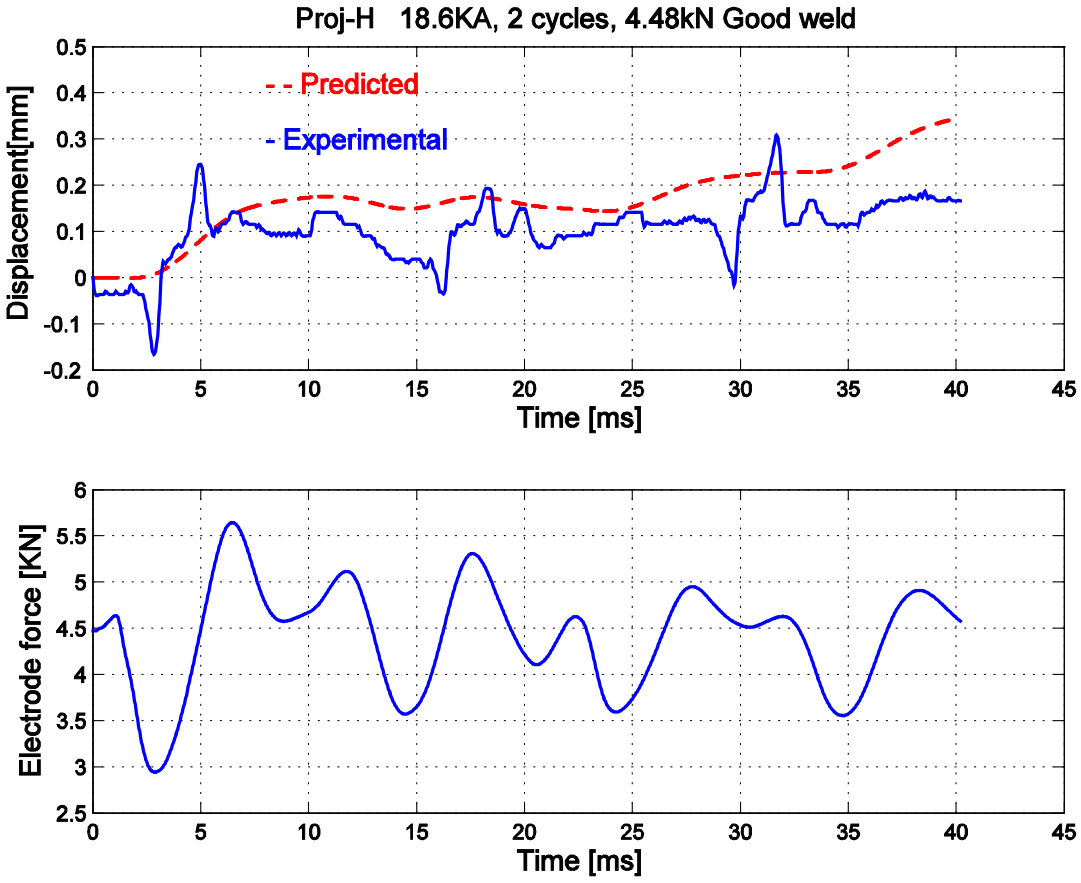

Upper trace — Comparison of tested and predicted displacements
Lower trace — Electrode force

Projection Welding 3.

Weld current: 18.9 kA
Weld time: 2 cycles (40ms)
Electrode force: 4.44 kN
Weld quality: splashed

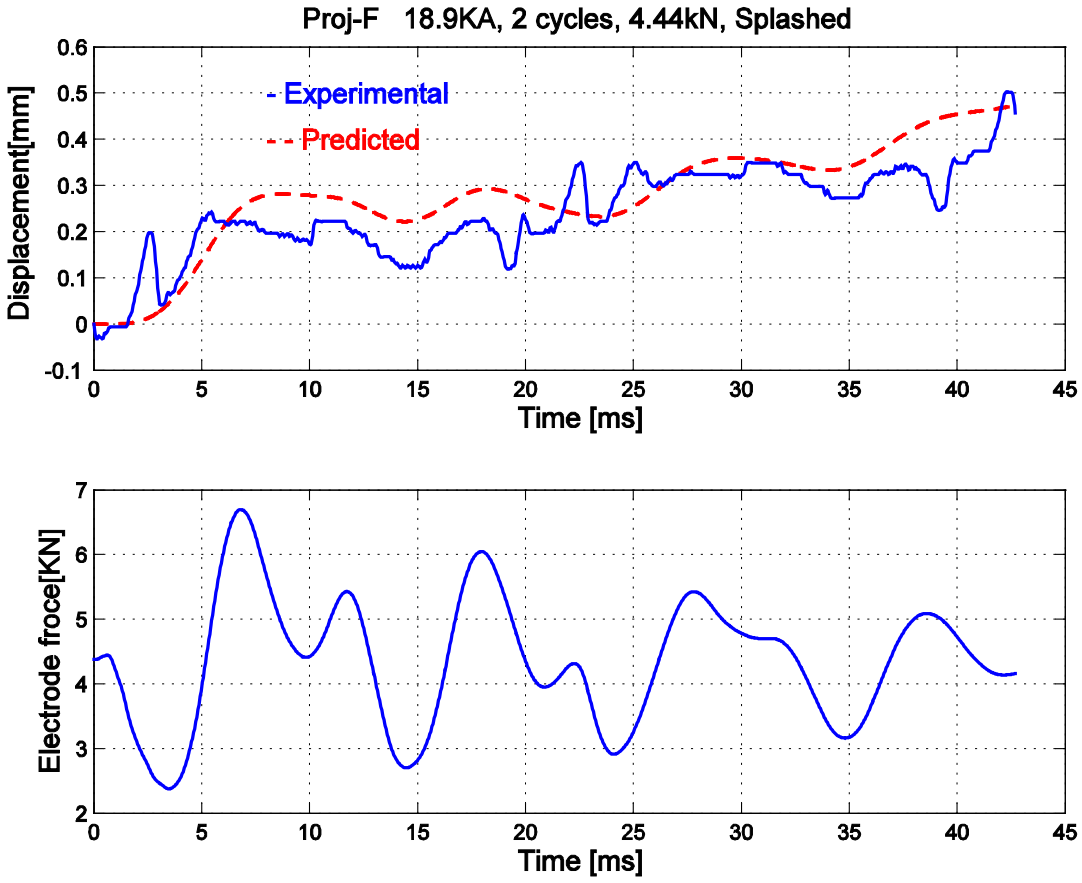

Upper trace — Comparison of tested and predicted displacements
Lower trace — Electrode force

Projection Welding 4.

Weld current: 16.3 kA
Weld time: 4 cycles (80ms)
Electrode force: 4.40 kN
Weld quality: splashed

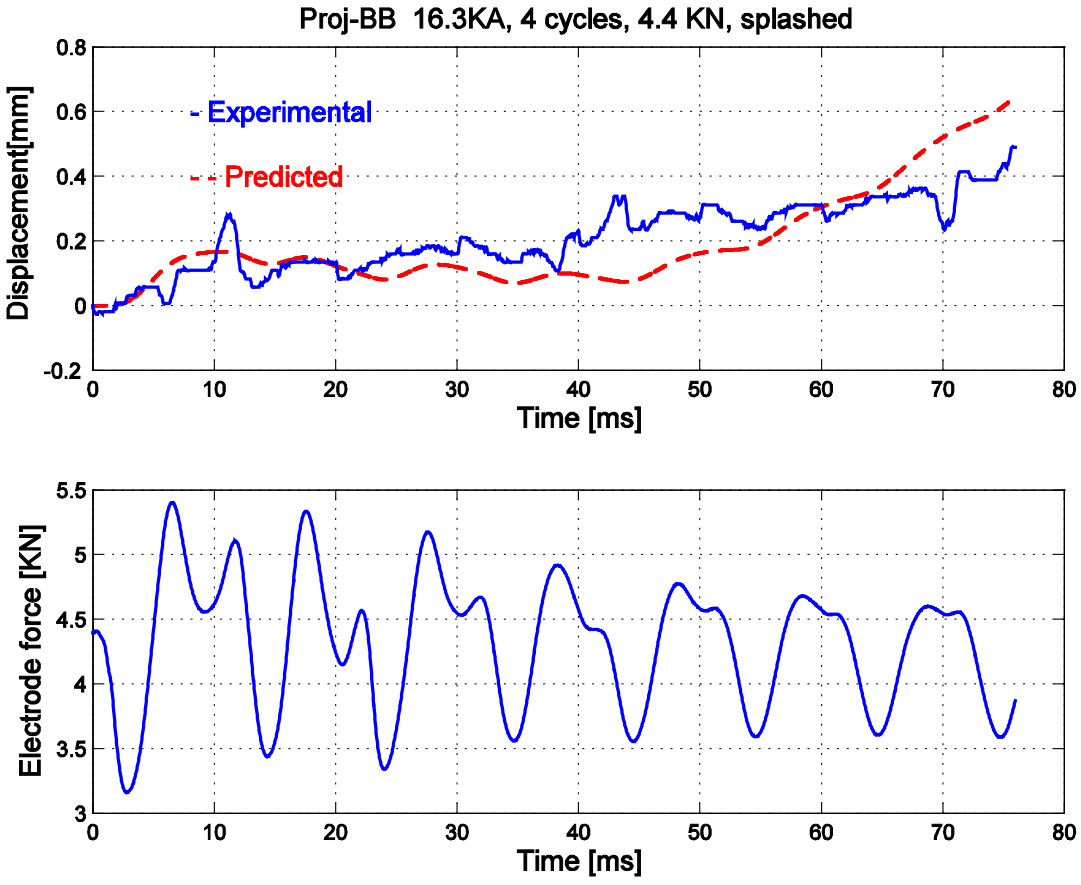

Upper trace — Comparison of tested and predicted displacements
Lower trace — Electrode force

Projection Welding 5.

Weld current: 16.6 kA
Weld time: 4 cycles (80ms)
Electrode force: 4.30 kN
Weld quality: splashed

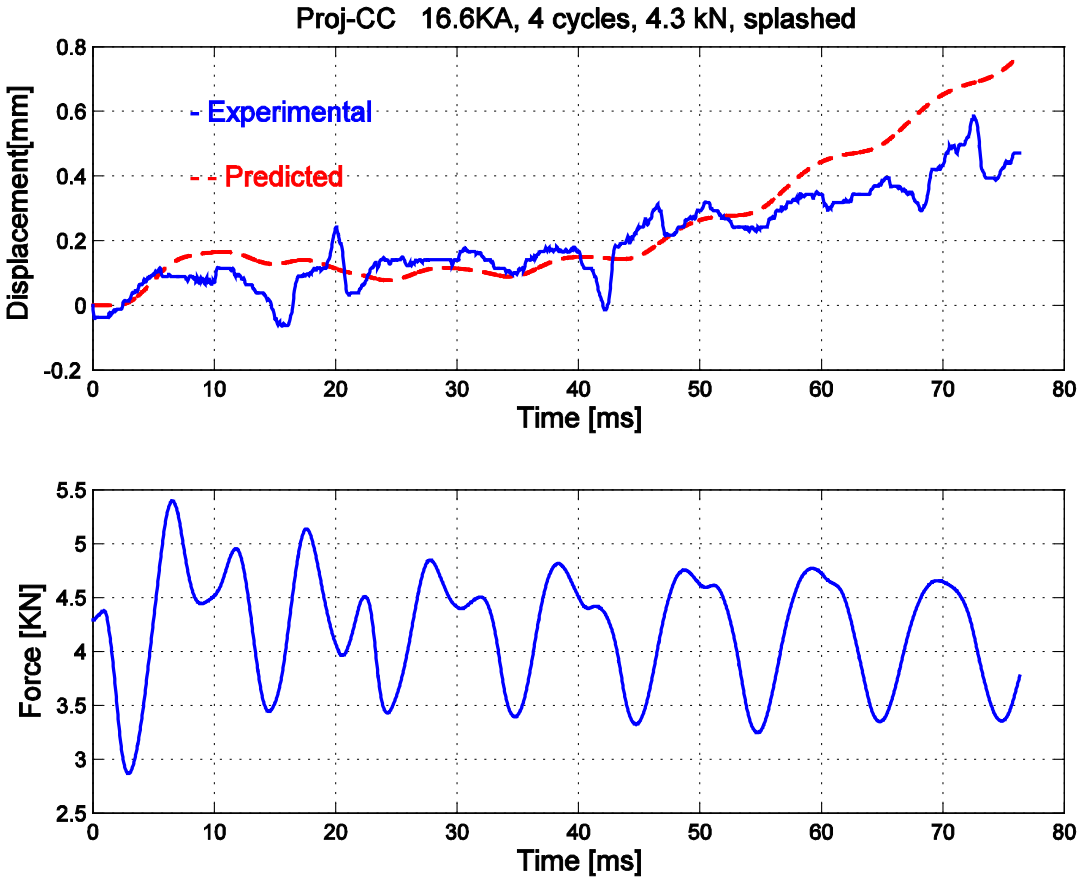

Upper trace — Comparison of tested and predicted displacements
Lower trace — Electrode force

Projection Welding 6.

Weld current: 18.9 kA
Weld time: 4 cycles (80ms)
Electrode force: 4.31 kN
Weld quality: splashed

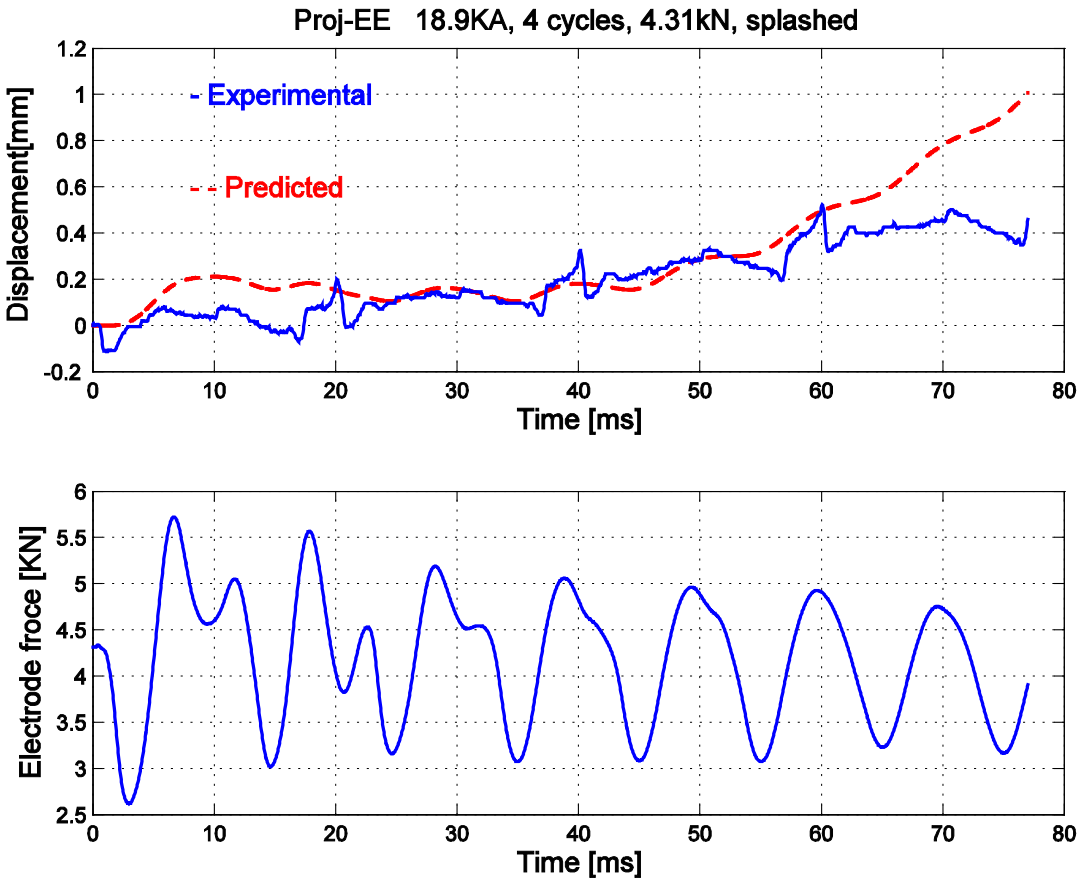

Upper trace — Comparison of tested and predicted displacements
Lower trace — Electrode force

Projection Welding 7.

Weld current: 14.9 kA
Weld time: 3 cycles (60ms)
Electrode force: 4.38 kN
Weld quality: good

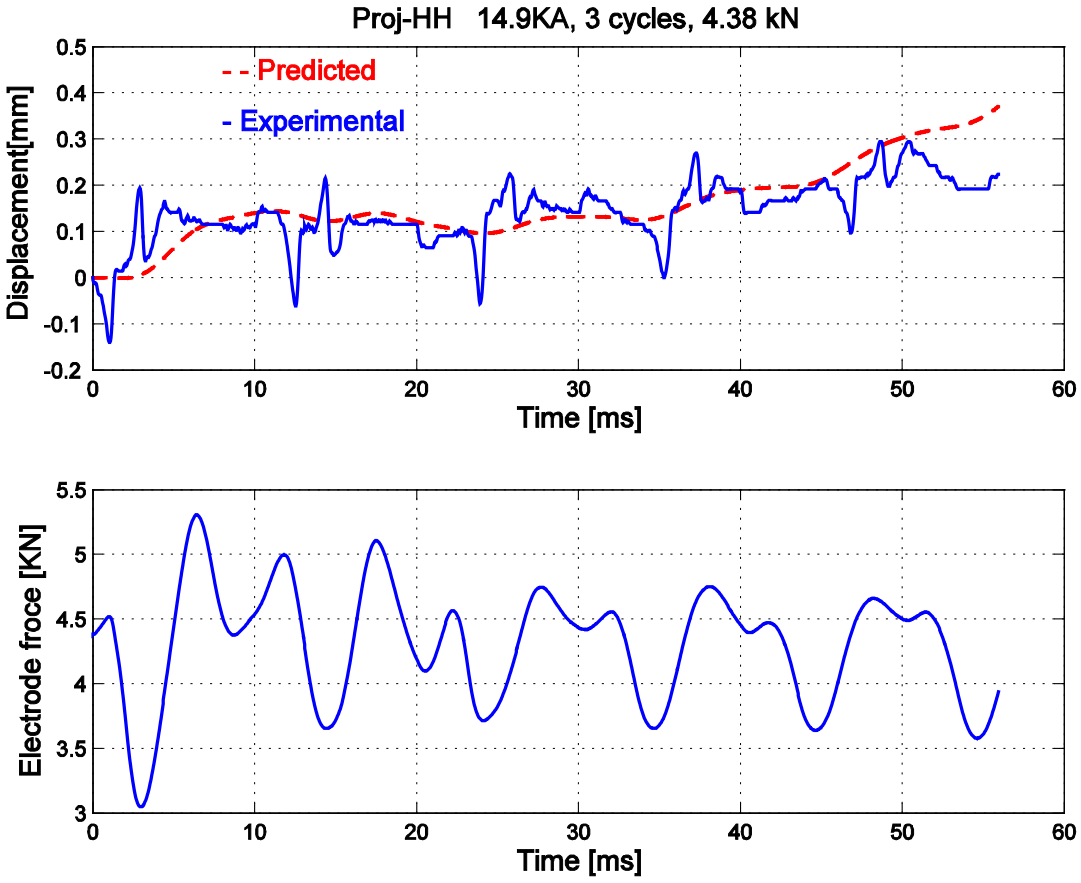

Upper trace — Comparison of tested and predicted displacements
Lower trace — Electrode force

Projection Welding 8.

Weld current: 16 kA
Weld time: 3 cycles (60ms)
Electrode force: 4.37 kN
Weld quality: little splash

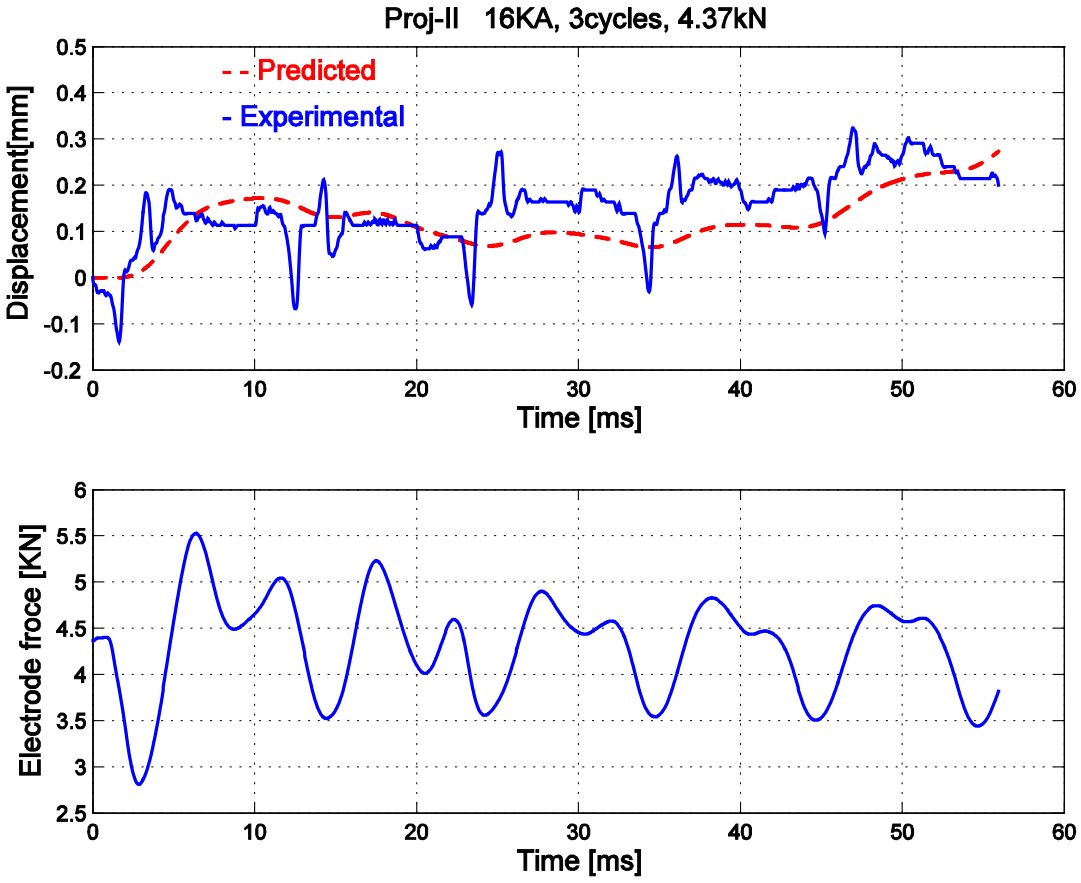

Upper trace — Comparison of tested and predicted displacements
Lower trace — Electrode force

Projection Welding 9.

Weld current: 17 kA
Weld time: 3 cycles (60ms)
Electrode force: 4.37 kN
Weld quality: good

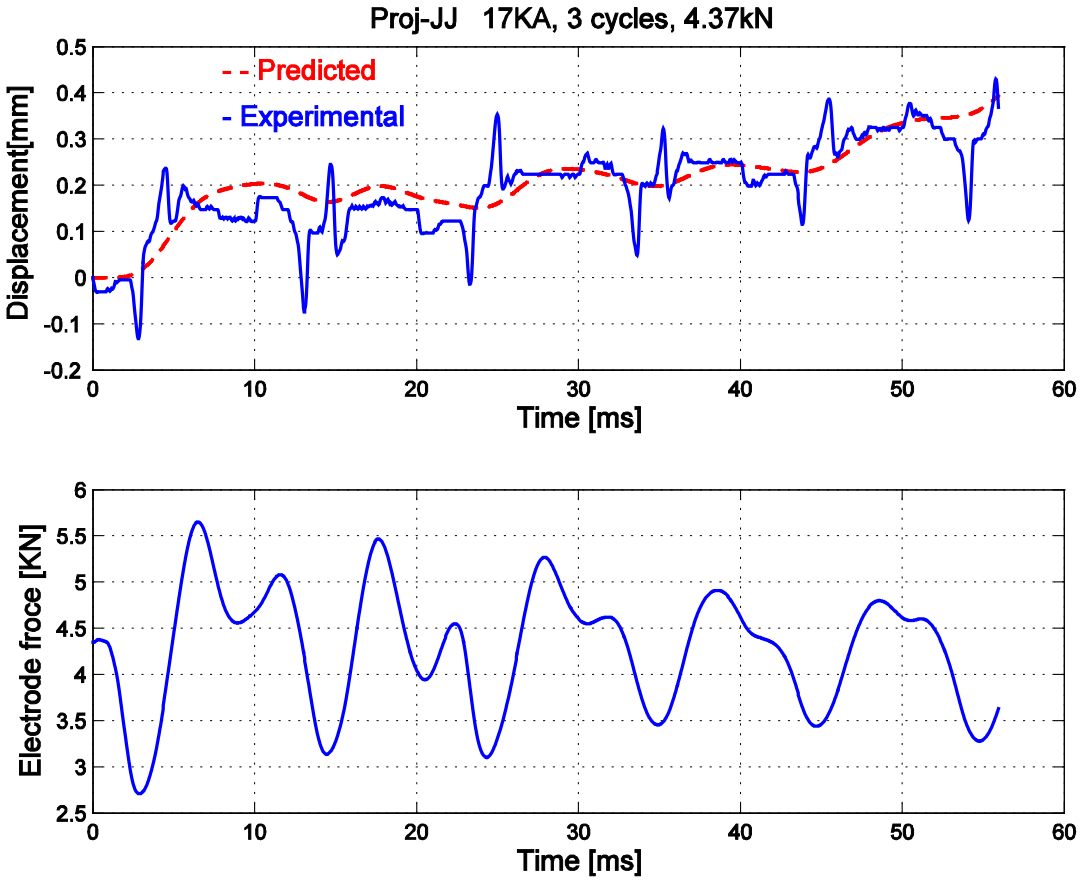

Upper trace — Comparison of tested and predicted displacements
Lower trace — Electrode force

Projection Welding 10.

Weld current: 18 kA
Weld time: 2 cycles (40ms)
Electrode force: 4.32 kN
Weld quality: splashed

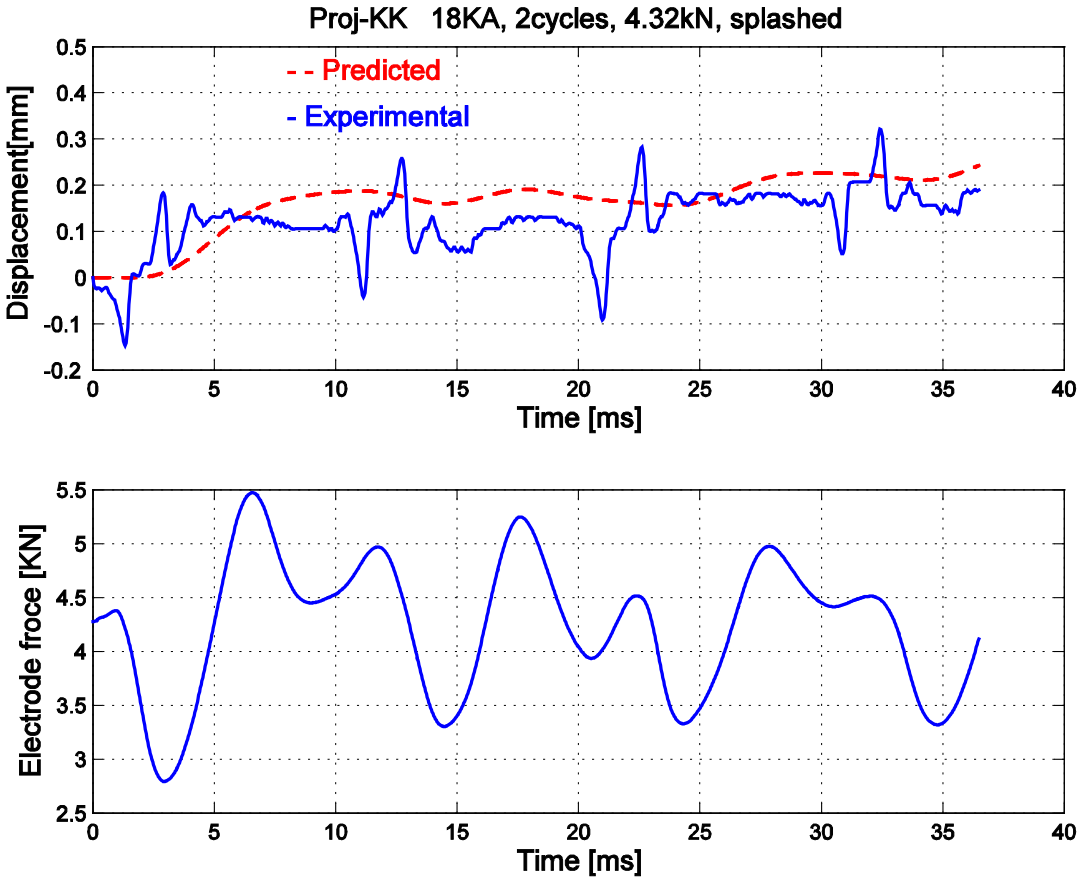

Upper trace — Comparison of tested and predicted displacements
Lower trace — Electrode force

Projection Welding 11.

Weld current: 18.6 kA
Weld time: 2 cycles (40ms)
Electrode force: 4.35 kN
Weld quality: little splashed

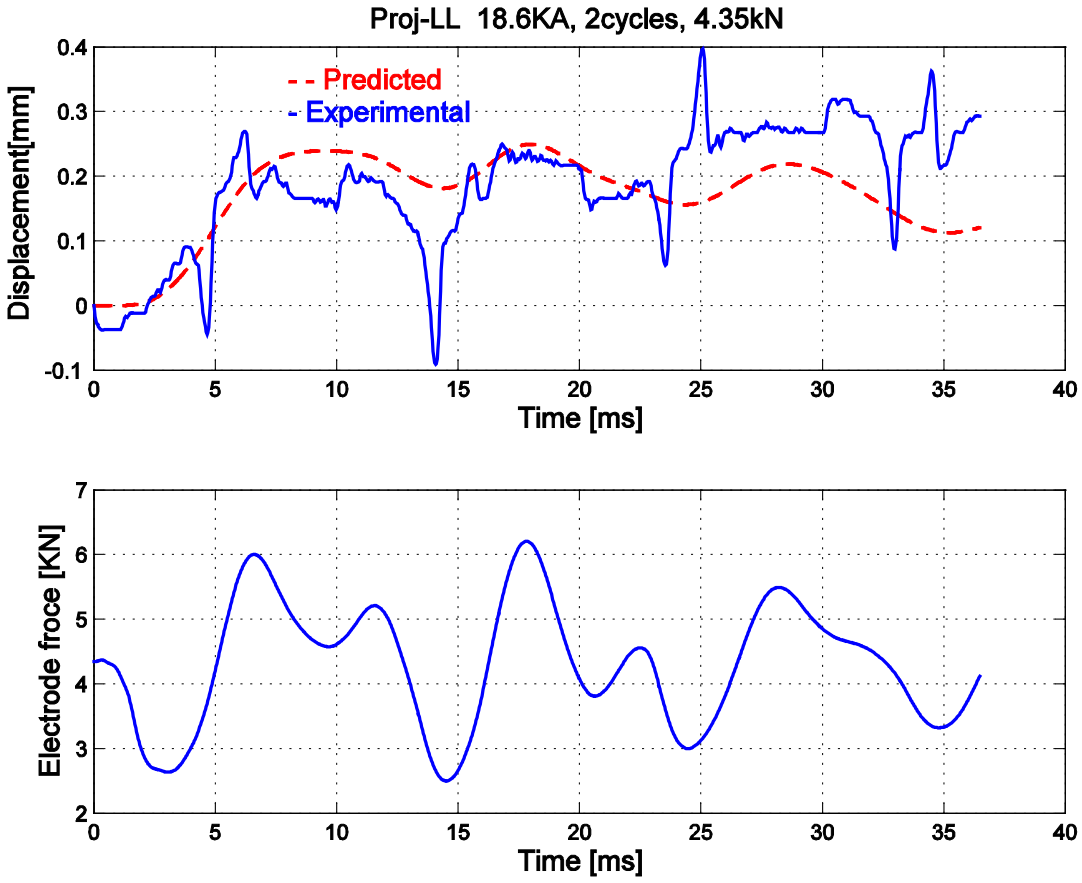

Upper trace — Comparison of tested and predicted displacements
Lower trace — Electrode force

Projection Welding 12.

Weld current: 17.1 kA
Weld time: 2 cycles (40ms)
Electrode force: 4.36 kN
Weld quality: splashed

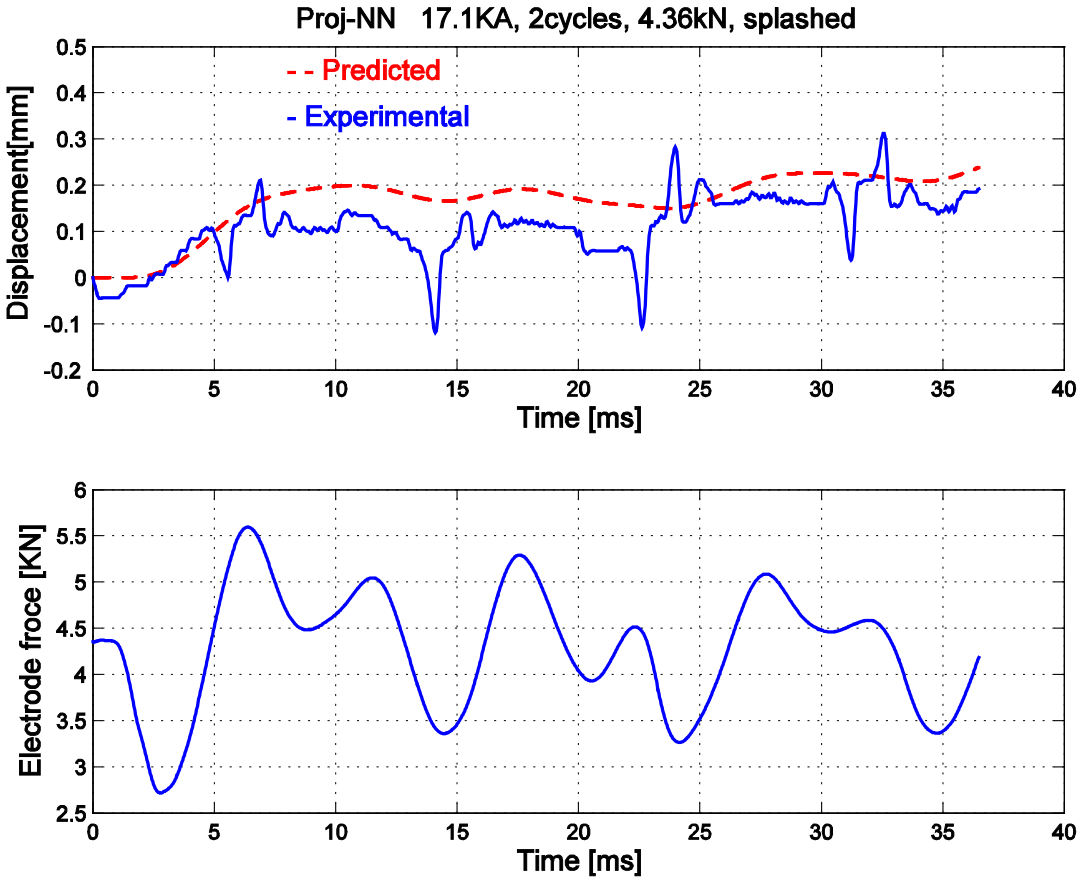

Upper trace — Comparison of tested and predicted displacements
Lower trace — Electrode force

Projection Welding 13.

Weld current: 17 kA
Weld time: 3 cycles (60ms)
Electrode force: 6.8 kN
Weld quality: little splashed

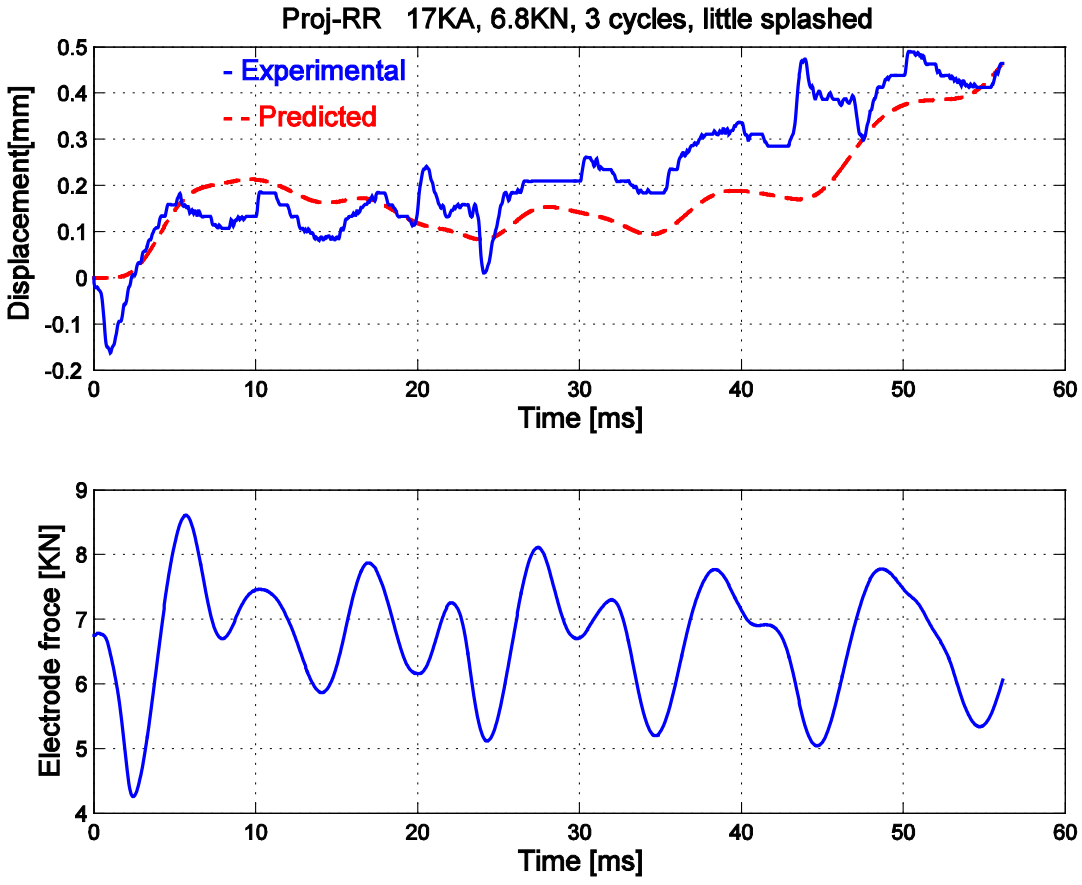

Upper trace — Comparison of tested and predicted displacements
Lower trace — Electrode force

Projection Welding 14.

Weld current: 17 kA
Weld time: 3 cycles (60ms)
Electrode force: 6.73 kN
Weld quality: good

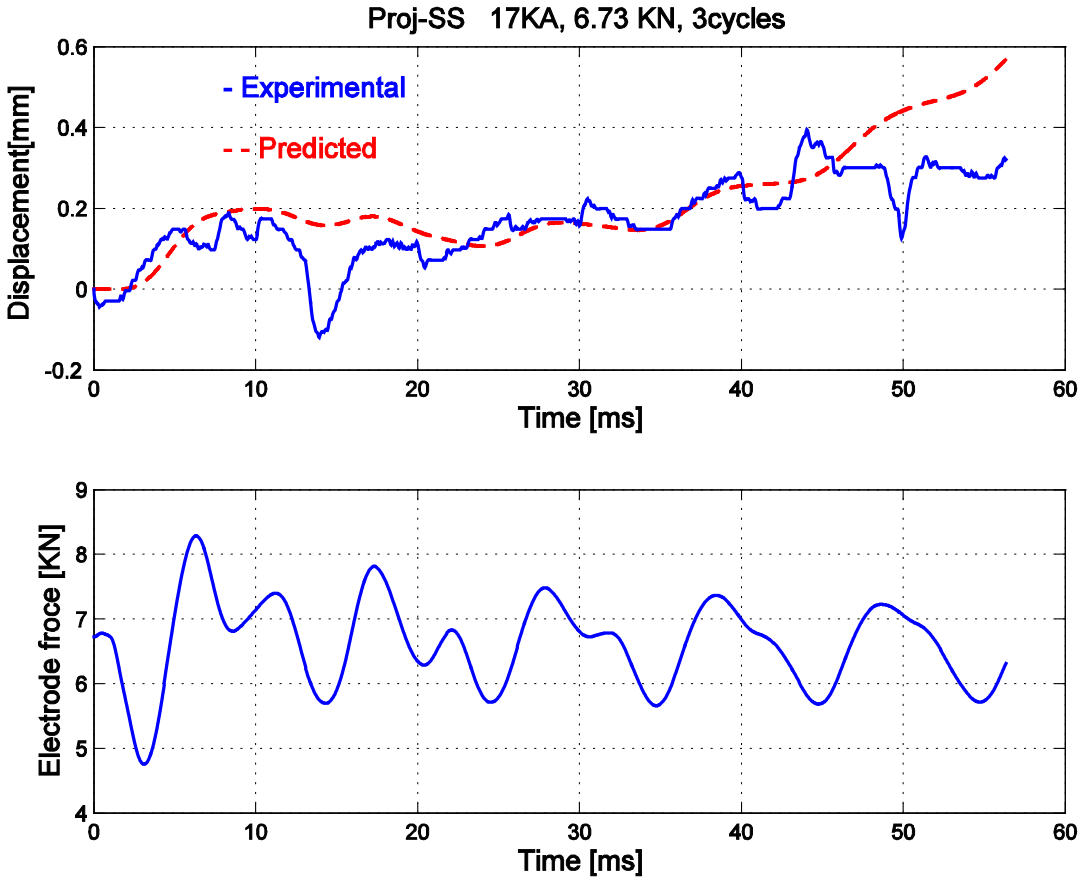

Upper trace — Comparison of tested and predicted displacements
Lower trace — Electrode force

Projection Welding 15.

Weld current: 18.8 kA
Weld time: 3 cycles (60ms)
Electrode force: 6.74 kN
Weld quality: good

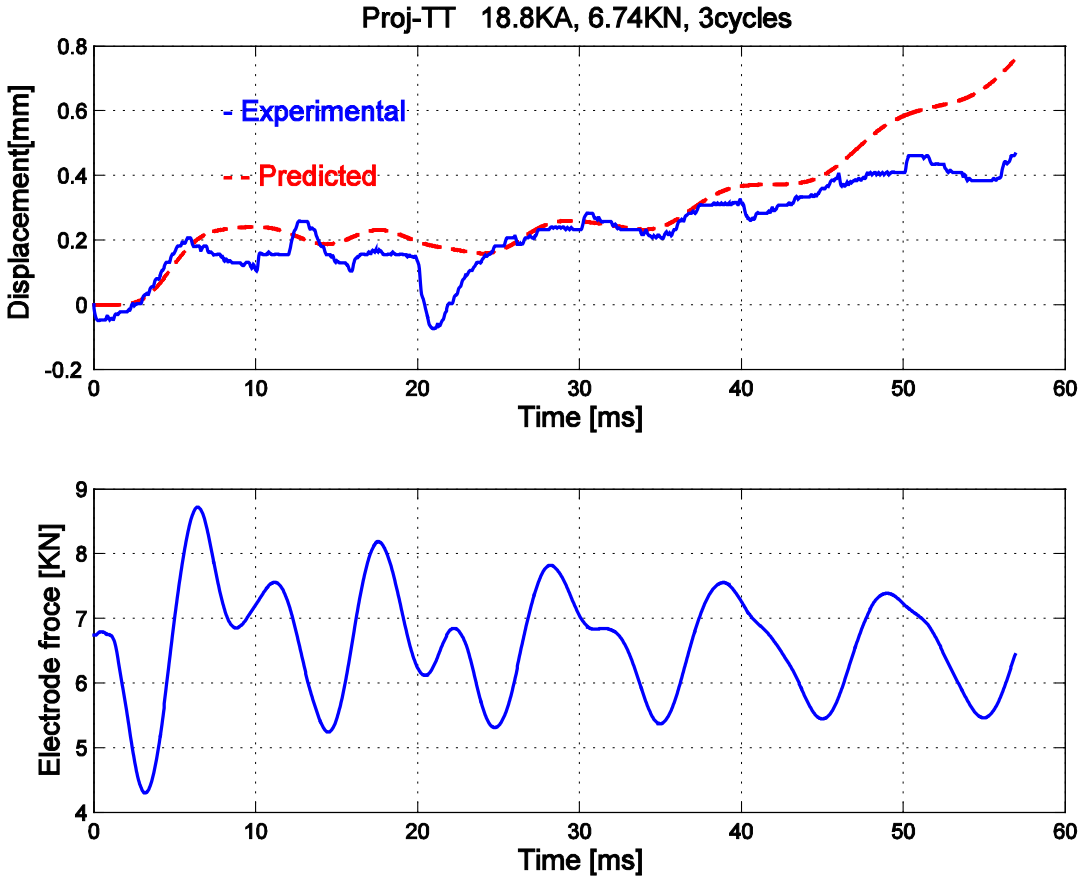

Upper trace — Comparison of tested and predicted displacements
Lower trace — Electrode force

Appendix D:

Electrical test results with reference resistances on TECNA-250kVA-machine

Table 1. Test results (1kA, 3kA, 5kA)

Test	Bar diameter (mm)	Set current (kA)	Measured current (kA)	Predicted current (kA)	Firing Angle (degree)	Conduction angle (degree)	R^2
I	8	1kA	1.71	1.73	142.7	43.7	0.997
	9		2.07	2.10	142.2	45.5	0.994
	10		2.32	2.35	142.7	46.3	0.995
	12		3.00	3.02	141.8	49.5	0.996
	14		3.37	3.45	141.7	51.3	0.990
	16		3.99	4.00	141.2	53.7	0.997
	18		4.21	4.25	141.2	54.6	0.994
	20		4.56	4.64	141.1	56.1	0.990
	24		5.52	5.24	140.3	58.6	0.992
	30		5.48	5.56	140.6	59.6	0.994
II	8	3kA	1.80	1.84	141.2	45.1	0.996
	9		2.19	2.23	140.9	46.9	0.995
	10		2.48	2.51	141.1	47.9	0.993
	12		3.21	3.30	139.7	51.7	0.991
	14		3.60	3.67	140.3	52.8	0.993
	16		4.28	4.36	139.2	55.9	0.991
	18		4.46	4.56	139.7	56.4	0.989
	20		5.00	5.11	138.9	58.6	0.990
	24		5.58	5.66	138.5	60.6	0.996
	30		6.13	6.22	138.2	62.6	0.995
III	8	5kA	2.01	2.04	138.5	47.8	0.998
	9		2.43	2.46	138.3	49.5	0.996
	10		2.74	2.79	138.5	50.5	0.995
	12		3.56	3.57	137.8	53.7	0.998
	14		4.01	4.06	137.8	55.5	0.994
	16		4.77	4.81	136.8	58.5	0.997
	18		5.07	5.10	137.1	59.3	0.997
	20		5.58	5.64	136.5	61.3	0.996
	24		6.30	6.37	135.7	63.9	0.998
	30		6.88	7.04	135.3	66.1	0.993

Table 2. Test results (7kA, 8kA, 10kA)

Test	Bar diameter (mm)	Set current (kA)	Measured current (kA)	Predicted current (kA)	Firing Angle (degree)	Conduction angle (degree)	R^2
I	8	7kA	2.10	2.15	137.1	49.3	0.991
	9		2.60	2.64	136.4	51.5	0.994
	10		2.94	2.93	137.1	51.9	0.995
	12		3.81	3.80	136.1	55.5	0.995
	14		4.25	4.27	136.5	56.8	0.993
	16		5.11	5.10	135.3	60.2	0.993
	18		5.48	5.52	135.1	61.6	0.996
	20		5.98	6.11	134.5	63.6	0.990
	24		6.70	6.79	1345.1	65.8	0.993
	30		7.30	7.42	134.0	67.7	0.992
II	8	8kA	2.19	2.19	136.6	49.8	0.997
	9		2.67	2.67	136.1	51.7	0.997
	10		3.03	3.08	135.7	53.3	0.992
	12		3.95	3.96	134.99	56.7	0.996
	14		4.43	4.48	135.2	58.2	0.993
	16		5.29	5.43	133.6	62.0	0.990
	18		5.59	5.65	134.4	62.3	0.994
	20		6.30	6.46	133.0	65.3	0.990
	24		6.78	6.88	133.8	66.2	0.993
	30		7.62	7.69	133.0	68.8	0.996
III	8	10kA	2.42	2.46	133	53.4	0.995
	9		2.92	2.98	132.8	55.0	0.996
	10		3.36	3.42	132.6	56.5	0.996
	12		4.35	4.40	131.95	59.8	0.999
	14		5.03	5.11	131.5	62.1	0.997
	16		5.91	6.02	130.6	65.2	0.997
	18		6.3	6.42	130.9	66.1	0.996
	20		6.99	7.11	130.3	68.3	0.997
	24		7.7	7.85	130.2	70.3	0.995
	30		8.51	8.62	129.95	72.4	0.998

Table 3. Test results (15 kA, 16 kA, 17 kA)

Test	Bar diameter (mm)	Set current (kA)	Measured current (kA)	Predicted current (kA)	Firing Angle (degree)	Conduction angle (degree)	R^2
I	8	15 kA	2.79	2.83	128.4	58.0	0.996
	9		3.43	3.46	127.9	60.0	0.998
	10		3.86	3.94	128.1	61.1	0.993
	12		5.02	5.02	127.7	64.1	0.998
	14		5.81	5.85	127.2	66.6	0.998
	16		6.96	7.05	125.6	70.5	0.997
	18		7.23	7.24	127.1	70.2	0.996
	20		8.22	8.35	125.4	73.8	0.996
	24		9.45	9.57	124.1	77.2	0.997
	30		10.10	10.30	124.5	78.8	0.994
II	8	16 kA	2.95	2.96	126.8	59.6	0.9979
	9		3.59	3.60	126.5	61.4	0.999
	10		4.15	4.16	126.1	63.1	0.9976
	12		5.424	5.50	124.5	67.4	0.995
	14		6.41	6.42	124.0	69.9	0.999
	16		7.33	7.30	124.4	71.8	0.997
	18		7.87	7.93	124.1	73.4	0.999
	20		8.75	8.75	123.6	75.5	0.999
	24		9.81	9.88	123.0	78.4	0.998
	30		10.8	10.81	123.0	80.5	0.999
III	8	17 kA	2.98	2.973	126.6	59.8	0.999
	9		3.61	3.62	126.3	61.6	0.999
	10		4.16	4.22	125.6	63.6	0.996
	12		5.44	5.42	125	66.9	0.999
	14		6.23	6.22	125.1	68.8	0.999
	16		7.47	7.53	123.3	72.9	0.999
	18		7.81	7.84	124.5	73.0	0.998
	20		8.9	9.02	122.7	76.6	0.998
	24		9.73	9.86	123.0	78.4	0.997
	30		11.12	11.33	121.4	82.3	0.995

Table 4. Test results (20 kA, 23 kA, 25 kA)

Test	Bar diameter (mm)	Set current (kA)	Measured current (kA)	Predicted current (kA)	Firing Angle (degree)	Conduction angle (degree)	R^2
I	8	20kA	3.2	3.25	123.1	63.3	0.992
	9		3.946	3.92	122.4	65.3	0.997
	10		4.56	4.56	122.6	66.6	0.998
	12		5.99	6.02	121.1	70.9	0.998
	14		6.927	6.96	120.95	73.0	0.999
	16		8.27	8.32	119.6	76.8	0.998
	18		8.98	9.04	119.3	78.5	0.999
	20		10.02	10.17	118.3	81.4	0.996
	24		11.32	11.46	117.5	84.4	0.997
	30		12.56	12.88	116.6	87.6	0.989
II	8	23 kA	3.48	3.50	120.0	66.4	0.997
	9		4.28	4.31	119.3	68.6	0.997
	10		4.92	4.96	119.2	70.0	0.998
	12		6.51	6.55	117.6	74.4	0.997
	14		7.52	7.55	117.6	76.4	0.999
	16		9.03	9.09	115.9	80.6	0.997
	18		9.72	9.75	116.2	81.7	0.999
	20		10.74	10.93	115.3	84.5	0.994
	24		11.82	11.93	115.9	86.2	0.998
	30		13.33	13.53	114.7	89.8	0.996
III	8	25 kA	3.6	3.63	118.4	68.0	0.997
	9		4.46	4.41	118.2	69.7	0.997
	10		5.09	5.11	117.9	71.3	0.999
	12		6.7	6.67	116.8	75.2	0.999
	14		8.09	7.94	115.45	78.6	0.997
	16		9.48	9.42	114.4	82.2	0.997
	18		10.1	9.41	113.9	82.5	0.996
	20		11.43	11.54	113.0	87.0	0.997
	24		12.73	12.83	112.9	89.4	0.999
	30		14.53	14.41	112.0	92.7	0.997

Table 5. Test results (28 kA, 30 kA, 32 kA)

Test	Bar diameter (mm)	Set current (kA)	Measured current (kA)	Predicted current (kA)	Firing Angle (degree)	Conduction angle (degree)	R^2
I	8	28kA	3.78	3.87	115.5	71.0	0.993
	9		4.67	4.75	114.8	73.1	0.994
	10		5.38	5.47	114.8	74.4	0.996
	12		7.18	7.26	112.9	79.2	0.996
	14		8.31	8.50	112.4	81.8	0.993
	16		10.10	10.21	110.7	86.0	0.995
	18		11.19	11.20	110.0	88.2	0.997
	20		12.20	12.31	110.1	90.1	0.997
	24		13.84	14.07	108.7	93.9	0.994
	30		15.40	15.63	108.3	96.7	0.995
II	8	30 kA	4.00	4.05	113.2	73.3	0.993
	9		4.94	4.99	112.4	75.5	0.993
	10		5.72	5.72	112.6	76.6	0.997
	12		7.63	7.63	110.4	81.6	0.996
	14		9.01	9.01	109.5	84.7	0.996
	16		10.7	10.80	107.9	88.8	0.995
	18		11.69	11.76	107.7	90.6	0.996
	20		13.12	13.20	106.6	93.6	0.995
	24		14.69	14.80	106.2	96.5	0.997
	30		16.5	16.65	105.3	100.0	0.995
III	8	32 kA	4.31	4.31	109.9	76.5	0.994
	9		5.35	5.35	108.8	79.1	0.995
	10		6.06	6.14	109.0	80.2	0.994
	12		8.17	8.27	106.2	85.9	0.991
	14		9.56	9.71	105.5	88.7	0.991
	16		11.60	11.72	103.5	93.3	0.994
	18		12.36	12.58	104.1	94.3	0.992
	20		14.11	14.35	102.2	98.2	0.992
	24		16.16	16.31	101.1	101.9	0.994
	30		17.22	17.57	102.6	102.9	0.993

Table 6. Test results (34 kA)

Test	Bar diameter (mm)	Set current (kA)	Measured current (kA)	Predicted current (kA)	Firing Angle (degree)	Conduction angle (degree)	R^2
I	8	34 kA	4.31	4.31	109.9	76.5	0.994
	9		5.35	5.35	108.8	79.1	0.995
	10		6.06	6.14	109.0	80.2	0.994
	12		8.17	8.27	106.2	85.9	0.991
	14		9.56	9.71	105.5	88.7	0.991
	16		11.60	11.72	103.5	93.3	0.994
	18		12.36	12.58	104.1	94.3	0.992
	20		14.11	14.35	102.2	98.2	0.992
	24		16.16	16.31	101.1	101.9	0.994
	30		17.22	17.57	102.6	102.9	0.993